



POLITECNICO MILANO 1863

Applied Space Mission Analysis and Design

AA 2024-2025

Professor: Michèle Roberta Lavagna

HORUS Mission

Person Code	Surname	Name
10710744	Bellini	Davide
10717230	Beretta	Beatrice
10725818	Biraghi	Giacomo
10738510	Braga	Matteo
10768663	Cappuccio	Manuel
10720695	Cataffo	Francesco
10741042	Cesarini	Lorenzo
10787552	Dowell	Matteo David
10726898	Juvara	Matteo Giovanni
10717720	Pacursa	Andrea Jimmy

Contents

1	Mission Overview	1
1.1	Mission Objectives	1
1.2	High Level Goals	2
2	Mission Environment Analysis	3
2.1	Environment Overview	3
2.2	Thermosphere	3
2.2.1	Atmospheric Density	4
2.2.2	Atmospheric Drag	5
2.2.3	Aerodynamic Heating	6
2.2.4	Atomic Oxygen and Molecular Nitrogen	6
2.2.5	Material Degradation	7
2.3	Electromagnetic Radiation	8
2.3.1	Solar Flux Overview	8
2.3.2	Earth Albedo Overview	8
2.3.3	Earth IR Radiation Overview	9
2.3.4	Refined Total Electromagnetic Flux Analysis	9
2.3.5	UV radiation	10
2.4	External Magnetic Field	10
2.4.1	Geomagnetic Storms	11
2.4.2	Magnetic Field Analysis	11
2.5	Charged Particles Effects	12
2.6	Optical Parameters Degradation	12
2.7	Eclipse Number and Beta Angle	12
2.8	Criticalities and Opportunities of the VLEO Environment	13
2.8.1	Criticalities	13
2.8.2	Opportunities	13
3	State of the Art	14
3.1	Introduction	14
3.2	Propulsion	14
3.3	Payload and On-Board Data Handling	15
3.4	Tracking, Telemetry, and Telecommand Subsystem	15
3.5	Attitude Determination and Control Subsystem	15
3.6	Electric Power Subsystem	15
4	Functional Analysis and Conceptual Operations	16
4.1	Functional Analysis and Decomposition	16
4.2	Phases	16
4.3	Conceptual Operations	17
4.4	System Modes	17
5	Mass Budget	19
6	Mission Architecture Solution	20
6.1	Trade-Off Analysis	20
6.2	Payload Selection	21
7	Launcher Analysis	24
7.1	Present Launchers	24
7.1.1	Launcher Performances	24
7.1.2	Fairing Volumes	25
7.2	Launchers Under Development	26

7.3	Launch Strategy	27
7.4	Launch Configuration	28
8	Mission Analysis	30
8.1	Nominal Orbit Design Process	30
8.1.1	Requirements Recap	30
8.1.2	Altitude and Eccentricity Selection	30
8.1.3	Downlink Strategy and J2 Perturbation	31
8.1.4	Coverage Analysis and Formation Flight	32
8.1.5	Revisit Time	37
8.1.6	Open points and Further developments	38
8.2	Orbit Insertion	40
8.3	Disposal Strategy	41
9	Guidance, Navigation and Control	42
9.1	Ballistic Coefficient	42
9.2	Station Keeping	42
9.2.1	Drag Compensation	42
9.2.2	Virtual Slot	43
9.2.3	Directional Adaptive Guidance	44
10	Propulsion Subsystem	49
10.1	Introduction	49
10.2	Propulsive Options	49
10.3	Design Process	50
10.3.1	Propellant Mass Required	50
10.3.2	Thruster Firing Time	51
10.4	Choice of the Propulsion System	51
10.5	System Design	52
10.5.1	Initial Design and Baseline	52
10.5.2	Design of the Feeding System	53
10.5.3	Tank Sizing	54
11	Tracking, Telemetry & Telecommand Subsystem	55
11.1	Mandatory Events	55
11.2	Data Budget	55
11.3	Architecture	56
11.3.1	Transmission Optimization	57
11.4	Link Budget	58
11.5	Communication Strategy	59
11.5.1	Contact Analysis	61
11.5.2	Relay Satellite Alternative	63
12	Electric Power Subsystem	64
12.1	Power budget	64
12.1.1	Margin Philosophy	64
12.1.2	EPS modes	64
12.2	EPS Drivers and Alternatives	66
12.3	Solar Arrays Design	67
12.3.1	Solar Cell Selection	67
12.3.2	Preliminary Analysis on Solar Arrays configuration	67
12.3.3	'Planar' Sun Pointing	69
12.3.4	Panels Sizing and Results	71
12.3.5	Solar Array Sizing Validation	72
12.3.6	Solar Array Atox Protection	73
12.4	Secondary batteries	73

12.5 Power Control and Distribution	73
12.5.1 Power Conditioning and Distribution Unit	73
12.5.2 Bus selection and DC-DC converters	74
13 Attitude Determination and Control Subsystem	75
13.1 Pointing Budget	75
13.2 ADCS Equipment and Configuration	75
13.2.1 Redundancy	76
13.3 Modes	77
13.4 Disturbances Analysis and Hardware Sizing	79
13.5 Navigation Solutions	80
13.6 ADCS Performances	82
13.6.1 Detumbling mode	82
13.6.2 Telecom mode	83
13.6.3 Stand-By mode	83
13.6.4 Imaging mode	84
14 Thermal Control Subsystem	85
14.1 Preliminary considerations	85
14.1.1 Operational and Non-Operational temperature ranges	85
14.1.2 Hardware thermal dissipations	85
14.2 Worst hot and cold cases	86
14.3 Mononodal Analysis	88
14.4 Multinodal Analysis	89
14.5 Specific Subsystem Hardware and Considerations	92
14.6 Multinodal Analysis Results	94
15 On-Board Data Handling	95
15.1 Computer System State Diagram	95
15.2 OBDH Preliminary Sizing	95
15.3 OBC selection and redundancy philosophy	98
15.4 OBDH Redundancy Philosophy	98
15.5 TID analysis	99
15.6 OBDH Architecture and Bus Selection	99
15.7 Telemetry	100
16 Structure	102
16.1 Structural design	102
16.2 Modal Analysis	103
16.3 Quasi-Static Analysis	104
16.4 Sine Vibration Analysis	105
16.5 Random Vibration Analysis	106
16.6 Buckling Analysis	107
17 Configuration	108
17.1 Internal Configuration	108
17.2 External Configuration	110
18 Assembly, Integration, Verification, and Testing Development Plan	112
18.1 Model Philosophy and Test Planning	112
18.2 Assembly and Integration	113
18.2.1 Assembly	113
18.2.2 Integration	113
19 Risk Analysis	114
19.1 Risk policy and Risk Matrix	114

20 Mission Timeline	117
21 Costs Analysis	119
21.1 Space Segment	119
21.2 Launch and Operations Costs	120
21.3 Results and Conclusions	121

Subsystems	Responsible
Mission Analysis	Andrea Jimmy Pacursa
Propulsion Subsystem	Matteo Giovanni Juvara
Tracking, Telemetry & Telecommand Subsystem	Manuel Cappuccio
Guidance, Navigation & Control	Davide Bellini
Structures & Configuration	Giacomo Biraghi
Electric Power Subsystem	Matteo Braga
Thermal Control Subsystem	Matteo David Dowell
Attitude Determination & Control Subsystem	Francesco Cataffo
On-Board Data Handling	Lorenzo Cesarin
Cost, Risks, AIVT	Beatrice Beretta



BELLINI
DAVIDE



BERETTA
BEATRICE



BIRAGHI
GIACOMO



BRAGA
MATTEO



CAPPUCCIO
MANUEL



CATAFFO
FRANCESCO



CESARINI
LORENZO



DOWELL
MATTEO DAVID



JUVARA
MATTEO GIOVANNI



PACURSA
ANDREA JIMMY

Acronyms

C_D Drag Coefficient

I_{sp} Specific Impulse

Δv Delta Velocity

[TBC] To Be Confirmed

[TBD] To Be Defined

ABEP Air-Breathing Electric Propulsion

ABET Air-Breathing Electric Thrusters

ADCS Attitude Determination and Control System

AIVT Assembly, Integration, Verification, and Testing

AKE Absolute Knowledge Error

AOCS Attitude and Orbit Control Subsystem

APE Absolute Pointing Error

ATOX Atomic Oxygen

AVUM+ Attitude and Vernier Upper Module

BC Ballistic Coefficient

BM Body Mounted

BoL Beginning of Life

CADU Channel Access Data Unit

CCSDS Consultative Committee for Space Data Systems

CERs Cost Estimating Relationship

CGT Cold Gas Thrusters

CMEs Coronal Mass Ejections

COCOMO Constructive Cost Model

CoM Center of Mass

CONF Configuration

ConOps Conceptual Operations

COP Commissioning Phase

COTS Commercial Off The Shelf

CSG Guiana Space Center

DAG Directional Adaptive Guidance

DET Direct Energy Transfer

DLS Dual Launch Structure

DoD Depth of Discharge

DTM Detumbling

ECSS European Cooperation for Space Standardization

Eff Efficiency

EM Engineering Model

EMC Electromagnetic Compatibility

EoL End of Life

EPS Electric Power Subsystem

ESA European Space Agency

ESD Electrostatic Discharge

ET Electric Thrusters

EUV Extreme Ultra Violet

F Filter

FDIR Fault Detection Isolation and Recovery

FDV Fill & Drain Valve

FEEP Field Emission Electric Thruster

FEP Fluorinated Ethylene Propylene

FoV Field of View
FR Flow Restrictor
FSS Fine Sun Sensor
FSW Flight Software

GBK Germanium Black Kapton
GEVS General Environmental Verification Standard
GNC Guidance Navigation and Control
GOCE Gravity Field and Steady-State Ocean Circulation Explorer
GS Ground Station
GSD Ground Sampling Distance

HC Hollow Cathode
HET Hall Effect Thruster
HORUS High-resolution Orbiting Reconnaissance and Universal Surveillance
HPGP High Performance Green Propulsion
HPSV High Pressure Solenoid Valve
HSS High Speed Streams
HT Heater

IM Imaging Mode
IMU Inertial Measurements Unit
IR Infrared
IS Interplanetary Shocks
ISS International Space Station

J2 Second Zonal Harmonic Perturbation

KIPS Kilo Instructions Per Second
KLOC Thousand of Lines of Code

LEO Low Earth Orbit
LEOP Launch and Early Operations
LMT Liquid Monopropellant Thrusters
LPSV Low Pressure Solenoid Valve
LQI Linear Quadratic Integral
LQR Linear Quadratic Regulator
LVLH Local Vertical Local Horizontal

MEKF Multiplicative Extended Kalman Filter
MIPS Million Instruction Per Second
MIT Michigan Institute of Technology
MLB MkII Motorized LightBand
MLS Multi Launch Services
MoS Margins of Safety
MPPT Maximum Power Point Tracking
MTQ Magnetorquer

NASA National Aeronautics and Space Administration
NEO NASA Earth Observations
NIST National Institute of Standards and Technology

OBC On-Board Computer
OBDH On-Board Data Handling
OBP Observation Phase
OCM Orbit Control Mode

P Pressure Sensor

PAN Panchromatic Band

PCDU Power Conditioning and Distribution Unit

PFM Proto-Flight Model

PL Payload

POV Point of View

PPT Pulsed Plasma Thruster

PPU Power Processing Unit

PS Propulsion Subsystem

PSC Planetary Systems Corporation

PTFE Polytetrafluoroethylene

QARMAN Qubesat for Aerothermodynamic Research and Measurements on AblatioN

QM Qualification Model

QSL Quasi-Static Load

RAAN Right Ascension of the Ascending Node

RAM Random Access Memory

RDT&E Research, Development, Test & Evaluation

RFA Rocket Factory Augsburg

RFIT Radio Frequency Ion Thruster

ROM Read-Only Memory

RS Reed-Solomon

RT Resistojet Thrusters

RTGs Radioisotope Thermo- electric Generator

RW Reaction Wheels

S/C Spacecraft

SA Solar Arrays

SAA South Atlantic Anomaly

SBM Stand-By Mode

SETS Space Electric Thruster Systems

SFM Safe Mode

SK Station Keeping

SNR Signal to Noise Ratio

Space RIDER Space Reusable Integrated Demonstrator for Europe Return

SSC Swedish Space Corporation

SSCM Small Satellite Costs Model

SSMS Small Spacecraft Mission Service

SSO Sun Synchronous Orbit

STM Structural Thermal Model

STR Structure

SWIR Short-Wave InfraRed Band

T Temperature Sensor

TCS Thermal Control Subsystem

THOR Thermospheric Orbital Reconnaissance spacecraft

TID Total Ionizing Dose

TM Telecommunication Mode

TRL Technology Readiness Level

TTMTC Telemetry, Tracking, and Telecommand

UTC Coordinated Universal Time

UV Ultraviolet

VCDU Virtual Channel Data Unit

VIS Visible Band

VLEO Very Low Earth Orbit

1 Mission Overview

The High-resolution Orbiting Reconnaissance and Universal Surveillance (HORUS) is an ambitious Earth Observation mission operating in Very Low Earth Orbit (VLEO), designed to deliver high-resolution images with minimal latency. The main objective is to achieve a spatial resolution lower than 1 m , downlink the payload data within 1 h from acquisition, and ensure flexible coverage for specific areas. Adaptability in target selection, according to customer needs, is the cornerstone of HORUS design. Therefore, the aforementioned qualities make HORUS ideal for a variety of applications, such as environmental monitoring, real-time response of natural disasters, along with dual use operations. In line with the strategic importance of the mission, HORUS is designed to rely completely on European technology: from components to ground segments and launcher.

1.1 Mission Objectives

To accomplish the ambitious goals of the HORUS mission, several key mission objectives have been set. Those include the following:

- **To provide specific area coverage of Earth with high resolution, low latency, and minimum time resolution**

The mission will focus on providing high-quality images of target areas while minimizing delays in both data acquisition and data downlink. Additionally, HORUS is designed to revisit and monitor areas of interest frequently, allowing for almost real-time updates.

- **To ensure flexibility in terms of target covered**

Flexibility is a key feature of the HORUS mission. Given the different type of applications the satellite needs to face, HORUS shall be very adaptable, being able to cover different areas as needed.

- **To provide fast data download**

Another crucial objective is to ensure rapid transmission of data from space to Earth. This near real-time data transmission is essential, as rapid data availability could help mitigate risks and enable quick response.

- **To limit the time to launch and launch costs**

To meet its mission objectives, it is fundamental that HORUS can be launched quickly in response to emerging needs. Minimizing the launch time ensures that critical areas can be observed during relevant time windows. Additionally, the mission aims to minimize expenses related to launch operations, especially if multiple satellite launches are needed.

- **To demonstrate the Technology Readiness Level (TRL) for VLEO**

HORUS is set to operate in a highly challenging and almost unexplored region of space. The most significant criticalities are the high aerodynamic drag and the Atomic Oxygen (ATOX), which can drastically reduce the operational lifetime of the spacecraft. Therefore, one of the objectives of HORUS is to demonstrate the technology readiness for VLEO, ensuring that its systems can withstand the harsh environment and maintain functionality over an extended period.

1.2 High Level Goals

Establishing a comprehensive set of high level goals for the HORUS mission is crucial, as these significantly constrain and influence the design of the spacecraft. The key high level goals for the mission are reported in **Table 1**.

High Level Goals	Design Influences
The mission shall provide a spatial resolution below 1 m and guarantee flexibility in target selection	<p>The payload shall be carefully selected to provide the high spatial resolution.</p> <p>The Attitude and Orbit Control Subsystem (AOCS) architecture shall be designed to ensure precise pointing accuracy, critical for maintaining this resolution.</p> <p>The orbit shall be carefully chosen selecting a proper altitude and revisit time.</p>
The mission shall provide a time resolution of less than one day and the data shall be downlinked within 1 h after acquisition	<p>The orbit shall be carefully chosen selecting a proper altitude and revisit time.</p> <p>The AOCS shall be designed to guarantee proper orientation for effective communication with Ground Station (GS).</p> <p>Telemetry, Tracking, and Telecommand (TTMTC) and On-Board Data Handling (OBDH) design shall account for the fast downlink requirement.</p>
The spacecraft shall provide a time to fly not larger than two months and shall have an operational lifetime as far as the interested event lasts	<p>A launch solution that can deliver the spacecraft to the desired orbit within the specified timeframe needs to be selected.</p> <p>The Propulsion Subsystem (PS) shall be designed to guarantee a fast orbit insertion while providing a sufficient station keeping time.</p>
The technology and the launcher shall be European	<p>All spacecraft components, from the payload to subsystems, shall be produced from European manufacturers.</p> <p>The design will prioritize compatibility with European launchers.</p>
Capability to survive VLEO environment	<p>The structural design shall be robust enough to withstand the increased aerodynamic forces and to resist degradation from ionosphere and radiation.</p> <p>The Thermal Control Subsystem (TCS) shall be designed to manage the extreme temperature variations experienced in VLEO.</p>

Table 1: High Level Goals and their design influences

2 Mission Environment Analysis

2.1 Environment Overview

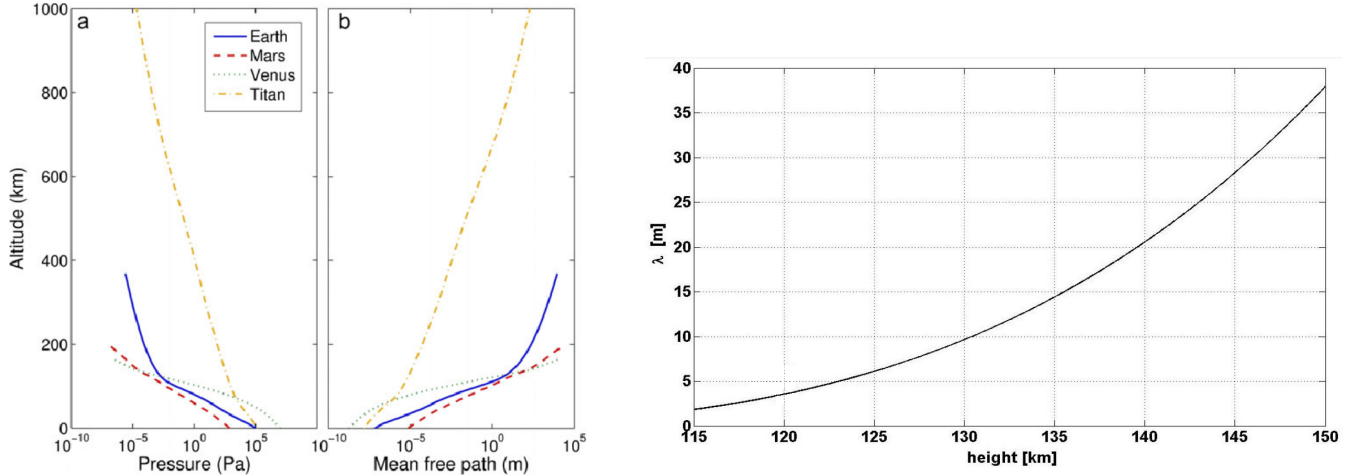
Flying in VLEO, at altitudes below 450 km , provides several advantages for space crafts. Key benefits include reduced communication power, improved revisit time, cost-effective high-resolution imaging, and a cleaner orbital environment with reduced space debris. However, despite these advantages, VLEO environment also presents some challenges. The operational lifetime of satellites is reduced due to high atmospheric density and increased damage from corrosion, mainly due to the concentration of ATOX. Furthermore, the design of the mission shall take into account the disturbances of the geomagnetic field, which depends on the solar activity, and the effects of the different sources of thermal radiation.

Lastly, for a precise analysis it is essential to consider that, under these conditions, the atmospheric fluid should be modelled as a free molecular flow due to the low densities [1].

2.2 Thermosphere

When operating in VLEO, the spacecraft is exposed to the conditions of the lower thermosphere. In this environment, the influence of various energy sources must be taken into account: distinct thermal, electromagnetic, and chemical processes in this region may result in gas density variability, which has to be thoroughly analysed [2]. Additionally, the presence of ATOX, molecular nitrogen, as well as air drag impact the spacecraft structural integrity and mission operations in several ways.

The thermosphere is commonly defined as the layer of Earth's atmosphere extending from approximately 80 km to 700 km above the surface. This region is characterized by intense molecular agitation, causing the kinetic temperature to exceed 1000 K at an altitude of 450 km . However, beyond altitudes of 100 km , atmospheric pressure decreases significantly, leading to an increase in the mean free path of particles: at 150 km , it is estimated to be around 38 m (Figure 1b), which is several times larger than the spacecraft projected dimensions. Consequently, under nominal conditions, the heat exchange between the spacecraft and the atmosphere will be primarily radiative, and the aero-thermodynamics will be governed by free molecular flow.



(a) Pressure and mean free path with respect to altitude for atmospheres of different planets [3]

(b) Mean free path of molecules within the lower thermosphere [4]

Figure 1: Plots illustrating the mean free path of molecules at different altitudes

The VLEO region is also entirely encompassed by the ionosphere, a layer of the atmosphere located between 80 km and 750 km of altitude where the density of charged particles is significantly higher than in other atmospheric layers, typically ranging from 10^9 to $10^{12}\text{ particles/m}^3$. This unique composition is attributed to the action of solar Extreme Ultra Violet (EUV), highly energetic radiation emitted by the Sun between 10 nm and 120 nm wavelengths. The quantity and distribution of these charged particles varies significantly according to the day/night cycle and solar activity, having numerous implications especially for the mission's telecommunication systems. The charged particles, forming the plasma, can

shield the spacecraft, blocking electromagnetic signals below the frequency of the plasma itself. Generally the ionosphere doesn't allow frequencies under 100 *MHz* to pass through, preventing the establishment of a radio link between the spacecraft and the ground stations.

As stated before, the composition of the ionosphere varies a lot depending mainly on the solar irradiation conditions. Some specific radiations, such as F10.7 and EUV radiation, emitted respectively at 10.7 *cm* and 10–120 *nm* wavelength [5], are considered to be directly correlated to the amount of ionized particles found in this layer of the atmosphere.

2.2.1 Atmospheric Density

One of the main implications of a VLEO is the significantly higher atmospheric density. Air density and pressure decrease sharply with altitude, following the thinning of the atmosphere due to the decreasing of the gravitational pull. A simple, though moderately accurate approach to model this behaviour is written as follows:

$$\rho = \rho_0 \cdot e^{-\frac{(h-h_0)}{H}} \quad (1)$$

where ρ_0 is the reference density, h and h_0 are the altitude and the reference altitude and H is the scale height. Using the *Jacchia-Bowman 2006* atmospheric model, the data shown in Figure 2 were retrieved for varying solar activity trends.

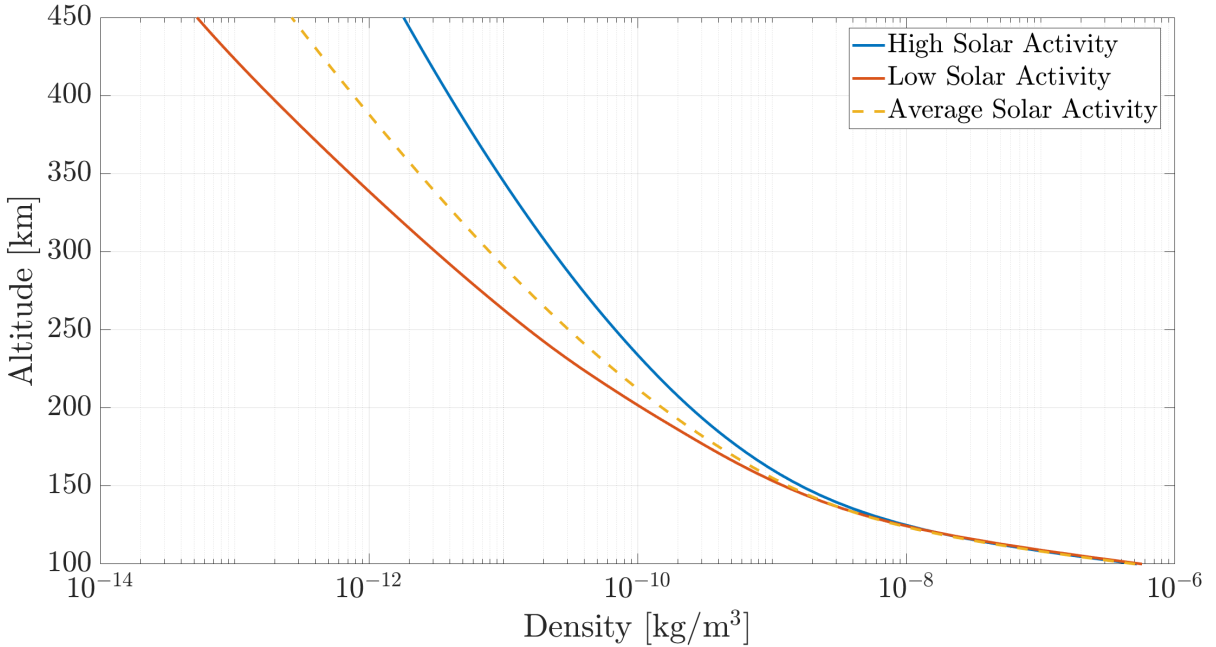


Figure 2: Density trend in VLEO during the 2000 solar maximum, the 2008 solar minimum and with average solar activity [6]

The lower bound of VLEOs is characterized by a density in the order of 10^{-7} kg/m^3 , which is significantly lower with respect to the sea level value, but still several orders of magnitude higher than the one found at altitudes around 400 *km*, where it is computed as 10^{-12} kg/m^3 . However, the maximum density gradient in the VLEO domain is experienced within the 100 – 150 *km* layer.

The actual trend of atmospheric density is more complex than previously stated. It is well known that temperature and density levels can exhibit strong local variations, primarily influenced by solar activity. A recent study [7] highlights the relatively strong longitudinal fluctuations in atmospheric density, showing how both solar and geomagnetic activity, such as aurora heating around the magnetic poles [8], shape both the gas mass and temperature distribution in this region. This research emphasizes the difficulty of obtaining precise information about the thermosphere's characteristics, given the dynamic nature of these influencing factors. Hence, although a simple model to approximate the atmosphere can be used in early design phases, validation through testing and simulation with more complex models is key for the positive outcome of the mission.

2.2.2 Atmospheric Drag

A higher atmospheric density implies the presence of significant drag torques acting on the spacecraft surfaces that could pose serious issues on the stability and duration of the mission. In general terms, the atmospheric drag can be modelled as follows:

$$D = \frac{1}{2} \rho \cdot v_{\text{rel}}^2 \cdot C_D \cdot S_{\text{ref}} \quad (2)$$

With density ρ , reference surface S_{ref} and relative velocity:

$$\vec{v}_{\text{rel}} = \vec{v}_{\text{sc}} + \vec{v}_{\text{atm}} \quad (3)$$

Such a force acts on every surface of the spacecraft generating a total torque that can be computed as:

$$\vec{T}_{\text{drag}} = - \sum_{i=1}^n \vec{r}_i \times \left(\frac{1}{2} \rho \cdot v_{\text{rel}}^2 \cdot C_{D,i} \cdot S_{\text{ref},i} \cdot \hat{v}_{\text{rel}} \right) \quad (4)$$

Where n is the number of aerodynamic surfaces while \hat{v}_{rel} is the direction of the relative velocity. These torques can be very disruptive: the ISS, orbiting between 370 and 460 km of altitude, experiences serious pull torques that cause its orbital decay at a rate of about 2 km/month [9]. Smaller satellites suffer less from drag effects by virtue of their limited cross-section area and mass, but orbit decay is present anyway and has to be addressed with periodic adjustments. On the other hand, past studies [10] have proven the feasibility of passive attitude stabilization of small satellites by exploiting the aerodynamic drag to align the S/C to the direction of the relative wind; however, this goes beyond the mission's scope and it won't be further analysed. As a reference for this VLEO mission the orbital decay caused by atmospheric drag acting on a 6U CubeSat, with the characteristics reported in Table 2, is analysed.

Mass	Dimensions	Max cross-section area	C_d
8 kg	(20 x 10 x 34.05) cm	0.04 m ²	2

Table 2: 6U CubeSat specifics

The following graph represents the orbital decay of the same satellite over time, computed at different altitudes and under different solar activities. The low solar activity corresponds to the 2008 solar minimum, and the high solar activity corresponds to the 2000 solar maximum.

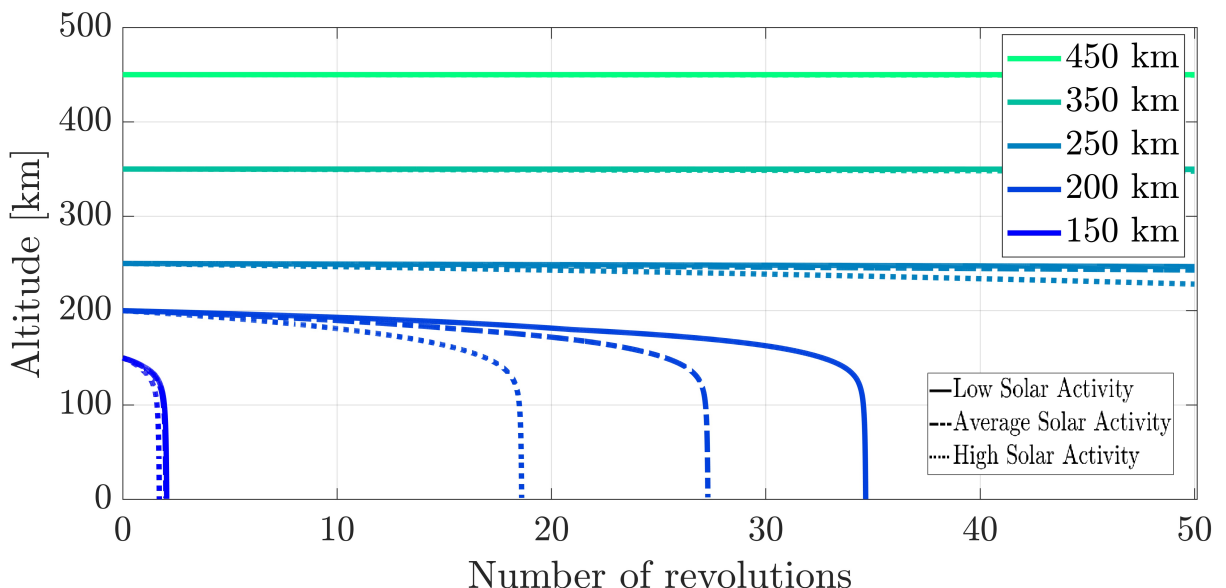


Figure 3: Orbital decay for different starting altitudes and different solar activities[6]

It is evident that the lower the orbit, the higher the decay caused by atmospheric drag. At the lowest altitude considered, the lifetime of the satellite is less than two revolutions. For the 200 km orbit, the

number of total revolutions depends greatly on the solar activity considered: the values range from less than 20 revolutions for the solar maximum case to almost 35 for the solar minimum case. Orbit higher than 250 km exist for more than 50 revolutions, but their altitude losses are detectable the more they decrease in altitude.

2.2.3 Aerodynamic Heating

Aerodynamic heating is the heat exchange between the spacecraft and the surrounding atmosphere, and it is mainly due to a phenomenon called screen friction heating. It occurs primarily on leading edges and surfaces that face the relative flow, where the friction between air molecules and the spacecraft acts as a significant source of heat. This effect constitutes a critical factor that affects design, operations, and longevity of satellites, especially when orbiting in VLEO. The main concerns arise for orbits below 300 km , since above this altitude the aerodynamic heating is a hundred times lower in magnitude than the solar radiation that hits the spacecraft. For example, at 150 km the two effects are comparable and therefore none of them is negligible. However, this effect is highly dependent on the spacecraft's size. If the particles mean free path is significantly larger than the satellite dimensions, the effect can be considered negligible.

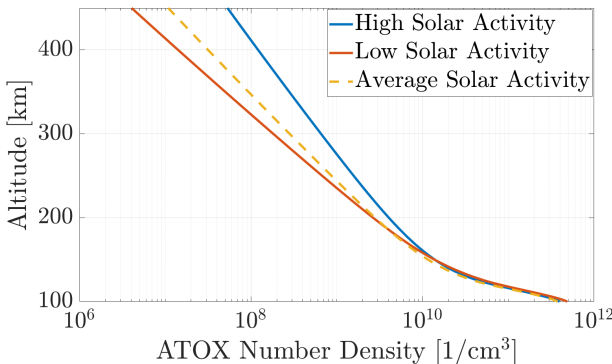
2.2.4 Atomic Oxygen and Molecular Nitrogen

In VLEO, the atmosphere is highly rarefied, composed of atomic oxygen, molecular oxygen, and molecular nitrogen, along with other gases present in smaller quantities.

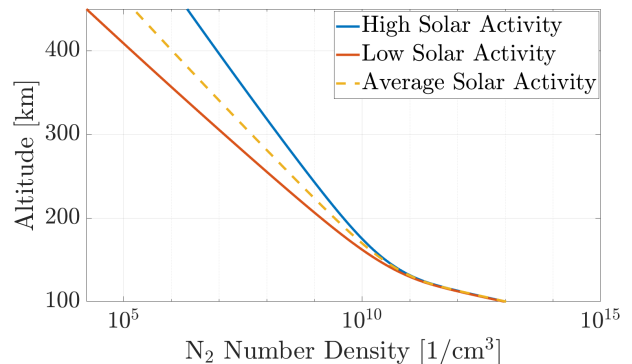
Although molecular nitrogen (N_2) is chemically inert compared to atomic oxygen, it still interacts with the satellite surfaces, and due to the velocity and mass of the particles, the collision can impart momentum to the satellite. Molecules collide at hyper-velocity speeds ($\approx 8\text{ km/s}$), causing erosion and sputtering, particularly when combined with atomic oxygen. This is highly affecting the performances of optical equipments and sensors on the external surfaces.

Atomic oxygen is primarily formed through the photo-dissociation of molecular oxygen due to ultraviolet radiation from the Sun. This process breaks down oxygen molecules into highly reactive atoms, leading to various problems for satellites. In VLEO, ATOX can constitute 30% to 60% of the atmosphere, depending on altitude, as its formation rate surpasses its recombination into molecules or oxides [11].

Additionally, atomic oxygen can penetrate cavities or gaps in satellites. This can create "hot spots" where ATOX concentration is high, increasing the risk of internal damage. It is crucial to predict these fluxes using analytical models and empirical data to ensure the survival of internal components and improve the overall satellite design. Measuring atomic oxygen flux is essential for understanding erosion rates and atmospheric density variations in VLEO orbits [12]. In Figure 4a and Figure 4b the levels of ATOX and N_2 at varying altitudes and solar activity are presented based on the *NRLMSISE-00* atmospheric model [13]. The low solar activity corresponds to the 2008 solar minimum, the average solar activity corresponds to typical solar activity, and the high solar activity corresponds to the 2000 solar maximum.



(a) ATOX levels at varying altitudes and solar activity



(b) N_2 levels at varying altitudes and solar activity

Figure 4: ATOX and N_2 densities at varying altitudes and solar activity [13]

To mitigate these effects, protective materials are used, such as silicon-based polymers, gold, or ceramic materials, along with carbon-based coatings to increase resistance to sputtering. Additionally, satellite

structures can be redesigned, adopting shields that aerodynamically deflect particles away from more vulnerable areas. The implementation of these measures is essential to improve the durability of satellites operating in VLEO and to ensure longer mission lifetimes.

2.2.5 Material Degradation

Considering the cases of maximum and minimum solar activity, as well as the specific position of the satellite with respect to the Earth's surface in terms of altitude, longitude and latitude, the number density of ATOX and N₂ were computed for one year. The results are shown in Figure 5 and Figure 6. The computations were made considering the nominal orbit illustrated in Section 8 with a RAAN angle of 45°.

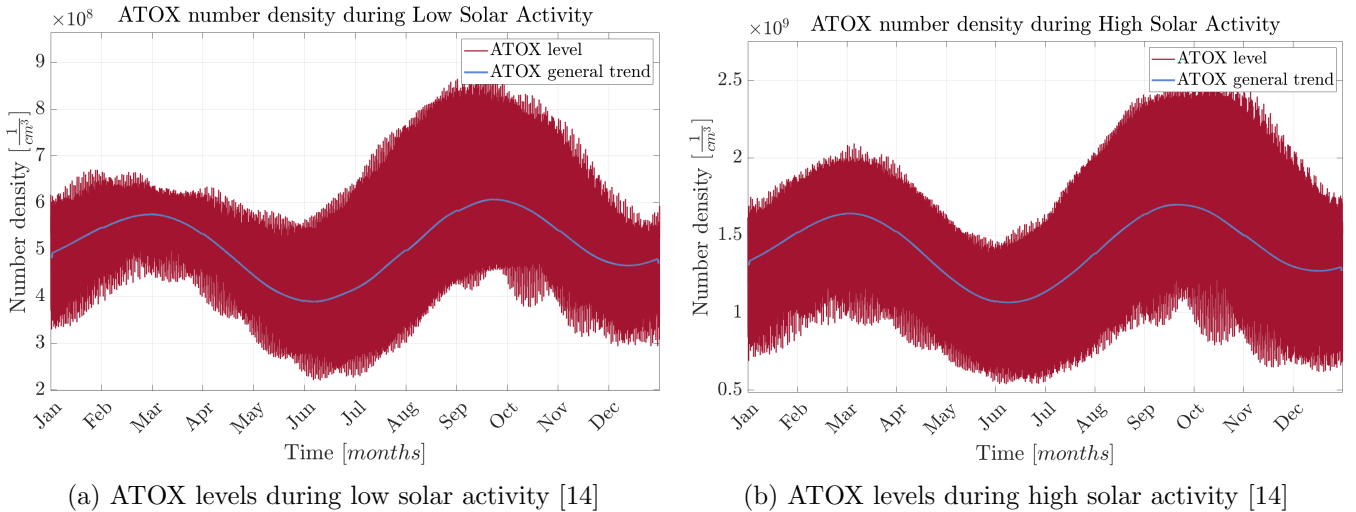


Figure 5: Plots illustrating the evolution of ATOX levels throughout a year in various solar activity conditions

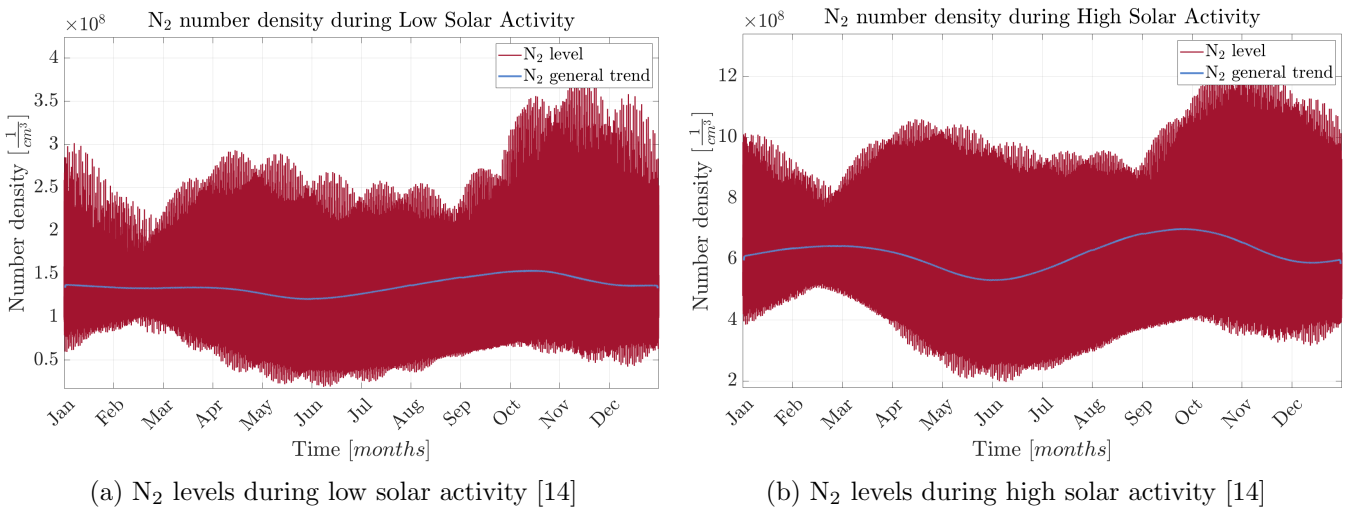


Figure 6: Plots illustrating the evolution of N₂ levels throughout a year in various solar activity conditions

Knowing the number densities of a specific particle throughout a year and the velocity of the S/C along its orbit, it is possible to evaluate the overall evolution of the ATOX and N₂ fluxes and the yearly degradation of any material knowing the respective yield or sputtering coefficients.

	High Solar Activity	Low Solar Activity
Kapton	0.995 mm/year	0.3604 mm/year
Black Paint	0.1255 mm/year	0.0455 mm/year
Epoxy-silica nanocomposite	0.061 mm/year	0.022 mm/year
Mg AZ31B	0.0015 mm/year	0.00056 mm/year
SiO₂ (coverglass)	0.0003 mm/year	0.0001 mm/year
Aluminum	Negligible	Negligible

Table 3: Degradation of materials due to ATOX over a year in the nominal orbit with $\Omega = 45^\circ$ [15][16]

From Table 3 it is evident that some materials have a lower ATOX resistance than others. This leads to considerably higher degradation, especially if we consider that the spacecraft operates in VLEO. Therefore materials and coatings with suitable yield and sputtering coefficients must be employed. Moreover, materials and coatings must be selected also taking into consideration other environmental factors that can have an impact on the overall lifetime of the mission, such as UV radiation. In Table 3 only the yearly degradation due to ATOX is presented because the effects of N₂ is certainly lower.

2.3 Electromagnetic Radiation

Given the closeness to the Earth's surface dictated by the requirements, it is crucial to accurately estimate the electromagnetic radiation encountered during the mission due to the solar flux, the Earth's Albedo and IR radiation, and their interaction with the planet's atmosphere.

2.3.1 Solar Flux Overview

Even though the spacecraft operates close to the Earth's surface, the Sun emitted flux is still the main contribution in terms of encountered electromagnetic radiation. Since it is almost constant, within a fraction of 1%, the Sun can be considered as a constant energy source [17]. However, over the lifetime of the mission, the amount of solar flux encountered varies also based on the distance from the Sun. Thus the maximum solar flux is found when the satellite is closest to the Sun, while the minimum is defined when it is furthest from the Sun. The values are shown in Table 4.

	Minimum [W/m ²]	Maximum [W/m ²]
Solar flux	1322	1414

Table 4: Maximum and minimum solar heat fluxes encountered depending on the distance from the Sun [17]

2.3.2 Earth Albedo Overview

The albedo from the Earth encountered during the mission varies depending on the location above the Earth and the altitude. In particular, the albedo coefficient ranges from values that are the lowest above oceans and the highest above snow-covered areas. However, the albedo coefficient usually assumes an intermediary value. Examples of the coefficients are found in Table 5.

	Minimum [-]	Maximum [-]	Typical [-]
Earth Albedo coefficient	~0.05	~0.9	0.37

Table 5: Examples of Earth Albedo coefficients [17][18]

Considering the changes in altitude within VLEO, the changes in the albedo coefficient, and the varying solar flux based on the distance from the Sun, the maximum and the minimum Earth albedo fluxes are presented in Table 6.

	Minimum [W/m ²]	Maximum [W/m ²]
Earth albedo flux	57.7	1234

Table 6: Range of values assumed by the Earth albedo flux in VLEO

It must be noted that in VLEO, for objects orbiting around the Earth in eclipse, the albedo planetary flux is null. Moreover, the presented values represent extreme cases and the typical values of the albedo flux fall within this range.

2.3.3 Earth IR Radiation Overview

The IR flux from Earth is proportional to the atmospheric altitude, the temperature of the Earth's surface and the emissivity of the area on the planet underneath the satellite. As opposed to the fluxes from the Sun and that of the Earth's Albedo, the IR radiation coming from Earth is always present in VLEO.

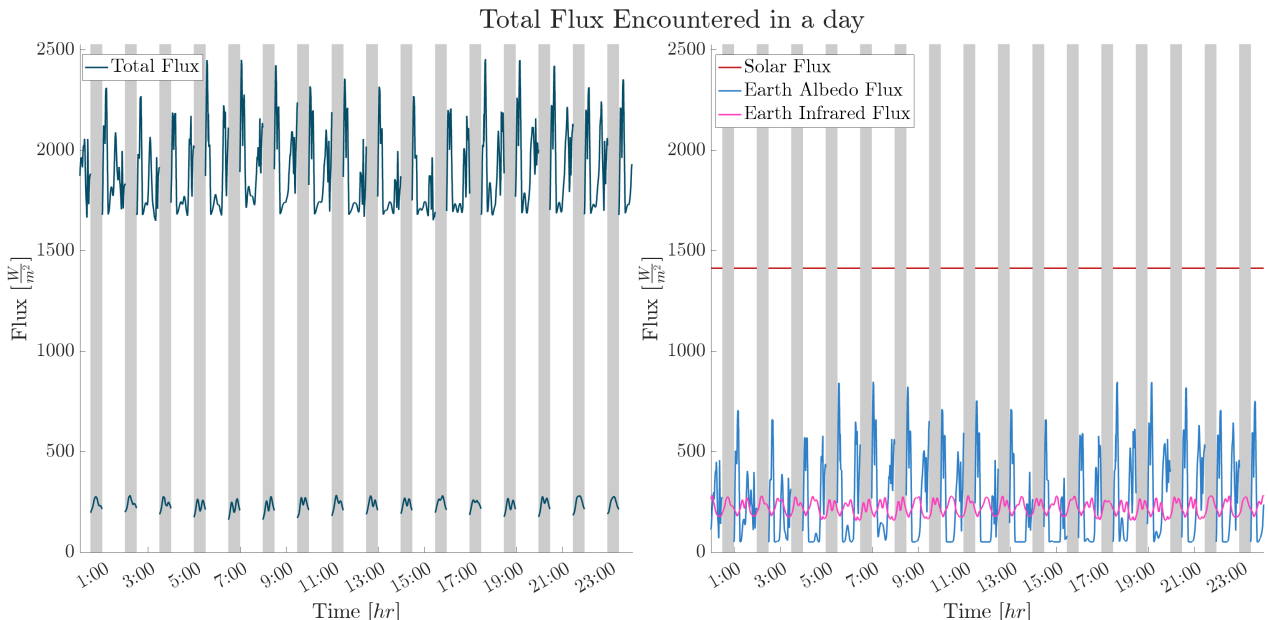
	Minimum [W/m ²]	Maximum [W/m ²]
Earth IR flux	107	358

Table 7: Range of values assumed by the Earth IR flux in VLEO [19][20]

2.3.4 Refined Total Electromagnetic Flux Analysis

Considering the components of the total electromagnetic flux, a more detailed and accurate analysis can be done taking into account the specific position of the S/C along the orbit. Knowing the Keplerian parameters defined for the nominal orbit in Section 8 and considering a RAAN of $\Omega = 45^\circ$, numerical simulations were performed to evaluate the solar flux, the Earth albedo flux and the Earth IR radiation flux throughout the mission. The variations of Earth surface properties were computed on an averaged monthly basis, utilizing various NASA NEO datasets [21].

Moreover, to more accurately estimate the albedo and IR fluxes, the conical visibility of the satellite with respect to the Earth's surface was also computed. This allows for a more accurate definition of these fluxes considering only the specific sections of planetary surface seen by the spacecraft. This approach ensures that, as we move farther from the nadir point, decreasing weights are assigned to albedo coefficient and IR flux, so that they contribute less to the overall effect. Considering the 1st of January 2026, characterized by the presence of eclipses, the flux evolutions presented in Figure 7 have been found.

Figure 7: Evolution of the total electromagnetic flux and its components on the 1st of January 2026

It has to be noted that, throughout the day, the solar flux is the highest of the three contributions. The Earth albedo flux comes second, with values which can reach $\approx 900 \text{ W/m}^2$. Moreover, throughout a random day, the solar flux can be almost considered constant, the same cannot be said, in general, for the

total flux. This is due to the erratic behaviour of the Earth albedo and IR fluxes, dictated by the varying surfaces seen by the spacecraft throughout its orbit. It is important to note that the algorithms have been modified to account for shadowed regions of the Earth observed by the spacecraft under non-eclipse conditions. This adjustment is particularly significant for orbits with high beta angles, where neglecting these shadowed sections could lead to an overestimation of the Earth albedo flux.

Throughout a random year, the total fluxes encountered vary greatly based on the parameters mentioned earlier. The values presented in Table 8 represent the maximum and minimum electromagnetic fluxes found in the numerical simulations over a year.

	Maximum Flux [W/m ²]	Minimum Flux [W/m ²]
Solar Flux	1387.21	//
Earth albedo Flux	945.84 ($a = 0.74$)	//
Earth IR radiation Flux	152.61	134.76
Total Flux	2485.67	134.76

Table 8: Maximum and minimum electromagnetic fluxes encountered over a year in the nominal orbit

2.3.5 UV radiation

When considering radiation coming from the Sun, UV and EUV radiation must be analysed separately. While it is true that UV radiation is reduced in VLEO, its possible effects on the mission should be considered. The reduction in ultraviolet radiation levels in the thermosphere is due to ATOX absorbing EUV radiation. The specific values and levels of UV vary based on solar activity, the current season, time of the day, geomagnetic activity and semi-annual variations [22]. Studies from past scientific missions report that the maximum absorption rate for EUV radiation occurs at altitudes of 170 km or below, which means that above this height, the radiation is present and its effects are not negligible [23]. Because of the effects provoked by UV radiation special attention must be given to properly defining the overall configuration and architecture of the spacecraft. In particular, materials and external coatings must be selected taking into consideration possible degradation effects, such as embrittlement or discolouration [24], [25].

2.4 External Magnetic Field

The Earth magnetic field is composed by a fixed dipole deriving from the Earth core and the effects of solar activities interacting with atmosphere. One of its key features is the South Atlantic Anomaly (SAA), a region over Brazil where the magnetic field lines re-enter the Earth, creating a concentrated radiation zone. This is the primary source of significant radiation for orbits with altitudes below 800 km and inclinations between 30° and 70°, causing significant damages to electronics and sensors. During the preliminary mission analysis, these effects shall be considered and the possibility of switching off the electronics shall be taken into account.

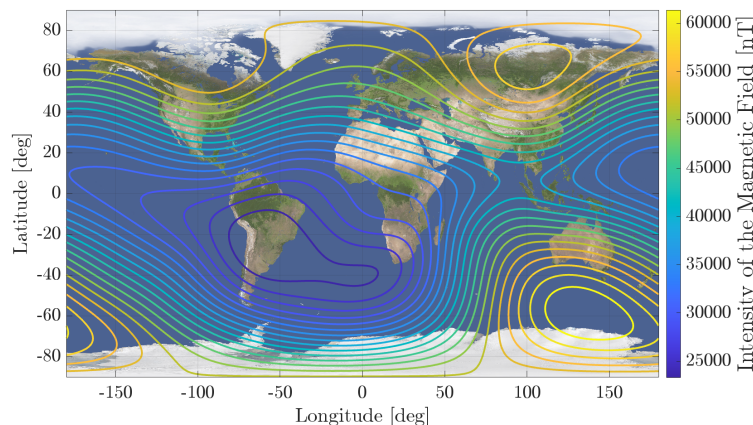


Figure 8: Magnetic field lines at 100 km altitude

The Earth magnetic field has great influence on plasma motions and trapped high-energy charged particles, which leads to surface charging and electronics damaging. If the magnetic field is nearly perpendicular to the spacecraft surface, electrons can escape along the field lines, as seen in Figure 9(a). On the other hand, if the magnetic field is inclined with respect to the surface, electrons may be redirected to the surface by the Lorentz force, as seen in Figure 9(b). This prevents the escape of electrons from the surface, increasing the negative surface charge.

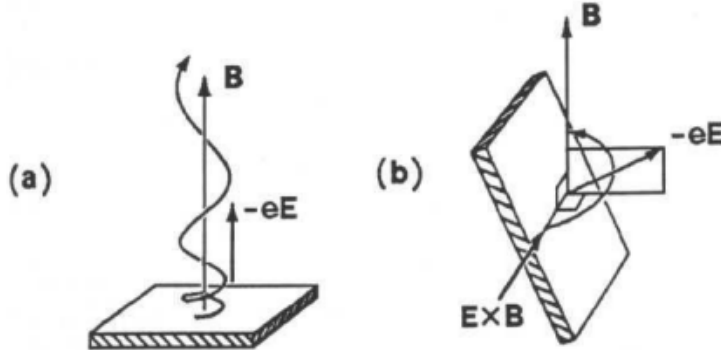


Figure 9: Magnetic field effects on secondary electron emission [26]

The most dangerous effect of spacecraft charging is the Electrostatic Discharge (ESD), which can be in the form of surface discharges or in the form of bulk dielectric discharges. A surface discharge occurs when the surface voltage exceeds the breakdown voltage of the surface material, and as a result, it can generate currents up to hundreds of amperes. On the other hand, a bulk dielectric discharge is triggered when dielectrics are exposed to space radiation. The charges involved in bulk discharges are relatively smaller compared to surface discharges but still introduce a direct hazard to electronics.

Additionally, arc discharges may occur as well and are a direct result of differential and internal charging of the spacecraft. To mitigate these effects it is of utmost importance to guarantee the electrical continuity and grounding of the external surfaces of the spacecraft. Degradation of sensors and solar cell panels is also a serious possibility, and it may decrease power generation. Moreover, localised heating, material loss, and surface contamination are a direct result of arc discharges as well [26].

2.4.1 Geomagnetic Storms

Solar activities such as solar wind, Coronal Mass Ejections (CMEs), High Speed Streams (HSS), Interplanetary Shocks (IS), their consequent geomagnetic storms, and magnetospheric substorms produce disturbances of different magnitudes.

These storms and substorms are not only time dependent, but are also affected by the solar activity, the magnetic latitude and altitude of the orbit, and the strength of the magnetospheric activity. It is crucial to properly investigate the effects of geomagnetic disturbances on the spacecraft attitude. Indeed, including these effects in the predictions of geomagnetic fields would highly improve the accuracy of the attitude predictions. [27].

2.4.2 Magnetic Field Analysis

Throughout the mission, the spacecraft encounters a varying magnetic field, which depends on the solar activity and the altitude, latitude and longitude of the spacecraft. The computations were made considering the nominal orbit illustrated in Section 8 with a RAAN angle of 45° . The results of numerical simulations referring to the maximum and minimum encountered magnetic field strengths are shown in Table 9.

Max Magnetic Field Strength	Min Magnetic Field Strength
55.097 T	29.244 T

Table 9: Maximum and minimum magnetic field strengths over a year

The effects of the magnetic field must be taken into account when selecting the instruments to be used for attitude control purposes and when determining the configuration of the system electronics.

2.5 Charged Particles Effects

Within the space environment, trapped charged particles can have a negative impact on the hardware present on board of the spacecraft. In Table 10 a synthesis of the results for some of the spacecraft components is shown. As it can be seen, no particular risks are encountered for exposure times similar to the spacecraft lifetime. It must be noted that for some components, such as the battery cells or OBCs, additional aluminium shielding may be designed to protect from radiation.

	Maximum Radiation	Radiation After 1 Year
Sun Sensor	30 Krad	1.343 Krad
PCDU	30 Krad	0.706 Krad

Table 10: Radiation levels encountered during one year [13]

2.6 Optical Parameters Degradation

Due to the damaging environment in which the spacecraft will operate, it is crucial to take into consideration the overall changes in optical parameters. Those are provoked by the constant presence of UV radiation and charged particles. The analysis is done in worst-case scenarios, considering no attenuation given by the atmosphere.

Variations in the absorptivity of the outer surfaces of the spacecraft have a significant repercussion on most of the subsystems to a certain degree. In Table 11, the changes in absorptivity given by the effects of UV radiation and charged particles on different materials are highlighted.

Materials	Initial α	α after 6 months	α after 1 year
Silver Teflon (2mm FEP)	0.075	0.09	0.11
Optical Solar Reflector	0.09	0.19	0.29
Black Kapton (GBK)	0.59	0.68	0.78

Table 11: Variation of material absorptivity given by UV radiation and charged particles [28][24][25]

2.7 Eclipse Number and Beta Angle

Knowing the position of the Earth with respect to the Sun and of the spacecraft with respect to the Earth, it is possible to calculate when the spacecraft is in eclipse during the simulation and the varying beta angle throughout a year. In Figure 10 the evolution in a year of the cited parameters is shown. It must be noted that during certain time intervals there is an absence of eclipses, while, when present, the number of eclipses is around 16 per day.

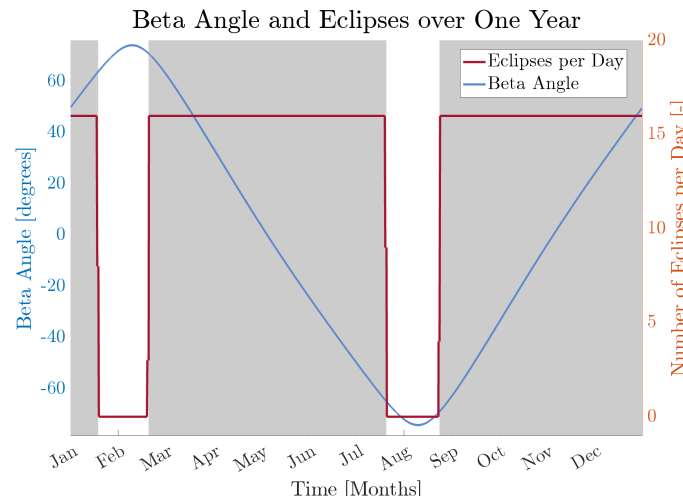


Figure 10: Beta angle and eclipse number per day during one year

Periods without eclipses are characterized by the beta angle reaching either its maximum or minimum values. Moreover, the length of the eclipses are shortest close to the beta angle extremes and longest in-between high frequency eclipse periods. The time lengths of the longest and shortest eclipses encountered over a year are reported in Table 12. Due to the high variability in eclipse duration and the possibility of having orbits without shadow, the EPS and TCS shall be sized accordingly.

Longest Eclipse [min]	Shortest Eclipse [min]
36.82	1.5

Table 12: Longest and shortest eclipse lengths

2.8 Criticalities and Opportunities of the VLEO Environment

2.8.1 Criticalities

The VLEO environment is characterized by some critical aspects that shall drive the design of the mission. First of all, the atmospheric drag represents an issue from the propulsion point of view, as the state of the art exploits traditional ion thrusters for drag compensation, which require a large amount of Xenon. Furthermore the thrusters are subject to degradation of the grids and require a neutralizer, lowering the overall mission lifetime. Air drag is a major issue also for the control of the spacecraft, especially in presence of high pointing requirements.

The very low altitude implies that the spacecraft passes over a interested region within a very short time window, and this represents a driver both for TTMTTC and OBDH subsystems. Regarding the telecommunications, both ground and spacecraft have to cope with the shielding effect of the atmosphere, and this shall be taken into account in the choice of the ground stations, the sizing of the antenna and the choice of the frequency bands. Eventually, in the VLEO environment, depending on the orbit type, the spacecraft could face rapid thermal changes due to the rapid eclipse cycles.

2.8.2 Opportunities

At the altitude range of interest mass-saving technologies can be used, such as Air-Breathing Electric Propulsion (ABEP). The residual gases present in the environment are collected and used for propulsion purposes, allowing for a lighter propellant mass at launch. The aforementioned technology might require years for development and is not yet mature, but represent a great opportunity to extend the mission lifetime[29].

The high atmospheric density could be a big issue for a traditional spacecraft, so a more aerodynamic shape would be beneficial for both the propulsion subsystem and the attitude control. Aerodynamic profiles would provide active or passive attitude control and they are adopted in some concepts as Shuttlecock and Feather configurations [30]. From a mission point of view, the VLEO environment is less cluttered with space debris, lowering the risk of collisions, and naturally enabling a rapid de-orbiting, in the order of weeks [1], representing a great opportunity to fulfil disposal regulations. Lastly, the very low altitude allows to improve the SNR for the resolution and the revisit time of optical payloads.

3 State of the Art

3.1 Introduction

In recent years, the exploration of VLEO has seen rising interest, due to the unique opportunities and technological advancements that this environment offers. However, despite these benefits, the state of the art in VLEO missions remains limited, particularly at altitudes below 300 km, due to the extreme conditions. Nevertheless, ongoing research and emerging technologies are paving the way for new solutions, notably for Earth observation missions, enhancing experimentation in this promising frontier [31].

Missions operating in VLEO are primarily characterized by the constraints imposed by the environment, which significantly influence spacecraft design. Indeed, most of these missions have a medium to low mass budgets, prioritizing compact, lightweight designs that can effectively mitigate these environmental challenges. The use of small satellites has become a common approach, allowing for reduced mass and enhanced manoeuvrability in response to the atmospheric drag. For instance, CubeSat-based missions like Colony-1 [32], SuperDove [33], SkySat [34] and QARMAN [35] are well-suited to the VLEO regime. These small spacecraft benefit from decreased drag forces, simplifying orbital maintenance and optimizing Δv budgets. Flight-proven missions are in the range of hundreds of meters per second [34] budget, while new concepts [31] aim it to reduce it further, however still needing to be validated.

In contrast, there are examples of larger VLEO missions that required heavier spacecraft designs due to their scientific objectives and payload requirements. A notable mention is the ESA GOCE mission [36]: despite a mass of over 1000 kg [36], needed by the high precision instruments onboard aimed at measuring Earth gravitational field, it operated successfully in VLEO, taking advantage of its aerodynamic shape [36] to reduce drag and extend its operational lifetime.

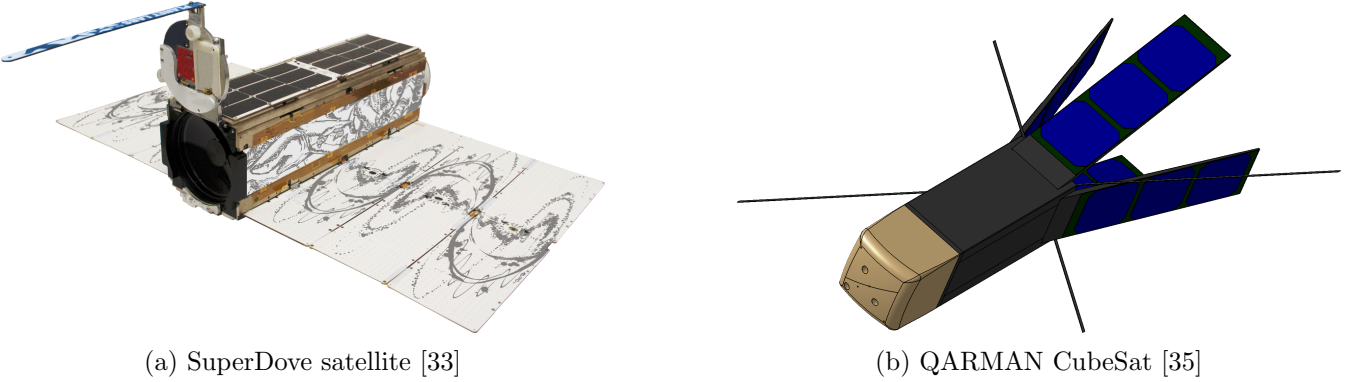


Figure 11: Latest VLEO satellites designs

3.2 Propulsion

Due to the environmental factors stated above, VLEO missions typically have a limited operational lifetime, ranging from months to a few years. The variation in lifespan largely depends on the design of the spacecraft propulsion system, which is key to counteract the effects of the atmospheric drag. The Δv budget and the necessity for continuous manoeuvres has lead to a preference for electric propulsion, more specifically ion thrusters.

For instance, the GOCE mission, equipped with continuous electric propulsion, had an operational lifetime of 4 years and 8 months before depleting its propellant and passively de-orbiting in the atmosphere [36]. Similarly, Planet Labs' SkySat satellites have a medium operational lifespan of nearly 4 years [34]. Emerging concepts, such as THOR and DMC-HD, are designed with propulsion systems and are expected to last up to 5 years. In contrast, the Colony program operated without propulsion systems, lasting only 39 days before de-orbiting and burning up in the atmosphere [32]. Other propulsion-less designs like QARMAN are estimated to have slightly longer lifetime, around 4 months [37].

A promising frontier in the field of electric propulsion is the development of Air-Breathing Electric Propulsion (ABEP), which utilizes residual atmospheric particles as propellant. This innovative approach conserves mass and extends mission lifetimes significantly, although the TRL is not mature enough. In the

case where chemical propulsion is required for design purposes, the research is moving towards the replacement of the standard practice hydrazine, in favour of green propulsion systems. This type of propulsion is much safer in terms of environmental impact, marking a significant step forward in the era of green space propulsion. Virtuous examples in this field are satellites part of the Skysat constellation, which implement High Performance Green Propulsion (HPGP) [34].

3.3 Payload and On-Board Data Handling

The most valuable payloads for missions operating at low altitudes are predominantly focused on Earth observation and analysis [34], [33]. This altitude range also presents a significant opportunity for studying Earth gravitational field and the external atmosphere [36]. Payloads designed for VLEO missions benefit from the limited distance to the observation targets, allowing for enhanced precision and reduced revisit times over specific ground locations.

The exceptional performance achievable by these payloads directly impacts the satellite's data handling capacity. For example, Planet Labs' SkySat [34] and SuperDove [33] satellites demonstrate a substantial data storage capability of up to 720 GB , which facilitates the retention of high-quality images captured by their onboard cameras. This storage capacity is crucial for accommodating the large volumes of data generated during imaging operations.

3.4 Tracking, Telemetry, and Telecommand Subsystem

The low altitude of VLEO significantly reduces coverage time windows and missions operating in this regime shall be designed to achieve high data rates for payload downlink communications. For instance, modern SuperDove satellites are capable of downlinking data at rates of 160 Mbit/s [33], while the SkySat satellites achieve even higher rates of 580 Mbit/s [34]. In contrast, the GOCE mission operated with a considerably lower data rate of 1.5 Mbit/s [38], primarily due to its different payload requirements and operational objectives. To address the challenges posed by limited communication windows, new mission concepts propose an innovative strategy involving the use of relay satellites, which are intended to facilitate continuous communication with ground stations by redirecting data from VLEO missions [37]. This approach extends the effective communication window, ensuring that high volumes of data can be transmitted efficiently.

3.5 Attitude Determination and Control Subsystem

For attitude and control strategy it is important to distinguish satellites operating at very low altitudes (below 300 km), such as Colony, GOCE, and THOR, from satellites like those in the Planet constellation, which typically orbit at altitudes between 400 km to 500 km . Attitude control in VLEO missions is typically achieved through a combination of reaction wheels and magnetorquers, commonly implementing the B-dot control. On average, the pointing accuracy for such systems is around 1° [34][33][36].

The first category also benefits from passive stabilization due to the presence of aerodynamic surfaces, drawing inspiration from high-altitude aircraft, both in terms of shape and geometry. These spacecraft are designed with streamlined bodies to minimize drag and enhance stability. Missions like GOCE, Colony, and concepts such as THOR or DMC-HD adopt designs where the centre of pressure is strategically positioned behind the centre of mass, ensuring aero-stability and improving their ability to maintain controlled flight in the residual atmosphere [36][32][37].

3.6 Electric Power Subsystem

On-board power generation relies on high-efficiency solar cells, with solar panels typically body-mounted on the spacecraft [32][36][34]. When additional appendices are present, they are typically equipped with solar arrays to maximize energy production [32][33]. Batteries are typically mounted to deal with the high frequency of eclipses, typical of the VLEO environment.

4 Functional Analysis and Conceptual Operations

4.1 Functional Analysis and Decomposition

The high-level goals aforementioned are achieved by a set of basic functions presented in Figure 12. These have to be performed by both ground and space segments.

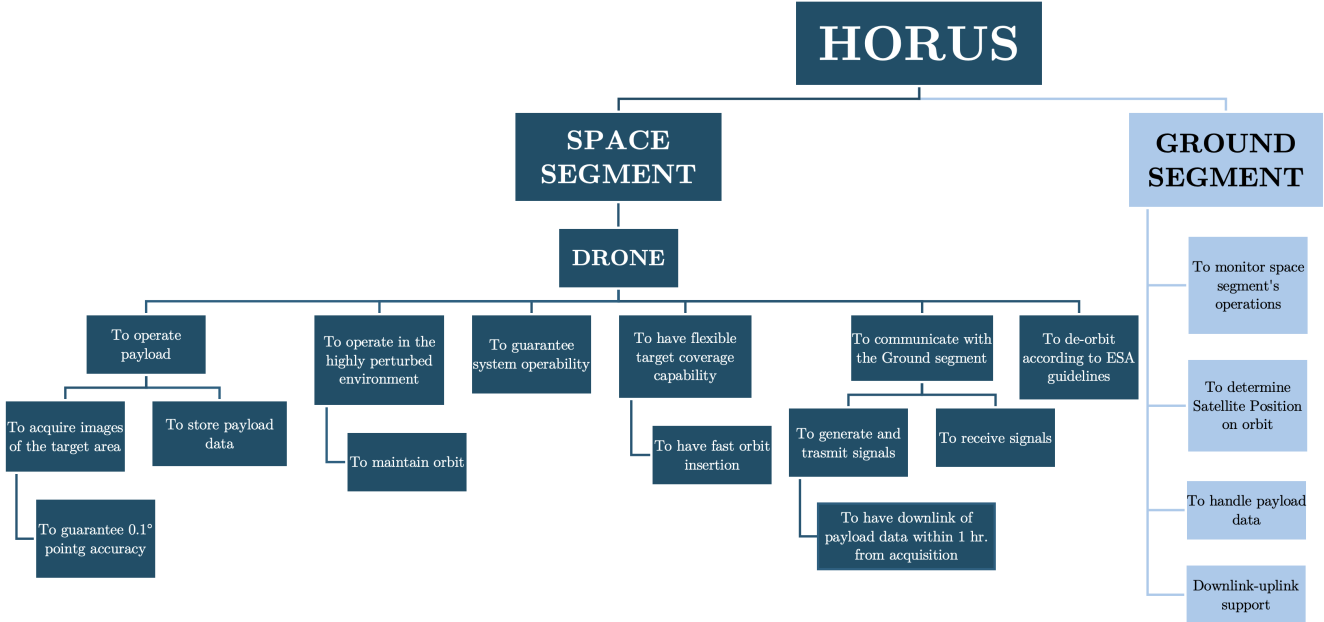


Figure 12: HORUS Functional Decomposition

4.2 Phases

The lifespan of the HORUS mission shall be classified into distinct phases according to the functionalities and tasks the system has to perform. These phases will be executed in a sequential order and have different durations depending on the number of operations required.

The phases for this mission can be categorized as:

- **Launch and Early Operations (LEOP)**

The Launch and Early Operations is the first phase of the mission. The initial functions to be performed in this phase are the launch and the release from the launcher's deployer. Once the spacecraft has been released, it powers up and activates the principal sensors and actuators for initial detumbling. Once the satellite has successfully detumbled, it establishes a first connection with the ground station, sending health status and launch logs.

- **Commissioning Phase (COP)**

In this phase the activation of all secondary sensors and actuators is performed, along with functional tests to ensure spacecraft health and operability. During this phase, the satellite communicates continuously with ground stations and mission operations center. This task is fundamental to receive telecommands and send further details on the status of the sensors and the components onboard. Once the required tests are completed, the spacecraft performs an initial orbital manoeuvre to enter the target orbit of the mission.

- **Observation Phase (OBP)**

The Observation Phase is the core of the entire mission. This phase begins once all satellite functionalities have been verified in the COP and the spacecraft has completed the orbital insertion manoeuvre. Once in the correct target orbit, the satellite begins to perform the nominal functionalities of the mission such as: orbital control and station-keeping, PL data acquisition, data processing and storage, communication with the GS and data transfer.

- **Disposal**

The Disposal phase represents the last portion of the spacecraft mission. Once the satellite ends its intended lifetime or once the mission is completed, the spacecraft enters into the disposal phase. During this phase, all the subsystems are progressively switched off, and the system is passivated and deactivated according to the ESA space debris mitigation requirements [39].

4.3 Conceptual Operations

Conceptual Operations (ConOps) fix the spacecraft functionalities on a timeline, defining their logical sequence and overlapping. In the following figure, all the functionalities presented have been categorized according to mission phases, clearly identifying their flow down. The table has a chronological rationale, describing the spacecraft operations from the very beginning of the mission up to disposal.

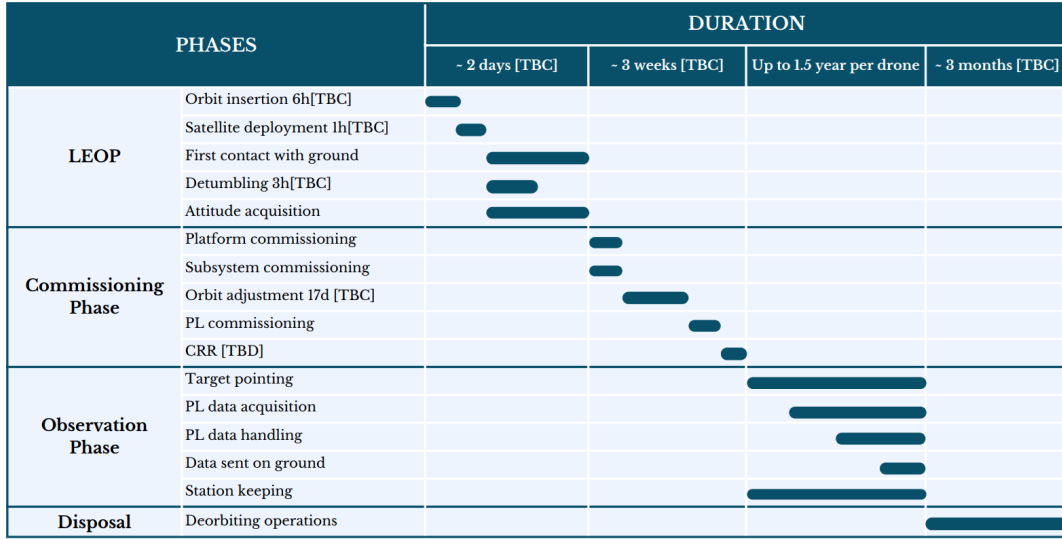


Figure 13: Satellite ConOps

The timeline serves as a critical tool for mission planning and execution. The durations indicated for each activity are still to be confirmed, while for the Observation Phase the duration could depend on the space drone lifetime and on the customer's needs, ensuring flexibility in adapting to unforeseen circumstances or evolving requirements.

4.4 System Modes

Figure 14 shows the main system modes along with their logical connections. This mode representation is crucial to understand the satellite state machine and how HORUS transitions between different operational modes throughout the mission. As it can be seen, six main modes are highlighted:

- **Activation Mode:** this mode activates the satellite after its deployment. During activation, the OBC is powered on, and health checks are performed to verify system integrity. The satellite establishes communication with the GS to confirm its status, and solar panels are deployed to initiate power generation. This mode ensures that the satellite is fully operational and ready to transition into Stand-by Mode.
- **Stand-by Mode:** it represents a go-through mode where the satellite fulfils only the Sun pointing requirement and charges the batteries. In this mode, non-essential tasks are not performed, allowing the satellite to save energy while remaining ready for further operations.
- **Safe Mode:** mode in which the satellite enters if autonomously detects a predefined operating situation considered as not nominal. In this mode all the payloads and non-essential components are turned off, guaranteeing only the course solar array Sun pointing and GS communications.

- **Orbit Control Mode** : This mode utilizes the thruster to perform various orbital manoeuvres, such as orbital insertion and station-keeping.
- **Imaging Mode** : This is the primary mission mode in which the payload is fully operational.
- **Telecom Mode**: In this mode, the satellite communicates with the ground station. Slew manoeuvres are performed to align communication antennas, ensuring an efficient data exchange.

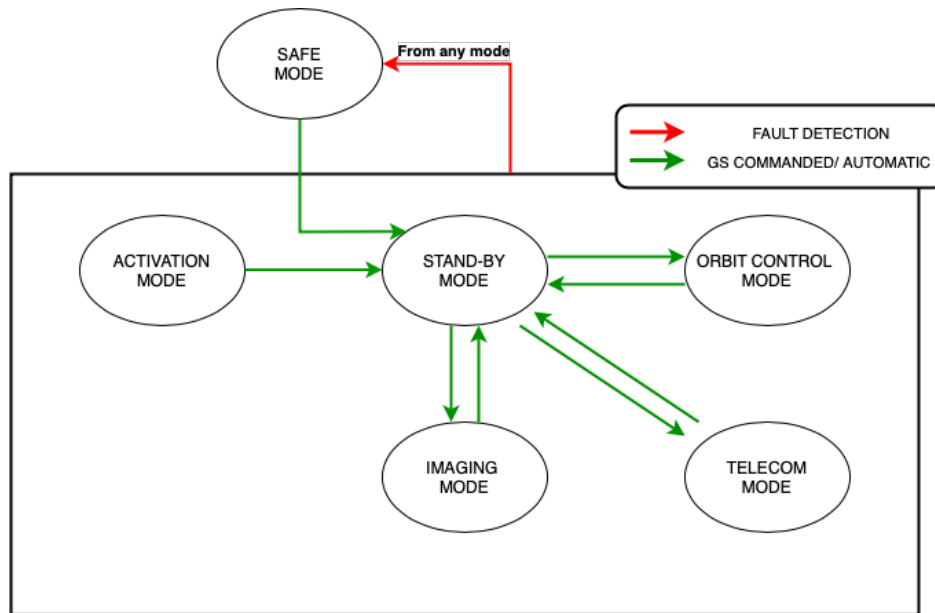


Figure 14: System Modes for drone architecture

5 Mass Budget

The estimated mass budget is an invaluable tool for preliminary mission analysis.

The mass budget is derived based on input data from the selected payload and all the subsystems, and the results are shown in Table 13.

Subsystem	Mass [kg]	Margins [%]	Mass margined [kg]	Mass percentage [%]
Payload	12.000	5	12.600	15.64%
AOCS	10.550	5	11.077	13.75%
EPS	9.992	5	10.492	13.02%
OBDH	1.139	5-10	1.250	1.55%
PS	9.462	5-10	10.111	12.55%
Structure	15.241	10	16.766	20.81%
TCS	16.517	5	17.343	21.53%
TTMTC	0.885	5	0.930	1.15%
Total mass	75.787	-	80.564	100%

Table 13: Mass budget

The adopted margins align with the ECSS Standards [40]. Specifically, a 5% margin was applied to COTS components, a 10% margin to modified COTS components, and a 20% margin to internally designed components. At the system level, a 20% margin on the total dry mass is also applied:

$$\text{Total Margined Mass} = 96.676 \text{ kg}$$

It should be noted that the Xenon propellant mass, which is approximately 8 kg, was not included in this evaluation, as the ECSS guidelines only consider the total dry mass of the S/C. However, this remains a critical consideration for further analyses, such as configuration and structural assessments.

Considering the obtained results from all the subsystems and evaluating the mass percentage of each one, a rationale can be drawn by also comparing with other similar missions in LEO and VLEO. From the literature, it is observed that the structure of satellites in LEO and VLEO typically accounts for 12% to 20% of the satellite's total mass [41] [42]. Moreover, it can be noted that the TCS is the heaviest subsystem on board. This can be explained by considering the type of mission, the orbit, and the altitude that the HORUS spacecraft must achieve in order to meet all the mission requirements. Being in a polar orbit with low altitude and frequent sunlight-eclipse shifts generates significant thermal stresses on the structure, which must be effectively managed, leading to a structured TCS. A 10% margin was also applied to the harness of the OBDH subsystem, which fits well, as literature suggests that the mass percentage of the OBDH subsystem in such missions typically ranges from 1% to 1.5% of the spacecraft's total mass.

6 Mission Architecture Solution

The architecture solution represents the foundational concept of the HORUS project, serving as the framework upon which all mission elements are built. This solution integrates insights derived from the detailed subsystem analyses and aligns them with the constraints and requirements identified during the Mission Analysis.

6.1 Trade-Off Analysis

The selection of the alternative was conducted considering a Trade-Off Analysis with quantitative parameters. The first step involved defining the possible architectures that could be analysed:

- **Scalable Architecture :** This approach consists of a single space drone, whose architecture can be scaled based on mission requirements. If the area to be covered is relatively small, a single drone may be sufficient. However, for larger areas, multiple launches of space drones, either in flight formation or as part of a constellation, would be required. This solution offers high flexibility in mission planning.
- **Single Satellite Deployer:** In this architecture, a deployer is used to release drones directly into space as needed. This significantly reduces the time of flight but comes with high development costs for the deployer itself. Additionally, this approach carries a high risk, because if the deployer fails, all drones onboard would be lost.
- **Space Drones Constellation:** This solution involves maintaining a permanent constellation of drones in VLEO. The primary advantage is the ability to cover a vast area while significantly reducing the time of flight. However, a major challenge is the high maintenance cost associated with operating at such a low altitude. Due to the limited lifetime of drones in VLEO, frequent replacements would be necessary, leading to substantial costs.

The choice of key trade-off parameters is another important step for the set up of the Trade-Off Analysis. The parameters are ranked as follows:

Parameter	Description
Time to Fly	As specified in the mission requirements, HORUS shall be operational no later than two months after stakeholders request the mission.
Delta-V	The necessity to perform orbital maneuvers is crucial for mission design. A lower need for orbital changes is preferable, as it can save on mass, cost, and power requirements.
Ground Visibility	One of the most critical requirements is to downlink the images in less than one hour. For that reason, ground visibility is an important parameter that must be considered in the alternatives trade-off.
Costs	Controlling mission and launch costs is crucial for the project feasibility and success.
Redundancy	It is a critical factor in satellite mission design to enhance reliability and ensure mission success.
Revisit Time	This is a key parameter since the HORUS mission requires frequent observations of a specific target, at least one per day.
Covered Area	This parameter is a fundamental metric in mission design, determining the geographical extent of observations during each orbital pass.
TRL	Even if the mission does not have stringent time requirements, it is important to consider the maturity level of different architectures. Developing systems with a lower TRL can introduce additional complexity to the design process and risks to mission success.

Table 14: Key mission parameters and their descriptions.

The Trade-Off Analysis is performed by evaluating a specific parameter, such as Δv , for each architectural alternative. The parameter is subsequently normalized using the following formulas:

$$P_i^{norm} = \frac{P_i - P_i^{min}}{P_i^{max} - P_i^{min}}; \quad P_i^{norm} = \frac{P_i^{max} - P_i}{P_i^{max} - P_i^{min}}$$

where the choice of the formula depends on whether a higher or lower value of the parameter is preferred. The normalized parameters satisfy the condition $P_i^{norm} \in (0, 1)$.

The first normalization formula is applied to trade-off parameters where higher values are preferable, such as Ground Visibility, Redundancy, Revisit Time, Covered Area, and TRL. Conversely, the second formula is used for parameters where lower values are advantageous, including Time to Flight, Δv , and Costs.

Once the parameters are normalized, they are weighted based on their relative importance in the analysis. Each parameter is multiplied by a weight factor ($w_i \in (0, 1), \sum_{i=1}^n w_i = 1$) assigned to it.

Finally, a composite score is calculated for each alternative by summing all the normalized parameters weighted by their respective factors:

$$S = \sum_{i=1}^n w_i P_i^{norm}$$

This score serves as the basis for comparing and ranking the alternatives. Given that this trade-off analysis is mainly qualitative, a **MonteCarlo** simulation was implemented to confirm the results. In this simulation, both the weight factors and the scores assigned to each category were varied in each iteration. The weight factors were randomly adjusted within a range of $\pm 10\%$ around each value. Similarly, the scores were varied by ± 1 from their assigned values. After running 1000 simulations, the results are presented in figure 15.

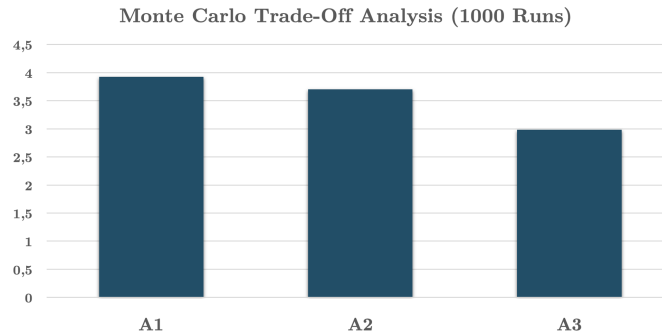


Figure 15: **A1**: Scalable architecture **A2**:Space-Drone Deployer **A3**: Permanent Constellation

Based on this analysis, the selected architecture is the **Scalable Architecture** (A1), chosen for its flexibility and scalability, which were key factors in the decision.

6.2 Payload Selection

One of the main goals of the mission is to observe the ground with a resolution of 1 m in terms of GSD. This requirement affects primarily the choice of the orbital altitude, having in mind that to demonstrate the technology readiness in VLEO the S/C shall fly at least above 100 km. This means that the cameras shall be selected either with a large focal length or with a very small pixel pitch (Equation (5)), which in most cases is synonym of massive and cumbersome payloads.

$$GSD = \frac{p \cdot h}{f} \tag{5}$$

Furthermore, to ensure an acceptable coverage, a good FoV is not always the solution. This because the ground footprint (i.e. swath width, Equation (6)) depends not only on the scan angle, but also on the altitude.

$$SW = 2 \cdot h \cdot \tan \frac{\text{scan angle}}{2} \tag{6}$$

The selection of the payload should consider not only performance but also key constraints, such as the storage capacity, which is important for the sizing of the OBDH subsystem, the operational range of temperatures, which represents a constraint for the TCS, and power requirements as input for the EPS sizing and selection.

Lastly, spectrum bands of interest need to be selected carefully, depending on the orbit, altitude and illumination conditions. A payload which works in Visible Band and Infrared band would be suitable as it can take images both in day and in night mode. Additionally, Panchromatic Band usually maximizes the resolution [43]. Table 15 and Table 16 show some cameras which might be suitable for this kind of mission.

	TriScape100	TriScape200	STREEGO	HRVI (multispectral)	HRVI (hyperspectral)
Origin	Simera Sense (South Africa)	Simera Sense (South Africa)	Media Lario (Italy)	BST (Germany)	BST (Germany)
Focal Length [mm]	580	1067	1200	500	500
Max altitude [km] (GSD $\leq 1\text{ m}$)	105	333	218	109	109
Mass [kg]	1.10	12.10	22.00	10.45	10.45
Dimensions [mm]	98 \times 98 \times 176	216 \times 216 \times 304	305 \times 525 \times 530	540 \times 320 \times 170	540 \times 320 \times 170
Power [W]	2.5 to 5.8	2.5 to 5.8	48	-	-
FoV [deg] (along / across)	1.66 / 2.22 (along / across)	1.20 / 1.60 (along / across)	1.08	8.01	3.09
Swath [km] (Max altitude)	3.05 / 4.08 (along / across)	6.98 / 9.31 (along / across)	4.11	15.22	5.87
Bands	VIS	VIS	9 bands VIS-NIR + PAN	PAN	PAN
Operational T [°C]	-10 to 50	-10 to 50	passive control	0 to 30	0 to 30
Storage [Gb]	128	128	-	1000	1000

Table 15: Suitable payloads (a)

Having in mind that a good resolution is needed in the range of VLEO altitudes, TriScape100 and HRVI are discarded as they can operate just very close to the minimum threshold. STREEGO offers the possibility to work both in VIS and IR bands but is discarded due to its high mass and low maximum altitude. The remaining alternatives have to be compared looking at the field of view and swath width, the operational bands, mass and power. Triscape200 has a very competitive power consumption but unfortunately it works only in VIS band and it has a smaller swath width with respect to the other, reducing the overall coverage area of the mission.

	iSIM-90 (1 channel)	iSIM-90 (2 channels)	iSIM-170 (1 channel)	iSIM-170 (2 channels)
Origin	Satlantis (Spain)	Satlantis (Spain)	Satlantis (Spain)	Satlantis (Spain)
Focal Length [mm]	1667	1667	3438	3438
Max altitude [km] (GSD $\leq 1\text{ m}$)	303	303	625	625
Mass [kg]	< 4	< 6	< 8	< 15
Dimensions [mm]	308 \times 114 \times 100	308 \times 216 \times 115	593 \times 276 \times 308	593 \times 471 \times 308
Power [W]	25.3	30.5	25.3	30.5
FoV [deg]	1.49	1.49 to 2.98	0.86	1.72
Swath [km] (Max altitude)	7.88	7.88 to 15.76	9.38	18.75
Bands	PAN,VNIR up to 4	PAN,VNIR up to 8	PAN,VNIR up to 5	PAN,VNIR up to 5
Operational T [°C]	active control	active control	active control	active control
Storage [Gb]	500	500	500	500

Table 16: Suitable payloads (b)

The iSIM single channel solutions have to be discarded as well, as the single channel can be set just in one of the two bands. Eventually, the iSIM-90 dual channel is selected, because it weights almost one third with respect to the iSIM-170, it has more contained volumes, the difference in FoV and swath width with respect to the iSIM-170 is not so large and eventually is a flight-proven product with TRL 9 [44] ensuring flexibility in terms of spectral bands. In fact, the producer offers the possibility to exploit the SWIR band as well, which has lower sensitivity to atmospheric scattering, improving image quality in the presence of fog, dust, or smoke.

Furthermore, to increase the swath width, a configuration with two iSIM-90 dual-channel is deemed to be the best solution.

7 Launcher Analysis

The choice of the correct launch vehicle is the base of a complete and correctly designed space project. The launcher is the first access to space and its performances and costs may vary significantly. For this reason a thorough analysis of the alternatives must be performed.

7.1 Present Launchers

As of the end of 2024, there are few European launchers readily available for launch. In particular the main launchers which are commercially available and flight proven are:

- The Ariane 6 launcher from the Ariane Group in its two main variations:
 - The Ariane 62, which has 2 auxiliary solid boosters
 - The Ariane 64, which has 4 auxiliary solid boosters
- The Vega-C (Vega Consolidation) from Avio, which is aiming to replace with better performances the previous Vega launcher.

7.1.1 Launcher Performances

These commercially available launchers have very different performances and reachable orbits, which are further explored in this paragraph.

Ariane 6

Both Ariane 6 variations launch exclusively from ESA Guiana Space Center (CSG), allowing access to almost any orbit inclination. Following the Ariane 6 launcher manual [45], the minimum reachable inclination is slightly less than 6° while the most common inclinations for commercial launches of the Ariane 6 are equatorial missions ($\sim 6^\circ$), polar missions ($\sim 90^\circ$) and Sun Synchronous Orbits ($\sim 98^\circ$). It must be noted that the Ariane 6 is able to launch spacecrafts outside of the LEO. Furthermore, Ariane 6 has an injection accuracy of $\pm 2.5 \text{ km}$ for the semi-major axis, $\pm 0.2^\circ$ for the Right Ascension of the Ascending Node (Ω), and $\pm 0.02^\circ$ for the inclination, considering a standard LEO SSO at an altitude of 800 km.

Launch frequencies of the Ariane 6 are not fixed yet, as the launcher has recently entered the commercial market. The desired frequencies declared by Ariane are around 4 launches per year for each launcher configuration (Ariane 62 or 64). As far as launchable payload masses, the values for the Ariane 6 vary widely depending on the altitude and inclination of the desired orbit as well as the launcher configuration used. The main reference values for LEO launches are collected in Table 17.

Orbit	Inclination	Altitude	PL Mass	
			Ariane 62	Ariane 64
SSO LEO	98°	500 km	7200 kg	15500 kg
Equatorial LEO	6°	350 km	10000 kg	21000 kg

Table 17: Maximum PL mass of the Ariane 6 for different standard orbits [45].

Vega-C

The Vega Consolidation, better known as Vega-C, is a newer and upgraded version of Avio's Vega, which debuted in July of 2022. As already seen for Ariane 6, the only commercial launch site for the Vega-C is ESA Guiana Space Center (CSG). Following the Vega-C launcher manual [46], almost all inclinations are obtainable, with a minimum reachable inclination of slightly less than 6° , similarly to the Ariane 6. The Vega-C, although its wide inclination range, has the capabilities of releasing payloads only in the LEO range with a maximum altitude of 1000 km. Furthermore it has an injection accuracy of $\pm 15 \text{ km}$ for the semi-major axis, $\pm 0.15^\circ$ for inclination and $\pm 0.2^\circ$ for the RAAN.

Although declared launch frequencies for the Vega-C are around 5 launches per year, in recent years this number has lowered significantly after the Vega-C was grounded in late 2022, due to a launch failure where both launcher and payloads were lost. The Vega-C is set to return in the last quarter of 2024, after completing all pre-launch tests, and the launch frequencies will increase gradually in the next few years. The maximum launchable mass for the Vega-C vary depending on the inclination and the altitude of the desired orbit. The main reference values are collected in Table 18.

Orbit	Inclination	Altitude	PL Mass Vega-C
Equatorial LEO	6°	1000 km	1700 kg
SSO LEO	98°	1000 km	1850 kg
Polar LEO	88°	500 km	2250 kg

Table 18: Maximum PL mass of the Vega-C for different standard orbits [46].

7.1.2 Fairing Volumes

When exploring launcher selections it is crucial to perform an analysis of the available fairing volume, in order to verify these are compatible with the system.

Ariane 6

The available fairing volume in the Ariane 6 varies widely depending on the configuration of the launcher and the Payload. For single launch configurations the volumes vary depending on the configuration of the launcher (Ariane 64 or 62) and are shown in Figure 17 and Figure 16.

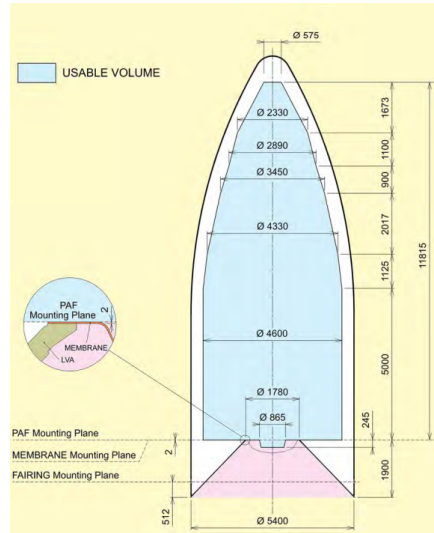


Figure 16: Available fairing volume for a Single Launch Ariane 62 configuration [45]

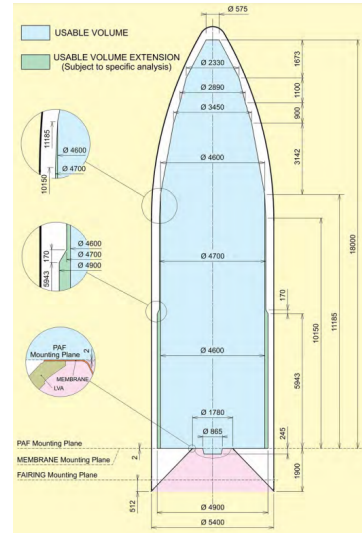


Figure 17: Available fairing volume for a Single Launch Ariane 64 configuration [45]

On the other hand, in the Dual Launch Structure (DLS) configuration, which can be mounted only on the Ariane 64, two configurations are available. The two configurations, shown in Figure 18 and Figure 19, differ in a meter of height one from another and their use depends on the mission requirements and constraints.

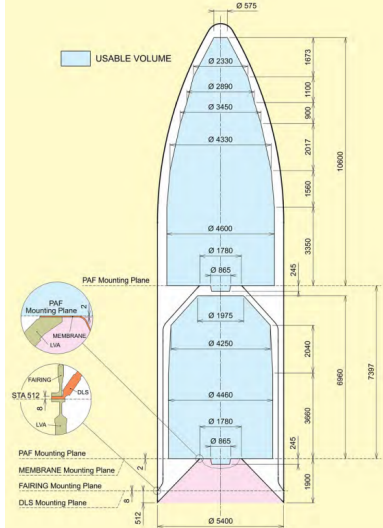


Figure 18: Available fairing volume for the long Dual Launch Structure configuration [45]

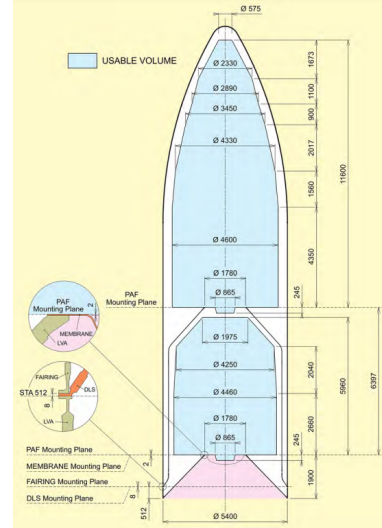


Figure 19: Available fairing volume for the short Dual Launch Structure configuration [45]

Vega-C

The available fairing volumes in the Vega-C vary depending on the configuration of the Payload. In Figure 20 the available fairing volume is shown in a dual S/C configuration, both in the short and long version.

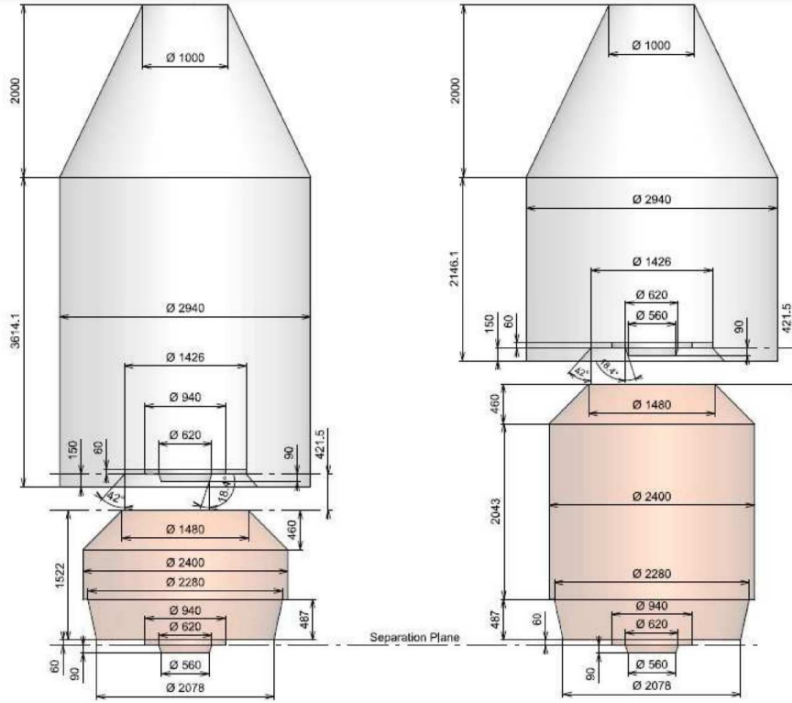


Figure 20: Available fairing volumes for the short and long Dual Launch Structure configurations [46]

7.2 Launchers Under Development

In this section a quick overview of all launchers under development will be presented. Only launchers which expect to launch before 2026 and have a minimum payload mass of at least 400 kg have been considered for this section, enough to contain multiple drones at once.

According to the European Rocket Index by European Spaceflight [47], in the years to come several new launchers currently under development will have their debut launch. Table 19 showcases all future launchers, their performances and future costs. These values are an initial estimate by each company and may change in the future after the launcher becomes commercially available.

Launcher	Company	Debut Year	Launch Frequency	PL Mass in LEO	Costs per kilo
Vega-E	Avio	2026	~ 4 launch/year	2300 kg	11500 €/kg
RFA One	RFA	2025	~ 20 launch/year	1350 kg	2300 €/kg
Spectrum	Isar	2025	~ 12 launch/year	1000 kg	10000 €/kg Rideshare 15000 €/kg Dedicated
SL1	HyImpulse	2025	~ 6 launch/year	500 kg	< 20000 €/kg
Sirius 13	Sirius Space	2026	~ 4 launch/year	500 kg	< 20000 €/kg
Maia	Maiaspace	2026	~ 6 launch/year	500 kg	10000 €/kg
Miura 5	PLD	2026	~ 10 launch/year	450 kg	15000 €/kg

Table 19: Future launchers with their relative performances and costs [47]

As seen in Table 19, there is a wide range of available options in the near future for possible launchers. In particular RFA One stands out, as it aims to drastically lower costs while increasing the launch frequency at the same time. On the other hand, it is also important to note that for all listed launchers the transition from the first commercial launch to the expected launch frequency might last several years and the actual frequency might vary during this period.

7.3 Launch Strategy

Since the mission requires a high launch frequency all-year round to ensure the correct coverage and short time to flight requested, it has been decided to use both the Vega-C and Ariane 6 launchers. This is because both launchers have a relatively low launch frequency and not every launch may be directed to the desired insertion orbit of the mission. Launching with both launchers would ensure a sufficiently high launch frequency for the mission.

Furthermore both launchers have similar performances in terms of desired insertion orbits for the mission and both lift-off from the same spaceport, the Guiana Space Center, which could lower assembly and integration costs. Each launcher has its own advantages and drawbacks, in particular:

- **Ariane 6** has lower launching costs and a higher launch frequency. At the same time, due to the high launchable payload mass and wide range of reachable orbits, it is possible that most of the Ariane 6 launches are outside the LEO region. Furthermore a satellite with an estimated mass similar to the one of this mission might not have a say when deciding the insertion orbit altitude, inclination and RAAN of LEO launches.
- **Vega-C**, on the other hand, might be more flexible in terms of insertion orbits as it has a much lower launchable mass and it is capable of only launching in LEO, especially thanks to its new projects such as the fourth stage Attitude and Vernier Upper Module (AVUM+) and the uncrewed spaceplane Space Reusable Integrated Demonstrator for Europe Return (Space RIDER). At the same time launch costs of the Vega-C are much higher with respect to the Ariane 6 and its launch frequency remains low after the late 2022 grounding of the launcher.

Table 20 the main performance parameters of each available launcher are highlighted and compared.

Launcher	Mass to LEO	Launch Frequency	Costs to LEO	Autonomous Deployer
Vega-C	1850 kg	~ 5 launch/year	11500 €/kg	Integrated and External
Ariane 62	7200 kg	~ 4 launch/year	7300 €/kg	External Only
Ariane 64	15500 kg	~ 4 launch/year	5300 €/kg	External Only

Table 20: Comparison of launcher performances

Furthermore most launchers under development detailed in Section 7.2 will be implemented in the launching strategy of this mission once commercially available. This will ensure an even further launch frequency, allowing continuous launch of satellites and enabling multiple Earth observation missions at once.

Since this missions is strongly dependent from the client requests it is important to generate specific launch strategies case by case. In general, the launch philosophy for the mission is to initially launch a small batch of drones, ensuring partial coverage and a rapid response time, and to complete the constellation through successive launches. This is also done to prevent having to change a whole constellation at once if the mission duration is longer than the drone lifetime. By doing so the drones can be interchanged in a phased manner, without having to cycle a large number of drones at once. This philosophy has to be adapted to the clients requests and, for mission with a low number of drones or a duration lower than the S/C lifetime, a complete constellation could be launched at once.

The implementation of spacecraft deployer in the near future would allow the drone to be released directly into the VLEO, thus eliminating the need for the orbital insertion manoeuvrer. The deployer could be an additional stage integrated directly into the launcher, such as the Space RIDER for the Vega-C, or an external deployer could be implemented at an additional cost, such as the D-Orbit ION deployer.

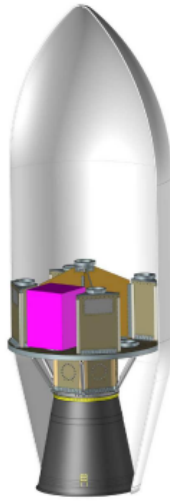
7.4 Launch Configuration

As one of the high level requirements consists in minimizing the time before being completely operational, it is crucial to design the launch configuration as efficiently as possible in order to maximise the number of satellites deployed with one launch.

Vega-C

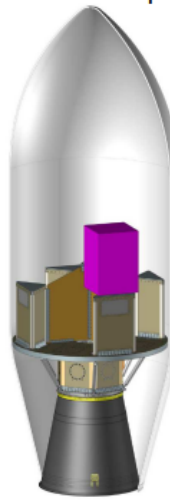
In the Vega-C user manual for Small Spacecraft Mission Service (SSMS) [48], the possible configurations for small satellites are explored. The HORUS spacecraft is classified as a micro spacecraft, due to its mass being over 60 kg. For this reason it was chosen to use the ride-share configuration **Flexi-4**, which grants 8 positions for mirco satellites, 4 in tower positions and 4 in the main deck position. There is space for one more spacecraft if the VESPA-R adaptor is implemented in series with the SSMS, for a maximum of nine drones capacity. Below, the possible fittings of the drones within the fairing are shown.

1. SSMS Main deck



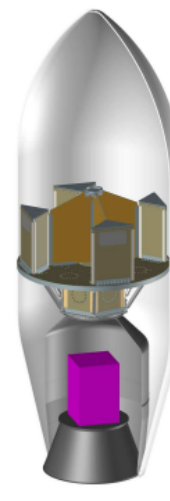
(a) SSMS Main Deck Position

2. SSMS Towers posit°



(b) SSMS Tower Position

3. VESPA+R Inner posit°



(c) VESPA+R Inner Position

Figure 21: Satellite possible positions inside the Vega-C SSMS [48]

For the mechanical interface with the launch vehicle it was chosen to use the Motorized LightBand (MLB MkII) from Planetary Systems Corporation (PSC). This interface was selected for its low mass retained on the spacecraft (0.6 kg) and its effective separation mechanism, allowing the spacecrafts to be deployed one after the other. Following the user manual, the smallest diameter for micro satellites adapters is 330 mm (13"). The adapter will be placed on the thruster face of the spacecraft as it is the face with less obstructions on its surface. The thruster will be left outside the spacecraft by at most 25 mm, not interfering with the adapter, which is 53 mm high.

Ariane 6

Following Ariane's user manual for Multi Launch Services (MLS) [49], the best interface for HORUS would be three HUB interfaces stacked one on top of the other. With the implementation of adaptation plates, shown in Figure 22, it would be possible to launch up to 36 drones simultaneously, allowing the deployment of full constellations.



Figure 22: Adaptation plat for the HUB interface
[45]

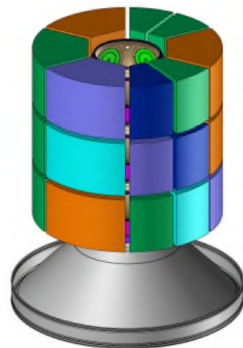


Figure 23: 3 HUB interfaces stacked

8 Mission Analysis

8.1 Nominal Orbit Design Process

The first step in mission analysis involves the identification of the nominal orbit for the drones, in compliance with the high level mission requirements. The feasibility of a single satellite solution is investigated.

8.1.1 Requirements Recap

To be considered as a candidate solution, the nominal orbit shall guarantee that the following requirements are satisfied:

- Acquire high-resolution images of a fixed target with a time resolution within 1 day
- Spatial resolution below 1 m
- Downlink within 1 hour from acquisition;
- Operate in VLEO environment;
- Guarantee flexibility in target coverage.

8.1.2 Altitude and Eccentricity Selection

To guarantee the passage over a specific target at least once a day, an orbit with repeating ground track shall be designed. Hence the semi-major axis can be easily computed as

$$a = \left(\frac{\mu}{\left(\frac{k \omega_E}{m} \right)^2} \right)^{\frac{1}{3}} = 6640.8 \text{ km} \quad (7)$$

where ω_E is the angular velocity of the Earth, m represents the Earth rotations (set to 1) and k is the number of revolutions of the satellite every Earth revolution. By setting $k = 16$, altitude and therefore semi-major axis are obtained within the VLEO range.

Next, by taking a look at the eccentricity, with a fixed semi-major axis and under the hypothesis of continuous thrusting and exponential atmospheric density model, the cost for drag compensation becomes the driver, as shown in Figure 24 (the drag coefficient and area-to-mass ratio have been arbitrarily taken, this does not influence the overall trend).

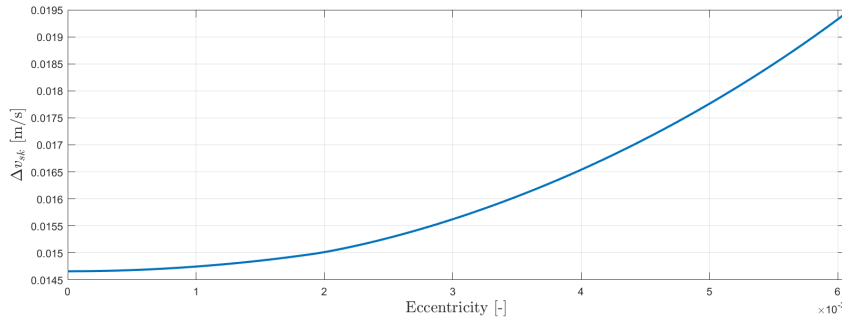


Figure 24: ΔV per orbit for Drag Compensation, with ref. values: $C_d = 2$ and $\frac{A_{cross}}{mass} = 0.001 \frac{m^2}{kg}$

The optimal orbit would be a circular one. Also, an upper bound on the eccentricity can be computed to ensure at any point on the orbit the desired image resolution compliant with payload specifics. This is done by setting, still considering a general elliptical orbit, an apogee altitude of 303 km. The so found value is an eccentricity of about 0.0061. Eventually, an eccentricity $e = 0$ is selected, which is a beneficial choice from the zonal harmonic effects point of view, better discussed in the next sections.

8.1.3 Downlink Strategy and J2 Perturbation

Hence, once both the semi major axis and the eccentricity have been fixed, further studies on the target orbit concern the requirement to downlink within 1 hour from acquisition. With no perturbations, a properly inclined orbit which passes over two points on the surface, taking into account Earth rotation, is always achievable. An example is shown in Figure 25:

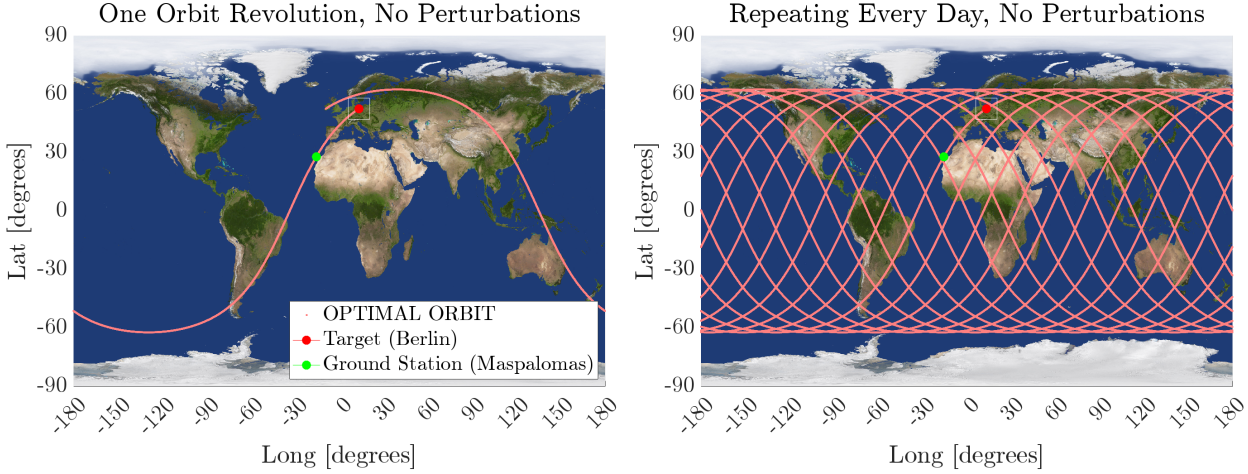


Figure 25: Representative example of a Retrograde Orbit passing over target then ground station

However, once the J2 perturbation is factored in, this ideal scenario shows its weaknesses. The drift of the orbital plane is definitely the major issue for missions requiring a fixed target observation. Keeping the same example above, after just few days from its first passage over the target, the ground track is no longer repeating and the drone drifts away from the target as shown below in Figure 26. Hence, since the behavior of the J2 perturbation can be easily predicted analytically and due to the shift in RAAN being linearly dependent with the cosine of the inclination, a limit was imposed on the candidate solutions: only orbits within the range $80 - 100^\circ$ inclination were to be considered. It's important to note that inside this range sun-synchronous orbits could be exploited for both TCS and EPS's sakes. A feasibility analysis was therefore performed within this range. Figure 27 shows the drift of an 88° inclined orbit over the same sample target.

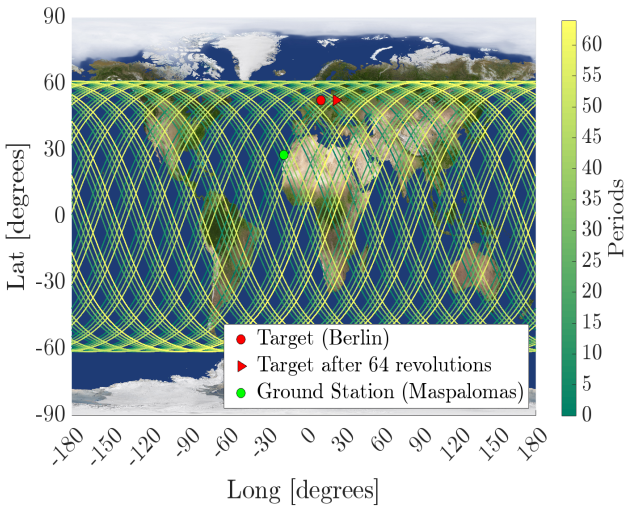


Figure 26: J2 effect on the Ground Track over 64 revolutions (4 days)

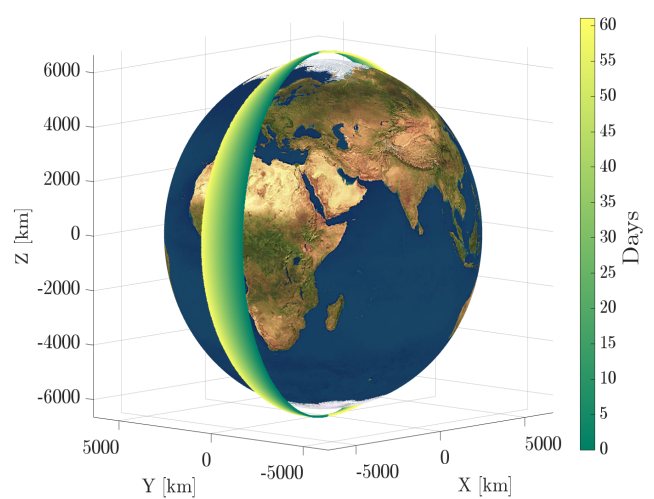


Figure 27: J2 effect on a 88° inclined orbit over two months

By looking at Figure 27 it's clear that the J2 induces a drift which, due to the low altitude operations, makes it impossible to guarantee consistent visibility over the target for multiple days. This is quantified in Table 21. Here, by assuming a maximum slew angle of 25° , the number of days at which the target

remains observable is computed for different altitudes.

Latitude [°]	0	15	30	45	60	75
Days	8.35	8.64	9.34	11.80	16.69	32.25

Table 21: Observation window in days for different latitudes for a single satellite.

It's clear that the closer the target is to the equator, the shorter the visibility of becomes.

Although J2 perturbation affects both RAAN and perigee, due to the very small eccentricity, a drift in terms of argument of perigee is accepted as resolution requirements are achieved even at apogee. Hence compensation of the RAAN-drift is investigated. The Δv budget is reduced due the close-to-polar inclination, however the compensation is still very demanding. The cost for J2 compensation is about 40.70 m/s per day for a 88° inclined orbit.

These considerations lead to two possible architectures from the mission analysis point of view:

- Constellation of drones placed in equally spaced planes with same inclination. This would allow for continuous observability over the target, although higher costs and complexity.
- Single drone in polar orbit to have $\Delta\Omega = 0^\circ$

For both alternatives, ground station availability and downlink capabilities have to be properly assessed: Section 11.5.

After some design iterations, cost considerations and flexibility assessments, the single drone in circular and polar orbit architecture has been selected, with a nominal altitude $h = 262.75 \text{ km}$ and *RAAN* which will be selected depending on target longitude and reference epoch selected by the customer.

Hereafter an example of repeating ground track passing over Paris:

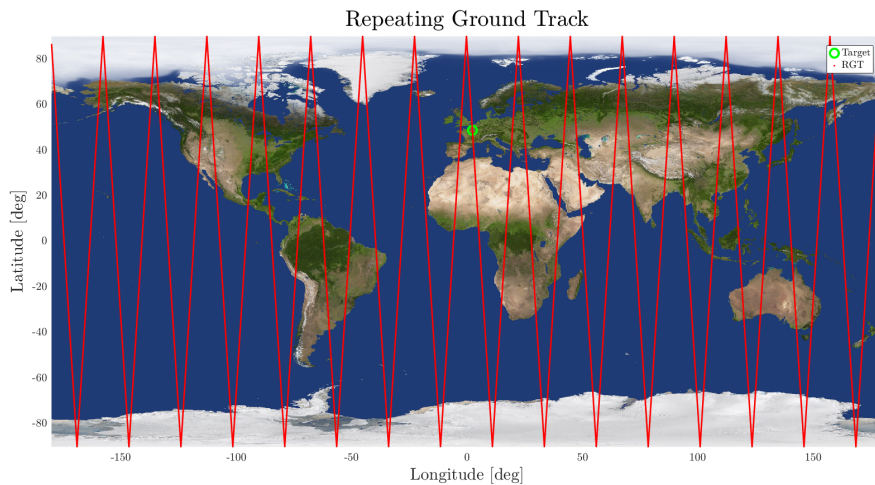


Figure 28: Repeating Ground Track related to the nominal orbit

8.1.4 Coverage Analysis and Formation Flight

Up to now, a solution just for small targets has been assessed. In this section, the limits and opportunities of a scalable architecture design will be discussed, depending on various customer needs scenarios.

A possible architecture solution which aims to enlarge the overall footprint on ground while exploiting the same orbital plane to minimize launch costs is to adopt a formation flight of a row of drones lined up.

Starting from the payload selection presented in Section 6.2 and the preliminary configuration, one single drone mounts two cameras with $FoV = 1.49^\circ$, so the FoV across-track for a single drone is doubled to $FoV = 2.98^\circ$. Considering the semi-major axis selected, which leads to an altitude $h = 262.75 \text{ km}$, and a margin for the FoV of about 0.1° ¹ (i.e. $FoV_{margined} = 2.88^\circ$), the performances in terms of resolution and

¹This margin corresponds to an assumed value of about 97% of the swath effectively covered during operations

across-track swath width for a single drone nadir pointing equipped with two optical payloads (Section 6.2) become:

$$SW = 2 h \tan(FoV_{margined}) = 13.21 \text{ km} \quad (8)$$

$$GSD = \frac{p}{f} h = 0.87 \text{ m} \quad (9)$$

with an along-track swath width of:

$$SW_{along} = 2 h \tan\left(\frac{FoV_{margined}}{2}\right) = 6.60 \text{ km} \quad (10)$$

The formation flight is made of drones to which specific coverage strips are assigned, as depicted in Figure 29, in order to build a bigger image. This is why a margin on the FoV has been considered, to ensure that in case of attitude errors the single images overlap and there are no strips on the ground left uncovered.

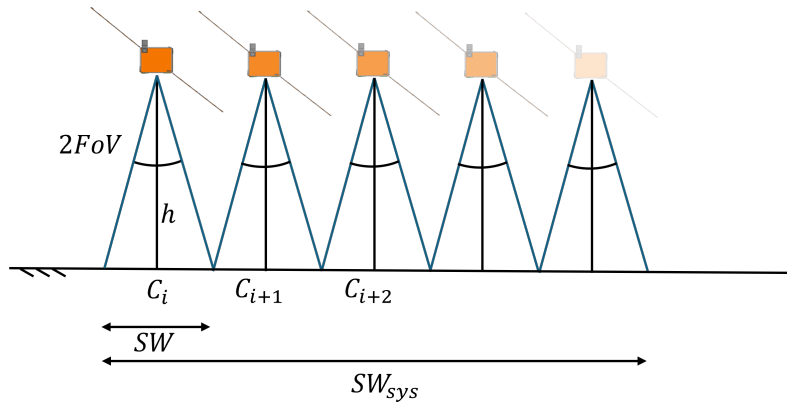


Figure 29: Nadir pointing formation flight concept

In this way, the system of drones is capable of reconstructing a bigger image by putting together all the different strips coming from each drone. The number of drones will be discussed with the customer depending on the coverage area needed, ensuring flexibility.

In principle, just square coverage areas (i.e. equal across-track and along-track image dimensions) have been considered, leading to a coverage area computed as:

$$A_{cov,max} = SW_{sys} n_{drones} SW \quad (11)$$

but, within the design iterations process, a limit on the along-track image acquisition came out from the TTMTTC sizing: a maximum of 20 consecutive images can be performed, to ensure that the high level objective of being capable to download the acquired data within 1 h is met.

For this reason, square images are allowed for formation flights up to 10 drones, while for more numerous formations the limit discussed above is considered in the computation of the maximum coverable area:

$$A_{cov,max} = SW_{sys} 20 SW_{along} \quad (12)$$

After these considerations, the coverable area curve can be obtained, and it is shown in Figure 30:

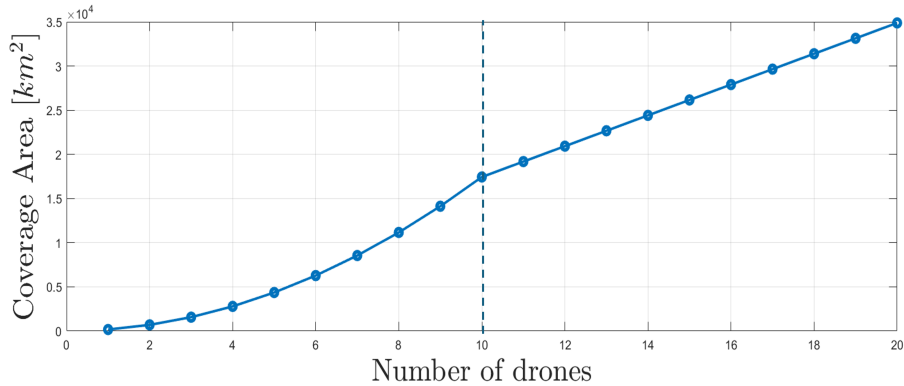


Figure 30: Coverable Area trend with increasing number of nadir pointing drones

This leads to 174.41 km^2 for a single drone architecture up to 34877.14 km^2 and $SW_{sys} = 264.13 \text{ km}$ using 20 drones.

It can be noticed how the downlink requirement limit impacts in the coverable area curve, whose trend switches from being quadratic to linear, reducing the advantage of implementing other drones.

For this reason, another method to gain coverage area is to impose that the imaging mode is performed with a different roll angle. This configuration increases the across-track swath width with respect to a nadir configuration, reducing the spatial resolution a bit.

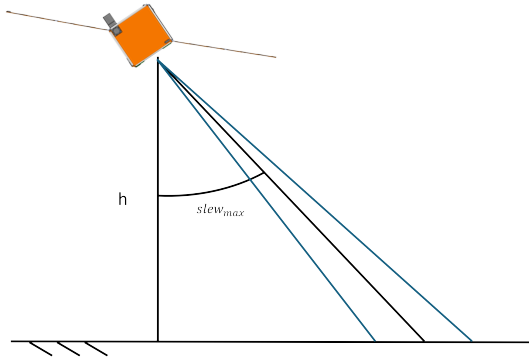


Figure 31: Rolled configuration during imaging mode

The maximum roll slew angle shown in Figure 31 can be computed from the payload performances, knowing that to obtain the desired resolution the boresight distance from ground shall be less than $h_{max} = 303 \text{ km}$:

$$slew_{max} = \arccos\left(\frac{h}{h_{max}}\right) - \frac{FoV}{2} = 28.44^\circ \quad (13)$$

With this limit configuration, the along-track swath width remains the same, while the across-track swath for a single drone is increased to $SW = 16.74 \text{ km}$ up to an overall swath width across-track of $SW_{sys} = 334.87 \text{ km}$ implementing 20 drones in a rolled configuration, as shown below:

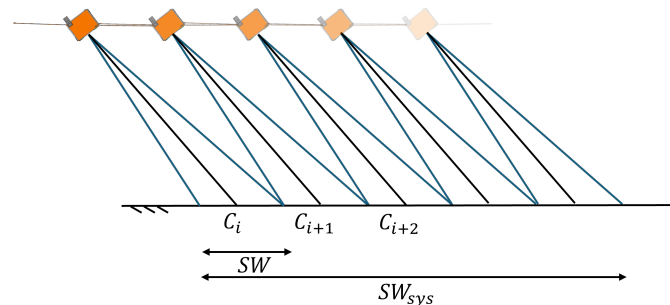


Figure 32: Rolled formation flight concept

With the very same reasoning as for the nadir pointing concept, the maximum coverable area can be retrieved, and a graphical comparison is presented hereafter:

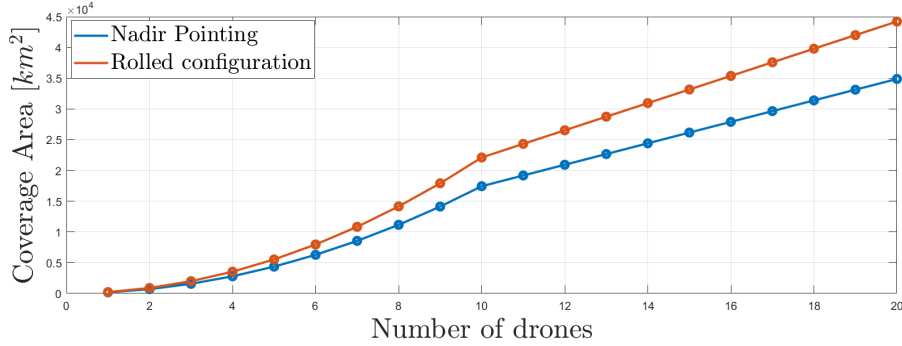


Figure 33: Coverage area comparison

For the new configuration considered, the maximum coverable area spans from 221.12 km^2 with one drone up to 44217.71 km^2 with 20 drones.

It can be noticed that, with this new strategy, the maximum area covered by 20 drones nadir pointing can be covered by 16 drones assuming the limit roll angle after a slew, which would be a big benefit in terms of costs. The drawback is that the swath width is increased renouncing to some spatial resolution, which now is set to $GSD = 0.99 \text{ m}$, so a trade-off shall be put in place depending not only on coverage requirements but also on resolution needs.

Now, it is important to check the shift in true anomaly between the different drones of a formation, regardless of the roll angle assumed during imaging mode. The idea is that, taking the tracks on ground related to the respective boresights of each drones, they can be converted in an information on the $\Delta\lambda$ from one track to the adjacent ones.

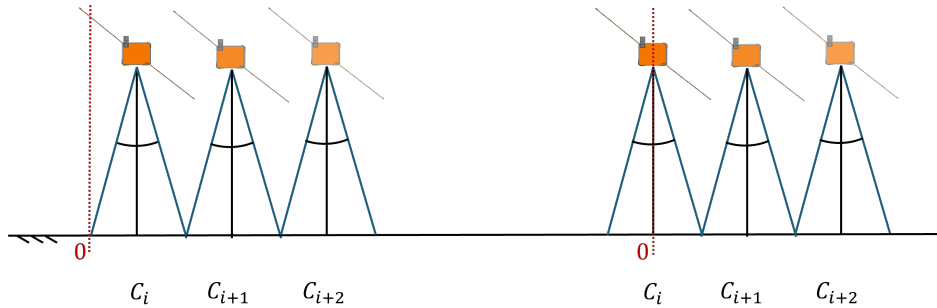


Figure 34: Track centers for both even (left) and odd (right) number of drones

Looking at the track centers in Figure 34, depending on the number of drones implemented and considering just half of the formation, the centers related to the boresight of each drone can be computed as:

$$\begin{cases} C_i = (2i - 1) \frac{SW}{2}, & \text{if } n_{\text{drones}} \text{ even} \\ C_i = 2i \frac{SW}{2}, & \text{if } n_{\text{drones}} \text{ odd} \end{cases} \quad (14)$$

It is important to say that the planar approximation of the Earth surface is a good one as for the available system swath the difference from the curved surface is minimal.

Another useful parameter is the inclination α_{tilt} of the ground track related to the nominal orbit with respect to the North-South axis. This angle is constant with respect to longitude and latitude for a polar orbit as it can be verified looking at Figure 28. Given a time interval dt , the associated $\Delta\theta$ that has been covered on the circular orbit, and the angular velocity of rotation of the planet ω_E , the needed angle, which in the neighbourhood of the target is constant, can be computed by trigonometric considerations on the longitude-latitude plane:

$$\alpha_{\text{tilt}} = \arctan \left(\frac{\omega_E dt}{\Delta\theta} \right) = 3.58^\circ \quad (15)$$

Once all the centers on ground are computed, their relative distances $C_{shift,ij}$ with the adjacent ones are useful to compute the difference on the parallel related to the target latitude:

$$\Delta\lambda_{km,ij} = \frac{C_{shift,ij}}{\cos(\alpha_{tilt})} \quad (16)$$

Now, the longitude shift in degrees is computed knowing the target latitude ϕ_T :

$$\Delta\lambda_{ij} = \Delta\lambda_{km,ij} \frac{360^\circ}{2\pi R_E \cos(\varphi_T)} \quad (17)$$

With this information available, it is possible to compute the time delay between two consecutive drones using the rotation of the Earth:

$$\Delta t_{ij} = \frac{\Delta\lambda_{ij}}{\omega_E} \quad (18)$$

and, finally, the true anomaly shift:

$$\Delta\theta_{ij} = \frac{\Delta t_{ij} 360^\circ}{T_{orb}} \quad (19)$$

In this formulation the target latitude φ_T plays a key role. In fact, on the equator the tangential velocity of the Earth is maximum, and the drones will need to be closer to each other, while for a target near to the poles their true anomaly differences can be greater and they will occupy a greater fraction of the orbit. For a 20 drones formation, the minimum $\Delta\theta$ among all the units and the percentage of the orbit occupied by the formation are shown below in Table 22:

Latitude [°]	0	10	20	30	40	50	60	70	80
$\Delta\theta_{min}$ [°]	1.90	1.93	2.02	2.20	2.48	2.96	3.80	5.56	10.95
Orbit Crowding [%]	10.0	10.2	10.7	11.6	13.1	15.6	20.1	29.3	57.8

Table 22: True anomaly shift and Orbit crowding with respect to target latitude

In conclusion, it is possible to scale the architecture by adding drones to a formation ensuring flexibility in terms of target size, as depicted in Figure 35, where for the coverage strips assigned to each drone are highlighted.

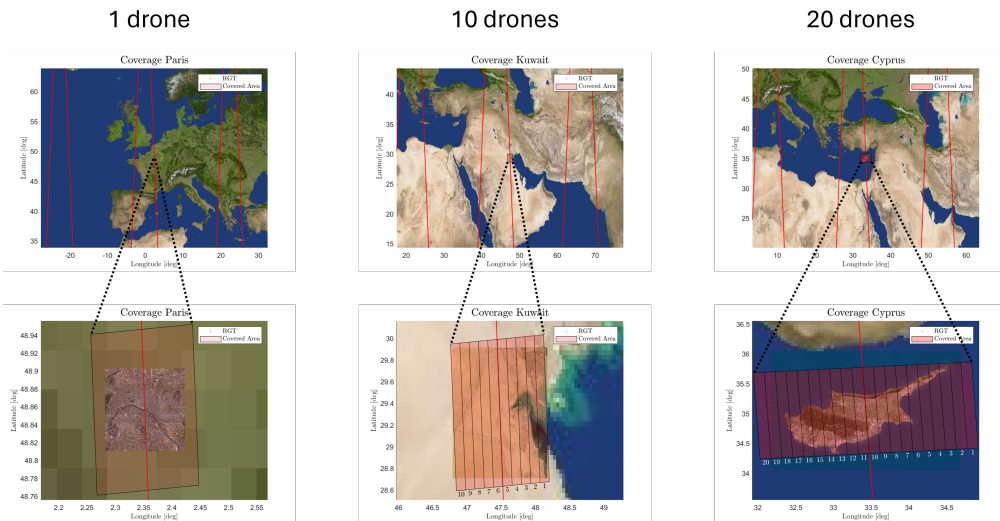


Figure 35: Repeating Ground Tracks and Details with three target examples with different area

8.1.5 Revisit Time

Up to now, the circular and polar orbit selected ensures that a repeating ground track is obtained, but every drone passes above the target just once a day. Further considerations and solutions are needed to improve the revisit time performances and ensure scalability of the architecture.

Thinking about the single drone architecture, a first solution, which exploits the same orbital plane to minimize launch and insertion costs, is to put a second drone that takes an image 12 h after. In fact, as the target rotates with the Earth, it crosses the orbital plane twice a day.

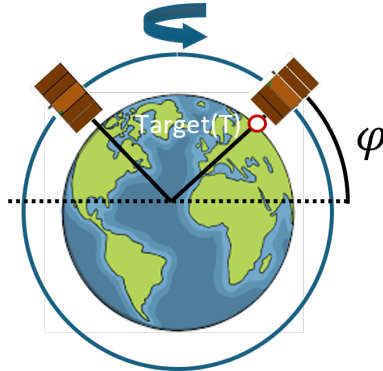


Figure 36: Two drones in one orbital plane to double the revisit time

As depicted in Figure 36, it is evident that the target latitude φ_T needs to be linked with the true anomalies of the two drones:

$$\theta_2 = \theta_1 + 180^\circ - 2\varphi_T \quad (20)$$

Regarding the RAAN, it is necessary to enforce that the orbital plane is such that at a certain hour in a certain epoch one drone passes over the target. Given a certain date and the target longitude λ_T in degrees, the RAAN can be computed as:

$$\Omega = \lambda_T + 360^\circ \left(\frac{Date_{j2000} - Spring_{j2000}}{365.25 \text{ days}} \right) \quad (21)$$

To further improve the revisit time, multiple orbital planes are required, but this gives a degree of freedom in terms of the choice of time schedule to perform imaging. This is controlled by properly setting the RAAN shift between the planes depending on the desired time delay between two images:

$$\Delta\Omega = \Delta t_h 15^\circ/h \quad (22)$$

In each orbital plane, the drones are placed such that they pass above the target, depending on the required schedule. This synchronization is performed by computing the time in seconds elapsed from a reference time to the requested imaging time by a simple proportion which takes into account the rotation of the Earth:

$$ToF = \frac{\Delta t_h 2\pi}{24 \omega_E} \quad (23)$$

This elapsed time is exactly the time of flight the drone takes to be above the target starting from a reference time. In this way, this time information can be translated into an angular position. By selecting an argument of perigee equal to the target latitude (this is done for simplicity since it is a circular orbit), the starting true anomaly of the drone is computed:

$$\theta_0 = -\sqrt{\frac{\mu}{a^3}} ToF \quad (24)$$

Summing up, with multiple orbital planes the orbital parameters for the i -th drone at the starting epoch are set as follows:

$$\begin{cases} a_i = 6640.75 \text{ km} \\ e_i = 0 \\ i_i = 90^\circ \\ \Omega_i = \lambda_T + \Delta\Omega_i + 360^\circ \left(\frac{\text{Date}_{j2000} - \text{Spring}_{j2000}}{365.25 \text{ days}} \right) \\ \omega_i \in [0, 360^\circ] \\ \theta_{0,i} = -\sqrt{\frac{\mu}{a^3}} T_{\text{of}} F_i \end{cases} \quad (25)$$

If the customer is willing to have imaging modes shifted by 12 h, two drones will exploit the same orbital plane as described in Equation (20).

In this way, the customer can choose the target to monitor, the starting epoch and the number of imaging modes per day.

Lastly, it is important to highlight the fact that some requested times of imaging can lead to collisions of two drones at the poles. To avoid this situation, some renegotiations about the schedule are needed, as the following conditions have to be respected for the i -th and the j -th drones:

$$(UTC_{T-NP})_i - (UTC_{T-NP})_j \neq k T_{\text{orb}} \wedge (UTC_{T-SP})_i - (UTC_{T-SP})_j \neq k T_{\text{orb}}, \quad k \in \mathbb{N} \quad (26)$$

where UTC_{T-NP} is the UTC time at which one drone passes above the North Pole arriving from the target, and UTC_{T-SP} is analogous for the South Pole. Providing a practical example, if the customer asks for a drone to take images at 9:00 UTC and another one to take images at 12:00 UTC, if their passage above the target is in the same direction (i.e. both North-ward or South-ward), the two drones involved are going to collide, as the time to reach the pole after the imaging is the same and the two requested times differ by 3 h, which is close to the double of the orbital period $T_{\text{orb}} = 1.496$ h.

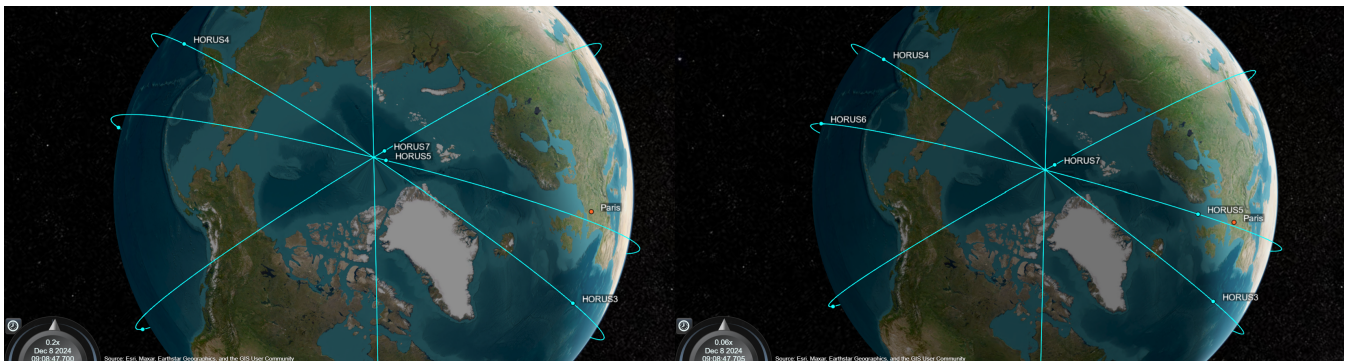


Figure 37: Collision (left) vs Collision Avoided by Renegotiation (right)

Adopting a proper margin, it is necessary to delay one of the two requested imaging times by few minutes, so, in the example depicted in Figure 37, it is sufficient to delay one imaging mode from 9:00 to few minutes later to give a margin and avoid the risk of collision between HORUS5 and HORUS7.

8.1.6 Open points and Further developments

The mission analysis performed has shown the feasibility of a scalable and highly adaptable architecture, but there are some open points to be further investigated in the next design phases.

The presented acquisition strategy is well suited to be customized depending on coverage, resolution and revisit time needs, but it does not take into account possible strategies to optimize the global image reconstruction: it is possible to study formation flight configurations made of drones assuming different roll angles (i.e. out-of-track pointing) to minimize the latency between the first acquired image and the last one belonging to the big global image.

The model presented in Section 8.1.5 is extendable to the formation flight concept. It is sufficient to change the collision avoidance time margin depending on the time elapsed between the passage above the target of the first drone and the passage of the last drone of the formation, which is directly connected to their difference in terms of true anomaly. As presented in Section 8.1.4, the target latitude plays a key

role because the fraction of orbit occupied by one formation increases more and more moving towards the poles. The consequence is that, for large formation flights, the customer will be more limited in the choice of the imaging schedule and further analyses have to be carried out. In fact, for high-latitude targets the arcs of circumference occupied by two formation flights in their respective orbits are more likely to intersect.

Collision avoidance manoeuvres would require a large amount of propellant and their frequency would be 32 times a day considering that manoeuvres are needed both for North Pole and South Pole passages, as the orbit selected is characterized by $k = 16$ revolutions per day (Section 8.1.2).

Other viable strategies are to accept the intersection of the two formation flights with a more accurate and active control near the poles, or imposing a small eccentricity, keeping the orbit quasi-circular, and monitoring the argument of pericenter drift such that, when the intersection takes place, one formation travels about the pericenter of its orbit and the other one at the apocenter (e.g. one eccentricity vector pointing northward and the other one southward).

Eventually, as a final remark, it is possible to address a limit case regarding the coverage area. If the size of the target is greater than what a 20-drones-formation can cover, multiple formation flights in the same orbit are needed and, again, the target latitude plays a key role in assessing the maximum number of formation flights which can be inserted in one orbit.

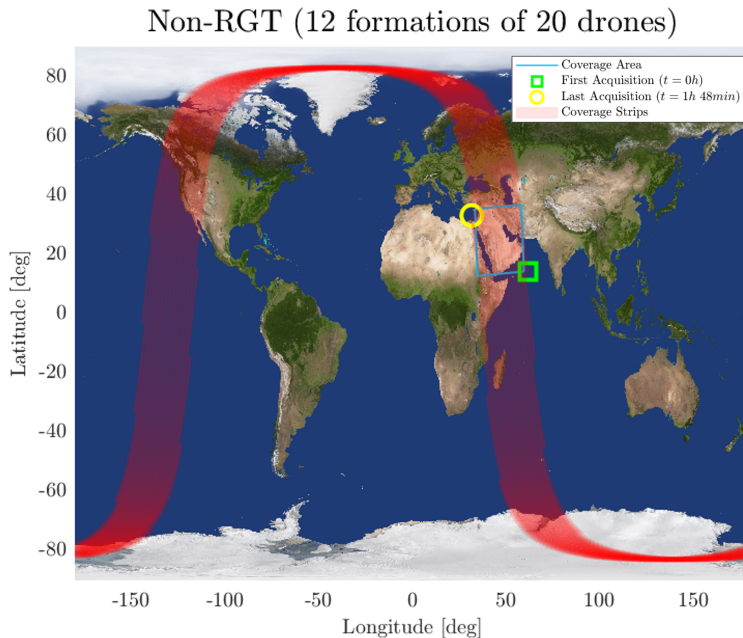


Figure 38: Middle-East Coverage, Altitude of 200 km and Sun-synchronous Orbit

In Figure 38 it can be appreciated how, with twelve formation flights of 20 drones it is possible in principle to entirely cover an area as great as the Middle-East in less than 2 h. It can be noticed that the ground track is not repeating and is not related to a polar orbit. This because, as the target area increases, the concept of repeating ground track can be relaxed for each drone, and has to be thought at a system-of-drones level. In fact, within one day, the twelve formation flights cover the entire globe and even if one drone does not pass above the same place due to a different altitude and the J2 effect due to a non-polar orbit, there will always be another drone available for that place.

Eventually, this is just a remark from the mission analysis point of view, but changing the orbital parameters would change the majority of the requirements for many subsystems and, in the example, twelve formation flights with the usual nominal parameters achieve the same goal. Moreover, it would be nearly impossible with the present technologies to meet other high-level goals as, for example, the downlink within one hour while managing such a huge number of satellites.

So, even if "more optimal" parameters might exist, the polar orbit baseline is frozen, and this is an absolute advantage from the perspective of a mass production of drones as they can be available in stock without discussing design changes due to different coverage areas.

8.2 Orbit Insertion

The initial orbital insertion maneuver must be refined and designed to be performed by an electric thruster, chosen for this mission in Section 10. The initial assumptions are that the launcher inserts the spacecraft in an initial orbit with an inclination of 90° , a RAAN deriving from the target and epoch selected and an altitude of 500 km, which is a standard LEO altitude [46]. After performing all Commissioning Phase functionalities, the spacecraft performs an orbital maneuver to reach the requested orbit at an altitude of 262.75 km.

The maneuver is performed through continuous thrusting assuming to use maximum thrust during the sunlight period of the orbit and by completely switching off the propulsive system when in eclipse, which is considered being 35% of the orbit. The solar disturbances are considered at a minimum, as the air drag and other disturbances favor this maneuver. The computed ΔV cost of this maneuver is approximately $\sim 130.57 \text{ m/s}$.

Initially the satellite shall rotate by 180° before firing, using the ADCS actuators, as the thruster shall be firing in the opposite direction of the satellite velocity to slow down the spacecraft. The thruster starts firing once the spacecraft has finished performing its slew. The maneuver was designed following a MIT paper on low thrust maneuvers [50]. This report suggests an acceleration method in which the thrust is treated as a perturbing acceleration on the spacecraft. The acceleration acting on the spacecraft can be computed as:

$$a_{prp} = T/m_{tot} \quad (27)$$

The maneuver is performed until the spacecraft altitude is lowered to the required altitude, from which the firing time of the thruster can be obtained. Then, knowing the mass-flow rate of the thruster, the propellant mass used for the maneuver can be computed. For the thruster used in this mission, the maximum thrust available is 11 mN and the mass-flow rate is 1 mg/s, composed of 0.9 mg/s for the anode thruster and 0.1 mg/s for the hollow cathode [51].

The maneuver is simulated for two possible scenarios. The first with an average value of Ballistic Coefficient, between the maximum and the minimum presented in Section 9.1. The second representing a worst case scenario, considering the maximum Ballistic Coefficient (BC_{max}). The results are presented in Table 23.

Scenario	BC	S/C's Mass	Time	Fuel Mass	Firing Time
Nominal case	285.7 kg/m ²	80 kg	15.6 days	0.878 kg	243.9 h
Worst case	398.0 kg/m ²	96.7 kg	19.2 days	1.076 kg	298.8 h

Table 23: Performance results for the initial orbital manoeuvre

These results respect the two month time-to-flight constraint, even in the worse case scenarios. The designed maneuver has the shape of a spiral and can be seen in Figure 39 referring to the average scenario.

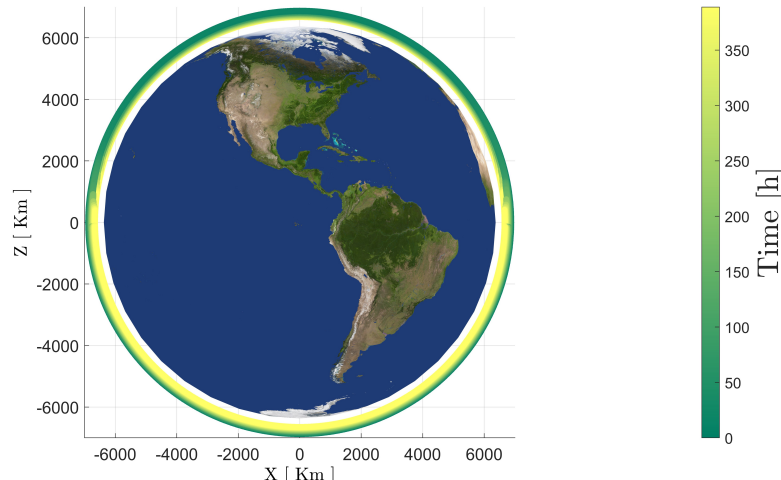


Figure 39: Decay time single drone

8.3 Disposal Strategy

Although this orbital regime is not highly congested, deorbiting remains a fundamental aspect of mission design. Satellites are required to re-enter the atmosphere or be relocated to graveyard orbits within 5 years of mission completion [52], making orbital decay a critical factor to consider.

The rate of orbital decay is influenced by several factors, including initial orbit features and the Ballistic Coefficient (BC). Satellites with a lower BC typically decay more rapidly [53] due to higher air drag effects. Studies indicate that small satellites at altitudes below 400 km can decay naturally in under 5 years.

The high atmospheric drag at these altitudes provides an opportunity to implement simple and cost-saving disposal solution leveraging natural atmospheric drag in VLEO. The decay time study is conducted for two different condition: the first considering an average value for both the solar flux and the BC and the second for the worst case scenario, which consists in a minimum of the solar activity and with the maximum BC, as for the orbit insertion. The decay time computations of a drone are presented in Figure 40 and validated using the ESA software DRAMA.

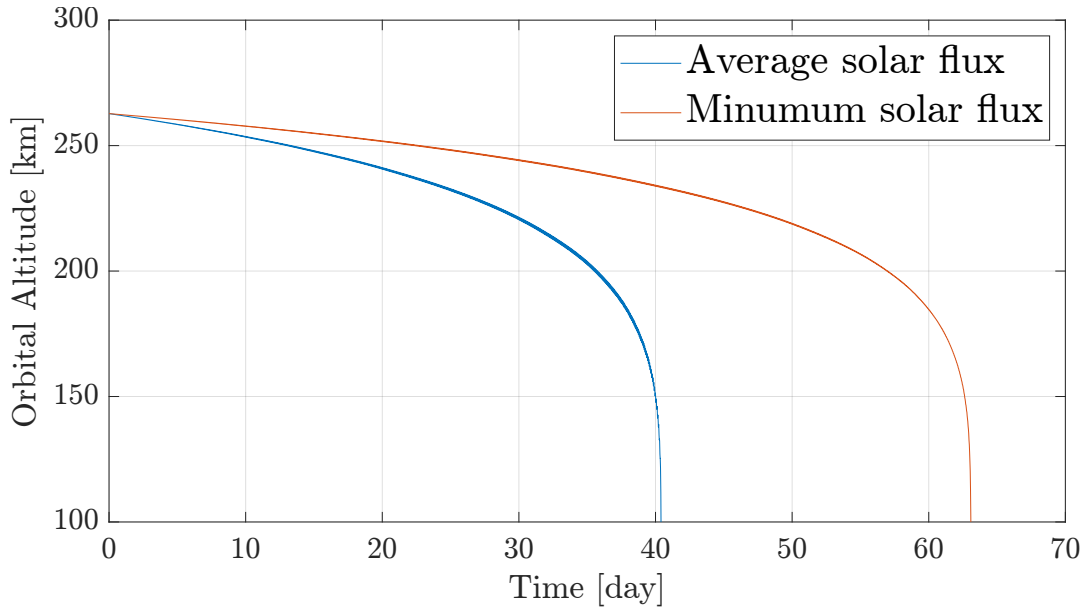


Figure 40: Decay time single drone

9 Guidance, Navigation and Control

In this section, the guidance and control strategy adopted for the HORUS drones is analyzed. The proposed strategy must ensure the correct positioning of the various satellites to guarantee optimal imaging performance, as well as the trajectories and orbits presented in Section 8.

9.1 Ballistic Coefficient

The mission analysis performed so far has considered the orbital perturbation due to atmospheric drag in each mission phase. The effect experienced by the drone is a non-conservative acceleration that progressively decreases the semi-major axis. The magnitude of this effect depends on the spacecraft mass, aerodynamic properties, and cross-sectional area. These three parameters can be grouped using the Ballistic Coefficient, defined as:

$$BC = \frac{m}{A_{cross}C_D} \quad (28)$$

where m is the spacecraft mass, C_D is the drag coefficient, and A_{cross} is the cross-sectional area perpendicular to the air-satellite relative velocity. The BC represents the ratio between inertial and aerodynamic forces acting on the spacecraft. A higher BC indicates that the spacecraft has greater inertia relative to the aerodynamic forces, making it less sensitive to atmospheric drag. Conversely, a lower BC means that aerodynamic forces have a stronger influence.

During the design process, the spacecraft mass and cross-section can vary significantly. Consequently, the BC must be determined iteratively. Starting from a preliminary mass and volume budget, the configuration is analyzed. The cross-sectional area is then estimated based on main body, solar panels and radiators sizing. However, this also depends on the power demand, which is in turn influenced by the mission analysis for orbit insertion and station-keeping. Since these parameters are interdependent, the design loop must be carefully managed, incorporating appropriate margins to prevent issues in later design phases.

For this study, two different values of the Ballistic Coefficient are evaluated. From Section 5, the margined initial mass, $m_{\text{margined}} = 96.676 \text{ kg}$, represents the full margined mass. The second case considers the unmargined mass, $m_0 = 75.787 \text{ kg}$, which corresponds to the lowest design estimate. The spacecraft cross-sectional area, including deployed components (as shown in Figure 91), is known to be $A_{cross} = 0.15518 \text{ m}^2$. Assuming a reasonable state-of-the-art value of $C_D = 1.8$, the nominal ballistic coefficients are computed as:

$$BC_{max} = \frac{m_{\text{margined}}}{A_{cross}C_D} = 346.1070 \frac{\text{kg}}{\text{m}^2}, \quad BC_{min} = \frac{m_0}{A_{cross}C_D} = 271.3229 \frac{\text{kg}}{\text{m}^2} \quad (29)$$

The Δv budgets for orbit insertion and station-keeping (Section 8.2 and Section 9.2) are significantly affected by potential variations in the ballistic coefficient during successive design phases. Therefore, the computed values are margined accordingly.

A perturbation of $\pm 15\%$ is applied to account for aerodynamic changes due to variations in C_D and cross-sectional area in non-nominal attitudes:

$$BC_{max} = BC_{max} \cdot 1.15 = 398.0230 \frac{\text{kg}}{\text{m}^2} \quad (30)$$

$$BC_{min} = BC_{min} \cdot 0.85 = 230.6245 \frac{\text{kg}}{\text{m}^2} \quad (31)$$

For orbit insertion and the disposal, the maximum BC value is selected as worst case. This choice is conservative, as the BC increases the difficulty of descending to the target orbit. Station-keeping is analysed using the minimum BC value to consider the worst-case scenario at the end of the satellite operational life.

9.2 Station Keeping

9.2.1 Drag Compensation

The mission constraints and the previous design iterations lead to operate in a low altitude orbit $h < 300 \text{ km}$, in a region characterized by a non-negligible air density. This could cause a significant disturb on

the spacecraft, affecting both its semi-major axis and eccentricity. Without any drag compensation, the aerodynamics forces will lead the spacecraft to decay in less than three months. Hence it is mandatory to consider continuous station keeping manoeuvres to counteract the drag. The aerodynamic acceleration is computed from:

$$\mathbf{a}_{\text{Drag}} = -\frac{1}{2} \frac{A_{\text{cross}} C_D}{m} \rho(h, t) v_{\text{rel}}^2 \frac{\mathbf{v}_{\text{rel}}}{\|\mathbf{v}_{\text{rel}}\|} \quad (32)$$

- $\rho(h, t)$ = atmospheric density
- \mathbf{v}_{rel} = air-relative speed (atmosphere rotates); $\mathbf{v}_{\text{rel}} = \frac{d\mathbf{r}}{dt} - \boldsymbol{\omega}_E \times \mathbf{r}$
- A_{cross} = reference area (i.e., cross-sectional area perpendicular to \mathbf{v}_{rel})
- m = spacecraft mass
- C_D = drag coefficient

Air density represents the most critical parameter to be taken into account since it varies not only with altitude but also with latitude and solar cycle. Hence to obtain an accurate analysis both the *Jacchia-Bowmann*[54] and the *nmlrsise-00* [6] atmospheric models are used. The ballistic coefficient is introduced to correlate A_{cross} , C_D and the mass, as presented in the previous section. In the first phases of the design, it was crucial to understand the order of magnitude and the fluctuations of the air drag. The dynamics of the spacecraft is propagated at the nominal altitude for one day (16 orbits), hence it is possible to evaluate the disturbing acceleration due to drag and to compute the Δv integrating over time. The simulation is performed for three different levels of solar flux associated to their relative levels of air density: a solar maximum ρ_{max} , a solar minimum ρ_{min} and for an average value ρ_{avg} . Solar maximum and minimum are selected respectively on March, 2000 and February, 1997 [55].

The average daily cost of a maneuver has been preliminarily estimated for the three different solar flux scenarios and for the minimum and maximum ballistic coefficients presented in Section 9.1. The results are reported in Table 24. This analysis highlights the influence of variations in solar flux and ballistic coefficient on the atmospheric drag-induced perturbation acting on the satellite.

Condition	Average Air Density [kg/m ³]	Δv_{sk} per day, BC_{max} [m/s]	Δv_{sk} per day, BC_{min} [m/s]
Average	3.28×10^{-11}	0.2812	0.3782
Solar Minimum	2.58×10^{-11}	0.2209	0.2971
Solar Maximum	8.89×10^{-11}	0.6885	0.9259

Table 24: Air Density and Δv_{sk} for different solar fluxes and BCs

As expected, the needed Δv for station keeping presents high values during the solar maximum, driving the design in terms of ballistic coefficient optimization.

9.2.2 Virtual Slot

In this section the concept of virtual slot for station keeping will be discussed. The idea is to propagate the ideal center of mass motion and, by giving finite dimensions to a box surrounding it, compare at each time step this ideal position with the actual position of the drone, subject to perturbations.

First of all, considering that J2 and drag perturbations have no out-of-plane contributions in a polar and circular orbit, defining an across-track dimension for the virtual slot is not strictly mandatory. However, introducing this dimension could be useful for monitoring potential anomalies (non-nominal conditions) and small orbital plane variations caused by other perturbations. The other two dimensions of the box, depicted in Figure 41, are computed considering that for the imaging mode an error of 0.1° is accepted.

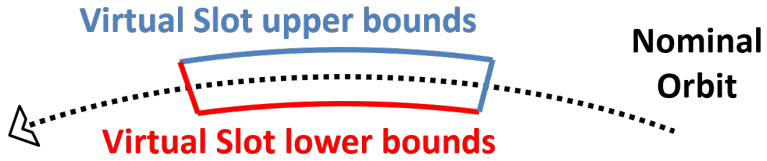


Figure 41: Virtual Slot representation

Regarding the along-track dimension, this error is firstly translated into a an error on ground both in km and in degrees using the same concepts seen in Equation (16) and Equation (17). This $\Delta\lambda_{err}$ on ground is useful to determine the time delay/advance and the consequent true anomaly shift:

$$\begin{cases} \Delta t_{err} = \frac{\Delta\lambda_{err}}{\omega_E} \\ \Delta\theta_{err} = \frac{2\pi}{T_{orb}} \frac{\Delta\lambda_{err}}{\omega_E} \end{cases} \quad (33)$$

So the ideal box is characterized by a finite along-track dimension:

$$Slot_{along-track} = 2 a \Delta\theta_{err} \quad (34)$$

Regarding the nadir-zenith dimension, taking the same $\Delta\lambda_{err}$, this is transformed into a semi-major axis error. Starting from the definition of the orbital period and knowing that the nominal difference between two adjacent ground tracks is $\Delta\lambda = T_{orb} \omega_E$, the resulting semi-major axis is:

$$a_{new} = \left(\mu_E \left(\frac{\Delta\lambda - \Delta\lambda_{err}}{2\pi \omega_E} \right)^2 \right)^{\frac{1}{3}} \quad (35)$$

In this way, the nadir-zenith dimension is:

$$Slot_{nadir-zenith} = 2 (a - a_{new}) \quad (36)$$

As in the previous sections, this is again strongly dependent on the target latitude. The most stringent case occurs when the target is on the equator. In this case the virtual slot assumes the smallest dimensions possible, leading to $Slot_{along-track} = 15.96 \text{ km}$ and $Slot_{nadir-zenith} = 1.69 \text{ km}$.

9.2.3 Directional Adaptive Guidance

As presented in Section 9.2.1, air drag will decrease the drone orbital altitude and consequently bring it away from its nominal orbit. This represents critical issues for the mission, as the repeating ground track on the target will no longer be guaranteed. Starting from the "Virtual Slot" concept presented in Section 9.2.2, a Directional Adaptive Guidance (DAG) strategy [56],[57] has been selected to perform the orbital maneuvers.

The following paragraph provides a detailed explanation of the DAG strategy, describing how it has been implemented and adopted in this context, as well as its operational principles:

- The Virtual Slot is propagated in time without considering external disturbances, while the drone is propagated accounting for the deceleration due to air drag.
- Whenever the drone exits the Virtual Slot, the thruster is activated, and the station-keeping maneuver begins.
- From the instantaneous state vector, thrusting angles α and β are computed in the RCN (Radial, Conormal, Normal) reference frame. These angles determine the maximum rate of change for each orbital element, depending on the drone's true anomaly.
- For each set of thrusting angles, the corresponding thrust directions are computed:

$$\vec{f}_{oe} = \begin{bmatrix} f_R \\ f_S \\ f_W \end{bmatrix} = \begin{bmatrix} \cos(\beta) \sin(\alpha) \\ \cos(\beta) \cos(\alpha) \\ \sin(\beta) \end{bmatrix} \quad (37)$$

Orbital Element	α	β
Semi-Major Axis (a)	$\arctan\left(\frac{e \sin(\theta)}{1+e \cos(\theta)}\right)$	0
Eccentricity (e)	$\arctan\left(\frac{\sin(\theta)}{\cos(\theta)+\cos(E)}\right)$	0
Inclination (i)	0	$\text{sgn}(\cos(\omega + \theta)) \cdot \frac{\pi}{2}$
Ascending Node (Ω)	0	$\text{sgn}(\sin(\omega + \theta)) \cdot \frac{\pi}{2}$
Argument of Periapsis (ω)	$\arctan\left(\frac{1+e \cos(\theta)}{2+e \cos(\theta)} \cot \theta\right)$	$\arctan\left(\frac{e \cot(i) \sin(\omega+\theta)}{\sin(\alpha-\theta)(1+e \cos(\theta)) - \cos(\alpha) \sin(\theta)}\right)$

Table 25: Optimal thrusting angles α and β .

- An adaptive ratio is computed to quantify the percentage of change in each orbital element:

$$R_{oe} = \frac{oet - oe}{oet - oe_0} \quad (38)$$

where oe is the instantaneous orbital element, oet the targeted one, and oe_0 the one at the beginning of the maneuver.

- A weight W_{oe} is assigned to each oe [56] to prioritize changes in the semi-major axis and eccentricity, as these are the most affected by air drag.
- The total thrusting direction is then computed:

$$\vec{f}_T = \sum_{oe} R_{oe} W_{oe} \vec{f}_{oe} \quad (39)$$

- The thrust, always considered on or off, is oriented toward the resulting direction vector.
- When the drone returns to the upper bounds of the Virtual Slot, the thrust is turned off.

Due to the polar orbits selected for the HORUS drones, the out-of-plane disturbances are minimal. As such, it is not necessary to continuously monitor and correct the inclination and the RAAN, which are excluded from the DAG control (weights set to zero). These parameters are still monitored to ensure correctness, and in case of anomalies, the drone can adapt its control logic, perform a 90° slew maneuver to change the thruster orientation, and execute out-of-plane corrections. The pericenter anomaly ω is also excluded from the DAG strategy due to the circular nature of the target orbit.

As shown in Section 9.2.2, the constraint on the true anomaly, computed in Equation (33), is very stringent. To accommodate this constraint and optimize power consumption, the proposed strategy adjusts the target semi-major axis used to compute the adaptive ratio, at each time step. The updated computation considers not only the target altitude but also the difference in the argument of latitude u between the target and the drone. As shown in [58] [59], the target semi-major axis is computed as:

$$a_{\text{target,new}} = \left(K_u \delta u + \sqrt{\frac{1}{a_{\text{target}}}} \right)^{-\frac{2}{3}} \quad (40)$$

where: δu is the **argument of latitude difference** between the target orbit and the drone, K_u is a **gain** to weight the phasing impact on the semimajor axis. Notice that when u vanishes, the modified reference semi-major axis matches the nominal reference value, ensuring proper synchronization.

The selected final strategy involves narrowing the nadir/zenith Virtual Slot bounds to minimize deviations from the target and applying adaptive control to the semi-major axis and the eccentricity.

The algorithm flow for the revised strategy is as follows:

- Narrow the Virtual Slot bounds in the nadir/zenith direction to ensure thrust activation on each satellite orbit. This is required since air density varies with different solar fluxes and RAANs, which impacts the drone's decay rate.

- Fine-tune the thrust level based on solar flux variations, RAAN, and updated Virtual Slot bounds. This regulation ensures a consistent maneuver frequency while accommodating imaging requirements.
- Perform orbital corrections during each orbit over short durations, with thrust direction computed via DAG.

The objective is to determine the thrusting windows and the required propellant mass, which will be used to check the power consumption and estimate the propulsion limits. A worst-case scenario is assumed, considering the minimum BC and maximum solar flux. The propagation is performed for a 4 months period to assess its long-term validity.

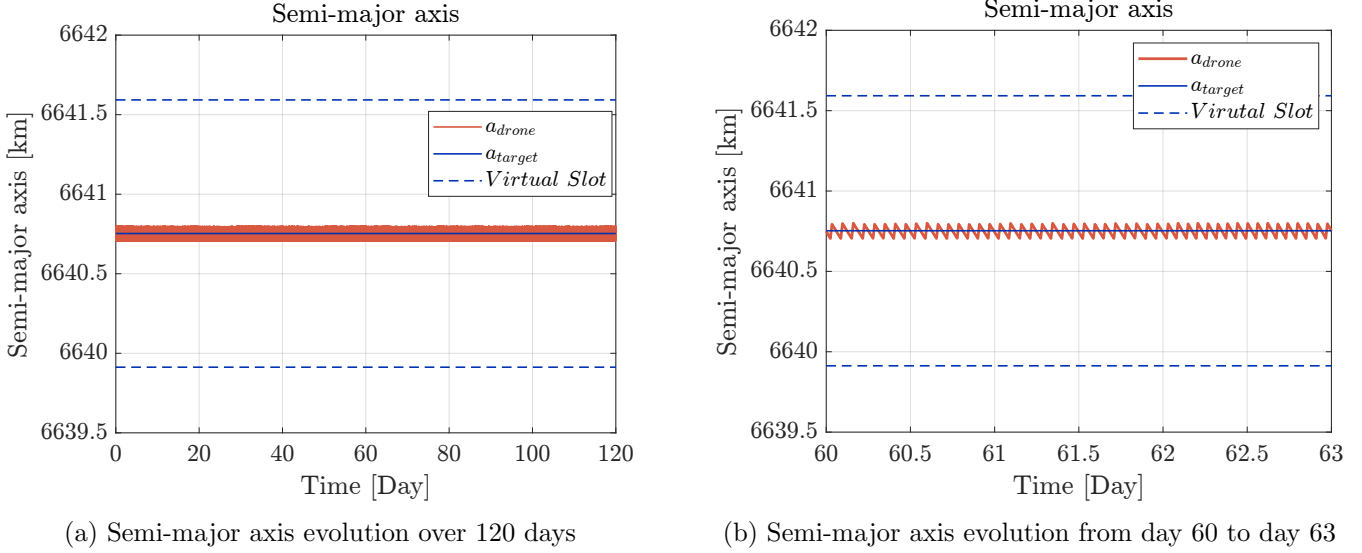


Figure 42: Semi-major axis

The propagation results demonstrate that both the semi-major axis and the phasing error consistently remain well within the prescribed bounds, highlighting the effectiveness of the adapted control law.

As shown in Figure 42a, the semi-major axis remains closely aligned with the nominal value, ensuring optimal imaging resolution during operational phases. Simultaneously, the high precision in the phasing, illustrated in Figure 43, guarantees excellent coverage of the specified target with the desired accuracy.

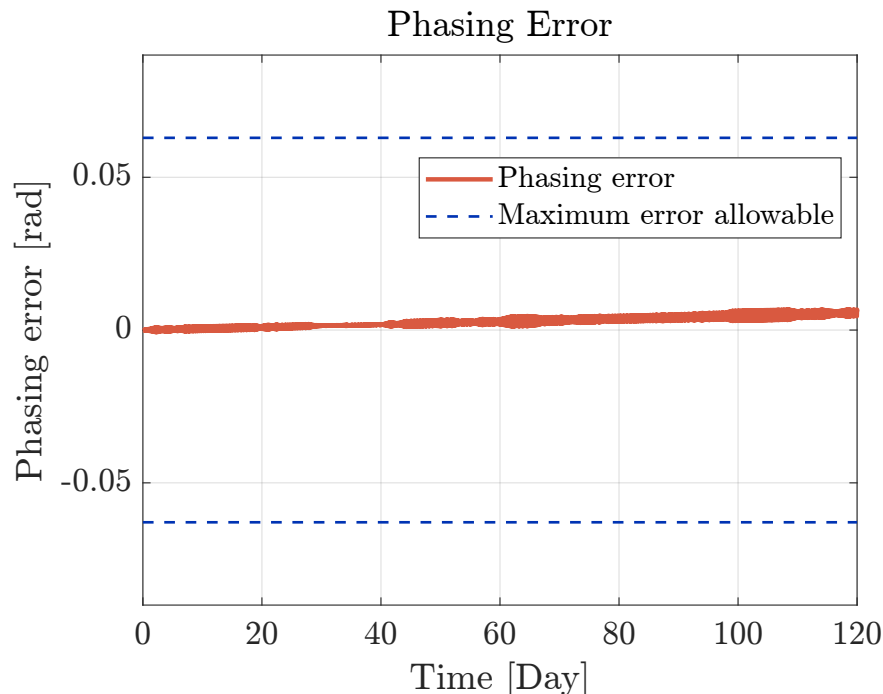


Figure 43: Phasing error over 120 days.

From Figure 44, it is evident that the eccentricity does not exhibit a prescribed evolution as observed for the semi-major axis. This behavior is attributed to the low weight assigned to it in the DAG strategy. Despite this, the eccentricity remains within a controlled range and does not diverge. Specifically, when it approaches values near 10^{-3} , it is effectively controlled and rapidly decreases. This mechanism ensures that the orbit remains sufficiently close to the target, thereby facilitating the satisfaction of constraints on the semi-major axis and phasing.

In contrast, the inclination, as illustrated in Figure 45, exhibits a slight decrease over the propagation period. This confirms that out-of-plane maneuvers are not required during the control phase, while showing the possible needs of small orbital plane correction for extended lifetime missions.

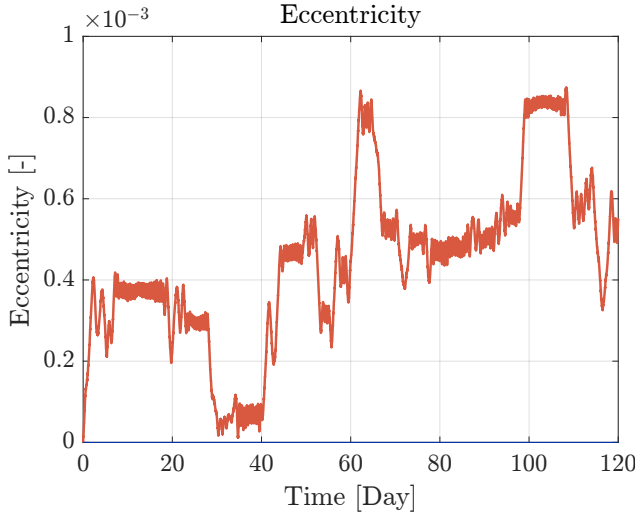


Figure 44: Eccentricity evolution over 120 days

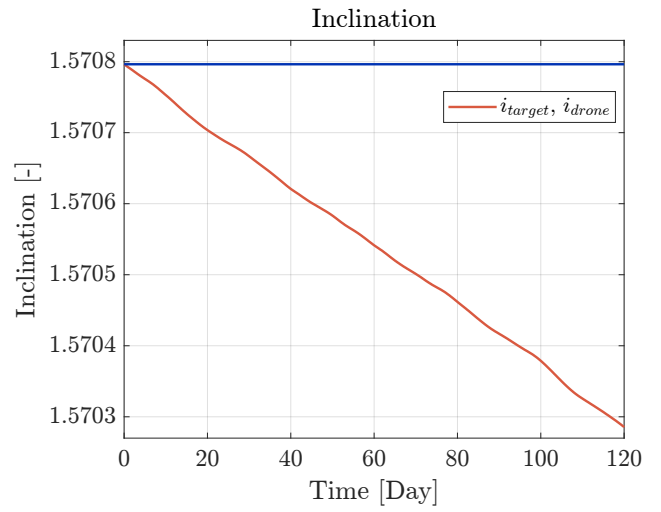


Figure 45: Inclination evolution over 120 days

Thrusting Direction: The thrust direction is always aligned with the velocity vector in the RCN reference frame. This alignment eliminates the need for slew maneuvers, simplifying the station-keeping operations and minimizing fuel consumption. By avoiding unnecessary reorientations of the spacecraft, this strategy ensures high efficiency and prolongs the operational lifetime of the mission.

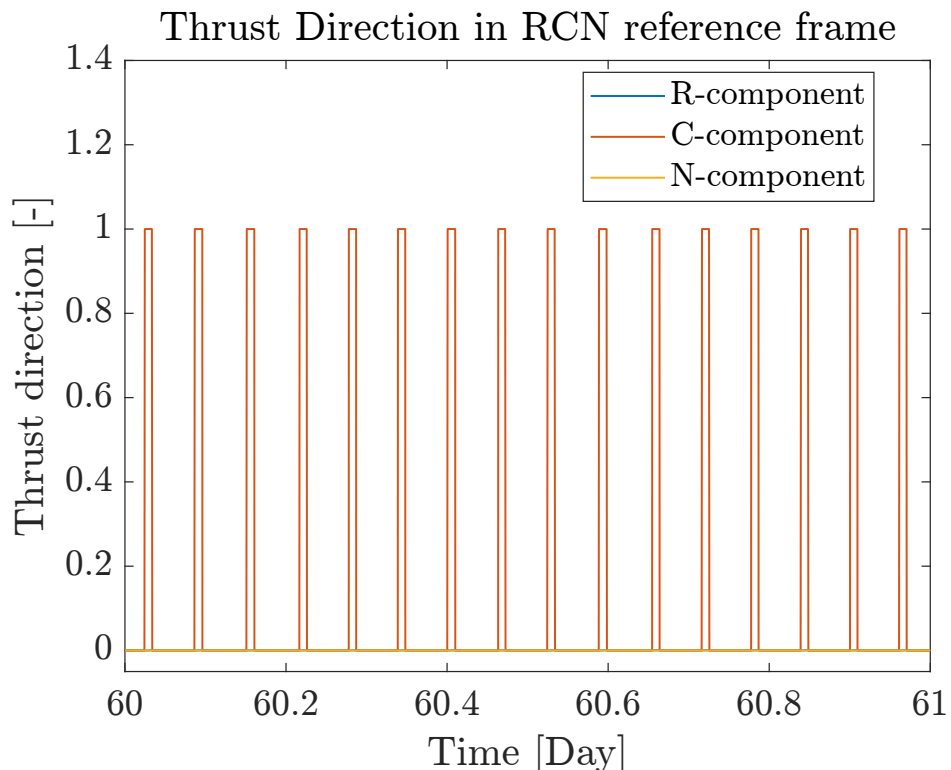


Figure 46: Thrust direction in the RCN reference frame over one day.

Lifetime and Station Keeping Results: To evaluate the mission lifetime, several potential limiting factors were considered, including the complete depletion of the propellant (6.5 kg), the margined maximum number of maneuvers that the Hall Effect Thruster (HET) can perform (9500 man.), and the margined maximum cumulative operational hours of the HET (2300 h), refer to Section 10 for more details. Among these, the primary limiting factor is the number of maneuvers the HET can execute within the available propellant budget, as presented in Table 26. A fraction of the propellant mass is intentionally reserved for non-nominal scenarios, such as out-of-plane corrections or target orbit changes. This reserve ensures the flexibility and robustness of the mission, allowing the spacecraft to adapt to unforeseen operational needs. The results of the station-keeping strategy, including the lifetime, are summarized in Table 27.

Total Thrusting Time [h]	Total Manoeuvres	Propellant Used [kg]
2186.11	9500	3.4

Table 26: Lifetime limiting parameters.

BC [kg/m ²]	Manoeuvres per Day	Thrusting Time [min]	Lifetime [days]
230.62	16	13.81	593.6

Table 27: Summary of station-keeping results.

10 Propulsion Subsystem

10.1 Introduction

The correct design of the propulsion system is important to ensure correct control of the spacecraft for the maneuvers required by its mission. An analysis of the required Δv during the mission lifetime has to be performed. By comparing this results with similar low-altitude, Earth observation missions and their architectures, it is possible to obtain a range of propulsive options.

The system has two main propulsive needs during its mission lifetime.

- The orbital insertion maneuver
- Station Keeping (SK) maneuver

Of which the values of the Δv are reported in the table below:

Maneuver	ΔV Required
Orbit Insertion	137.1 m/s
Station Keeping	0.81 m/s per day

Table 28: Required ΔV from the satellite maneuvers

Due to the low Δv required by the mission and the low mass constraint imposed by the configuration, a single primary propulsion system is sufficient to accomplish the mission.

10.2 Propulsive Options

For low-altitude missions a few different propulsive options are available. Current studies [60] in the small satellite propulsion field have highlighted five possible main propulsion options:

- **Cold Gas Thrusters (CGT)**

Cold Gas Thrusters are the simplest thrusters of all, composed of a valve and a nozzle. Thrust is produced by releasing cold gas, usually nitrogen or helium, from a pressurized tank. These thrusters are lightweight, require a small amount of power and have a extensive flight history. A major drawback of this technology is the very low specific impulse, which restricts its use to missions with low total impulse requirements.

- **Resistojet Thrusters (RT)**

The working principle of Resistojet Thrusters is similar to that of a CGT. In addition, the propellant is heated by an electrical resistance to improve the fuel efficiency, at the price of an increased power consumption. Its lifetime is strongly influenced by the number of thermal cycles which can be sustained by the resistance element. Both gaseous, such as nitrogen and xenon, and two-phase, such as butane, propellants are used.

- **Liquid Monopropellant Thrusters (LMT)**

Liquid Monopropellant Thrusters are chemical engines that exploit the decomposition of liquid propellants to produce thrust. Liquid Monopropellant Thrusters are generally simpler and more reliable than bipropellant thrusters. Their power consumption is relatively low and their specific impulse lies between 220 s and 240 s, depending on the propellant type.

- **Electric Thrusters (ET)**

Electric Thrusters, in order to produce thrust, accelerate a ionized propellant to high velocity by using electrical energy. ET have specific impulse ranging from 600 s to 4500 s, hence, their propellant consumption is by far lower than the other propulsive options. HET and RFIT are preferred for applications involving 100-kg-class satellites, thanks to their relatively high thrust and total impulse capacity, while PPT and FEEP thrusters can be considered for smaller satellites, due to their lower

thrust, power consumption and impulse capability. Disadvantages of these technologies include the high power consumption and the need of a complex Power Processing Unit (PPU).

- **Air-Breathing Electric Thrusters (ABET)**

The basic concept of Air-Breathing Electric Propulsion is to collect air from the atmosphere through an inlet, which is positioned on the face of the satellite with a normal vector in the same direction of the spacecraft velocity. Using electric power, atmospheric air is then ionized and accelerated through a nozzle, thus generating thrust [61]. Due to its low TRL major drawbacks are present when using this technology. Mainly the operating altitude has a narrow fixed altitude range for optimal use, as if the air density is too low no thrust is generated while if the density is too high the power consumption of the system may exceed the spacecraft power availability. Furthermore this technology, as of today, is meant for larger satellites, having very high power consumption (from hundreds of W to several kW) and high system masses. Lastly, another major drawback of this technology is the air intake shape and cross section. To guarantee a sufficient amount of air flowing in the system, the inlet must have a minimum cross section area and collection coefficient. This could create a conflict with the spacecraft configuration and volume constraints [61].

10.3 Design Process

In this section, the design and the preliminary sizing of the propulsion subsystem as well as the rationale behind this process are explained in detail

10.3.1 Propellant Mass Required

The first step of the design process is to compute the propellant mass required to perform the maneuvers which have to be performed independently from the mission objective and target. In particular this Δv depends on:

- **Initial Orbital Injection**

The initial orbital injection is the maneuver performed upon release from the launcher to accurately insert the spacecraft in the target orbit. It mainly depends on the launcher accuracy and reachable orbits seen in Section 7.1.1. The worst case scenario considers an orbital maneuver from a circular polar orbit with an altitude of 500 km, a typical altitude for a LEO launch, to the mission desired orbit at an altitude of 270 km. This maneuver is margined following ESA guidelines [40], and produces a Δv of $\sim 137.1 \text{ m/s}$.

- **Station Keeping Maneuvers** Due to the strong influence of the air drag at VLEO altitudes, an effective station-keeping approach is needed to compensate these effects. A station-keeping period of 360 days was assumed, with a daily Δv cost of $\sim 0.93 \text{ m/s/day}$, which results into a total Δv of $\sim 334.8 \text{ m/s}$ after applying adequate margins [40].

The total Δv needed for these maneuvers adds up to a total of $\sim 465.4 \text{ m/s}$, already margined. To compute the propellant mass, the Tsiolkovsky Equation (41) is used, considering the total dry mass of the spacecraft at launch.

$$\Delta v = v_e \cdot \ln \left(\frac{m_0}{m_f} \right) = I_{sp} \cdot g_0 \cdot \ln \left(\frac{m_0}{m_f} \right) \quad (41)$$

The propellant mass required depends mainly on the Specific Impulse (I_{sp}) of the thruster. A range of specific impulses were considered for each propulsive option and reported in Table 29. These values are based on actual data of propulsive systems used by small satellites for LEO missions [60]. The total dry mass of the spacecraft used to compute the propellant masses is 96.7 kg, the same one estimated in Section 5 margined following ECSS standards [40].

Propulsion Type	I_{sp} Ranges	Thrust Ranges	Required m_p Ranges
CGT	65 s	5 – 50 mN	136 kg
RT	50 – 125 s	1 – 200 mN	58 – 201 kg
LMT	220 – 255 s	0.5 – 50 mN	26 – 30 kg
ET	650 – 4500 s	0.1 – 15 mN	2 – 10 kg

Table 29: Ranges of I_{sp} , thrust, and required propellant masses for each propulsive option [60].

The propellant masses shown in Table 29 have already been margined following ESA guidelines [40]. From Table 29 it is clear that Electric Thrusters not only have the lowest required propellant mass but also have the only acceptable propellant mass range, as all other propulsive options have propellant mass constraints which are too high.

10.3.2 Thruster Firing Time

Electric propulsion seems the optimal propulsive option mass-wise, but its performances depend significantly on the type of electric propulsion utilized in the system. To rank the various types of electric thrusters, the firing time of each thruster was analysed and compared to the estimated time needed to complete the initial insertion maneuver. The main electric propulsion types are:

- Radio Frequency Ion Thruster (RFIT)
- Hall Effect Thruster (HET)
- Field Emission Electric Thruster (FEEP)
- Pulsed Plasma Thruster (PPT)

To compare all available electric propulsion , the time needed to performed the orbital insertion maneuver is analysed. The mass and drag coefficient used for this simulation are the ones reported in Section 8.2 for the nominal case. In Table 30 the main electric propulsion options are reported with their performances and the taken to perform the maneuver.

ET Type	Specific Impulse	Thrust	Total Impulse	Firing Time
RFIT Xe	3000 s	2.5 mN	$2 \cdot 10^5 \text{ Ns}$	72.8 days
RFIT I_2	3500 s	1.6 mN	$3.5 \cdot 10^4 \text{ Ns}$	113.3 days
HET	1300 s	11 mN	$5 \cdot 10^4 \text{ Ns}$	17.1 days
FEEP	4500 s	0.5 mN	$5 \cdot 10^3 \text{ Ns}$	340.5 days
PPT	640 s	0.1 mN	200 Ns	1378 days

Table 30: Performances and firing times for each electric propulsion type [60].

Analysing Table 30 it can be noted that HET are by far the most flexible thruster and the only one able to respect the two months time-to-flight constraint imposed by the mission.

10.4 Choice of the Propulsion System

Considering the mission profile, the satellite estimated masses and the Δv constraints of the mission, the optimal solution for the propulsive subsystem is to implement a **Hall Effect Thruster** as primary propulsion system.

This technology allows low propellant masses required for the initial insertion maneuvers and the station-keeping, as well as flexibility during maneuvers to ensure a wide range of mission functionalities.

The main drawbacks of this choice are the power consumption, which could peak at 250 W depending on the required thrust, and the configuration constraints, as the nozzle exit of the system must be positioned in the face of the satellite opposite to the spacecraft trajectory, allowing the thrust vector to be parallel to the trajectory. Lastly the system must accommodate a specific PPU to ensure proper functionality of the propulsive system.

An initial mass analysis of the system can be conducted through a statistical analysis for satellites with masses in the 100 kg range. According to recent studies [60] the Equation (42) can be used to estimate the total mass of the system.

$$m_s = 10 + 0.3 \cdot m_p \quad (42)$$

This equation takes into consideration both the fixed hardware mass, such as the PPU and the nozzle, and the mass which depends on the amounts of propellant on-board, such as the tanks and feeding system. For a fixed propellant mass of 8 kg, including margins [40], the system mass can be approximated to **$m_s = 14 \text{ kg}$** , after applying the proper margins [40].

An honourable mention must be given to Air-Breathing Electric Propulsion as it could, in the near future, represent a viable and more efficient solution for propulsion of small satellites in VLEO environments. Currently this technology is not mature and scalable enough to guarantee the reliability and performances needed for this mission.

10.5 System Design

10.5.1 Initial Design and Baseline

Due to the earliest launch date in 2026 and the strict time-to-fly constraint, a modular Commercial Off The Self (COTS) propulsion system was selected for this mission, in which the tank size can be adjusted to accommodate the required propellant.

Two distinct COTS systems have been found to be suitable for the mission. The main performance parameters are reported in Table 31.

Thruster	Company	Thrust	I_{sp}	Power	Mass	TRL	Lifetime
SPS-25	SETS	11 mN	1300 s	250 W	7.1 kg	9	> 3000 h
HT100	Sitael	15 mN	1350 s	300 W	6.8 kg	6	> 2250 h

Table 31: COTS thruster main performance parameters [62][51]

The system chosen for the mission is the **SPS-25**, manufactured by the company Space Electric Thruster Systems (SETS) [51]. Although the HT100 has slightly higher performances, the SPS-25 was chosen for its flight heritage, its maturity (TRL 9), its flexibility in performances and its extensive operational lifetime (Lifetime > 3000 h). Furthermore, the system has a relatively low mass, weighing approximately 7 kg without the tank. The system is composed by four main component assemblies:

- **Thruster and Hollow Cathode** to accelerate the xenon particles and generate thrust.
- **Xenon Feeding Line** to filter and feed the propellant to the thruster.
- **Xenon Tank** to contain the propellant throughout the whole mission.
- **Power Processing Unit** to distribute the power to all components and record data

It must be noted that, although the increased lifetime of the SPS-25 system, the thruster lifetime remains the most limiting factor for the spacecraft lifetime, ensuring up to 1.5 years of operativity in VLEO environment.

10.5.2 Design of the Feeding System

The feeding system is designed to filter and bring to the hollow cathodes and the thruster the required propellant mass at a fixed pressure. The feeding line for the propulsion system is based on a pre-existing design of an SPS-25 system [51] with the addition of extra solenoid valves, temperature sensors, and pressure sensors to ensure redundancy and a more precise control. The sketch of the feeding line is shown in Figure 47.

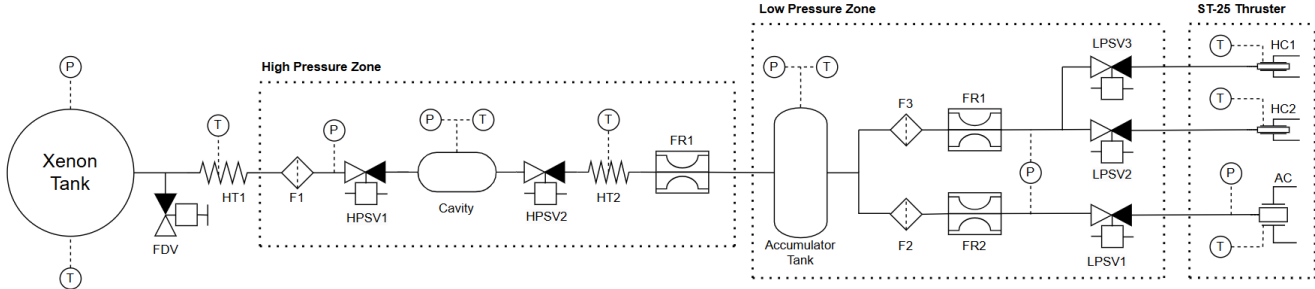


Figure 47: Feeding line of the propulsion system [51]

The main components of the xenon feeding line are:

- **Xenon Tank:** contains the propellant required for the mission.
- **Fill & Drain Valve (FDV):** used to fill drain the propellant tank before launch.
- **Heater (HT):** used to heat the propellant, increasing its pressure and keeping it inside its operational temperature bounds.
- **Filter (F):** used to remove impurities in the propellant before firing.
- **High Pressure Solenoid Valve (HPSV):** used to regulate the pressure to and from the cavity in the high-pressure zone.
- **Low Pressure Solenoid Valve (LPSV):** used to regulate the pressure to the thrusters and hollow cathodes.
- **Flow Restrictor (FR):** used to regulate the flow rate of the propellant and add safety checkpoints which limit the flow and pressure in the system in case of failure.
- **Cavity/Accumulator Tank:** are used to accumulate the gaseous propellant and dampen the pressure changes inside the feed line.
- **Hollow Cathode (HC):** used to neutralize the ionized gas expelled from the thruster.
- **Anode Thruster (AC):** used to accelerate the propellant and generate thrust.
- **Pressure Sensor (P):** used to measure pressure in critical points within the system.
- **Temperature Sensor (T):** used to measure temperature in critical points within the system.

The feed line is composed of a high-pressure zone and a low-pressure zone, which bring the propellant to the required pressure conditions before firing. The high-pressure zone is meant to decrease the operating pressure of the line from 150 bar to ~ 2 bar. This is done through the use of a cavity to dampen pressure fluctuations and high-pressure solenoid valves as well as flow restrictors to lower the operating pressure. The low-pressure zone, on the other hand, is meant to accumulate the propellant in the accumulator tank, filter it, and provide it to the anode thruster and the hollow cathodes.

10.5.3 Tank Sizing

The tanks provided by SETS are not big enough to contain the propellant required by the total mission lifetime of HORUS. As a result, an internally developed design has been proposed. To optimize the available volume, two cylindrical tanks have been considered.

First, the volume of a single propellant tank is calculated based on half of the required propellant mass, with an additional 10% margin applied, as per ECSS margins [40].

$$V_{\text{tank}} = 1.1 \cdot \frac{M_{\text{prp}}}{2 \rho_{\text{prp}}} = 0.0021 \text{ m}^3 \quad (43)$$

The precise propellant density was obtained through the National Institute of Standards and Technology (NIST) WebBook [63]. The total volume of a single cylindrical tank is given by the sum of the cylindrical central body and the two hemispherical components, with the following formula:

$$V = \pi r^2 h + \frac{4}{3} \pi r^3 \quad (44)$$

where r is the cylinder radius and h is the height of the cylindrical section. The height of the cylindrical section is assumed to be $h = 2r$ to respect configuration constraints. Imposing the height-radius relation, the tank radius can be computed as:

$$r = \sqrt[3]{\frac{3V_{\text{tank}}}{10\pi}} = 0.0587 \text{ m} \quad (45)$$

The chosen tank material is aluminium, due to its low density and proven flight maturity. The thickness can be calculated as:

$$t_{\text{tank}} = \frac{3P_{\text{tank}} \cdot r_{\text{tank}}}{\sigma_{\text{Al}}} = 4.9043 \text{ mm} \quad (46)$$

The operating tank pressure of the feeding system [51] of 15 MPa , margined by a safety factor of three, was used for the computation of the tank thickness. Eventually, the total mass can be computed as seen in the equation below:

$$R_{\text{ext}} = r + t_{\text{tank}} \quad (47)$$

$$m_{\text{tank}} = \pi \rho_{\text{Al}} \cdot \left(\frac{4}{3} (R_{\text{ext}}^3 - R_{\text{int}}^3) + h \cdot (R_{\text{ext}}^2 - R_{\text{int}}^2) \right) = 1.1811 \text{ kg} \quad (48)$$

Considering the configuration constraints, the tank architecture remains flexible and may still vary depending on the implementation of different design solutions. This adaptability allows for the exploration of alternative configurations to better address mission requirements and accommodate potential challenges.

11 Tracking, Telemetry & Telecommand Subsystem

The TTMTTC subsystem proved to be a critical part of the design of the HORUS mission. Since one of the major mission requirements is the fast and reliable download of high resolution images of any target on the planet, the design of the communication architecture and strategy was quite complex and needed thorough investigation.

11.1 Mandatory Events

During the S/C lifetime there are some mandatory events for which communication with ground is required.

- The first mandatory event is **LEOP**, this phase is very complex and requires frequent contact with ground. Indeed, as soon as the satellite is released from the launcher, it starts sending intermittent beacon signal, hence to assure the correct locking with GS, S/C release point shall be in visibility. Since this is a very complex phase, the S/C shall be capable to download its telemetry at least twice per orbit, while the uplink is required to command the transition to the commissioning phase.
- **Commissioning** phase is still critical and requires to frequently communicate with ground. In this specific time frame at least one downlink per orbit is required to communicate telemetry and to asses that the commissioning operations are properly performed, while at least two uplink contacts shall be guarantee to command transition between tests, if needed.
- During **OBP**, TTMTTC is subject to the tightest requirement, indeed the data acquired from the payload shall be downloaded within one hour from acquisition. Moreover, since tracking the satellite is a demanding task for such low altitude and since GS is in charge for sending commands to the satellite, two downlinks and one uplink per day are required.
- The last mandatory event to be manage is the **disposal** transition. Indeed the ground segment shall assure decommissioning operation correctness and command the transition to the disposal phase.

11.2 Data Budget

The data budget is an estimation of the size of the information stored and transmitted by the TTMTTC subsystem: its size has consequences on the on board mass memory and, mainly, on the required downlink datarates and communication time windows.

The data handled by the TTMTTC fall in two categories: payload data and telemetry data. The payload data are the picture frames taken by the onboard cameras and sent to ground less than one hour after acquisition. Their size can vary according to the specifics of the instrument, so in order to have a correct sizing, the parameters are retrieved from the chosen payload (described in section 6.2): a colour picture is composed by 12 Megapixels (4096 x 3072 px), with each pixel representing a combination of an RGB triplet weighting 8 bits each. The size of a single RGB picture is then:

$$S_{pic} = 12 \text{ Mpx} \cdot 24 \text{ bit/px} = 288 \text{ Mbit} = 36 \text{ MBytes} \quad (49)$$

In order to reduce the weight of the payload data it's possible to compress the frames down to 33% or 50% of their original size without losing any information (exploiting lossless techniques) [64]. As a safety margin, a compression of 50% was considered.

For what concerns the telemetry load, the Consultative Committee for Space Data Systems (CCSDS) [65] dictates the standards: every second throughout the lifetime of the S/C, the on-board computer creates a Virtual Channel Data Unit (VCDU), a file containing the information on the telemetry of the spacecraft coming from all the systems, together with the state of health of each one of them (payload included). The VCDU is stored inside a standard information packet called Channel Access Data Unit (CADU), which by regulations occupies 256 Bytes of memory [66]. Further analysis in Section 15.2 will get to a more precise value.

In order to have a meaningful sizing of the data budget, the baseline design of the mission was considered: the single drone solution will provide a given number of pictures when flying over its target, but in case of

20 drones in formation flight, each of them will collect 20 pictures per camera (40 pictures in total). Let's assume that the on-board systems allow a lossless compression of 50% and that the spacecraft will be in contact with a ground station at least once every 6 hours (worst case scenario), so with the corresponding telemetry to be downloaded. The total data budget will then be:

$$S_{max} = 40 \cdot S_{pic} \cdot 0.5 + 6 h \cdot 3600 s/h \cdot 256 B/s = 725 MB \quad (50)$$

So the maximum data budget for the mission is set at *725 MBytes*.

On another note, to ease this constraint, an alternative operative solution is proposed. In order to guarantee the download of the pictures within the 1-hour window after their acquisition, black and white pictures can be generated on board starting from the originals and then sent to the ground station: a b&w picture weights a third of a coloured one, lowering the total data budget to

$$S_{pic, bw} = 12 Mpx \cdot 8 bit/px = 96 Mbit = 12 MBytes, \quad (51)$$

$$S_{max, bw} = 40 \cdot S_{pic, bw} \cdot 0.5 + 6 h \cdot 3600 s/h \cdot 256 B/s = 165 MB \quad (52)$$

This solution is to be preferred. The result is not margined since the 50% compression is already a worst-case hypothesis.

11.3 Architecture

The constraints on the architecture design come from the mission's requirements: a high datarate is required to ensure the download of the mission data; S-band frequency is preferred because of the low orbital altitude (good trade-off between transmission power and atmospheric losses); a wide-FOV antenna is needed to maximize the visibility windows; a BER lower than 10^{-5} is required for communication quality purposes.

The architecture frame is a classical system made of a transmitter and a receiver, both connected to the same 4 patch antennas. The number of antennas is enough to guarantee a redundancy in the design. In order to maximize the downlink signal's strength an amplifier was also included in the architecture. The components reported hereafter are all off-the-shelf and TRL 7+.

	Patch Antenna	Transmitter	Receiver	Amplifier
Producer	AAC Clyde Space	CubeCom	AAC Clyde Space	Microwave Amps
Model	Pulsar SANT-2	STXG2	RX-2000	AM38A
Frequency Range [GHz]	2.2 - 2.3	2.2 - 2.29	2.0 - 2.4	0.7 - 15
Half Beamwidth [deg]	60	/	/	/
Gain [dB]	7	/	/	45
Data Rate [Mbps]	/	25	0.2	/
Size [mm]	90x90x10	96x90x13	135x50x25	150x70x25
Mass [g]	50	137	200	500
Power consumption [W]	0 (passive)	12	1.5	40
TRL	9	7	9	7

Table 32: Architecture specifics
[67][68][69][70]

All the components share a portion of the lower S-band so communication is guaranteed for both downlink and uplink.

The chosen patch antenna is lightweight and works with circular polarization, providing a 60° half-beamwidth; the transmitter combines a high datarate with good options in terms of coding schemes supported; the receiver is enough to receive the telemetry expected during the uplink communications; finally, the amplifier is the most massive element of the system, but its high gain is fundamental for the success of the downlink.

A sketch of the onboard architecture is reported here.

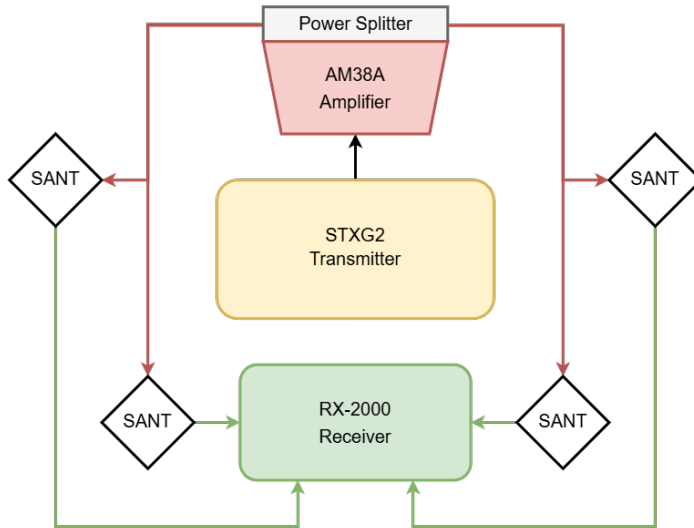


Figure 48: Architecture conceptual scheme

The patch antennas will be distributed as follows: two on the nadir pointing face of the spacecraft, each of the other two on the adjacent lateral faces. This configuration will broaden the total field of view during nominal operations, as well as guaranteeing communication even during the LEOP tumbling conditions.

11.3.1 Transmission Optimization

Key elements in ensuring reliable and efficient data transmission for the mission are the coding and modulation techniques employed.

Coding methods

Coding techniques are used to enhance data integrity by correcting errors that may occur during transmission and reducing the weight of transmitted data without compromising the required quality.

- **Reed-Solomon (RS)** error correction is the technique chosen for HORUS communications: its versatility and efficiency fit nicely with the tight requirements and harsh environment that characterize the mission.

This method is robust, with strong error correction and minimal overhead; it contains both internal and external parity encoding, and it guarantees data recovery even under high noise conditions. RS is suitable for missions with high data rates, it optimizes latency performance and overcomes bandwidth constraints through its block path and interval depth capabilities.

- **Lossless compression** is necessary to maintain the quality of the original images while reducing their sizes down to 33%. Among the different compression algorithms, PNG, TIFF-LZW, or standards such as JPEG-LS and FLIF can be explored as options.

Modulation techniques

Modulation techniques act on transmission speed and signal robustness. Among the different existing methods, the combination of **OQPSK** with filtered **GMSK** results in the optimal choice for the mission requisites. This is the combination of choice for a mission where solid signal transmission must be

conducted in very short visibility windows [71], allowing high-speed data transmission with acceptable noise tolerance in VLEO environments. OQPSK represents a technique that can minimize out-of-band emissions featuring very high reliability and compatibility. GMSK signals have a constant envelope and very good spectral characteristics, which reduce interference with other channels. Besides that, GMSK acts optimally in conditions with high effects of Doppler shift.

Robustness assessment

Robustness is a key feature to assess since the early stages of mission design. The architecture and the transmission techniques chosen aim to guarantee high and continual performance of the TTMTC subsystem. The antennas, considered the most fragile and essential components, were given a large level of redundancy that helps mitigate the effects in case of damage or malfunctions of one of them. As for the transmission, the selected coding method ensures effective error correction together with a very low BER even in presence of signal disturbances; the modulation on another hand is capable to strengthen the signal even more, giving the communication an adequate level of reliability.

11.4 Link Budget

A great part of the sizing of the TTMTC subsystem is done by establishing the conditions that ensure the closure of the link between the spacecraft and the ground station of choice.

Some constraints came from the mission's requirements and brought to the chosen architecture. In particular, to guarantee a BER lower than 10^{-5} , the minimum E_b/N_0 was set to 10 dB (according to literature [72]).

Some specifics of the ground stations were defined a priori based on literature and typical values (taking ESA's network as example). All the parameters used in the simulations are reported here:

Ground station			
Diameter D (m)	Efficiency μ	Data rate R (Mbps)	Pointing accuracy η (deg)
2.4	0.55	1.0	1

Table 33: Specifications of the ground station.

The ground station diameter was set at 2.4 m, which corresponds to the smallest dish antenna we will exploit (the one in Redu, Belgium [73]). Since the diameter of the receiver is directly correlated to its gain over the signal and higher gains bring a better communication, choosing the smallest dish size allows to size the system considering the worst case scenario.

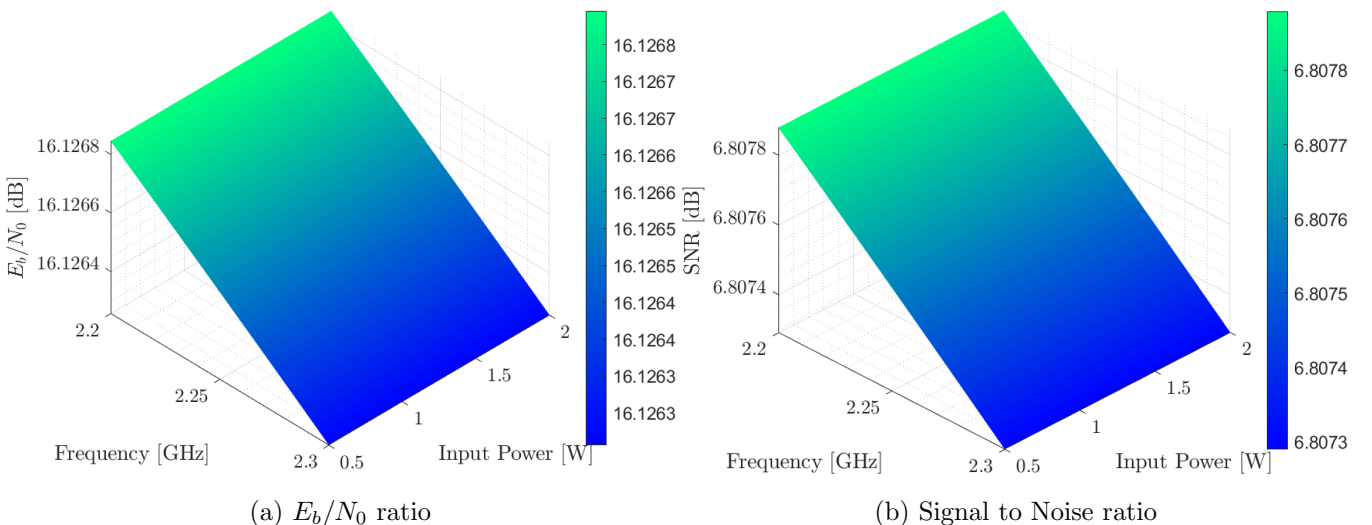


Figure 49: Surface plots for the downlink study

Signal frequency and input power of the transmitter were the design variables (according to the architecture constraints). The graphs in fig. 49 show the results as functions of the two. Given the chosen transmitter-amplifier combination, the frequencies and powers available are right to guarantee acceptable values of the two parameters. It's worth noticing how the power doesn't affect the signal quality at all: that's because the amplifier enhances the power coming from the transmitter by 30 dB, reaching values of about 60 dBm. The amplifier however has also a maximum output power it can convey to the antennas, which is 43 dBm: so for every input power of the transmitter, the combined power is saturated at 43 dBm.

The uplink was modelled with the same parameters, this time considering a wider range of input powers since ground stations are generally well served power-wise. The results showed no particular demands on power supplies and frequency selection, which might be one of the perks of orbiting at a very low altitude.

11.5 Communication Strategy

The chosen communication strategy for HORUS is a direct space-to-ground link; the choice was driven by the tight requirements that mandated a global coverage and a fast communication rate. At first, the exploitation of ESA's Etrack [74] ground station network was simulated, but the results were not satisfying: during the first hour after image acquisition, the spacecraft was not guaranteed to be in visibility of a ground station for any location of the target, as shown in Figure 50(a). An additional constraint on the contact windows was given by the data budget and the TTMTTC architecture: considering the low data budget solution and the scenario with the maximum amount of pictures taken (40), HORUS would need at least 53 seconds of full downlink window to transmit the data; this, together with 60 seconds needed by every ground station to contact and release the spacecraft amounts to about 2 minutes of minimum visibility window.

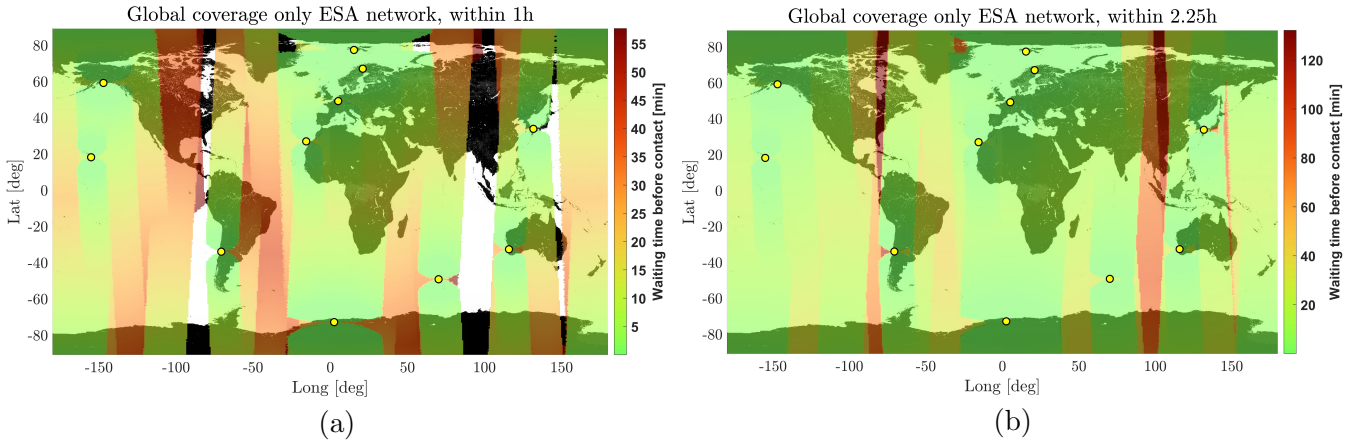


Figure 50: Etrack global coverage within 1h and 2h15

For reference, it's also reported how if the time constraint were to relax (from 1 hour to 2:15 hours after acquisition), the coverage would be global. However, this solution was not pursued because of the importance of the 1-hour requirement on the overall performance of the mission.

So, the Etrack network alone couldn't meet the mission's requirements: ground stations from private companies were added to the network to improve coverage and reduce latency. Those were still selected from European companies, namely from SSC[©] and LeafSpace[©] networks. The output of this analysis is reported in Figure 51, where ESA's GS are marked in yellow while commercial ones are in cyan.

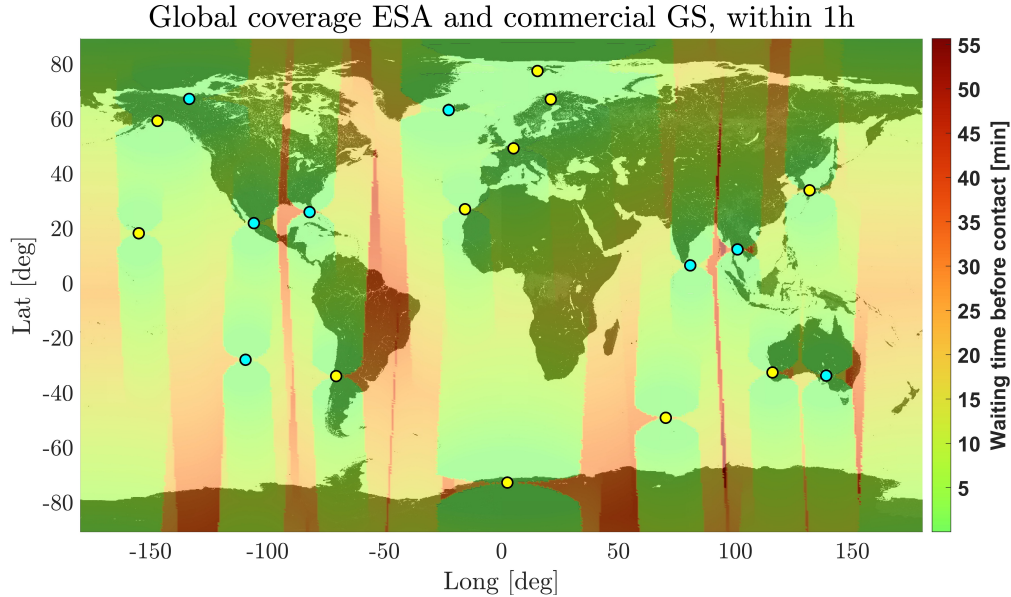


Figure 51: Global coverage ESA and commercial network within 1h

This is the best communication strategy, since it guarantees both global coverage and low communication latency. For sure though the exploitation of such a number of ground stations will impact on the costs for the costumer.

Following a thorough visibility analysis, the right ground stations among the ones at disposal were carefully selected based on key criteria, including antenna diameter, frequency band and geographic location. The main constraint for the selection was the HORUS mission's operation in a very low orbit, which results in a high relative velocity between the satellite and the ground stations. This implies that only antennas capable of rapid tracking can be employed for communication. As a result, large-diameter antennas, which are less agile in tracking fast-moving targets, were excluded from consideration. An upper limit of 8 meters for the antennas diameter was established. Regarding frequency selection, as explained in Section 11.3, S band has been employed. For what concerns the GS location, since HORUS orbit is highly inclined, stations at high latitude have to be preferred. The outcome of the selection process is illustrated in Figure 52, which highlights the geographical locations of the chosen ground stations.

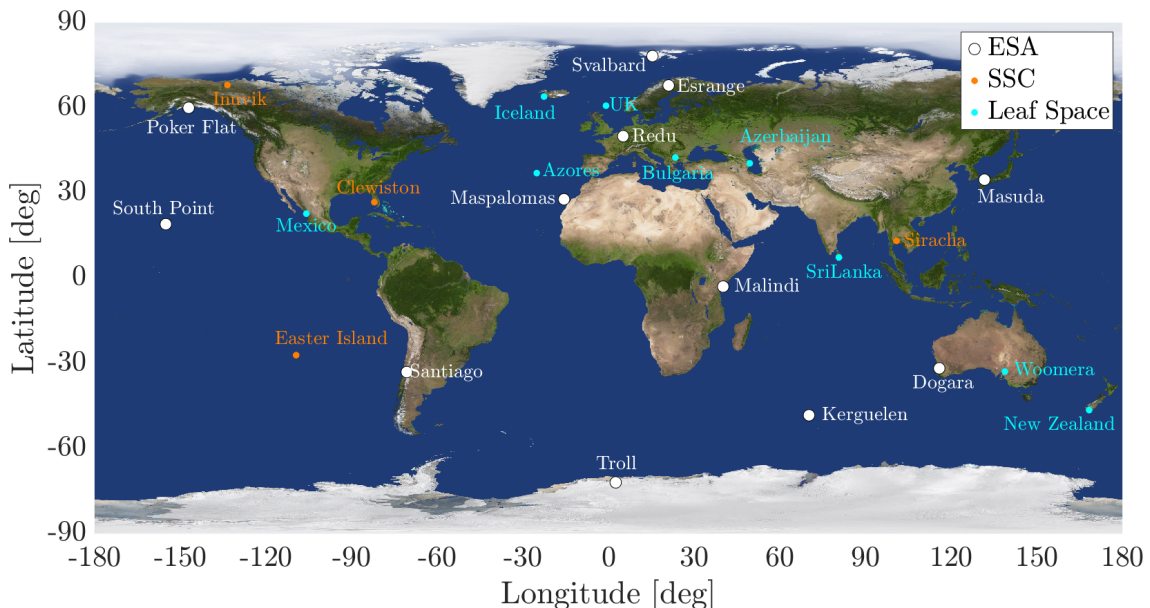


Figure 52: Selected ground stations

Name	Lat. ($^{\circ}$ N)	Long. ($^{\circ}$ E)	Alt. (m)	Name	Lat. ($^{\circ}$ N)	Long. ($^{\circ}$ E)	Alt. (m)
Redu	50.00	5.17	340	Bulgaria*	42.48	23.44	-
Maspalomas	27.77	-15.58	0	Clewiston*	26.44	-82.02	5
South Point	19.00	-155.07	367	Siracha*	13.06	100.55	0
Santiago	-33.13	-70.67	731	Inuvik*	68.24	-133.30	15
Troll	-72.01	2.53	1240	Woomera*	-32.96	138.85	-
Svalbard	78.23	15.40	460	Iceland*	63.96	-22.58	-
Dongara	-31.80	115.89	22	Sri Lanka*	7.27	80.72	-
Poker Flat	60.02	-147.07	514	Mexico*	22.70	-105.85	-
Esrangle	67.89	21.08	368	Easter Island*	-27.18	-109.42	-
Kerguelen	-48.35	70.26	30	Azores*	37.00	-25.13	-
Masuda	34.68	131.72	65	New Zealand*	-46.53	168.38	-
Malindi	-3.00	40.19	65	UK*	60.75	-0.86	-
				Azerbaijan*	40.46	49.48	-

Table 34: Ground Stations Coordinates

*Commercial Ground Stations

To summarize, the low data budget option (b&w pictures) allows to meet the mission requirements by exploiting the ground stations network just presented; of course, the costumer will have access to the RGB pictures as soon as all the spacecrafts in the batch have had enough time in visibility of a ground station. This happens after about 3 full revolutions ($\simeq 4:30$ h) according to our simulations.

11.5.1 Contact Analysis

The analyses carried out up to this point show the complete feasibility of the single drone configuration of the mission. When the number of spacecrafts starts to rise some issues arise.

Even in the slightly more complex case of 2 drones orbiting with a certain phase difference, their distance can vary greatly based on the location of the target. The worst case happens for a target on the Equator: in order to be able to picture a coherent surface by composition of the pictures of the 2 spacecrafts, they would fly at short distance, meaning they would pass over the same ground station with a short time delay (of only tens of seconds). The problem here is clear: when the second s/c gets to the ground station to downlink its data, the GS will be still linked to the first s/c, thus making it impossible for the two drones to download their pictures to the same ground station. Moreover, studies conducted show that only after 3/4 drone passages the same ground station can be ready to connect to a new s/c, making the quest even harder.

Following some thorough investigations, it was found out that every location on the planet can be serviced by a single drone as a worst case scenario, while the best case consists in some areas (such as the Middle East) that can provide coverage for up to 19 drones, even though not perfectly aligned (an example will be showed later). Here the case of a 5-drone flight formation targeting Paris Metropolitan Area (4200 km^2) is reported: each number represents a different drone.

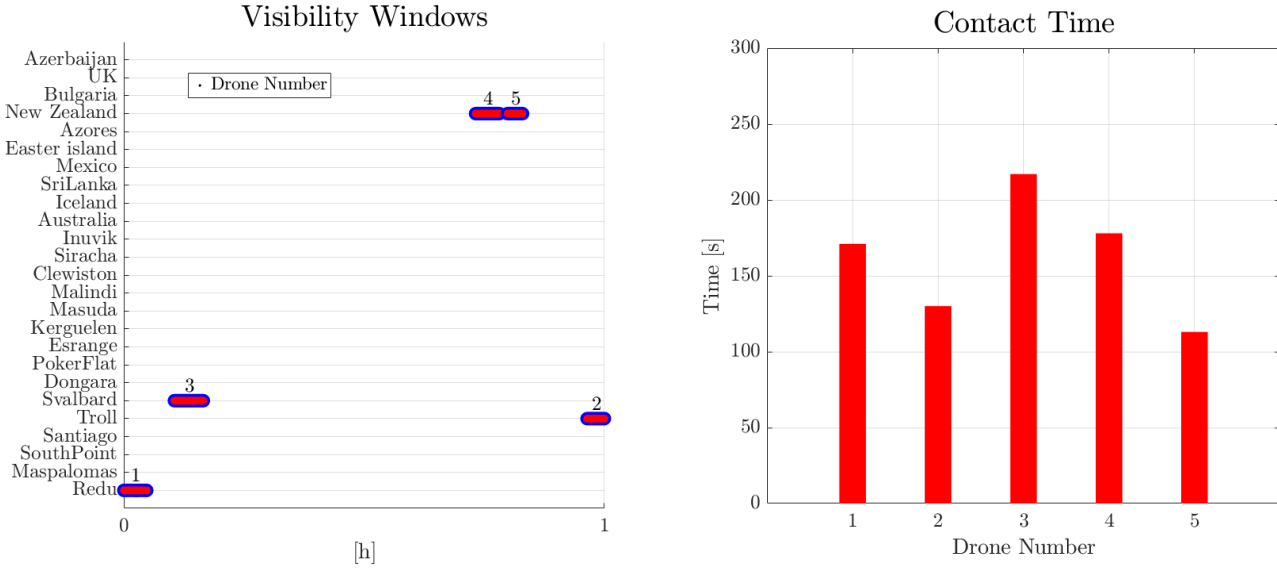
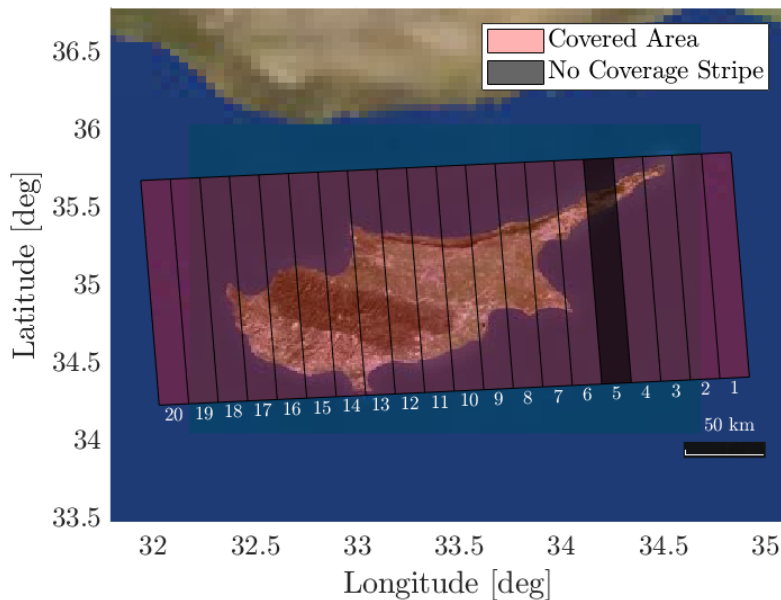


Figure 53: Visibility study over Paris

The figure on the left displays the visibility windows associated to each of the 5 drones, aligned with the ground stations to which they are connecting. On the right side of the figure, the contact time for each drone is reported. For example, it's possible to notice that drone n. 1 contacts the ground station in Redu immediately after the acquisition of the pictures (time 0 in the x-axis) and stays connected for about 170 seconds, while drone n. 2 arrives at the Antarctic ground station of Troll some 120 seconds before the closing of the 1-hour window after acquisition.

In this case, the drones are perfectly positioned to ensure a complete coverage over the desired area; however, in some cases a higher number of drones could be servicing the same target, although not being able to cover the entirety of the area and respect the 1-hour latency requirement. This means that out of the 20 spacecrafts aligned to take the widest possible composed picture, some of them wouldn't be able to contact a ground station in the desired time window (due to all the available ground stations being occupied by other drones); this would result in a coverage area with missing stripes. An example is found when observing the Eastern Mediterranean Sea, so we conducted a visibility study over the island of Cyprus:



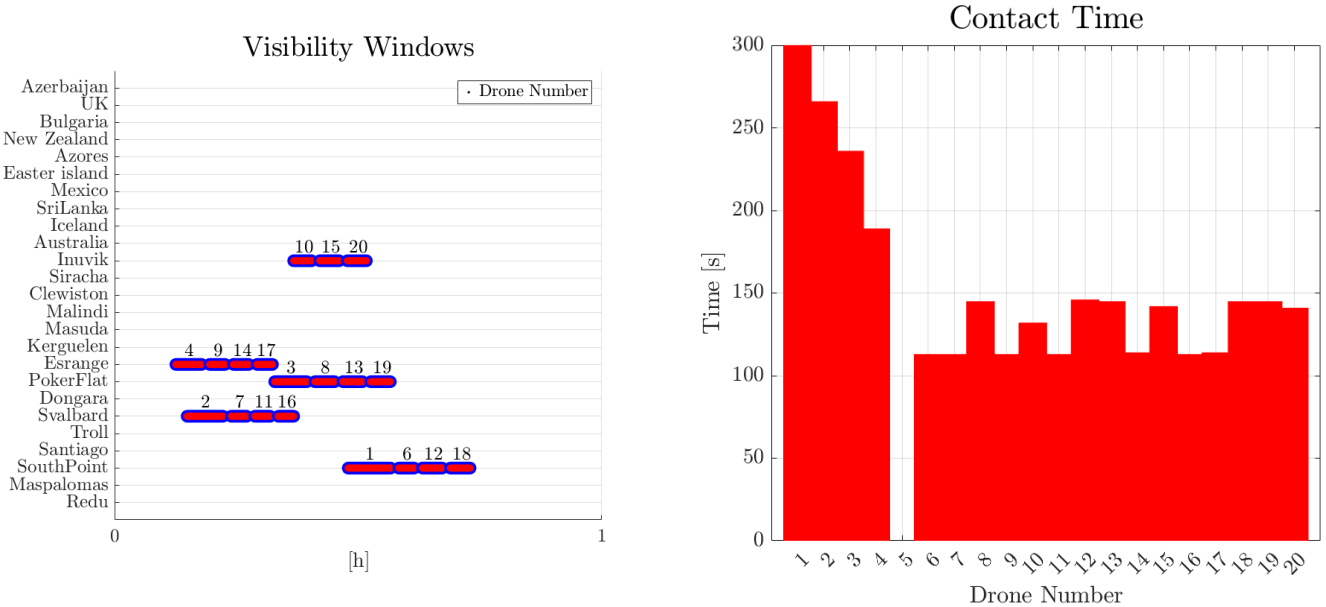


Figure 54: Coverage and contact analysis for Cyprus

The total area covered by the drones is about 35000 km². In the case reported, 19 out of 20 satellites are able to take their pictures and establish a connection with a ground station in the following hour, while the remaining one cannot do so. This results in a discontinuous image, as shown above. A feasible solution can be studied by Mission Analysis, since it would be possible to have that drone in a different orbit spaced so to cover exactly the stripe left uncovered.

11.5.2 Relay Satellite Alternative

After having discussed on the feasibility of the S/C-ground communication, an alternative solution was introduced: the exploitation of a relay satellite constellation to mediate the link between the spacecraft and the ground stations.

The main alternatives are both GEO constellations: the Tracking and Data Relay Satellites (TDRS) by NASA and the European Data Relay System (EDRS) by ESA. They both offer good ground coverage (although not total) and high downlink datarates that could improve the efficiency of the communications. However, the coverage provided by these constellations is not enough to fulfill the mission requirements and they have been discarded.

In the LEO domain there aren't suitable options for our needs. Currently, no constellation offers a service capable of dealing with satellite tracking and data downlink at the rates requested. Looking at the future, starting in 2022 NASA has begun funding private companies to develop and demonstrate space relay communication capabilities, looking at the upcoming saturation of the current relay constellations capabilities [75]. These possibilities are still work in progress, so they don't represent a valid alternative for HORUS (at least not for the next 3-5 years).

12 Electric Power Subsystem

The Electric Power Subsystem (EPS) is responsible for supplying electrical power to all spacecraft components, ensuring their proper operation across all modes and phases of the mission.

12.1 Power budget

To proceed with a design suitable for the mission requirements, it is necessary to start with the definition of the preliminary power budget, which illustrates power consumption per each subsystem in each mode. To compute it, for each subsystem, select the components that require power and list:

- Maximum power request per unit (from data-sheets, where available), number of units employed;
- Fraction of the maximum power used per each mode (value from 0 to 100%), required for both average and peak power consumption.

The difference between Peak and Average power consumption lies in how much power a subsystem draws at specific times versus over a longer period: peak is computed as the maximum amount of power a component draws when operating at full capacity. In contrast, average is the amount of power consumed over a complete operational cycle, including both active and idle phases. In the end, the EPS is sized around the average power, as it reflects the satellite's typical power needs over an operational mode. Particular care shall be given to the power budget in the successive design phases, updating it with the newly selected components and verifying that peak power demands are handled.

12.1.1 Margin Philosophy

Margins were adopted according to ECSS standards [40]:

- +5% for off-the-shelf components without modifications;
- +10% for off-the-shelf components with minor modifications;
- +20% for newly designed and developed products.

Such margins were applied at the component level. However, HORUS mission still being at a Phase A level of development, a system-level margin of 20% was applied [40].

12.1.2 EPS modes

Recounting the modes presented in section Section 4.4 from the EPS Point of View:

- STAND-BY MODE: both payload and propulsive system are inactive. ADCS partly operational as star trackers are not required for Sun pointing;
- SAFE MODE: all unnecessary elements are switched off to prioritize battery charging. Hysteresis shall be implemented to guarantee that battery charge level reaches a [TBD] threshold to avoid switching loops. Sun pointing is maximized to guarantee power production by the means of SA;
- ORBIT CONTROL MODE: the most power demanding mode, as the PS requires large amounts of power to operate the thruster used to perform orbit maintenance manoeuvres. To reduce the strain on the batteries and on the overall EPS, thrusting is performed only during daylight conditions.
- IMAGING MODE: first a slew manoeuvre is performed to align the camera with the target, which is then switched on to perform imaging. Precise pointing accuracy is required, achieved by star trackers.
- TELECOM MODE: TTMTTC components affect the most the budget of this phase.
- ACTIVATION MODE: all components are switched on and off to check the proper functioning of the system. Peak power for this mode is extremely high. However, due to the little time each component is required to stay active, Average power is critically lower.

COMPONENT		TYPE	Power Margined (W)										TCS				
Avg.	%		W	COTS	0.05	50	5	2.42	100	80	50	30					
	N°																
Total	Margin: (%)		W														
ADCS & GNC		Payload	TIMTC	Thermistors	COTS	0.05	50	5	2.42	100	80	50	30	TCS			
DC-DC: 28-12 V				COTS	88%	1	5	84%	-	-	-	-	-	DC-DC: 28-12 V			
DC-DC: 28-12 V				COTS	88%	1	5	84%	-	-	-	-	-	DC-DC: 28-12 V			
DC-DC: 28-5 V				COTS	88%	1	5	84%	-	-	-	-	-	DC-DC: 28-5 V			
DC-DC: 28-3.3V				COTS	85%	1	5	81%	-	-	-	-	-	DC-DC: 28-3.3V			
PCDU			EPS⁽²⁾	COTS	94%	1	5	89%	-	-	-	-	-	PCDU			
Current Sensors				PROB	0.01	30	20	0.36	100	80	50	30	100	Current Sensors			
Voltage Sensors				PROB	0.01	30	20	0.36	100	80	50	30	100	Voltage Sensors			
NanoMind A3200				COTS	3.6	1	5	3.78	50	50	50	50	50	NanoMind A3200			
DARA OBC				COTS	5.87	1	5	6.16	50	50	50	50	50	DARA OBC			
OBDDH		Payload	STR	FBG Sensors	PROB	0.07	1	20	1.00	50	50	50	50	50	FBG Sensors		
Acoustic Emission				PROB	3.5	1	5	4.2	10	10	10	10	10	10	Acoustic Emission		
Amplifier AM38A				COTS	40	1	5	42.00	2	0	2	0	2	2	Amplifier AM38A		
Receiver RX-2000				COTS	1.5	1	5	1.58	60	40	60	40	60	40	Receiver RX-2000		
Transmitter STXG2				COTS	12	1	5	12.6	40	20	40	20	40	20	Transmitter STXG2		
PSU			TTMTC	iSim90	COTS	30.5	2	5	64.05	0	0	0	0	0	iSim90		
PPU				COTS	95%	1	5	90%	-	-	-	-	-	-	PPU		
Heaters				COTS	10.0	2	5	21.00	0	0	0	0	0	0	Heaters		
Temperature Sensors				COTS	0.03	12	5	0.38	100	100	100	100	100	100	Temperature Sensors		
Pressure Sensors				COTS	0.03	6	5	0.19	100	100	100	100	100	100	Pressure Sensors		
High Pressure Valve		Payload	TTMTC	COTS	6.00	2	5	12.6	59	59	59	59	59	59	High Pressure Valve		
Low Pressure Valve				COTS	2.40	3	5	7.56	59	59	59	59	59	59	Low Pressure Valve		
Thruster				COTS	200	1	5	210.00	0	0	0	0	0	0	Thruster		
Reaction Wheel				COTS	65.0	4	5	273.00	1	0	0	0	0	0	Reaction Wheel		
Magnetorquer				COTS	15.8	3	5	47.25	4	4	2	2	2	2	Magnetorquer		
Magnetometer		EPS⁽²⁾	TTMTC	COTS	0.45	1	5	0.47	70	40	70	70	70	70	Magnetometer		
Gyroscope				COTS	1.50	1	5	1.58	70	20	70	70	70	70	Gyroscope		
GNSS				COTS	1.85	1	5	1.94	100	0	70	70	70	70	GNSS		
Sun Sensor				COTS	0.08	5	5	0.43	70	0	70	70	70	70	Sun Sensor		
Star tracker				COTS	2.00	2	5	4.20	0	40	70	70	70	70	Star tracker		
STANDBY MODE		Total Average Power Margined: 53.41 W										8.44 W		2.42 W			
Avg.	%													80			
Avg. Tot.		8.30 W										6.00 W		1.93 W			
Margined		9.96 W										7.2 W		2.32 W			
SAFE MODE		Total Average Power Margined: 38.77 W										26.80 W		2.42 W			
Avg.	%													100			
Avg. Tot.		2.70 W										32.16 W		2.90 W			
Margined		3.24 W										16.28 W		2.90 W			
ORBIT CONTROL MODE		Total Average Power Margined: 281.94 W										10.08 W		2.42 W			
Avg.	%													100			
Avg. Tot.		19.04 W										15.92 W		2.42 W			
Margined		22.85 W										12.10 W		2.90 W			
IMAGING MODE		Total Average Power Margined: 75.07 W										10.96 W		2.42 W			
Avg.	%													100			
Avg. Tot.		20.30 W										13.57 W		2.42 W			
Margined		24.36 W										16.28 W		2.90 W			
TELECOM MODE		Total Average Power Margined: 95.59 W										13.15 W		2.32 W			
Avg.	%													80			
Avg. Tot.		6.25 W										5.96 W		2.90 W			
Margined		7.5 W										19.10 W		2.90 W			
ACTIVATION MODE		Total Average Power Margined: 82.49 W										10.08 W		2.42 W			
Avg.	%													100			
Avg. Tot.		9.50 W										11.29 W		2.42 W			
Margined		11.4 W										13.55 W		2.32 W			

Figure 55: Power Budget (average) per Mode

- 1) Proprietary PPU power efficiency considered over the whole power budget for PS
 - 2) DC-DC converters and PCDU efficiencies [76] [77] considered in EPS power computation. Refer to Figure 65 for power flowing through each DC-DC converter.

12.2 EPS Drivers and Alternatives

The main drivers that affect the design are:

- high TRL: this affects the technology selection, preferring well established components which are state of the art for Earth observation missions;
- Aerodynamics: the cross section shall always be minimized, as an higher value would cause the S/C to decay faster;
- the potential lifetime is estimated to be approximately 1.5 year according to Section 9
- VLEO Polar orbit.

The latter affects mostly the frequency and duration of eclipses, as well as the sunlight conditions. In particular, eclipses vary from a minimum of approximately one minute to a maximum of 37 minutes per orbit. Periods with no eclipses are also present and are highly dependent on the selection of the RAAN of the orbit, which is a non-fixed parameter of the design. For instance, the variation in this parameter strongly impacts the evolution of the beta angle over the year (Figure 56a). The most representative cases are when Ω is 90° or 270° . For these values, there is the highest variation of Sunlight conditions throughout the year. In particular, with $\Omega=90^\circ$, periods of approximately 30 days are present, in correspondence of the equinoxes, where there are no eclipses. This could be beneficial from the solar panel perspective; however, it's critical for the TCS. In contrast, near the solstices, the solar vector becomes perpendicular to the orbital plane's normal, resulting in the longest eclipses (Figure 56b).

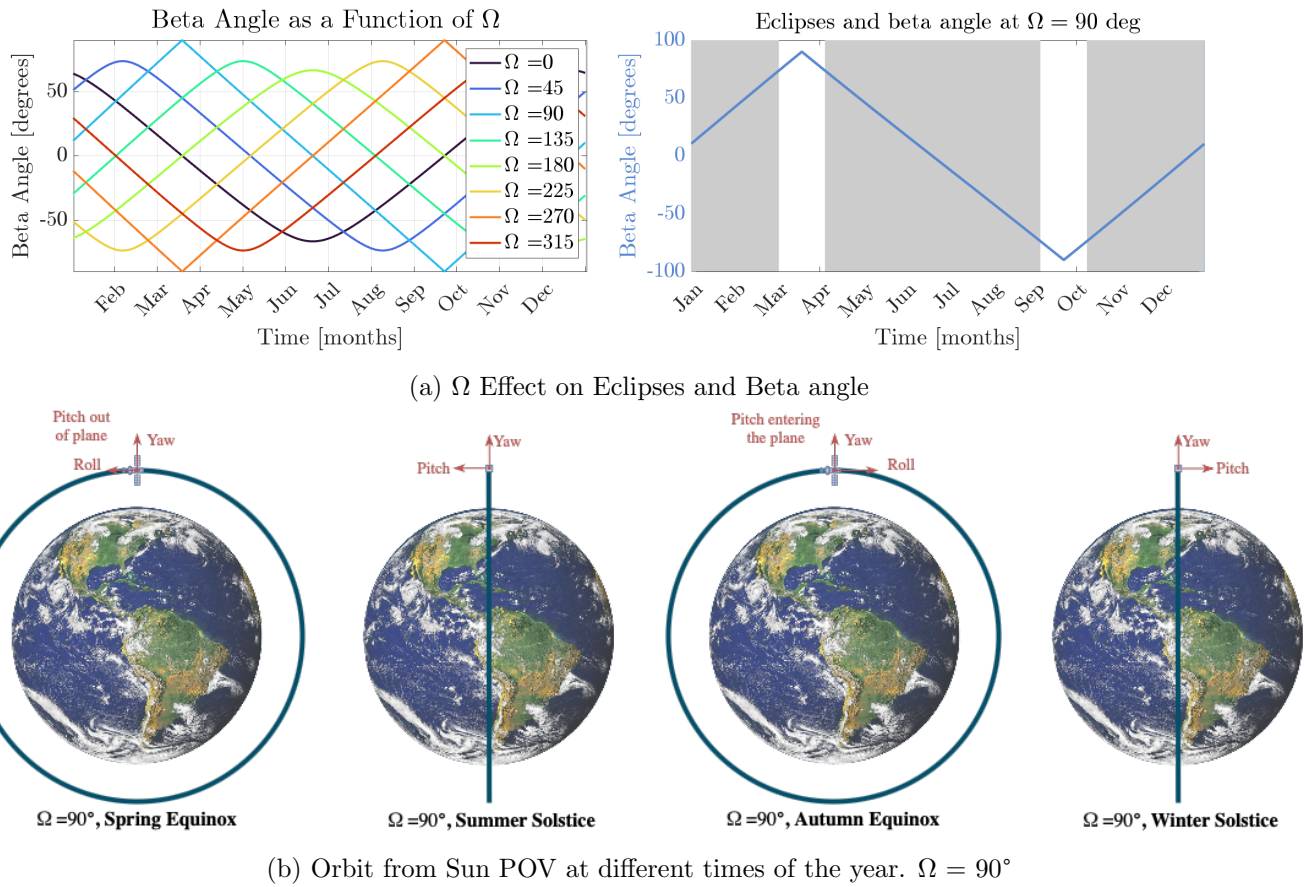


Figure 56: Beta Variation

In investigating state-of-the-art technologies, the following considerations can be made: RTGs are unsuitable for VLEO Earth observation missions due to their high cost, complexity, and potential safety concerns. In particular, de-orbiting could present critical safety hazards. On the other hand, primary batteries are more suited for shorter missions and they remain unpractical for a mission lasting more than 1 year. In the end, these considerations lead to a well established design consisting of solar arrays as primary energy source, together with secondary batteries to couple with eclipse periods.

12.3 Solar Arrays Design

12.3.1 Solar Cell Selection

In the design of solar arrays, high cell efficiency is required to maximize energy production, which in turn reduces the total SA surface area required. For this reason triple-junction cells are selected. They use three layers of semiconductor materials, each specifically selected to absorb different wavelengths of the solar spectrum (typically infrared, visible, and ultraviolet light). This guarantees BoL efficiency up to 30-35%. In particular, the selected cell, SPECTROLAB XTE-SF [78], can reach efficiencies up to 32.2% at BoL. EoL efficiency is estimated by interpolating the efficiency degradation from the data-sheet with respect to the fluence of 1 MeV electrons/cm² throughout the mission (Figure 57). The aforementioned value was estimated using ESA-SPENVIS software [13] for 1.5 years mission duration (and an extra margin of 20% was added). This process led to an EoL efficiency of approximately 30.4%. The degradation resulting from electrically charged particles is particularly low for two main reasons: low mission lifespan and specific VLEO environment, due to the operational orbit being set well below the Van Allen belts.

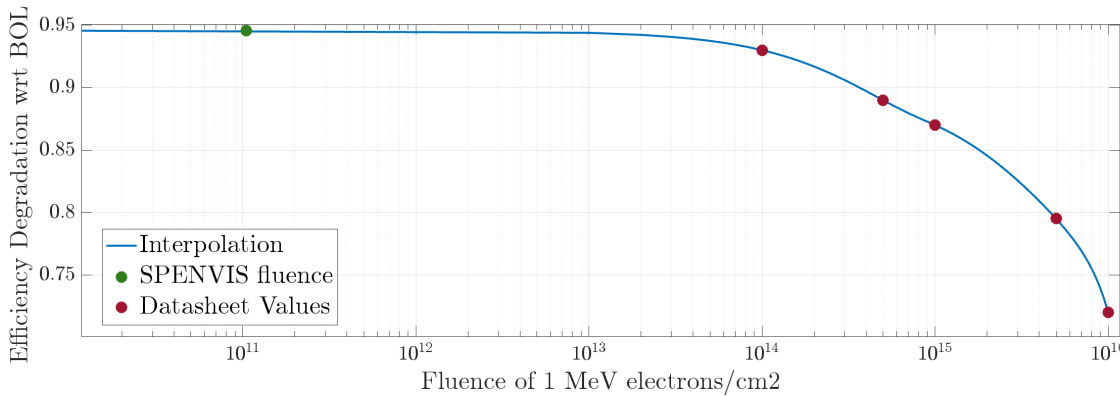


Figure 57: Data-sheet Interpolation and EoL Efficiency computation through SPENVIS [78] [13]

Standard operating temperature of 25°C is selected for cell efficiency. The design carefully accounts for typical cell loss factors. Finally, Maximum Power Point Tracking (MPPT) is preferred over Direct Energy Transfer (DET) because of its higher versatility, as it continuously adjusts the operating point of solar panels to extract required power from the solar panels, adapting to the external conditions.

Array Efficiency			Cell Losses		
Pointing Accuracy	X_e (Eclipse Line Eff)	X_d (Daylight Line Eff)	Current cell mismatch	Measurement error	Wiring and Diode Losses
4°	60% [17]	80% [17]	99% [79]	99% [79]	94% [79]

Table 35: Solar Array Efficiency. Cell losses are accounted for as efficiency reductions in the total power generation.

12.3.2 Preliminary Analysis on Solar Arrays configuration

Once the cell is selected and the baseline is defined, it is important to identify the potential configurations for the solar panels, particularly in this challenging context of ever changing Sunlight conditions. A preliminary analysis on the possible orientation of the SA is performed. For this study, the orbit is selected with RAAN equals to 90°, due to being a highly representative case for the mission, as well as being the most challenging scenario from the EPS POV. To facilitate computations, the S/C is initially assumed to maintain a nadir-pointing orientation throughout the entire revolution, resulting in the body reference frame coinciding with the LVLH frame. This assumption is a reasonable approximation, as the spacecraft will adopt similar configurations during both imaging and telecommunications modes, as detailed in Section 13.3. As evident in Figure 56b, the Solstices represent a critical case study for power production. That is, for two main reasons: shorter daylight, as it coincides with the longest eclipse periods, and the beta angle being zero, meaning that the Sun-S/C vector lies on the orbit plane. In Figure 58 it

is depicted the orbit at Winter Solstice, together with the Sun aspect angle evolution over six hours (~ 4 revolutions).

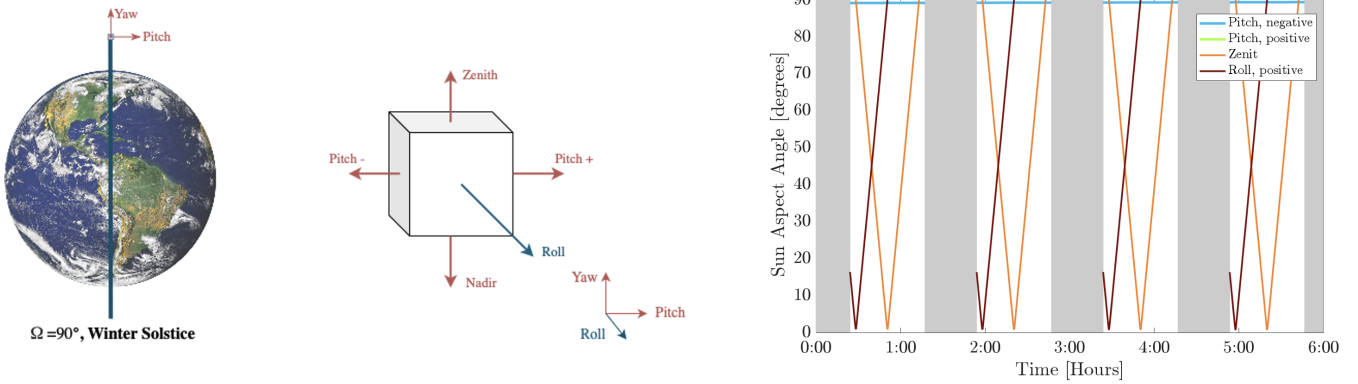


Figure 58: Winter Solstice Sun aspect angle over 1/4 of a day

Upon initial consideration, it is evident that roll-oriented solar arrays should be avoided, as they would significantly increase the spacecraft's cross-sectional area. Furthermore, body-mounted cells on the back of the S/C are unfeasible, since the electric thruster is placed there. Hence, the only way to exploit these faces is to have body-mounted cells in front of the S/C, although impractical. By referring to Figure 58 the evolution of the the Sun aspect angle for pitch- and zenith-oriented panels over the Winter solstice orbits can be observed. It is evident that pitch-oriented panels generate nearly zero power because they are almost perpendicular to the Sun vector. In contrast, zenith-oriented panels could produce enough energy to sustain the satellite. However, it is crucial to note that near the poles, the most unfavourable configuration occurs, as the Sun Aspect Angle approaches 90°, resulting in a complete loss of energy production. Nonetheless, due to rapidly changing conditions, the EPS could compensate for power shortages using batteries. Thus, the average energy generated during Sunlight periods should suffice to meet power demands and recharge the batteries, accounting for these critical points and eclipses.

Taking as a reference just this particular condition over one year, one could think that a combination of zenith oriented panels could be enough to guarantee power production for the entire mission duration. However, by looking at Figure 59 which depicts the behaviour on the Vernal Equinox day, the results show that this is not the case. As previously discussed, close to the equinoxes no eclipses are present over the day, which might relax the power production requirements. On the other hand, power production from zenith and roll faced panels is close to zero as their Sun Aspect Angle approaches 90°. Therefore, pitch-oriented panels would be necessary to ensure energy production during these times of the year.

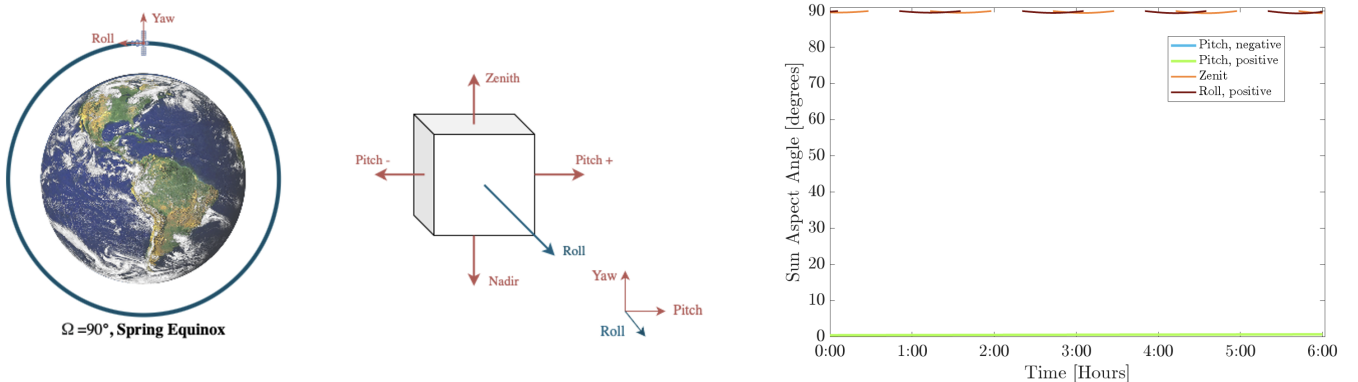


Figure 59: Spring Equinox Sun aspect angle over 1/4 of a day

These considerations led to two possible design solutions: the first being to implement a combination of differently oriented SA to guarantee energy production throughout the year, while the second to include Sun-pointing maneuvers to maximize energy production with fewer panels. Although the first alternative could alleviate the burden on the ADCS subsystem, it is ultimately deemed impractical due to several drawbacks, such as higher costs, increased cross-section, and significant challenges in thermal management.

12.3.3 'Planar' Sun Pointing

A study has been conducted on the feasibility of slew maneuvers to optimize solar arrays' power production, with the aim of minimizing both size and number. This optimization aims to maximize pointing efficiency while adhering to constraints imposed by the spacecraft's ballistic coefficient, which is to minimize the exposed cross-sectional area of the spacecraft. Consequently, only slews about the roll axis are considered. The idea is to obtain an optimal orientation profile for the S/C within this work-frame. Eventually, in the phase of operations, once the target is fixed, this control could be uploaded onto the spacecraft to be used as a reference by the ADCS in Stand-By and Orbit Control modes.

Instead of using traditional Sun-pointing methods that maximize the Sun aspect angle by performing slews about all three axes, this study investigates a "planar" Sun-pointing technique, wherein the Sun is projected onto the yaw-pitch plane. The optimal orientation of the solar panels is then determined by minimizing the angle between the panel's normal vector and the projected Sun-satellite vector onto the yaw-pitch plane. It must be noticed that the so-minimized angle is not the Sun Aspect Angle, as in order to compute it both vectors need to be traced back into a three-dimensional reference system. The outcome of this operation is the variation of the optimal orientation angle over the course of the year. This angle is defined within the Yaw-Pitch plane, measured from the Pitch axis (Figure 61), and indicates the attitude, within the LVLH frame, the S/C must maintain to maximize solar power generation.

The analysis reveals significant oscillations in solar panel orientation throughout the whole year (Figure 62). That said, such oscillations are particularly pronounced close to the solstices:

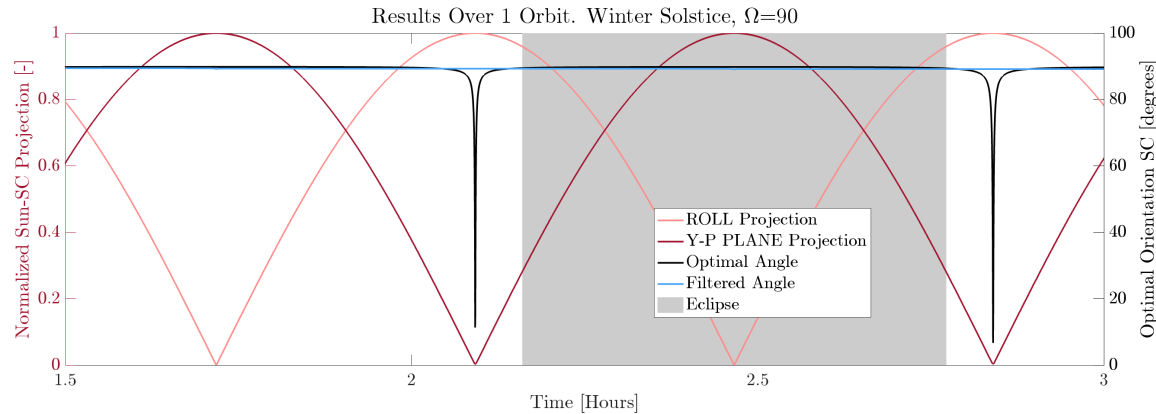


Figure 60: Optimal Orientation vs Filtered, per one orbit, during Winter Solstice Day

During this period, the optimal panel orientation approaches 90°, resulting in yaw-oriented panels. This is consistent with the previous considerations (Section 12.3.2). Near the poles, however, singularity conditions cause sharp variations in the optimal orientation angle. This occurs because the Sun-satellite vector in these instances aligns closely with the normal to the Yaw-Pitch plane (roll direction), resulting in a very small projection onto the plane, ultimately converging into a point at the moment of the solstice. Consequently, the control system attempts to reorient the S/C to align with this vector. However, attempts to align with the projection are impractical from the ADCS perspective and yield negligible increases in power generation, as the Sun-satellite vector remains largely perpendicular to the yaw-pitch plane. To address these problems, filtering is introduced to derive a more suitable control profile. This solution effectively reduces oscillations and smoothens the optimal orientation curve.

In Figure 61 three out of the four previously introduced peculiar cases are represented. A classical configuration of two SA, one per side, is selected. On the left the evolution of the Optimal Orientation Angle is plotted over the day. The aforementioned oscillatory behaviour is well evident from these plots. Compatibly with previous considerations done in Section 12.3.2, the control re-orients the spacecraft towards yaw and pitch axis depending on the time of the year. This strongly affects the ADCS subsystem, as it shall guarantee flexibility in slews about the roll axis. On the right, the corresponding Sun aspect angle is plotted for both optimal orientation and filtered results, the two almost overlapping. Finally, it is important to emphasize that this strategy does not maintain the same level of efficiency throughout the year. As demonstrated by the second set of plots, near the equinoxes, the Sun aspect angle remains consistently close to 0°. Conversely, during the solstices, the aspect angle exhibits significant variation over the course of an orbit. This behaviour is fully consistent with the considerations outlined in Section 12.3.2 and arises

as a direct consequence of restricting Sun-orienting maneuvers to the roll axis alone.

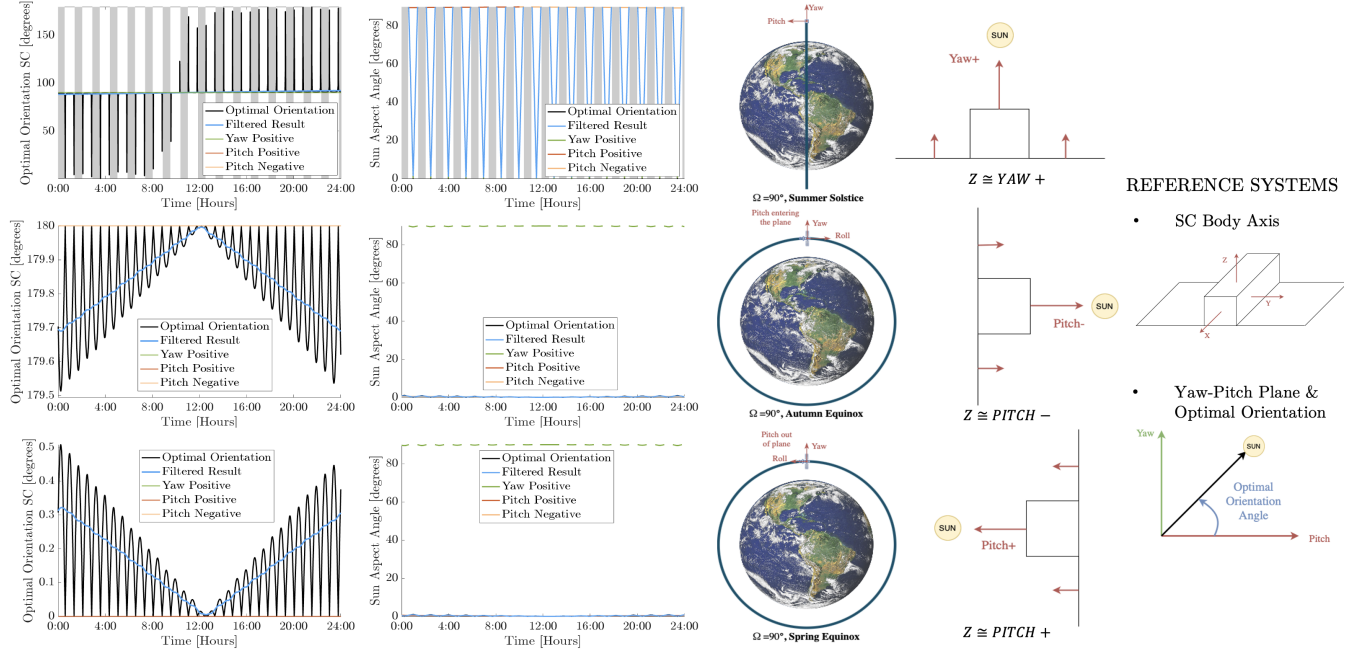


Figure 61: Optimal Orientation, filtered and unfiltered, Sun Aspect angle and S/C sketch orientation. Evolution of the parameters over 1 day for specific cases: Equinoxes and Summer Solstice

Plotting the results over the whole year (Figure 62) brings closure to the design and reaffirms the solidity of the hypophyses. On the left plot results indicate that the filtered optimal orientation rate of change is approximately 1° per day, or 0.06° per orbit, making it far more manageable from the ADCS perspective.

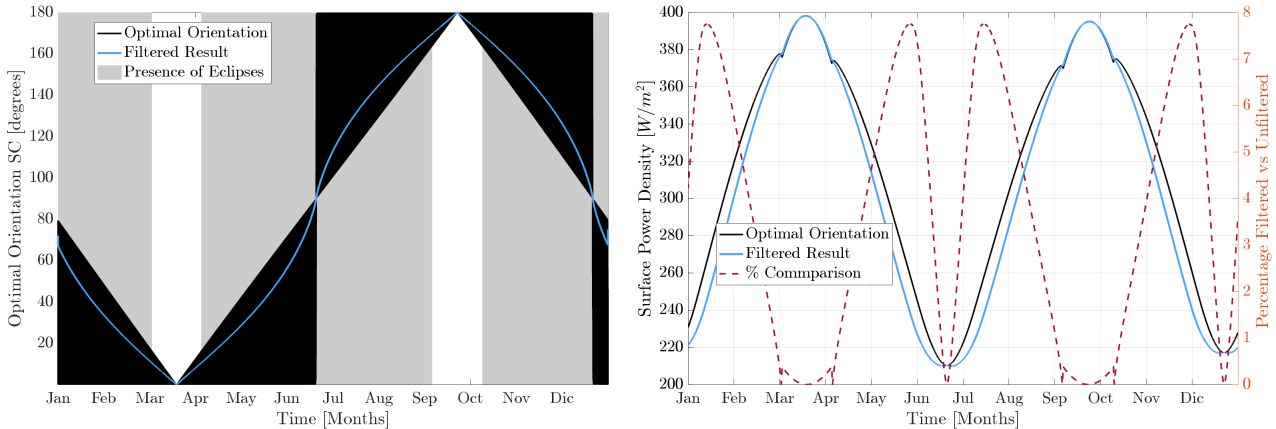


Figure 62: Filtered vs Unfiltered results over the year and Average Surface Power Density per Orbit.

On the right, the evolution throughout the year of the average Power density per orbit is plotted. Power output for the optimal orientation exceeds the filtered profile by up to 8%, though this variation fluctuates throughout the year. In some periods, the filtered and optimal results are comparable.

Annual variations in power production per orbit are evident for both filtered and unfiltered results. As previously discussed this strongly depends by the control being more efficient further away from the solstices. Furthermore, the distance from the Sun over the year slightly varies, due to the Earth's orbit not being perfectly circular. Notably, power generation during the Winter solstice is marginally higher compared to that produced at the Summer solstice, as the Earth is at its closest point at the perihelion. This identifies the worst case scenario for the sizing, which will be performed at the Summer solstice for an orbit with RAAN equals to 90° .

12.3.4 Panels Sizing and Results

Since now both the control logic and the power budget are properly defined, the actual size of the solar panels and their configuration can be properly selected. The sizing is computed following a worst-case scenario approach. This implies the selection of the Summer Solstice with RAAN equals to 90°, which represent the worst possible Sunlight condition together with the longest eclipse duration, meaning that the solar panels shall provide extra power to charge completely the batteries. Power requests for both eclipse and daylight are estimated through a weighted average computation: this means that power request per each mode is scaled accordingly with the duration of such mode over one revolution (Table 36). Since imaging and telecommunication must be carried out sequentially at least once per day (or every 16 revolutions), they may occur either during eclipse or daylight. The most critical scenario arises when both operations take place during an eclipse, as this affects battery sizing and demands higher power production due to the reduced line efficiency in eclipse conditions. For these modes, the total duration is calculated by considering both the action time and the slew maneuvers required for reorientation.

	Stand-By Mode	Imaging Mode	Telecom Mode	Orbit Control	Weighted Average
Daylight	P. Req. [W]	53.41	75.07	95.59	281.94
	Time [min]	39.13	0	0	113.02 W
Eclipse	Time [min]	0.82	16	20	85.73 W

Table 36: Operational Modes and Corresponding Power Requests and Time in Daylight and Eclipse

The power requests for the SA is computed as follow:

$$P_{SA} = \left(\frac{P_e T_e}{X_e T_d} + \frac{P_d}{X_d} \right) \quad (53)$$

Both efficiencies of the power lines during eclipses and daylight conditions are listed in Table 35, together with cell losses. The sizing is performed considering EoL cell efficiency. Due to TCS constraints, in the final iteration of the design the panels are shifted by 45° with respect to the main body axis. This is essential to reduce the view factor between radiators and SA. Shadowing is also reduced as a consequence of the new placement. Two faces of the spacecraft main body are allocated to body-mounted solar panels. However, since the planar Sun-pointing strategy described in the previous section is applied to the Solar Arrays (SA), the body-mounted panels will experience a Sun aspect angle offset by ±45°.

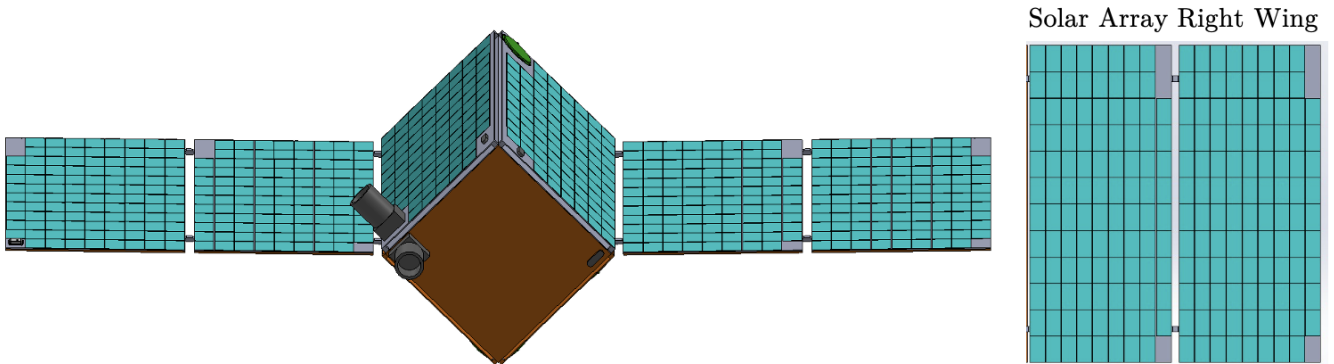


Figure 63: Final Iteration Solar Panels Design

The minimum area of the solar arrays is then computed to guarantee that power production equals the requests in the aforementioned worst case. Finally, the design is refined once more to meet the CONF and STR requirements, ensuring that the arrays incorporate a foldable structure. (Figure 63). The final design consists in a set of six panels in total: two of them body mounted and four SA, two per side. Each panel present series of 15 cells, so to obtain a nominal voltage at BoL of approximately 36.53 V. This will inevitably reduce at EoL (estimated value is 34.7 V [78]). Solar Arrays are slightly larger than body mounted solar panels as one extra string of cells was added to each panel to avoid critical failures. This

extra string was not considered in the sizing, meaning that the system is capable of operating in standard conditions when loosing up one string of per panel.

Type of Panel	n°	n°cells per Panel	Cell Config.	Nominal Voltage	Area of the Panel [m ²]	% Surface
Body	2	90	15S-6P	36.53	0.32 x 0.83	92.96%
Array	4	105	15S-7P	36.53	0.36 x 0.83	96.40%

Table 37: Final Iteration Solar Panel Properties

12.3.5 Solar Array Sizing Validation

In order to properly validate the sizing over the different conditions, the following approach is implemented:

- Per each orbit compute daylight and eclipse times;
- Accordingly to the weighted average power requests (Table 36) compute the average power request per each orbit. This will not be constant over the year. Particularly: closer to the solstices, longer eclipses, higher power demand for the solar arrays. In contrast, close to the equinoxes, orbits without eclipses are present, hence a lower power request for SA;
- Compute the Sun-aspect angle for each panel during the daylight part of the orbit;
- Compute the power produced at every instant and finally compute the average per orbit.

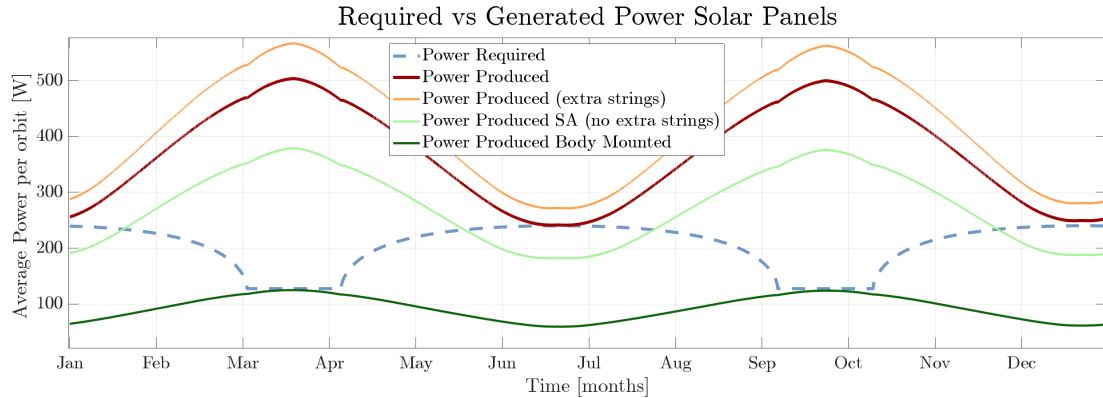


Figure 64: Average Power Produced vs Power Required by the Solar Arrays in one year

Once again, in correspondence to solstices and equinoxes, two opposite behaviours can be observed. In proximity of the equinoxes, due to the absence of eclipses, power request from the system is critically lower, while power production is at its maximum, due to the better efficiency of the planar Sun-pointing. Hence, this becomes a critical point for the TCS, as all the extra power generated and not used has to be dissipated by radiators. This issue can be easily addressed by rotating the spacecraft away from the optimal power-generation attitude, thereby limiting power production to a fraction of its maximum capacity to reduce incoming heat, but always ensuring that the generated power is higher than the request. Conversely, solstices remain critical for the EPS POV. From Figure 64, the power generated by the solar arrays appears sufficient to meet the energy requirements. However, the plot presents a simplified representation of the system's behavior, as it assumes Sun-pointing as the only attitude maneuver throughout the orbit, neglecting other reorientations that strongly depend on target selection. Consequently, the power output shown in Figure 64 represents the maximum achievable under continuous Sun-pointing conditions. While this is generally non-critical for most of the year, since power production largely exceeds requests, it becomes a concern at these specific points where energy margins are reduced. Furthermore the study is performed only taking into account average power consumption. Peak power can be higher than average in certain instances. In such cases panels might not output enough power to operate the whole system.

Fortunately, both these criticalities are mitigated by the presence of batteries and the intrinsic nature of the mission design. Since the drone is tasked with acquiring and transmitting images of the target only once or twice every 16 orbits, the batteries can supplement the solar arrays (SA) during these demanding conditions. They can then be fully recharged in the subsequent orbits, where slew maneuvers are unnecessary, allowing for optimal Sun-pointing and maximum power generation. Finally, it is essential to emphasize that the sizing was conducted under the worst-case conditions. As previously emphasized, a RAAN of 90° represents the most demanding scenario. The line efficiencies used in Equation (53) were derived from [80] due to their inherently conservative nature. After implementation, the actual values may exceed those used in the sizing process by 10–20%.

12.3.6 Solar Array Atox Protection

Finally, before proceeding with the other EPS components, it is crucial to highlight the environmental challenges posed by VLEO to the solar panels, particularly ATOX degradation, which can lead to significant deterioration of the panels' surface. Therefore, special attention must be given during the implementation phase to the selection of cover-glass materials, ensuring that the chosen material effectively protects the cells. The producer Excelitas, for example, offers highly customizable, ATOX resistant cerium doped glass in the form of a super-thin protective layer [81].

12.4 Secondary batteries

Batteries are implemented to ensure that the components can properly operate during eclipses or in the critical cases aforementioned, when power produced by solar arrays is not enough to satisfy the requirements. For the HORUS mission, a set of SAFT VES16 Li-Ion cells [82] was selected. The selection Li-Ion chemistry ensures a long life cycle, widespread availability in Europe, and a well-established track record. The total number of cycles was estimated to be in the order of 10500 (one eclipse per orbit over 1.5 years + 20 % margin). Eventually, DoD was computed by interpolating fig. 21-16, Wertz [80].

	DoD	C [Ah]	Power Capacity [Wh]	Voltage range [V]	η
VES16	40%	4.5	16	[2.7, 4.9]	0.80

Table 38: Single cell properties [82]

The batteries were sized considering the worst possible case in terms of eclipse power loads, as defined in table Table 36. To ensure mass and volume efficiency while maintaining compatible voltages, the battery sizing was performed by evaluating all possible series-parallel configurations of the cells. The final configuration, presented in Table 39, includes an additional string of cells, same approach used for the solar arrays. This extra string was not considered in the initial sizing process but was incorporated to account for potential failures, ensuring greater reliability. With the selected configuration, single battery is obtained, operating at the nominal voltage of 28.44 V and occupies a total volume of 30 x 10 x 8 cm³.

n° of cells	Config.	Voltage range [V]	Power Cap. Required	Tot. Power Capacity	Cap. With Extra String
24	8S 3P	21.6-32.8	163.80 Wh	230.4 Wh	345.6 Wh

Table 39: Battery Sizing

12.5 Power Control and Distribution

12.5.1 Power Conditioning and Distribution Unit

The SuperNova PCDU was selected as the PCDU for HORUS EPS, as a reliable and light component for satellites within the [50 500] kg range, under 1.5 kW power. It supports up to 15 input sections for the

solar arrays, each controlled by MPPT, with a maximum power input per section of 100 W. This means that the 6 panels will be connected separately to the PCDU. As for the battery, the TRL is 9, as both components have already flown on different mission, although neither of them have ever flown in VLEO.

Power [W]	Mass [kg]	Volume [cm ³]	Max Input Voltage [V]	Battery Voltage [V]	TRL
up to 1.5	0.85	14.1 x 9 x 6.8	80	[22-34]	9 (LEO)

Table 40: PCDU data [76]

12.5.2 Bus selection and DC-DC converters

The general bus is selected to be controlled at 28V, as it minimizes power losses in distribution compared to lower voltages while avoiding insulation and arcing issues present at higher voltages. Additionally, it is compatible with the most critical components from power request and consumption: reaction wheels, payload and Propulsion Subsystem all work directly at 28V. Furthermore, such selection aligns with industry standards set by ESA. The controlled regulation ensures stable power delivery, ensuring a reliable flow of power to all critical components. However, not all components operate directly at 28V. For instance, most sensors used by other subsystems require 3.3V. Since these sensors are distributed across various locations within the spacecraft, the centralized VPT VSC100-283R3S DC-DC converter [77] was selected to step down the 28V supply to 3.3V, thereby establishing a secondary power bus.

Finally, certain components within the TTMTTC and ADCS subsystems require different input voltages, specifically 5V and 12V. In this case, in order to minimize losses, decentralized DC-DC converter are preferred. They are selected from to the same VSC100-2800S series [77] used for the other converter.

A comprehensive representation of the subsystem described until now can be appreciated in Figure 65:

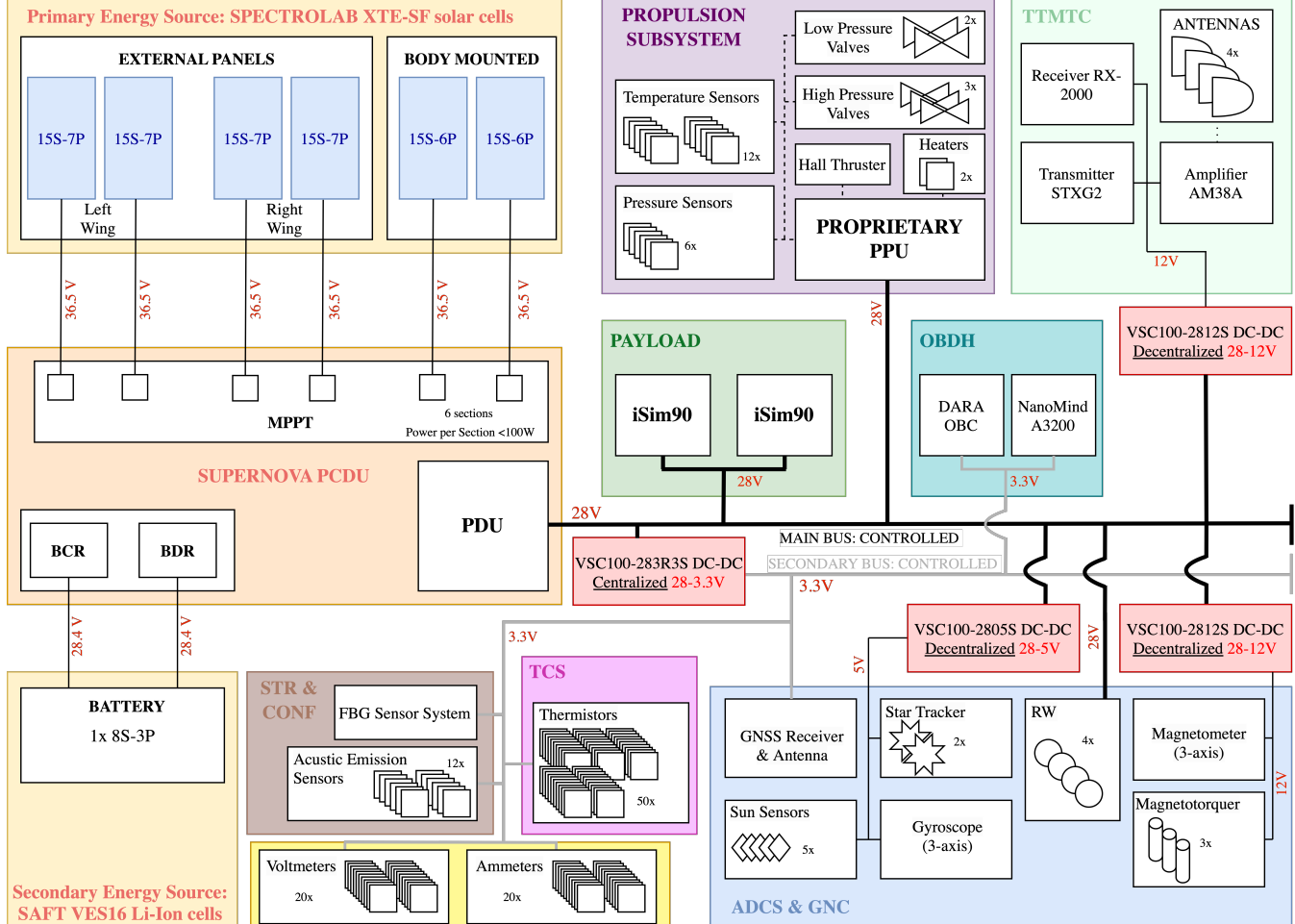


Figure 65: EPS Final Architecture Scheme.

13 Attitude Determination and Control Subsystem

13.1 Pointing Budget

To define HORUS overall Attitude Determination and Control System (ADCS) architecture, it is essential to assess accurately the pointing budget for the different operational modes. The main parameters considered are the Absolute Pointing Error (APE) and Absolute Knowledge Error (AKE), which are critical for defining the subsystem architecture. Additionally, ensuring that the spacecraft maximum angular velocity remains within allowable limits is particularly significant during mission phases where highly sensitive components, such as the star sensor, operates nominally. Table 41 presents the pointing budgets allocated to various subsystems for each operational mode.

The most demanding requirements arise from the **Payload** during the IM mode, where high stability is critical for images acquisition. To calculate the APE, it is assumed that the spacecraft must capture at least 97% of the total swath width of the optical payload. For the AKE, a maximum deviation of 50 m from the nadir direction is considered to ensure that the position of the image can be reconstructed properly. Additionally, the maximum angular rate is set below the star sensor operational limit to ensure their usage.

Focusing on the **EPS**, for accurate Sun pointing during the SBM it is assumed that the maximum deviation from the desired attitude is 4°. In SFM this constraint is based on the percentage of maximum power absorbed, according to S/C attitude. Since 60% of the maximum power shall be guaranteed, the APE is set to approximately 50°. Additionally, it is assumed that the AKE is half the APE to ensure the required pointing accuracy.

For the **PS**, the pointing budget is determined by the accuracy required to properly align the S/C with the thrust direction.

Another constraint is imposed by the **TTMTC** subsystem. To ensure smooth downlink communication, it is assumed that the GS must remain within the antenna field of view. Consequently, the required APE is set to 10° to avoid excessive reduction of the antenna field of view. As above, the AKE is assumed to be half the APE.

Finally, **TCS** adds other pointing requirements. However, in each mode they are more relaxed compared to the other, therefore, they are not used as sizing conditions. Eventually, when star sensors are not employed, the maximum angular rate is set to 1.5 °/s to avoid oscillations of flexible appendages.

Subsystems	Imaging Mode			Safe Mode			Orbit Control Mode		
	APE [°]	AKE [°]	ω_{max} [°/s]	APE [°]	AKE [°]	ω_{max} [°/s]	APE [°]	AKE [°]	ω_{max} [°/s]
Payload	0.10	0.01	0.3	—	—	—	—	—	—
EPS	—	—	—	53.1	26.6	1.50	4.00	2.00	1.50
TTMTC	—	—	—	—	—	—	—	—	—
TCS	—	—	—	—	—	—	5.00	2.50	1.50
Propulsion	—	—	—	—	—	—	1.00	0.50	0.30
Subsystems	Stand-By Mode			Telecom Mode			Activation Mode		
	APE [°]	AKE [°]	ω_{max} [°/s]	APE [°]	AKE [°]	ω_{max} [°/s]	APE [°]	AKE [°]	ω_{max} [°/s]
Payload	—	—	—	—	—	—	—	—	—
EPS	4.00	2.00	1.50	—	—	—	53.1	26.6	1.50
TTMTC	—	—	—	10.0	5.00	1.50	—	—	—
TCS	5.00	2.50	1.50	—	—	—	—	—	—
Propulsion	—	—	—	—	—	—	—	—	—

Table 41: Pointing budget across operational modes

13.2 ADCS Equipment and Configuration

Given the constraints derived from the pointing budget, the selection of appropriate equipment for HORUS has been finalized.

The reasoning and configuration of the Sensor selected is the following:

- **Star sensor:** Given the high AKE required during payload operations, it is essential to include two star sensors onboard. These are the only sensors capable of achieving the precision necessary for accurate attitude determination. However, due to their high power consumption, they will only be activated during operational modes with strict pointing requirements, such as the Imaging Mode and the Orbit Control Mode. To ensure optimal functionality and avoid Sun interference, the sensors will be positioned on two orthogonal faces of the spacecraft. This configuration minimizes the risk of simultaneous blinding from the Sun. The selection of two star sensors also provides redundancy.
- **Fine Sun Sensor:** This sensor will be used during all mission phases that do not require highly fine attitude determination. A total of five fine Sun sensors have been selected to ensure coverage across all spacecraft faces, excluding the one housing the thruster. By being co-located with the star sensors, Sun sensors can assist in deactivating them if sunlight directly enters their field of view.
- **Gyroscope:** Two three-axis gyroscopes have been selected to accurately measure the spacecraft angular velocity. Each of them is integrated respectively in the primary and in the secondary OBC to ensure a proper level of redundancy.
- **Magnetometer:** The magnetometer plays a critical role in the execution of the augmented B-dot for detumbling. Its measurements are essential for attitude determination, particularly in LEO where the magnetic field strength is significant. Due to its critical tasks, two magnetometers are employed, respectively housed inside the main and the secondary OBC.
- **GNSS:** A GNSS receiver will be installed onboard to enable precise orbit determination. This is essential for reconstructing the location of the images taken during Imaging Mode and for performing effective station-keeping maneuvers. The antenna for this receiver must be mounted on the side of the S/C opposite to the nadir, to ensure unobstructed visibility of GNSS satellites.

Instead, regarding the actuators, the selection was based on both the fine pointing requirements and the results obtained from the onboard ADCS simulator, presented in Section 13.4. The suite selected comprises:

- **Reaction Wheels:** A set of four reaction wheels, arranged in a pyramidal configuration to ensure redundancy, was chosen to provide precise spacecraft attitude control. To optimize the performance, the reaction wheels are mounted to deliver higher torque along the z-axis, which corresponds to the axis of maximum inertia and is therefore the most challenging to control. The reaction wheels have a maximum momentum higher than the one computed from simulations of the IM mode, whose results are presented in Section 13.4.
Due to high-momentum requirements, no COTS solution with a pyramidal configuration was available. Consequently, the actuator assembly will be custom-built in-house.
- **Magnetorquer:** A three-axis magnetorquer is selected to fulfil several critical functions. Firstly, it will perform DTM, moreover, it will also be used for wheels desaturation purposes. The three magnetic rods will be mounted to three orthogonal internal faces of the satellite, ensuring that they are carefully aligned at 90° with each other. This design choice is critical because it entails possible misalignments, but allows for a more optimized configuration. Moreover, no COTS pre-assembled solutions with the required features were available.

13.2.1 Redundancy

Ensuring ADCS correct functioning is a critical task, therefore the system design shall entail risk mitigation. Since this subsystem relies on several sensors and actuators, their number and configuration are selected according to this philosophy. Regarding sensors, two star sensors are on-board in warm redundancy. In addition, two magnetometers are employed, integrated in the primary and the secondary OBC respectively. The same holds for three-axis gyroscopes, whose number is doubled to ensure system robustness. Doubling the number of sensors is a very powerful solution for risk mitigation. This solution is preferred since gyros and magnetometers are very lightweight, and doubling their number has minimal impacts on the overall mass budget. Moreover, since they are already integrated in the OBCs, also the overall occupied volume is not increased. Eventually, the primary OBC houses an IMU. Therefore, when

the GNSS receiver does not work, this platform is used to perform orbit determination together with GS data. Regarding actuators, 4 RW in pyramidal configuration are employed; this choice enhances system robustness. Indeed, even if only three out of four RW are operative, the system is still fully controllable.

13.3 Modes

Since the system modes were already introduced in Section 4.4, this chapter focuses only on how the ADCS devices are used during each mode.

Mode	Active Hardware	Algorithms
Safe Mode	Attitude determination is performed with Sun sensors and magnetometer. The satellite is controlled only by MTQ to achieve rough Sun pointing. Gyros are employed to measure angular velocity.	<i>Control:</i> LQR - Rough Sun pointing [TBC] <i>Navigation:</i> Wahba problem solution <i>Guidance:</i> Rough Sun pointing [TBC]
Stand-By Mode	Attitude determination is performed with Sun sensors, gyros, and magnetometer. The satellite is controlled with RW to achieve precise planar Sun pointing without increasing the cross-section area.	<i>Control:</i> LQR - Planar Sun pointing <i>Navigation:</i> MEKF <i>Guidance:</i> Slew about the roll axis to maximize power production, without increasing the satellite cross-section.
Imaging Mode	Attitude determination is performed using star sensors. The satellite is controlled with RW to achieve precise target pointing. Gyros are on to ensure angular velocity does not exceed star sensors threshold.	<i>Control:</i> LQI - Imaging <i>Navigation:</i> Wahba problem solution - Star sensors <i>Guidance:</i> Satellite relative orientation follows Local Vertical Local Horizontal (LVLH) reference frame.
Orbit Control Mode	Attitude determination is performed with star sensors measurements. The satellite is controlled with RW to achieve precise alignment of the thruster. Gyros are on to ensure angular velocity does not exceed the threshold.	<i>Control:</i> LQR - Orbit control mode <i>Navigation:</i> Wahba problem solution - Star sensors <i>Guidance:</i> x axis directed as the orbital velocity, Planar Sun pointing is performed to maximize power production.
Detumbling Mode	Attitude determination is roughly performed. The satellite is detumbled with MTQ. Gyros are on to measure angular velocity and allow transition out of the mode when a threshold is reached.	<i>Control:</i> B-dot augmented <i>Navigation:</i> Wahba problem solution [TBC] <i>Guidance:</i> Reduce angular velocity using MTQ, as $\omega_z < 3^\circ/\text{s}$ RW are employed to complete the mode.
Telecom Mode	Attitude determination is performed using Sun sensors, gyros, and magnetometer. The satellite is controlled with RW to achieve precise GS pointing. Gyros are on to ensure angular velocity does not exceed the threshold.	<i>Control:</i> LQR - Telecom <i>Navigation:</i> MEKF <i>Guidance:</i> Earth pointing, but with lower constraints in terms of accuracy with respect to Imaging mode.

Table 42: ADCS modes overview

As shown in Table 42, a Desaturation Mode has not been included. This decision is based on the assumption that this mode can be intended as a background activity in which MTQ desaturates the reaction wheels as needed. As shown in Figure 66, the transitions between different modes during the mission phases are defined. In most cases, transitions can be either GS commanded or automatic, when specific conditions in the state machine are met. However, transitions with DTM are automatic, and ruled by angular velocity thresholds, which depend on the different modes. Transitioning into SFM is designed to be either GS commanded or entirely automatic. Namely, once the autonomous onboard fault detection system identifies potential failures, the system shall enter this mode.

While the lower part of the chart displays mode transitioning during operational phases, the upper part focuses on the beginning of the mission. After the launcher release, the satellite enters DTM mode. Then, once solar array deployment is completed, the satellite transitions between safe and Stand-By mode before entering into its operational state.

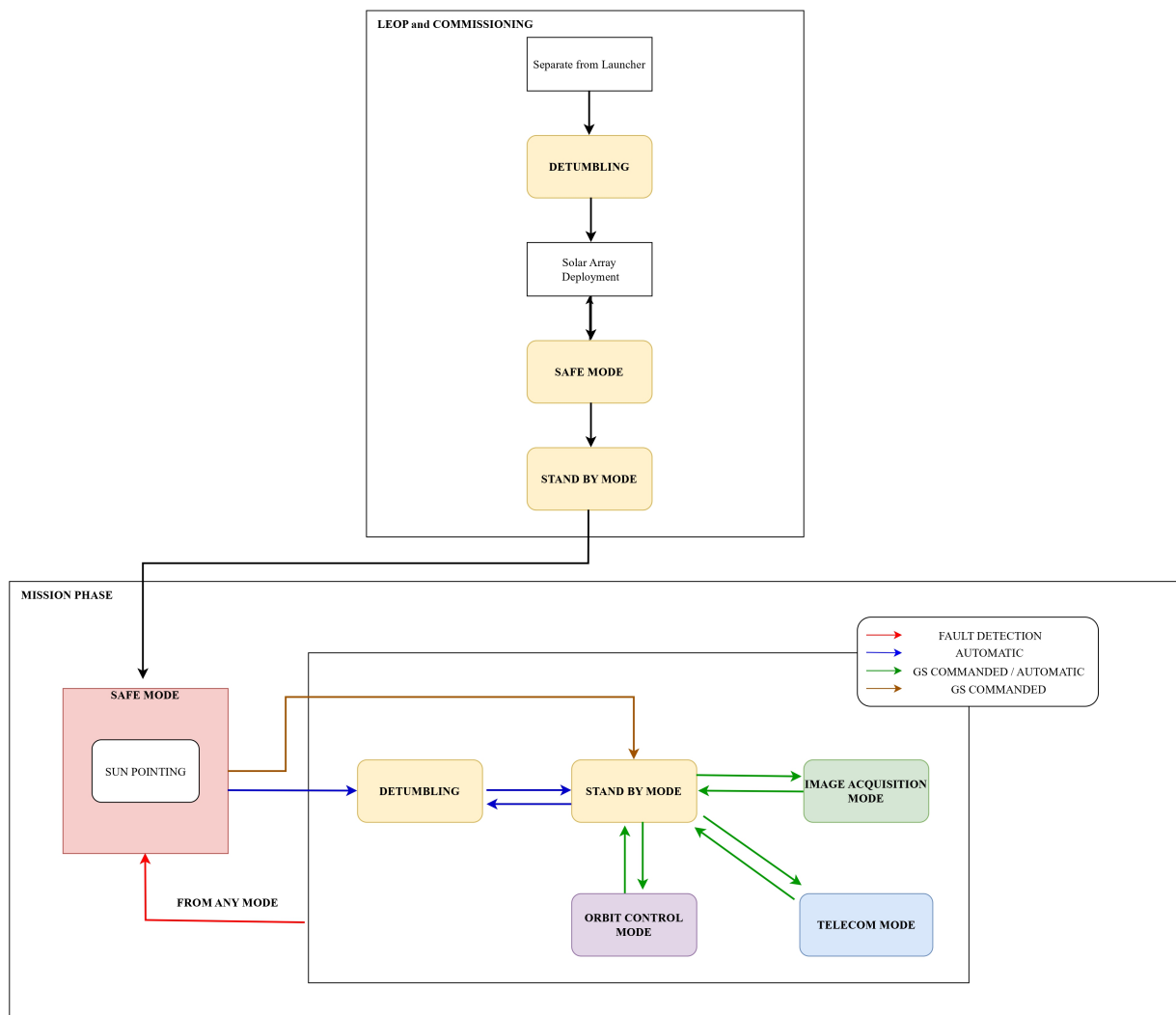


Figure 66: ADCS mode transitioning logic.

13.4 Disturbances Analysis and Hardware Sizing

To appropriately size the actuators required for the ADCS subsystem, the first step is to assess the magnitude of the disturbances the spacecraft will encounter in orbit. As HORUS is an Earth observation satellite, the disturbances remain relatively constant throughout all the different mission phases.

At the reference altitude of 270 km, the disturbances are shown in Figure 67 along with eclipse condition (gray background). Clearly, for torque calculations, the center of mass offset from the geometrical center plays a crucial role. From structural simulations, this value is less than 3cm on each axis.

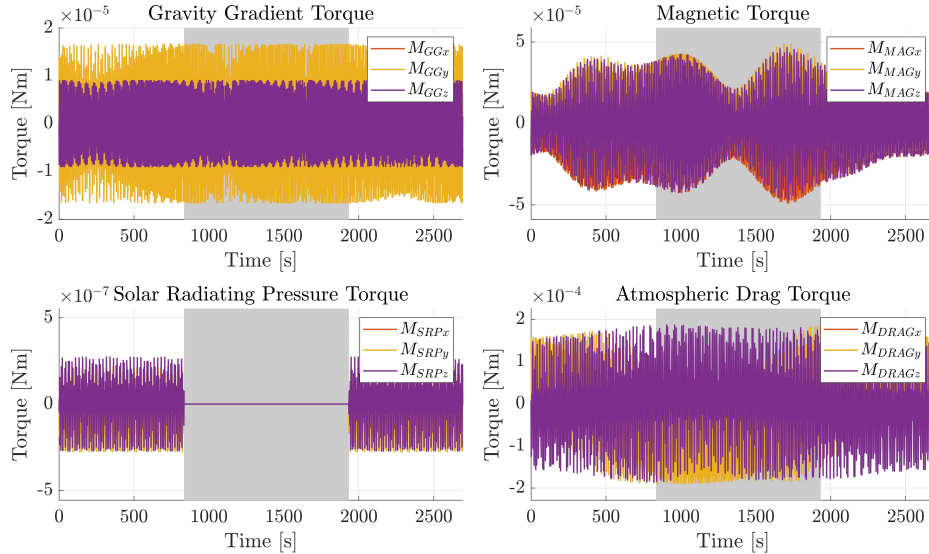


Figure 67: Disturbances acting on the spacecraft at 270 km altitude.

As illustrated in the figure, the primary contribution to disturbances comes from aerodynamic drag. This drag must be effectively counteracted using reaction wheels control and periodic station-keeping manoeuvres with thruster to prevent rapid orbital decay. The solar radiation pressure disturbance exhibits transients, during which it is temporarily absent due to the eclipse.

Considering the relatively high magnitude of the disturbances, these values are important for sizing the actuators, especially for all modes that require precise station keeping. To gain further insight into the problem, other simulations are performed. In Figure 68 the satellite is forced to stay in LVLH configuration, simulating imaging mode. The simulation lasts 3 orbits, during which the RW stored momentum increases. Therefore, to avoid wheel saturation in a very short time, the hardware selection shall be performed accordingly. In simpler terms, as the maximum angular momentum stored is approximately 1 Nms, the corresponding minimum value for the selected RW is 2 Nms. This choice ensures long-term pointing stability and decreases the desaturation maneuvers frequency.

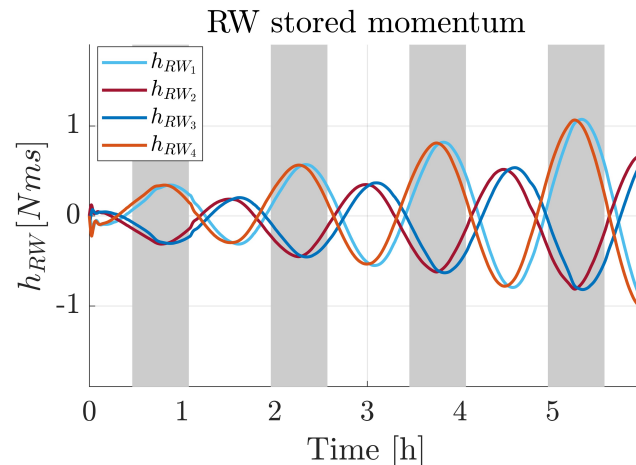


Figure 68: RW stored momentum for 3 orbits simulation

Then, the required slew maneuvers during the various mission modes have been analysed to determine the critical cases for actuator dimensioning. A summary of these maneuvers is provided in Table 43.

Mode	Slew Angle	Slew Time
SBM	A maximum slew of 45° is required to align with the Sun.	5 minutes
TM	A maximum slew of 45° is required to reorient the satellite toward the Earth.	The time constraint is determined by the minimum interval between target acquisition and the first contact with the ground station.
IM	A maximum slew of 45° is required to aim the satellite at the target, assuming the most critical condition.	The slew time is [TBD] seconds, based on the minimum interval between the beginning of the mode and the expected epoch in which the images have to be taken.
OCM	A maximum slew of 180° is needed to reverse the satellite direction during phasing maneuvers, ensuring the thruster points in the correct direction to complete the phasing.	The slew time is [TBD] seconds, determined by the period of the phasing orbit.

Table 43: Required Slew Angles and Times for Different Operational Modes

13.5 Navigation Solutions

HORUS is a high-resolution imaging mission with several constraints. Those arise from the tight requirements regarding power generation, thermal dissipation, telecommunication, and payload resolution. Therefore, having a reliable and accurate navigation solution is of utmost importance. Since AKE varies from 5° during telecom to 0.01° during imaging, three solutions are selected according to the accuracy required, the available sensors, and the computational cost required.

Precise pointing - Star sensors

The most demanding modes, from pointing accuracy point of view, are Imaging Mode (IM) and Orbit Control Mode (OCM). The only sensors capable of fulfilling these tight requirements are the star sensors. Therefore, during these modes, the attitude is retrieved directly from star sensors measurements, solving the **Wahba Problem**. This solution is highly reliable and accurate and does not require measurements from Sun sensors or magnetometers. Indeed, since they are less accurate with respect to the star sensors, they do not improve navigation estimate. The estimation errors in terms of Euler angles are reported in Figure 69 for half orbit. From the graph, the 0.01° requirement is respected.

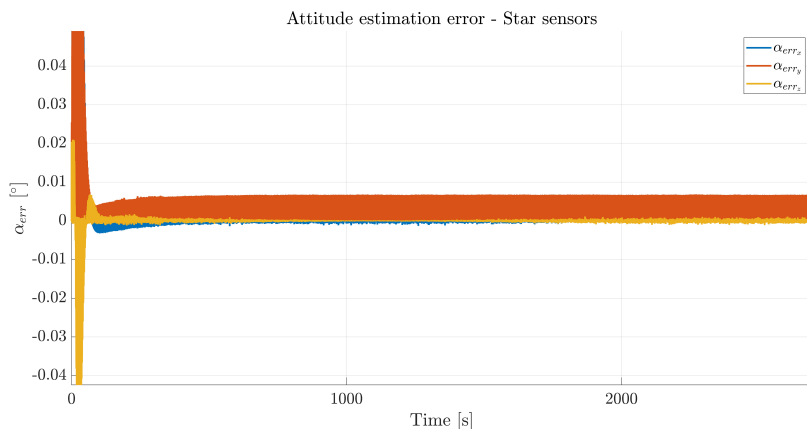


Figure 69: Attitude estimation error solving Wahba problem with star sensors measurements

Coarse pointing - High complexity MEKF solution

The need to implement a Multiplicative Extended Kalman Filter (MEKF) for satellite attitude estimation arises from several reasons. During Stand-By and Telecom modes the pointing requirements are more relaxed in comparison to Imaging and Orbit Control mode. Therefore, using star sensors is not worthwhile, while merging Sun sensors, magnetometer, and gyros measurements is a smarter choice. However, attitude computation via static methods is not as precise as the requirements dictate. Moreover, Telecom mode requires 10° pointing accuracy also during eclipses, where Sun sensors measurements are unavailable. Here comes the need to implement a filter merging Sun sensors, magnetometer, and gyro measures to compute satellite attitude and angular velocity. Moreover, the filter shall adapt from sunlight and eclipse conditions according to Sun sensors availability.

The filter selected is a MEKF due to its reliability, flight heritage, and high performance. This filter is preferred to the simpler Additive Extended Kalman Filter for two reasons. The Multiplicative filter entails quaternion normalization, while its Additive alternative needs to set it numerically. Moreover, this filter has a reduced size state. The Additive filter employs the full quaternion (4 elements) for the attitude part of the state, while the Multiplicative filter selected needs just the vector $\mathbf{a} = 4\delta\mathbf{p}$ which has only 3 elements (In the formula, \mathbf{p} are the Modified Rodriguez Parameters). Eventually, the Multiplicative filter estimates only the local error quaternion, while the global attitude of the satellite is set externally. A brief explanation of the filter is here reported for the sake of completeness, for full formulation refers to "Fundamentals of Spacecraft Attitude Determination and Control - Markley, Crassidis" [83].

The state \mathbf{x} of the MEKF selected has two parts, the attitude part and the angular velocity part. The attitude part is made by the vector \mathbf{a} defined above, while the second part is directly the angular velocity estimate. Initially, the filter state undergoes a reset: the attitude part (corresponding to the initial attitude error) is zero, while the angular velocity part is its estimate. Then Kalman gain is computed using the measurements sensitivity matrix and sensors uncertainty. The gain is employed together with the predicted measurements to compute the "a posteriori" state. The updated local state modifies the global attitude and angular velocity estimate. Eventually, the filter state is propagated until the next time step. The sensitivity matrix H_k and the predicted measurements are computed as:

$$H_k(\hat{\mathbf{x}}_k^-) = \begin{bmatrix} [A(\hat{\mathbf{x}}_k^-)\mathbf{S}_N \times]_1 & 0_3 \\ \vdots & \vdots \\ [A(\hat{\mathbf{x}}_k^-)\mathbf{S}_N \times]_{n_{SS}} & 0_3 \\ [A(\hat{\mathbf{x}}_k^-)\mathbf{B}_N \times] & 0_3 \\ 0_3 & I_3 \end{bmatrix} \quad \mathbf{h}_k(\hat{\mathbf{x}}_k^-) = \begin{bmatrix} A(\hat{\mathbf{x}}_k^-)\mathbf{S}_N \\ \vdots \\ A(\hat{\mathbf{x}}_k^-)\mathbf{S}_N \\ A(\hat{\mathbf{x}}_k^-)\mathbf{B}_N \\ \hat{\mathbf{w}}_k^- \end{bmatrix}$$

Where $A(\hat{\mathbf{x}}_k^-)$ is the direct cosines matrix computed at time t_k , \mathbf{S}_N and \mathbf{B}_N are the Sun and the magnetic field vectors in the inertial frame, and n_{SS} is the number of available Sun sensors. The filter pseudo-code is reported below.

Algorithm 1 Multiplicative Extended Kalman Filter (MEKF)

Require: $\mathbf{q}_k^-, \mathbf{w}_k^-, P_k^-, \mathbf{y}_k, \mathbf{S}_N, \mathbf{B}_N$

Ensure: $\mathbf{q}_k^+, \mathbf{w}_k^+, P_k^+, \mathbf{q}_{k+1}^-, \mathbf{w}_{k+1}^-, P_{k+1}^-$

1: **Initialize Filter State**

2: $\mathbf{x}_k^- = [0, 0, 0, \mathbf{w}_k^-]$

3: **Compute Kalman Gain**

4: $K_k = P_k^- H_k^{-T} (H_k^- P_k^- H_k^{-T} + R_k)^{-1}$

5: **Update Local Filter State**

6: Compute predicted measurements \mathbf{h}_k^-

7: $\mathbf{x}_k^+ = \mathbf{x}_k^- + K_k(\mathbf{y}_k - \mathbf{h}_k^-)$

8: $P_k^+ = (I_6 - K_k H_k^-) P_k^-$

9: **Update Global Attitude and Angular Velocity**

10: Compute attitude error quaternion \mathbf{q}_{error} from \mathbf{x}_k^+

11: $\mathbf{q}_k^+ = \mathbf{q}_{error} \otimes \mathbf{q}_k^-$

12: $\mathbf{w}_k^+ = \mathbf{x}_k^+(4 : 6)$

13: **Propagate State and Covariance**

14: Compute next state $\mathbf{q}_{k+1}^-, \mathbf{w}_{k+1}^-, P_{k+1}^-$ propagating filter state and covariance

15: **return** $\mathbf{q}_k^+, \mathbf{w}_k^+, P_k^+, \mathbf{q}_{k+1}^-, \mathbf{w}_{k+1}^-, P_{k+1}^-$

Once the algorithm is completed, the filter is implemented in Simulink[©] environment. The performance of this solution is reported in terms of Euler angles in Figure 70 simulating Stand-By mode for half orbit. Clearly, the 2° requirement is respected.

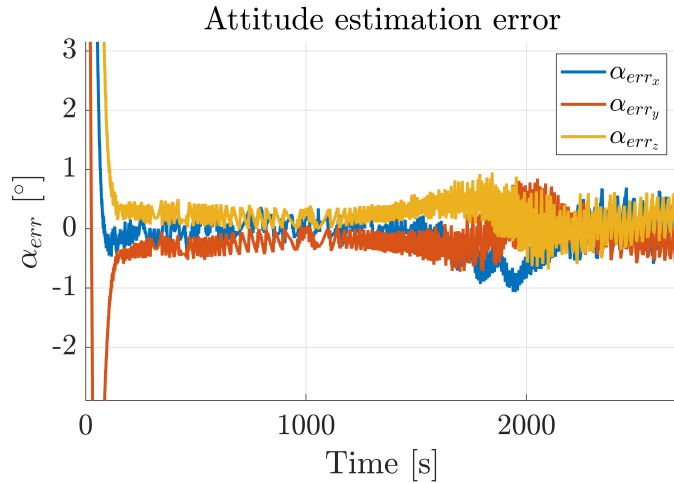


Figure 70: MEKF estimation performance during Stand-By mode

Coarse pointing - Low complexity Wahba problem solution

During Safe, Activation mode, and Detumbling the pointing requirements are very low because, in the first two, only EPS is constraining the satellite to a rough Sun pointing, while in Detumbling there are no pointing requirements at all. Therefore, employing MEKF is not required, and a more simple algorithm such as Wahba problem solution becomes more suitable. Moreover, the filter is much more complex and computationally expensive, while using a lower complexity solution helps to reduce power consumption and OBC effort. Therefore, during these modes, Sun sensors and magnetometer measurements are used to retrieve satellite attitude, with fair performances.

13.6 ADCS Performances

In this section, all modes are analysed in terms of guidance, navigation, and control solutions to assess the system performance.

13.6.1 Detumbling mode

The purpose of detumbling mode is to reduce S/C angular velocity. The satellite enters this mode immediately after its release in orbit, and each time that $\omega > 3^\circ/s$ [TBC]. During this mode, magnetorquers are switched on to decrease angular velocity according to the classic B-dot algorithm. Since the inertia about the z-axis is the highest, dumping out its angular velocity is not trivial and leads to a very high convergence time. To speed up the convergence, RW is employed to slow down ω_z as soon as it drops below $3^\circ/s$. The threshold is set to balance the convergence time of the mode and the final angular momentum stored by the reaction wheels. During this mode, gyros are employed to measure angular velocity, while approximated attitude determination is roughly performed with Sun sensors and magnetometer. The performances of the control are reported below. The initial conditions of the simulation are a random attitude and a prescribed angular velocity of $20^\circ/s$, about each axis. The angular velocity value is quite an extreme case but is used to test the goodness of the selected solution. The mode is completed as the angular velocity over all the axes drops below $0.3^\circ/s$, to allow star sensor usage. In the simulation reported in Figure 71, the mode is completed in less than 3 hours.

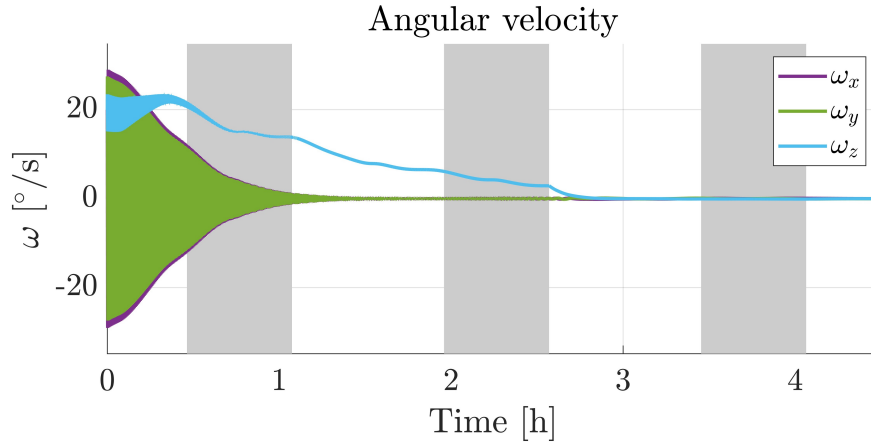


Figure 71: Angular velocity behavior during detumbling

13.6.2 Telecom mode

During this mode, a rough Earth pointing is performed to point the $-z$ patch antenna toward the ground. The accuracy of the pointing is relaxed but, since telecommunication has to be performed also in eclipse, MEKF is employed to perform attitude determination. The more relaxed accuracy request is reflected by the way in a minor RW usage. That is, the effort required by the reaction wheels is reduced, giving priority to power consumption. A Linear Quadratic Regulator (LQR) control has been selected to answer both attitude, angular velocity, and minor power consumption requirements. The guidance of the mode depends on the scenario, indeed Telecom could be performed after Imaging or Standy-By mode. In both cases, the final satellite attitude shall be the LVLH, but the initial offset depends on the initial condition. Since in all these modes, the satellite has always the x-axis aligned with the velocity vector, in both cases only a slew about the roll axis is required. However, if telecom is performed right after imaging, the satellite is already Earth pointing; on the other hand, if telecom starts after Stand-By mode, the maximum slew angle is 45° , corresponding to the orbit with $\beta = 90^\circ$ ². The testing of the mode reflects these two scenarios, and the performances are reported in Figure 72 for the first case and in Figure 73 for the second case. In the first case, since the satellite already has the proper orientation, the mode requirement is immediately fulfilled. Instead in the second case, the control reduces the angular error below the threshold after the first short transient, according to the requests.

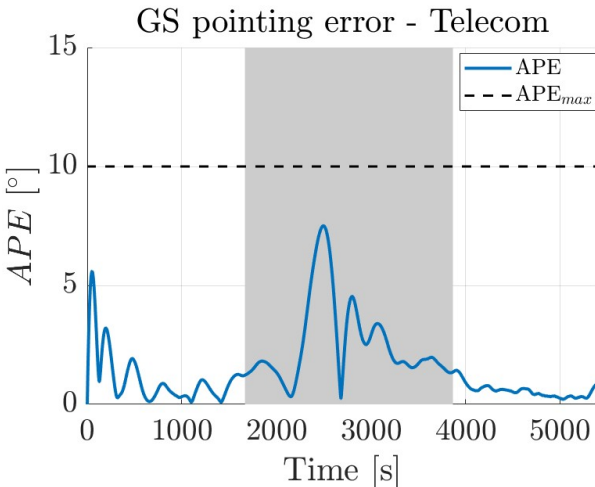


Figure 72: APE, telecom after imaging

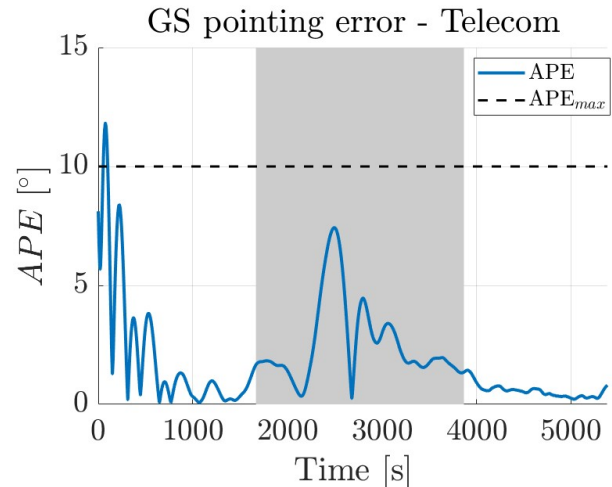


Figure 73: APE, telecom after Stand-By

13.6.3 Stand-By mode

Stand-By mode is performed for most of the satellite lifetime and is the backup mode in which the satellite enters before starting each of its nominal operations. During this mode, the idea is to maximize power production without increasing the cross-section. The problem is solved by performing a slew about the

² β is the angle between the Sun direction and the orbital plane.

roll axis to maximize the area facing the Sun but always having the same cross-section. The slew angle is changing slowly with time, and therefore it is updated on a daily basis. Since Sun pointing is expected only during sunlight, Sun sensors, magnetometer, and gyros are enough to retrieve satellite attitude. However, a very effective and reliable navigation filter, such as the MEKF, is required to satisfy the tight 4° accuracy requirement during sunlight. Regarding the control, an effective LQR is selected, whose performance, in terms of angular error and actuator usage, is reported in Figure 74 and Figure 75 for a 4-orbit simulation.

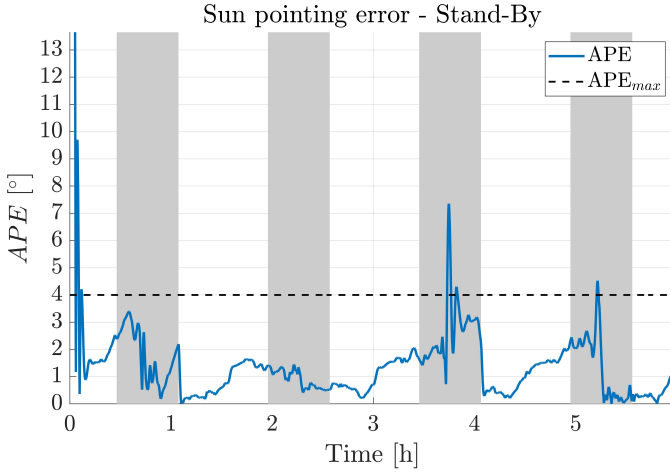


Figure 74: APE during Stand-By

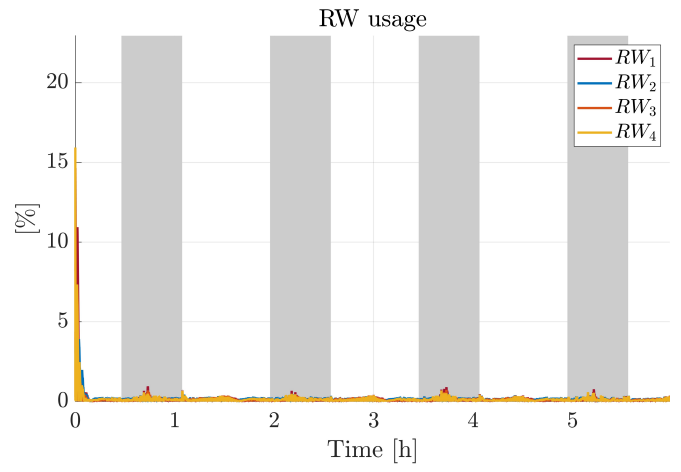


Figure 75: RW usage during Stand-By

13.6.4 Imaging mode

This is the most critical and demanding ADCS mode both from angular error and attitude estimation point of view. Therefore, to meet those tight requirements, star sensors and reaction wheels are employed. During this mode, the satellite is reoriented to point the PL toward the Earth with an initial offset from the nadir dictated by the Stand-By mode orientation. Since the offset allowed from the nadir direction is very small, a powerful Linear Quadratic Integral (LQI) control is implemented. The integral part of the control aims to reduce the bias at steady state that arose with the simpler LQR solution. The control performance in terms of angular error is reported in Figure 76. After approximately 7 minutes, the convergence is reached and the satellite is ready to operate the payload properly.

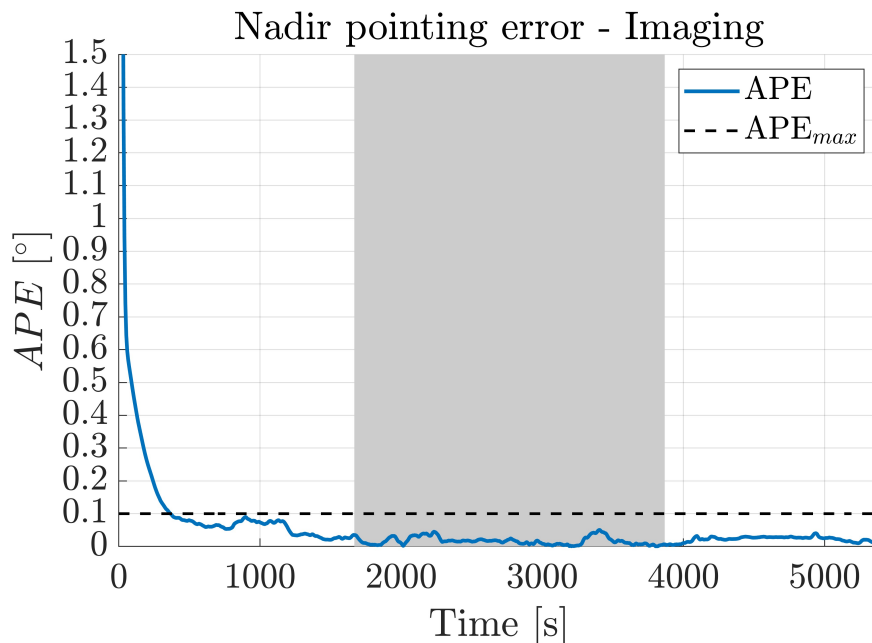


Figure 76: APE during imaging mode

14 Thermal Control Subsystem

The Thermal Control Subsystem (TCS) is responsible for maintaining spacecraft components within their allowable temperature ranges throughout the mission. For the HORUS mission, accurately sizing and designing the TCS is critical to ensure operational conditions are maintained across various phases and modes, even under harsh environmental conditions from a thermal point of view.

14.1 Preliminary considerations

Due to the criticality of the TCS for the HORUS mission, it is fundamental, before starting the mononodal and multinodal analyses, to conduct an initial evaluation of the spacecraft operational temperature ranges and internal dissipations.

14.1.1 Operational and Non-Operational temperature ranges

Regarding the specific hardware of the S/C, research was made to define, if necessary with a certain degree of conservatism, the required temperature ranges. These were divided into operational, survival and storage temperature ranges. An overview of the acquired data is showcased in Table 45. The reference temperature ranges were identified and selected based on specific component datasheets or scientific publications. For components without reference temperatures reported in the respective datasheets, data were taken from analogous components after appropriate considerations. An example of such a case is the payload: no specific operational temperature ranges were found for the component and, for this reason, the data of a similar camera (specifically infrared due to the higher sensitivity in terms of temperature) was used [84]. It is important to note that a conservative approach was adopted when defining temperature ranges. If specific temperature limits for a given category were unavailable, the limits from a stricter category, deemed more critical for the mission, were applied. For instance, if the operational temperature range of a component was known but the survival range was not, the survival range was assumed to coincide with the operational range in our analyses.

14.1.2 Hardware thermal dissipations

In terms of heat dissipations given by the various components of the spacecraft, an analysis was conducted based on the different operational modes. In Table 44 can be seen the internal dissipations of the spacecraft during the different mission modes, subdivided into subsystems. These are subdivided into mission subsystems and were retrieved from the EPS power budget, assuming complete transformation of electric power into heat for most components. Some cases, however, required additional computations, as was the case for the S/C battery, which required both charge efficiency data and Joule heating effects to be considered in order to estimate the power directly dissipated as heat (computations performed using cell datasheet and similar Li-Ion cell documents [82][85]). For the spacecraft solar cells, on the other hand, dissipated heat is estimated dynamically based on the solar flux seen by the components in each moment of time considering their efficiency.

Subsystem	Stand-by [W]	Safe [W]	Orbit Control [W]	Imaging [W]	Telecom [W]	Activation [W]
ADCS	8.30	2.70	19.04	20.30	6.25	9.50
PS	13.57	13.57	174.90	13.57	13.57	26.88
EPS	53.85	51.24	72.26	55.16	61.38	56.3
TCS	1.93	2.42	1.93	1.93	1.93	1.93
TTMTC	6.83	3.15	6.83	2.84	36.54	11.29
STR	0.69	0.69	0.69	0.69	0.69	1.69
OBDH	4.97	4.97	4.97	6.96	4.97	4.97
Payload	0	0	0	6.4	0	3.2
Total Sum	90.14	78.74	280.62	107.85	125.33	115.76

Table 44: System and subsystem level heat dissipations of HORUS for the different operational modes

HORUS Temperature Limits						
Component	Min. Stor.	Min. Surv.	Min. Oper.	Max. Oper.	Max. Surv.	Max. Stor.
ADCS [86][87][88][89][90][91][92]						
Star Tracker	-35°C	-35°C	-35°C	+65°C	+70°C	+70°C
Sun Sensor	-30°C	-30°C	-30°C	+85°C	+85°C	+85°C
GNSS	-55°C	-40°C	-40°C	+85°C	+85°C	+95°C
Gyroscope	-40°C	-40°C	-40°C	+85°C	+85°C	+85°C
Magnetometer	-55°C	-40°C	-40°C	+85°C	+85°C	+125°C
Magnetorquer	-45°C	-45°C	-45°C	+45°C	+45°C	+45°C
Reaction Wheel	-40°C	-20°C	-20°C	+70°C	+70°C	+80°C
PS [93][94][95]						
Thruster	-20°C	-20°C	-20°C	+110°C	+110°C	+110°C
Low-pres. Sol. Valv.	-20°C	-20°C	-20°C	+100°C	+100°C	+100°C
High-pres. Sol. Valv.	-20°C	-20°C	-20°C	+100°C	+100°C	+100°C
Press. Senors	-40°C	-40°C	-40°C	+150°C	+150°C	+150°C
PPU	-50°C	-50°C	-35°C	+80°C	+100°C	+100°C
TCS [96][97]						
Heat Switches	-130°C	-130°C	-130°C	+100°C	+100°C	+100°C
Thermal sensors	-269°C	-269°C	-269°C	+400°C	+400°C	+400°C
TTMTC [98][99][67][100]						
Transmitter	-20°C	-20°C	-20°C	+60°C	+60°C	+60°C
Receiver	-20°C	-20°C	-20°C	+60°C	+60°C	+60°C
Antenna	-40°C	-40°C	-40°C	+85°C	+85°C	+85°C
Patch Ant. + Amp.	-40°C	-40°C	-40°C	+85°C	+85°C	+85°C
Structure [101][102]						
Main body	-250°C	-250°C	-250°C	+150°C	+150°C	+150°C
Aero-appendices	-250°C	-250°C	-250°C	+150°C	+150°C	+150°C
FBG sensor system	-250°C	-250°C	-250°C	+800°C	+800°C	+800°C
Acoustic Sensors	-50°C	-50°C	-50°C	+100°C	+100°C	+100°C
OBDH [103][104]						
NanoMind HP MK3	-40°C	-40°C	-40°C	+50°C	+85°C	+85°C
NanoMind A3200	-30°C	-30°C	-30°C	+85°C	+85°C	+85°C
Payload [84]						
iSim90	-10°C	-10°C	-10°C	+40°C	+40°C	+40°C
EPS [17][82]						
Battery	0°C	0°C	0°C	+45°C	+45°C	+45°C
Solar Cells	-200°C	-200°C	-150°C	+110°C	+130°C	+130°C
PCDU	-40°C	-40°C	-30°C	+60°C	+70°C	+70°C

Table 45: Operational, survival and storage temperature ranges for each of the components and subsystems of the S/C, no margins applied

14.2 Worst hot and cold cases

For a proper thermal analysis and thermal control design to be made, it is crucial to size the system in the worst hot and cold case scenarios. These have to be identified in terms of encountered heat fluxes, which mostly depend on the S/C orbit, and internal dissipations, which vary based on the operational mode.

For the HORUS mission, in orbital terms different combinations of dates and RAANs were analyzed to identify two worst case orbits for eclipse duration and overall solar flux strength. Moreover, in terms of total internal dissipations, the data shown in Table 44 was utilized, selecting the Orbit control mode for the worst hot case and the Safe mode for the worst cold scenario.

In Table 46 are summarized the parameters that identify the thermally relevant worst case scenarios. As can be seen, the selection was made taking into account the eclipse duration (if present) for the selected orbits, attempting to minimize that of the hot orbit and to maximize that of the cold scenario.

	Date [dd/mm/yr]	RAAN [deg]	Operat. mode	Eclipse duration
Worst Hot	06/02/29	50	Orbit control	//
Worst Cold	20/03/29	0	Safe	$\sim 37\text{ min}$

Table 46: Parameters of the worst hot and cold orbits

As can be seen from Section 14.2, the hot case orbit is characterized by two periods throughout the year without eclipse, given by the extreme values assumed by the beta angles, which come up to approximately 74.32° . Considering cases such as these, for the hot case analysis is fundamental to make sure that the S/C can withstand continuous external heat fluxes, sizing the radiators and overall TCS accordingly. The cold case orbit, on the other hand, is characterized by eclipse periods throughout the whole year and, as such, the orbit with the longest eclipse period was considered for the cold case sizing, with a beta angle of 8.77° . Moreover, the RAANs of the two orbits were also chosen taking into account, especially for the hot case orbit, the value of the incoming solar flux: the orbits were selected trying to maximize for the hot case and minimize for the cold scenario the value assumed by the solar flux, which varies throughout the year.

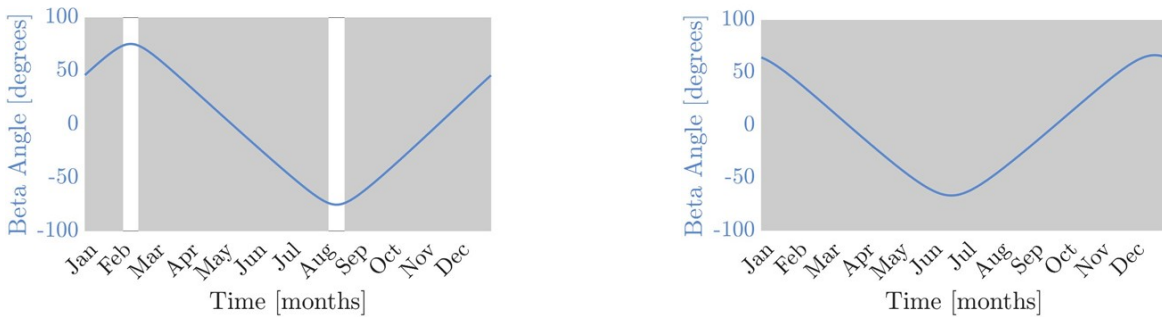


Figure 77: Evolutions of the beta angles for the worst case orbits, with grey strips indicating eclipse periods for the S/C (left: hot case, right: cold case)

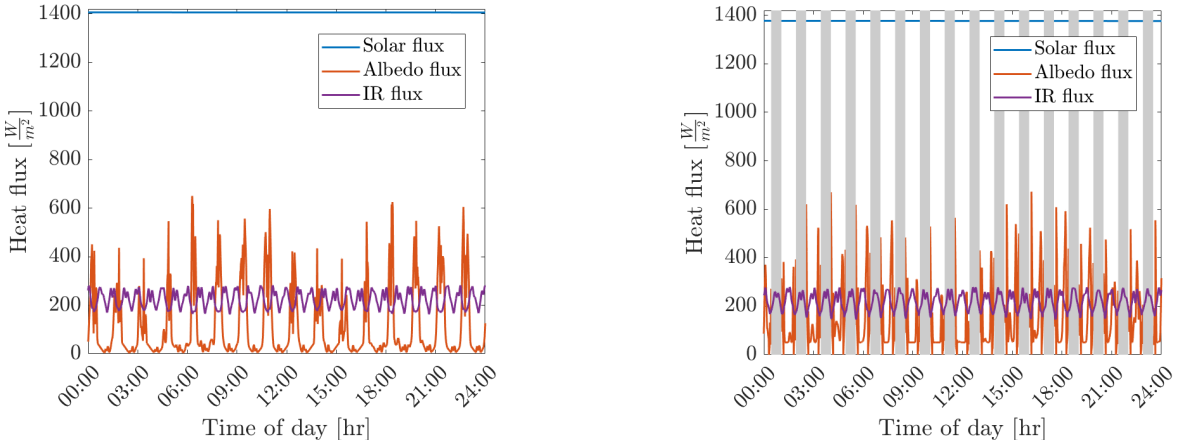


Figure 78: Evolutions of the environmental fluxes throughout a day for the hot case and cold case orbits, with grey strips indicating eclipse periods for the S/C (left: hot case, right: cold case)

Given the different heat fluxes and loads encountered in the two orbits, for the hot case, the steady state thermal equilibrium equation is:

$$Q_{sun} + Q_{IR} + Q_{albedo} + Q_{int.} = 0$$

For the cold case, on the other hand, it is given, due to the absence of daylight, by:

$$Q_{IR} + Q_{int.} = 0$$

The data associated to the heat fluxes and loads encountered in the two worst cases is represented in Table 47.

	$q_{\text{solar}} \left[\frac{\text{W}}{\text{m}^2} \right]$	$q_{\text{albedo}} \left[\frac{\text{W}}{\text{m}^2} \right]$	$q_{\text{IR}} \left[\frac{\text{W}}{\text{m}^2} \right]$	$Q_{\text{internal}} [\text{W}]$
Worst Hot	1405.90	650.18	152.60	280.62
Worst Cold	//	//	145.42	78.74

Table 47: Heat fluxes and thermal loads encountered in the worst hot and cold scenarios

As can be seen, the encountered loads vary greatly and, for the hot case, the albedo flux can be significant. It must be noted, however, that the scenarios refer to worst cases also considering the specific sections of the Earth surface seen by the satellite and varying Earth surface properties. Moreover, it must be remembered that the real behavior of the spacecraft from a thermal point of view is transient, translating to lower maximum temperatures and higher minimum ones, especially considering the relatively short orbital periods for the mission. After considering the presented factors, a passive thermal control system is proposed for HORUS, designed with adaptability and flexibility to accommodate the thermal environment at each stage of the mission. Mononodal and multinodal analyses of the spacecraft are conducted to create and validate the proposed design.

14.3 Mononodal Analysis

To identify and quantify possible solutions for thermal control, it is good norm to start by conducting a steady-state mononodal analysis. In particular, a spherical node was considered, defining its operational temperature ranges, its surface optical parameters and external surface area and cross area.

Regarding the operational temperature ranges for the single node, the most stringent temperature limits of the critical subsystems (all excluding STR and TCS) listed in Table 45 were averaged, and the resulting values were used to define the temperature limits of the spherical node. It must be noted that, in accordance with ECSS-E-10-03-A, a 15 K margin was applied on the temperatures as shown in Table 48.

	Min. T Surv.	Min. T Operat.	Max. T Operat.	Max. T Surv.
Node Limits	-15°C	-15°C	+51.7°C	+60.8°C
With Margins	0°C	0°C	+36.7°C	+45.8°C

Table 48: Operational and survival temperature ranges for the single spherical node, both without margins and with ECSS margins

After having computed an external surface area of 1.17 m^2 and a cross section area of 0.33 m^2 , a sensitivity analysis was conducted to obtain the best combination of absorptivity and emissivity to utilize for the node. The results of the sensitivity analysis can be seen in Figure 79.

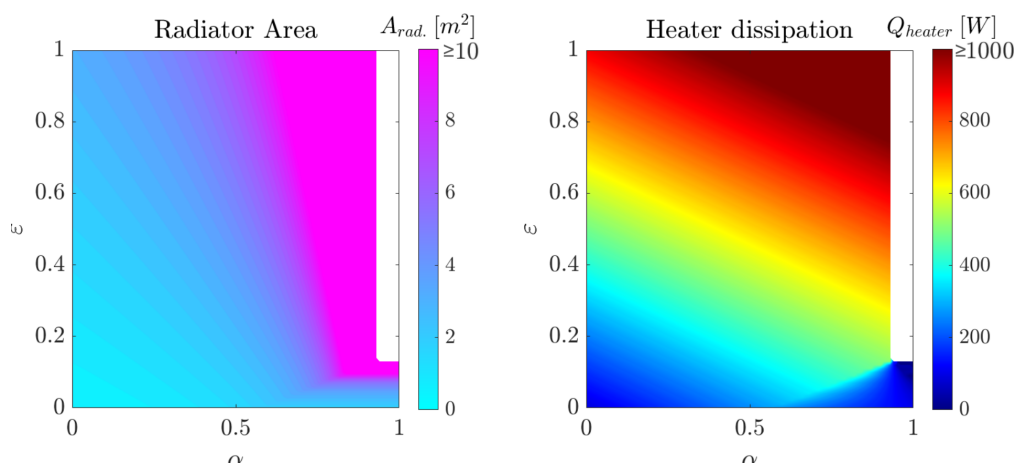


Figure 79: Mononodal analysis results in terms of total radiator surface area and heater dissipations with varying absorptivity and emissivity

Generally speaking, lower radiator areas and lower heater dissipations are obtained for lower absorptivities and emissivities applied to the external surface of the main body. In the two graphs presented in Figure 79, certain regions lack data due to unusable values (e.g., negative radiator areas). For practical reasons, the optical properties of Vapor Deposited Aluminum were utilized and used as reference parameters for the analyses (EoL: $\alpha = 0.38$, $\varepsilon = 0.02$, see Table 11, Optical Solar Reflector degradation after 1.5 years taken as reference), obtaining an overall radiator area of $A_{rad} = 1.63 m^2$ and a heater dissipation in the worst cold case of $Q_{heater} = 399.11 W$. It must be noted that special attention was paid in making sure that the system heaters did not activate during the mononodal simulations in daylight conditions, which is not always the case for analyses performed with very low absorptivities.

The heater dissipations obtained with the mononodal, steady state analysis are high. The same can be said for the total radiator area, which is high with respect to the HORUS S/C dimensions, exceeding the available surfaces of the main spacecraft body. A transient multinodal analysis is performed maximizing radiator surfaces and attempting to isolate the S/C body and internal components as much as possible.

14.4 Multinodal Analysis

Following the single node analysis, discretizations are done in order to more accurately determine thermal control solutions to be adopted for the mission.

A set of 14 nodes are defined considering the overall criticality of components and the need to improve the accuracy of thermal behavior predictions, such as more realistically modeling heat exchange between physical parts of the spacecraft. These are the two Lateral Solar Assembly nodes (mainly solar cells, PCBs and related electronics), the two Body Mounted Solar Assembly nodes, the two Lateral Radiator nodes, the four Body Mounted Radiator nodes, the Main Body, the Battery, the Payload and the Tanks. Figure 80 showcases a commented image to help visualize the layout of the external thermal nodes.

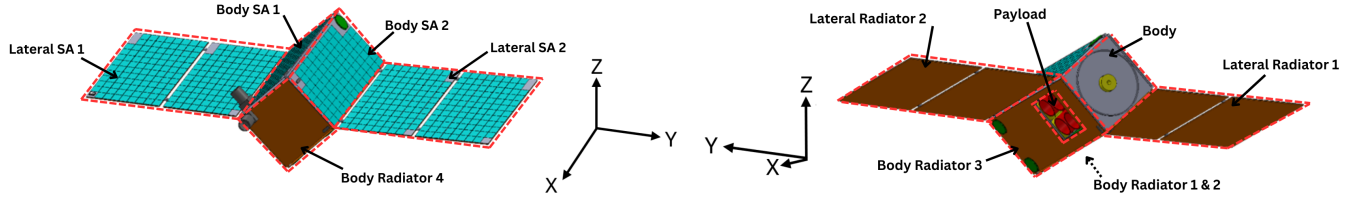


Figure 80: Graphical representation of the S/C thermal multinodal model nodes

It is important to note that, in the proposed analysis, the nodes do not necessarily correspond to individual components or macro-components. Instead, the primary objective is to ensure thermal representativeness of the actual S/C. For instance, the Lateral SA nodes encompass two actual SAs in the real spacecraft. Similarly, the Lateral Radiator nodes also account for the mass of the structural elements in each spacecraft wing. These considerations were made with thermal representativeness as the guiding principle. The properties of the different nodes are reported in Table 49.

	Mass [kg]	Heat Cap. [$\frac{\text{J}}{\text{kg K}}$]	α [-]	ϵ [-]
Main Body	26.63	961.20	int: 0.08 ext: 0.28	int: 0.02 ext: 0.02
Battery	7.50	1040.50	0.20	0.03
Payload	12.00	1075.00	0.1	0.04
Tanks	8.18	750	0.1	0.04
Lat. SA 1	0.52	600	0.62	0.85
Lat. SA 2	0.52	600	0.62	0.85
BM SA 1	0.22	600	0.62	0.85
Lat. Radiator 1	10.07	961.2	0.91	0.94
Lat. Radiator 2	10.07	961.2	0.91	0.94
BM Radiator 1	1.11	2700	0.91	0.94
BM Radiator 2	0.37	2700	0.91	0.94
BM Radiator 3	1.39	2700	0.91	0.94
BM Radiator 4	0.60	2700	0.91	0.94

Table 49: Masses, specific heat capacities, absorptivities, and emissivities of the nodes present in the multinodal thermal analysis

Most of the properties utilized for the thermal nodes were retrieved either from material databases such as the Granta database [105] or from the datasheets of the associated components or similar ones. The Batteries, Payload and Tanks were analyzed as separate nodes due to component criticality from a thermal point of view. The SAs and Radiators are represented by separate nodes to estimate their thermal behavior based on different interfaces between them and the spacecraft Main Body for the analysis iterations.

The operational and survival temperature ranges of the nodes are reported in Table 50, with a $\pm 15^\circ\text{C}$ margin to be considered for Phase A work.

	Min. Surv.	Min. Operat.	Max. Operat.	Max. Surv.
Main Body	-5°C	-5°C	+45°C	+45°C
Battery	+15°C	+15°C	+30°C	+30°C
Payload	+5°C	+5°C	+25°C	+25°C
Tanks	-5°C	-5°C	+65°C	+85°C
Lat. SA 1	-135°C	-135°C	+95°C	+95°C
Lat. SA 2	-135°C	-135°C	+95°C	+95°C
BM SA 1	-135°C	-135°C	+95°C	+95°C
BM SA 2	-135°C	-135°C	+95°C	+95°C
Lat. Radiator 1	-235°C	-235°C	+135°C	+135°C
Lat. Radiator 2	-235°C	-235°C	+135°C	+135°C
BM Radiator 1	-235°C	-235°C	+135°C	+135°C
BM Radiator 2	-235°C	-235°C	+135°C	+135°C
BM Radiator 3	-235°C	-235°C	+135°C	+135°C
BM Radiator 4	-235°C	-235°C	+135°C	+135°C

Table 50: Operational and survival temperature ranges of the multinodal thermal model nodes, with $\pm 15^\circ\text{C}$ according to ECSS standards

Dissipations of the different nodes were evaluated for the different modes. The values can be seen in Table 51.

	Orbit Control mode [W]	Safe mode [W]
Main Body	234.99	33.11
Battery	45.63	45.63
Payload	0	0
Tanks	0	0
Lat. SA 1	Computed Dynamically	Computed Dynamically
Lat. SA 2	Computed Dynamically	Computed Dynamically
BM SA 1	Computed Dynamically	Computed Dynamically
BM SA 2	Computed Dynamically	Computed Dynamically
Lat. Radiator 1	0	0
Lat. Radiator 2	0	0
BM Radiator 1	0	0
BM Radiator 2	0	0
BM Radiator 3	0	0
BM Radiator 4	0	0

Table 51: Multinodal analysis node dissipations for the hot and cold case scenario modes, respectively Orbit Control and Safe modes

For the multinodal, transient analysis, a Simulink/SimScape model is used. The simulations are run also taking into account the operational modes and their respective attitudes and pointing. The thermal resistances and radiative heat exchanges are estimated based on material properties and geometries. In Figure 81 can be seen the diagram of the multinodal model.

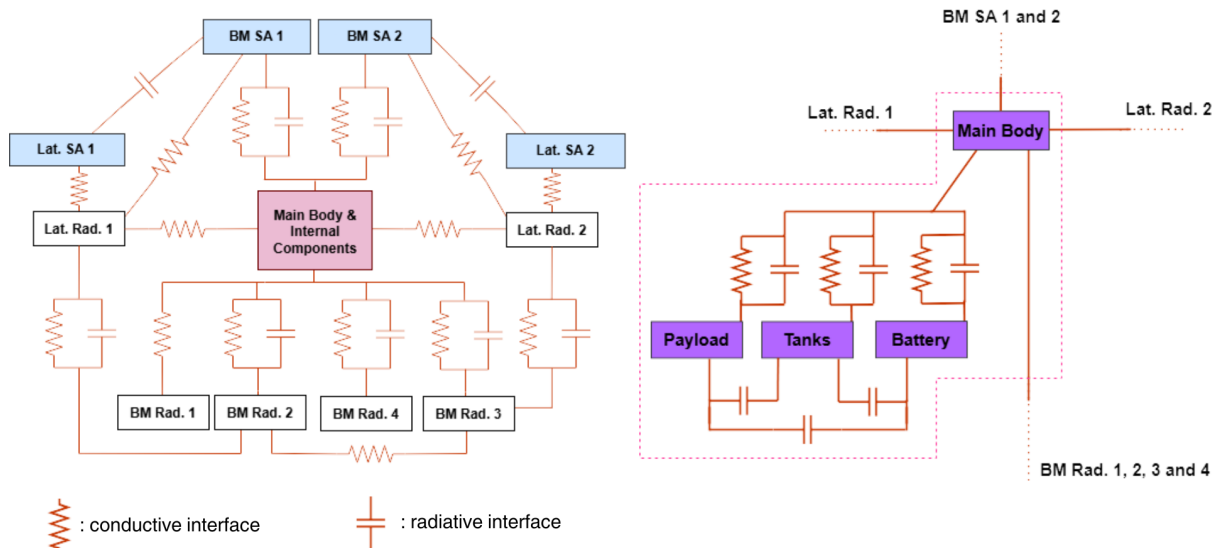


Figure 81: Diagram of the Simulink/SimScape thermal model (left: external nodes, right: internal nodes and Payload)

As can be seen from the presented diagram, within the multinodal model, conductive and radiative heat exchanges between the S/C nodes are simulated.

A distinction can be made between internal nodes and external nodes. The external nodes are entities which exchange heat with the rest of the S/C and with the environment. These are the SA nodes, the Radiator nodes, the Main Body and the Payload. When studying the thermal behavior of these nodes and the effect environmental fluxes have on them, it is important to monitor the Sun Aspect Angles and Earth Aspect Angles during all the simulations to accurately estimate the generated heat loads. Moreover, special attention was given, due to the configuration of the S/C, to properly calculate the view factors between the different nodes when valid. This was done primarily to estimate the radiative coefficients and exchanges occurring between the Lateral and BM Radiator nodes and the Lateral and BM SAs. Due to the

overall nature of the geometries, the view factors between adjacent surfaces were computed by discretizing the considered areas into differential elements and by adding the different radiative exchange contributions using a cross-string method, obtaining the total surface view factor and keeping in mind differences in dimensions. From this result, it is possible to compute the view factor of the other surface by inverting the simple relation $A_1 F_{1 \rightarrow 2} = A_2 F_{2 \rightarrow 1}$. Due to the symmetrical configuration of the satellite external body, the view factors between adjacent faces are identical for the elements listed previously. When computing the fluxes coming from the environment and dissipated by the S/C, computations were performed throughout the analyses to correctly estimate the view factors of all nodes and surfaces with respect to deep-space. This was done by studying the evolutions and relations between the Sun Aspect Angles and Earth Aspect Angles of each surface for each simulation step. Regarding the Payload node, the entity can be technically classified as an external node due to the interactions had with the outer environment through the Main Body aperture, even though heat exchanges characteristic of internal nodes are found.

The internal nodes of the HORUS multinodal thermal model are two: the Battery and the Tanks. It was decided to model these components as separate nodes both for thermal representativeness and due to their strict operational temperature ranges, which make it fundamental to characterize the components behavior to adopt, if necessary, tailored thermal control solutions. The studied internal nodes exchange heat conductively and radiatively amongst themselves and with the Main Body node, which incorporates most of the components of the spacecraft and structure. For both internal and external nodes, the node dissipation, as well as the component mass and specific heat capacity are considered. The different heat inputs from the nodes in proximity, computed taking into account the respective view factors, as well as the environmental IR, solar and albedo fluxes for external nodes are taken into account for. Moreover, as stated earlier, the view factor with respect to deep-space is computed dynamically and utilized to compute the component dissipation to deep-space with a modified SimScape "Radiative Heat Transfer" block.

14.5 Specific Subsystem Hardware and Considerations

Within HORUS, hardware is implemented according to the TCS design in order to maintain the different components within operational ranges. Some of the utilized thermal control hardware is produced in-house, and most is constituted by COTS. Below are listed the components and elements used to obtain a nominally passive thermal design:

- Spacers** - Spacers are used as thermal insulators or connectors between components and have been widely employed to isolate the S/C body from the BM SAs, a necessity identified during preliminary analyses. Their size and materials are selected based on temperature requirements for the different components.

	N° of Units	Length [cm]	Radius [cm]	Location
Al 7075-T6 Type 1	8	1	1	Between Payload and Structure
Al 7075-T6 Type 2	8	1	0.5	Between Battery and Structure
PTFE	20	1	1	For ex., between BM SAs and Structure

Table 52: Descriptions of the spacers implemented for thermal control purposes inside the spacecraft

- Radiators** - Aluminum slabs coated in Martin Black Velvet paint are implemented in the design. Two are present for each lateral panel and 4 are mounted on the spacecraft body. To be more specific, of the body-mounted radiators, one can be connected or isolated from the spacecraft with a set of heat switches based on temperature needs.

	N° of Units	Size [m ²]	Thickness [mm]
Lateral Radiator	4	0.31	4
Body Radiator 1	1	0.20	2
Body Radiator 2 (with heat switches)	1	0.07	2
Body Radiator 3	1	0.26	2
Body Radiator 4 (frontal)	1	0.11	2

Table 53: Descriptions of the Martin Black Velvet coated, Aluminium 7075-T6 radiators found within HORUS

- **Thermal straps** - Aluminum thermal straps are employed to link the BM SAs to the lateral radiators and interconnect the radiators. Azimut Space thermal straps have been selected for HORUS due to the high degree of configurability allowed by the manufacturer [106]. In total, 20 are implemented which are 10 cm in length each.
- **Heat switches** - To help maintain the operational temperature ranges of the S/C internal components, heat switches are used to vary the conductive interface between the spacecraft body and frontal radiator. The thin-plate switches are passive, working with a measured temperature activation logic, and greatly inspired by the Sierra Space counterpart [107]. The devices regulate based on the Main Body temperature to maintain the Battery and Payload within their operational ranges. With a 2°C activation margin with respect to the two components ranges, analyses determined that the switches should open at 22.2°C and close at 11.4°C.

N° of Units	Conductance [$\frac{W}{m^2 \circ C}$]	Size [mm x mm]	Thickness [mm]
10	Closed: 607 Open: 7.8	25.4 x 25.4	8.13

Table 54: Specifications of the heat switches used within HORUS

- **Coatings, Surface Treatments and Tapes** - Surface treatments and tapes are used within the spacecraft to thermally isolate components. Martin Black Velvet coating is applied on radiative surfaces. The employed solutions in terms of modifications of optical parameters for spacecraft surfaces are shown in the table below.

	Absorptivity [-]	Emissivity [-]	Location
Vapor Deposited Aluminum	BoL: 0.08 EoL: 0.38	0.02	Outer and inner S/C Structure
Martin Black Velvet Paint	0.91	0.94	On the radiators
Aluminum Tape	0.1	0.04	Covering inner components, for ex. the Battery

Table 55: Surface treatments, coatings and tapes used within HORUS

- **Attitude Control** - During the mission, attitude control is used to help support the TCS, as is done, for example, in the hot case scenario. Depending on the spacecraft power needs and the orbit HORUS is positioned in a given moment, an off-set of up to 60° can be obtained in Sun-pointing modes.

Components which in the multinodal analysis may have been englobated in the Main Body are still studied and positioned so as to maintain operational temperature ranges. For example, in the configuration of the S/C, the PCDU is positioned close to the walls of the structure and the radiators so as to efficiently dissipate heat.

14.6 Multinodal Analysis Results

The results of the multinodal model analyses are found in Table 56, with a graphical overview of the maximum hot case temperatures and minimum cold case temperatures for each node in Figure 82 accompanied by a Phase A margined representation of each entity's operational temperature ranges.

Hot Case			Cold Case		
Node	Min. Temp. [°C]	Max. Temp. [°C]	Node	Min. Temp. [°C]	Max. Temp. [°C]
Main Body	+15.5	+21.6	Main Body	+13.2	+14.7
Battery	+21.2	+26.1	Battery	+18.8	+20.1
Payload	+15.5	+20.8	Payload	+13.2	+14.6
Tanks	+16.6	+17.6	Tanks	+14.4	+14.5
Lat. SA 1	+31.3	+57.4	Lat. SA 1	-22.8	+52.7
Lat. SA 2	+42.0	+72.3	Lat. SA 2	-17.4	+38.6
BM SA 1	+18.0	+62.6	BM SA 1	-28.3	+58.9
BM SA 2	+44.1	+70.8	BM SA 2	-19.3	+49.4
Lat. Rad. 1	+30.0	+53.4	Lat. Rad. 1	-22.6	+50.4
Lat. Rad. 2	+40.5	+71.4	Lat. Rad. 2	-17.2	+36.2
BM Rad. 1	+14.7	+20.7	BM Rad. 1	+12.4	+14.5
BM Rad. 2	+32.7	+57.9	BM Rad. 2	-22.3	+43.0
BM Rad. 3	+35.7	+66.8	BM Rad. 3	-21.26	+39.6
BM Rad. 4	+10.5	+16.0	BM Rad. 4	-73.4	-66.3

Table 56: System and subsystem level heat dissipations of HORUS for different operational modes (split view)

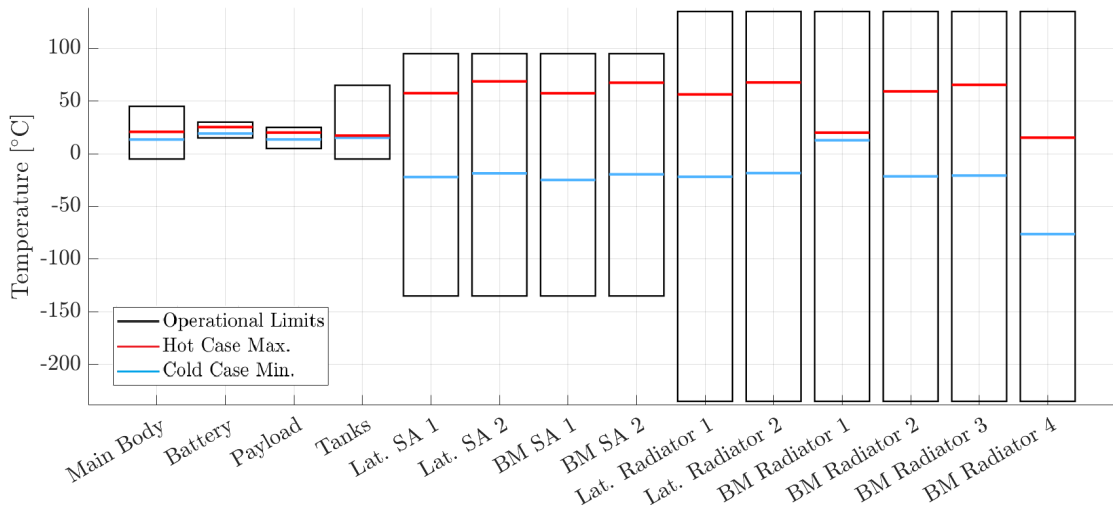


Figure 82: Maximum hot case temperatures and minimum cold case temperatures obtained for each node, with operational limits margined according to Phase A ECSS standards

As shown in Figure 82, the SAs successfully maintain operational temperature ranges, ensuring satisfactory power generation. The Main Body and internal components remain insulated due to the implemented thermal control solutions. To minimize temperature fluctuations in the Payload caused by the opening in the spacecraft body, a glass cover could be considered to enclose the aperture, avoiding undesired thermoelastic effects affecting the performances during the imaging mode. Proper material selection should account for potential degradation and discoloration effects to ensure long-term performance.

15 On-Board Data Handling

The On-Board Data Handling (OBDH) subsystem is responsible for managing data of the whole satellite. Key tasks include executing the FSW, processing and storing data from sensors and payloads, preparing data for downlink, and handling FDIR operations. This chapter focuses on the sizing and detailed design of the OBDH subsystem for the HORUS mission.

15.1 Computer System State Diagram

To effectively design the OBDH subsystem, it is essential to define its state diagram, which outlines the various states of the system and the transitions between them. While the OBDH is a subsystem that must remain operational for the whole mission duration, including an **Off** state is crucial to ensure that the system can handle unexpected shutdowns smoothly.

During mission operations, the system must be able to enter a safe state, represented in red in the Figure 83, to recover from failures. This process consists of two states: **error contingency** and **self-test**. If the failure is successfully resolved, the system transitions back to its previous state. However, if the failure cannot be recovered, the system will proceed to a shutdown state. The state diagram illustrating these transitions is shown in Figure 83.

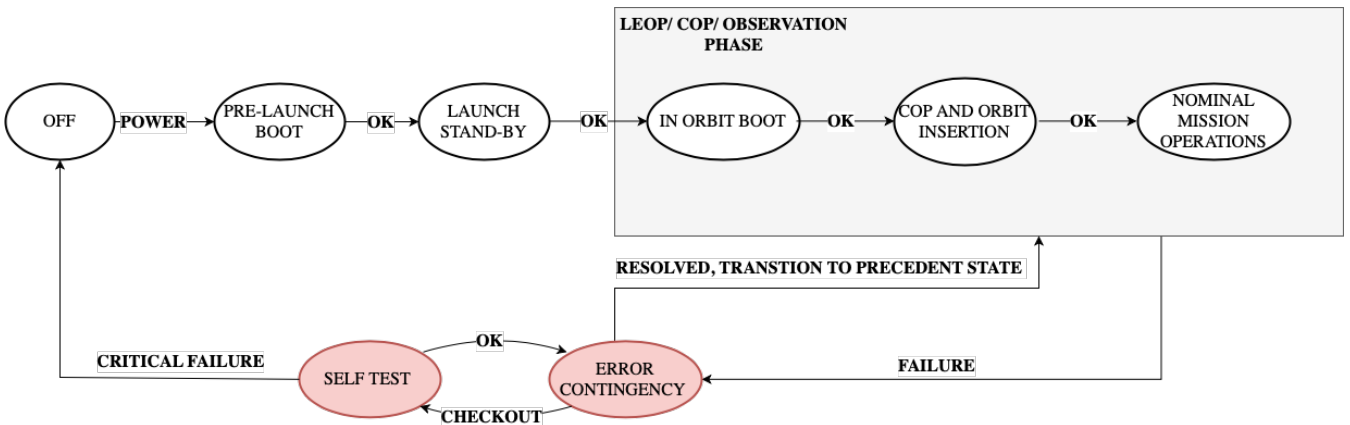


Figure 83: OBDH State Diagram

15.2 OBDH Preliminary Sizing

The selection of the OBC for the satellite is driven by a preliminary assessment of the computational power and memory requirements. This process involves identifying all the functionalities and components within each subsystem. Specifically, both hardware elements and software processes have been considered to estimate the necessary amount of code, data storage and the number of instructions per second (KIPS) the processor must execute. As detailed in Table 57, the values for code size, data size, typical KIPS and typical frequency have been sourced from literature [17]. The acquisition frequency generally aligns with typical values, with some specific adjustments. For example, the ADCS necessitates a higher acquisition frequency for its control hardware to ensure precise attitude control, requiring frequent updates. For the PS, the frequency of the control valves is set higher to enable frequent monitoring, which is critical especially during the OCM. It is worth noting that in this analysis the PLs have not been considered, due to the fact that they have their own CPU and mass memory.

Component	Nb	Code [words]	Data [words]	Typical KIPS	Typical freq [Hz]	Acquisition freq [Hz]	KIPS
ADCs							
RW	4	1000	300	5	2	2	12.5
Fine Sun Sensor	5	500	500	1	1	50	50
Star Tracker	2	2000	15000	2	0.01	2	20
MTQ	3	1000	900	4	2	10	20
Gyroscope	3	800	500	9	10	20	180
GPS	1	1000	1200	8	1	1	8
Kinematic Integration	1	2000	2000	15	10	10	15
Error Determination	1	1000	100	12	10	1	1.2
Attitude Determination	1	15000	3500	150	10	10	150
Attitude Control	1	24000	4200	60	10	10	60
Complex Ephemerides	1	3500	2500	4	0.5	1	8
Orbit Propagation	1	13000	4000	20	1	1	20
PS							
Tank	2	-	-	-	-	-	-
ST25-Hall Thruster	1	1200	1500	5	0.1	0.1	5
Propulsion System Controller	2	600	400	1.2	2	2	1.2
Pressure Transducer	2	800	1500	3	0.1	0.1	3
Tank Control Valve	4	800	1500	3	0.1	1	3
Tank Pressure Sensor	4	800	1500	3	1	1	30
TCS							
Thermal Control (TBC Temperature Sensors)	1	900	2000	3	0.1	1	30
SYSTEM							
Fault Monitors	1	4000	1000	15	5	5	15
Fault Correction	1	2000	10000	5	5	5	5
I/O Device Handlers	1	2000	700	50	5	1	10
Math Utilities	1	1200	200	0.5	0.1	1	5
Diagnostic and Test	1	700	400	0.5	0.1	1	5
Kalman Filter	1	8000	1000	80	0.01	0.1	80
Executive	1	3500	2000	60	10	10	60
Run Time Kernel	1	8000	4000	60	10	10	60
Complex Autonomy	1	15000	10000	20	10	10	20
TTMTC							
S-band Patch Antenna	4	-	-	-	-	-	-
GNSS Antenna	1	-	-	-	-	-	-
S-Band Downlink Transmitter	2	1000	2500	3	10	10	3
S-Band Uplink Receiver	2	1000	4000	7	10	10	7
GPS Receiver	1	1000	4000	7	10	10	7
EPS							
Solar Panels	5	-	-	-	-	-	-
Batteries	2	-	-	-	-	-	-
Cable & Harness	1	-	-	-	-	-	-
PCDU	1	1200	500	5	1	1	5
Power Voltage Control	1	1200	500	5	1	1	5
Power Current Control	1	1200	500	5	1	1	5

Table 57: Functions for each subsystem

Starting from the values retrieved in the tables above, a further analysis has been conducted. Properly sizing the OBC requires understanding which subsystems operate simultaneously during different mission modes. This analysis focuses on the two most critical modes: the TM, where all subsystems are operational except for the PS and the payload, and the OCM, the maneuvering mode where all subsystems are nominally active except for the TTMTC and the payload.

	ADCS	PS	EPS	TCS	TTMTC	SYSTEM	TOT
TM							
Throughput [KIPS]	1202.2	0	15	30	27	980	2254.2
Margined [KIPS]	6011	0	75	150	135	4900	11271
Code [words]	75400	0	3600	900	4007	44400	128307
Margined [words]	377000	0	18000	4500	20035	222000	641535
Data [words]	53600	0	1500	2000	17000	29300	103400
Margined [words]	268000	0	7500	10000	85000	146500	517000
OCM							
Throughput [KIPS]	854.2	253.4	15	30	0	980	2132.6
Margined [KIPS]	4271	1267	75	150	0	4900	10663
Code [words]	75400	10400	3600	900	0	44400	134700
Margined [words]	377000	52000	18000	4500	0	222000	673500
Data [words]	53600	17300	1500	2000	0	29300	103700
Margined [words]	268000	86500	7500	10000	0	146500	518500

Table 58: KIPS and word memory for TM and OCM (margin 400%)

Table 58 demonstrates that the OCM is the most demanding mode in terms of memory and computational requirements for the OBC. Therefore, it has been selected as the sizing scenario for the processor. The required RAM, ROM and MIPS were computed. Results are reported in Table 59.

TM	ROM [Mb]	RAM [Mb]	TP [MIPS]
No Margin	0.256614	0.456414	2.9542
Margined	1.28307	2.31707	11.271
<hr/>			
OCM	ROM [Mb]	RAM [Mb]	TP [MIPS]
No Margin	0.2984	0.4768	2.1336
Margined	1.947	2.984	10.663

Table 59: Sizing results for ROM, RAM, and MIPS (margin 400%)

Before finalizing the selection of the OBC, a detailed analysis of the payload data was conducted. According to the datasheet of the iSIM90 [44], the camera is equipped with a 500 GB mass memory and has the capability to compress images, utilizing its own CPU. To ensure a certain level of redundancy, the main OBC shall include a mass memory to store compressed images when needed, allowing them to be downlinked later. Understanding the size of the compressed data generated by the payload is critical for determining the mass memory required on board. The following considerations were made to estimate this value:

- The maximum number of photos that can be taken by each drone is 20, considering a formation flight of 20 drones.
- Each drone is equipped with 2 cameras operating simultaneously, doubling the **number of photos** to **40**.
- **Each photo weights** approximately **36 MB**,
- The datasheet specifies that lossless **compression** is possible, reducing the image size by **50%**.

- In the worst-case scenario, the total size of the payload data to be stored onboard is **720 Mb**.

From this analysis it is clear how the OBC selected needs to ensure a mass memory of at least 720 Mb.

15.3 OBC selection and redundancy philosophy

Based on the results from the preliminary sizing, the **DARA** from Alèn Space is a possible candidate to be the main OBC. Table 60 presents some of its key characteristics. As shown, the RAM, ROM, and mass memory capacities are more than sufficient to meet the requirements. This OBC will be responsible for managing and processing the data from the entire platform and executing the FSW. Additionally, it features an Inertial Measurement Unit, a 3-axis magnetometer, and an external GNSS interface.

Additionally, a **secondary OBC** has been included into the design, dedicated specifically to the AOCS subsystem. Given that the GNC algorithms are not computationally demanding, the selected OBC does not need to be highly powerful. However, it is crucial to consider the possibility of utilizing this secondary unit as a backup in the event of a failure of the primary OBC. Moreover, It will handle the FDIR of the AOCS subsystem. The OBC that best aligns with the required performance specifications is the **NanoMind A3200** from GOMspace. Table 60 presents some of its key characteristics. This OBC will be coupled with the **Nanodock ADCS-6**, always from GOMSpace, to proper interface with the sensors and actuators.

	RAM	ROM	Mass Memory	Interfaces	Power	Dim.	Mass
NanoMind A3200	32 MB	128 MB	128 MB	CAN, SpaceWire, I2C	0.17 W	65×40 $\times 7.1$ mm	24 g
DARA OBC	32 MB	128 MB	128 GB	CAN, SpaceWire, I2C	2 W	93.3×89.3 $\times 12.6$ mm	115 g

Table 60: Comparison between NanoMind A3200 and DARA OBC [104, 108]

15.4 OBDH Redundancy Philosophy

The redundancy philosophy adopted for the OBDH subsystem is to avoid implementing an overly complex level of redundancy. This approach is justified by the fact that, in the event of a drastic failure of this subsystem, making the mission unable to continue, the space drone can be quickly replaced. Consequently, this risk is considered sustainable for this type of mission. That said, a certain level of redundancy is still implemented on both the hardware and software sides.

- **Hardware redundancy:** Payload data can be stored in the main OBC mass memory, ensuring that, in the event of a failure of the payload mass memory, the data can still be stored for downlink. If the bus connection between the payload and the main OBC fails, the secondary OBC is capable of independently managing the payload data flow via the CAN bus. A redundant CAN bus further guarantees reliable data transmission, enhancing the overall system safety. Additionally, both OBCs are protected by a 1 mm aluminum shield to mitigate the risk of radiation-induced failures, ensuring stable and continuous operation in the harsh VLEO environment.
- **Software redundancy:** A checksum approach is employed to verify data integrity, enabling the detection of any data corruption or inconsistencies. To enhance reliability, multiple copies of the FSW are stored across different memory modules, ensuring that backup copies can be booted if the main FSW is corrupted. Furthermore, watchdogs are utilized to monitor the proper functioning of various subsystems, providing early detection of malfunctions and enabling prompt corrective actions.

15.5 TID analysis

Both the main and secondary OBCs are flight-proven and have been qualified for operation in the LEO environment. To evaluate and mitigate the risk of failure due to the radiation levels in VLEO, a detailed analysis of the Total Ionizing Dose, one of the primary causes of OBC failure, was conducted. Using the software **OMERE**, the total TID from various particles was calculated, assuming a mission duration of 1.5 years, which is the maximum lifetime achievable by a single space drone. The analysis showed that during this period, a total dose of 100 krad is absorbed by an element made of silicon, which can represent an OBC.

According to the datasheet of the **DARA**, it has been tested to withstand a total absorbed dose of 30 krad, while the **A3200** to withstand 20 krad, which are both insufficient to ensure the integrity of the system over the full mission duration. To mitigate this issue and prevent potential failures due to radiation, a thin shielding layer of aluminium could be applied. As demonstrated in Figure 84, just 1 mm of shielding is enough to protect the OBCs from radiation damage over the mission's lifetime.

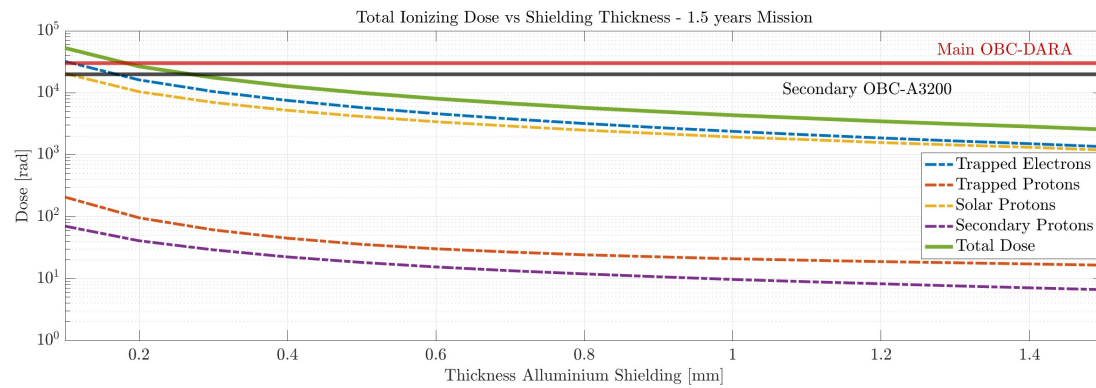


Figure 84: TID analysis for OBCs

15.6 OBDH Architecture and Bus Selection

Once the OBCs have been selected, the next step is to define the overall architecture of the subsystem. One of the key decisions is selecting the appropriate bus architecture. After evaluating various options, a **federated bus architecture** was chosen due to its ability to ensure deterministic data transmission, thereby enhancing reliability and minimizing troubleshooting time.

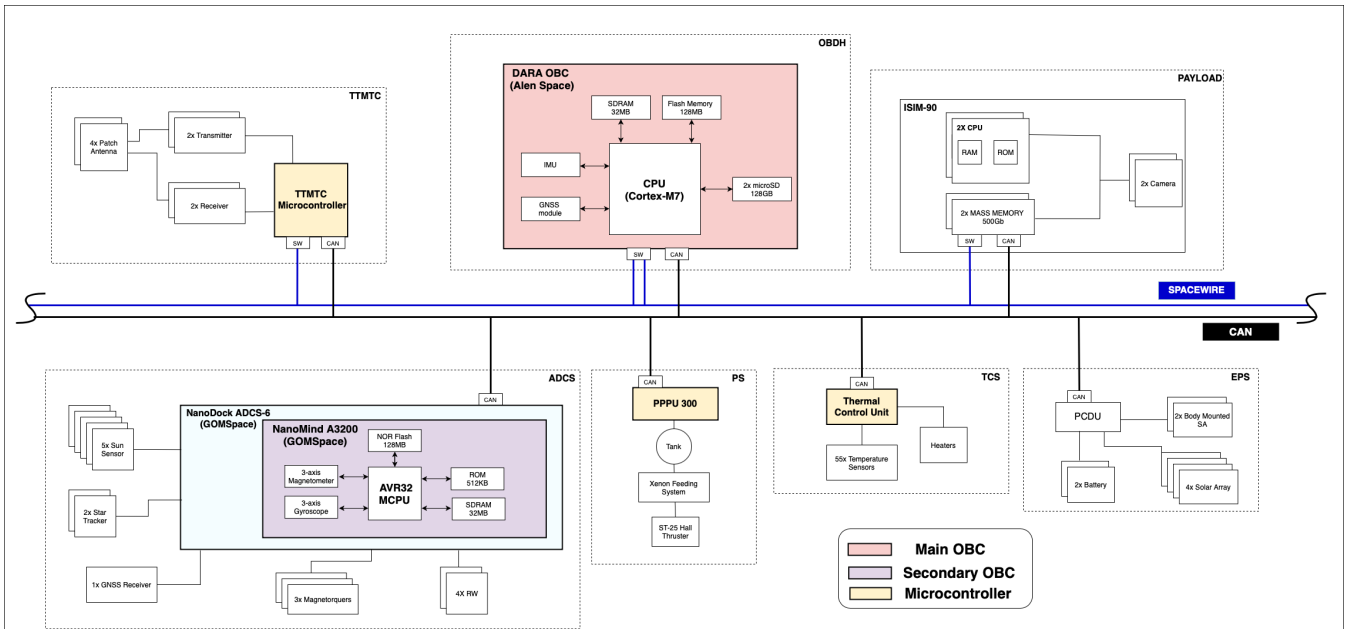


Figure 85: HORUS OBDH architecture

The architecture overview of the OBDH system is illustrated in Figure 85. Two distinct bus systems were selected for different purposes: the **CAN bus** and the **SpaceWire** protocol.

The CAN bus serves as the main communication bus, handling all non-payload data. It was chosen given the relatively low data rate requirements and its high reliability. The SpaceWire protocol is specifically designed to handle payload data, where high data rates are crucial to minimize latency between data acquisition and downlink. In this system, SpaceWire is used for point-to-point connections resulting in three distinct connections: one between the payload and the main OBC, another between the OBC and the TTMTC system, and a third directly linking the payload to the TTMTC.

A microprocessor has also been selected to manage the tasks associated with TTMTC. This microprocessor interfaces with the hardware involved in data transmission and reception, ensuring proper communication across the system.

For thermal control, a Thermal Control Unit has been included. This unit monitors the temperatures of various thermistors and, if necessary, activates heaters to maintain optimal thermal conditions.

Finally, the Power Processing Unit, specifically the PPU 30 microprocessor, is integrated with the Hall thruster to manage its control and operation.

15.7 Telemetry

To finalize the design of the OBDH subsystem, a detailed analysis of the telemetry was conducted. This analysis is based on the parameters that need to be transmitted via downlink, which were determined by evaluating the key requirements for each subsystem. The following considerations were made:

- The FSW will operate at a frequency of 10 Hz .
- The AOCS software will operate at a frequency of 20 Hz .
- In case of FDIR, different parameters may need to be communicated compared to the regular ones.
- Each Sun Sensor has 4 photodiodes, each providing a separate voltage reading.

Based on these initial considerations, the HORUS telemetry is reported in Table 62, with the total data rate to be downlinked with a 400% margin included. This data rate is considered realistic for a mission like HORUS.

Variable	Dimensions	Data type	Data size downlink [bits]	Acquisition Frequency [Hz]	Data rate [bit/s]
AOCS					
Quaternion (estimated)	4	float	128	10	1280
Control mode	1	uint8	8	1	8
Pointing Error	1	boolean	1	5	5
Health Status	1	uint8	8	5	40
Gyro Measurment	3	float	96	5	480
Magnetometer Measurment	3	float	96	1	96
Sun Sensor Voltage +X	4	uint16	64	5	320
Sun Sensor Voltage +Y	4	uint16	64	5	320
Sun Sensor Voltage +Z	4	uint16	64	5	320
Sun Sensor Voltage -Y	4	uint16	64	5	320
Sun Sensor Voltage -Z	4	uint16	64	5	320
Star Tracker Quaternion +X	4	float	64	1	64
Star Tracker Quaternion +Z	4	float	64	1	64
TCS					
Temperature sensors	50	int16	800	0.1	80
EPS					
Battery Voltage	1	int16	16	5	80
Battery Current	1	int16	16	5	80
+50V Bus Voltage	1	int16	16	5	80
+50V Bus Current	1	int16	16	5	80
+25V Bus Voltage	1	int16	16	5	80
+25V Bus Current	1	int16	16	5	80
Solar Array 1 Voltage	1	int16	16	5	80
Solar Array 2 Voltage	1	int16	16	5	80
Solar Array 3 Voltage	1	int17	16	5	80
Solar Array 4 Voltage	1	int18	16	5	80
Solar Array 5 Voltage	1	int19	16	5	80
Solar Array 1 Current	1	int20	16	5	80
Solar Array 2 Current	1	int21	16	5	80
PROPELLION					
Pressure tank	1	uint16	16	0.05	0.8
Pressure Cathode	1	uint16	16	0.05	0.8
Pressure Feeding Line 1	1	uint16	16	0.05	0.8
Pressure Feeding Line 2	1	uint16	16	0.05	0.8
TTMTC					
Transmitter Current	1	int19	16	5	80
Receiver Voltage	1	int20	16	5	80
Receiver Current	1	int21	16	5	80
OBDH					
BER	1	float	32	5	160
Reset Counter	1	uint16	16	5	80
Health Status System	1	uint8	8	5	40
Memory Usage	1	uint8	8	5	40
OBC uptime	1	uint16	16	5	80
Fault Detection	1	boolean	1	5	5
Fault Correction	1	boolean	1	5	5
Total [Kbit/s]					6.5
Total Margined [Kbit/s]					32.7

Table 61: HORUS Telemetry Overview

16 Structure

The structure is a key factor in the design of a S/C. The focus of this chapter is to design, analyse, and optimize the structural aspect of the HORUS space drone. The discussion covers the materials selection, structural layout, and the methods employed to ensure the reliability and resilience of the S/C in the most difficult moments of the mission. Additionally, the chapter examines the results of structural analyses, providing a comprehensive understanding of the mechanical integrity of the system.

16.1 Structural design

Starting from the configuration, the S/C structure is a $330 \times 330 \times 830$ mm cuboid, featuring hollow walls and strategically placed structural supports to ensure the overall strength and integrity of the design. This structure has been specifically engineered to be both lightweight and robust, with the goal of providing reliable performance throughout the mission duration in the challenging VLEO environment. The design prioritizes durability while simultaneously supporting all critical systems. As illustrated in Figure 86, the cuboid shape is complemented by reinforcements at key points where internal subsystems are mounted, ensuring that these connections maintain mechanical integrity under dynamic operational conditions. This structural configuration allows the HORUS satellite to withstand the rigours of space while optimizing weight efficiency.

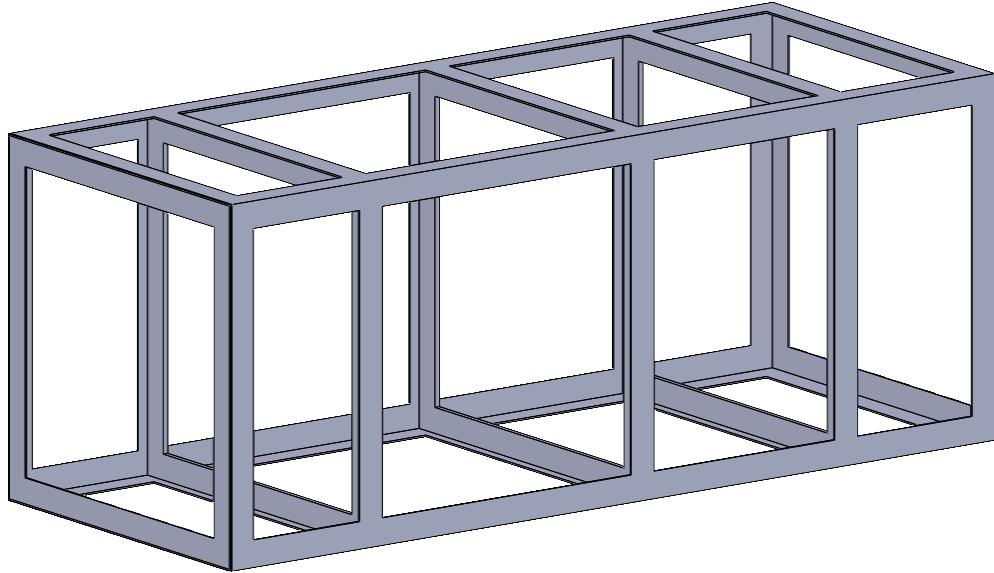


Figure 86: HORUS Internal Structure

The structure is designed on FEMAP, a software for structural analysis and design. The mesh generation was performed using quadrilateral elements to ensure a balanced representation of the structure. The mesh was refined to improve accuracy and better capture the structural behavior. Additional localized refinements were applied to critical areas, such as the lateral supports, to enhance the analysis in regions of higher stress concentration. The internal components are modelled as concentrated masses at their attachment points to the structure, enhancing the structural response in the analyses carried out.

A thickness of 1.6 mm is now chosen, since it is the minimum thickness that guarantees acceptable results in the subsequent analyses.

The material chosen is Aluminium Al-7075-T6, which is a high-strength, heat-treated alloy primarily composed of aluminium, zinc, magnesium, and copper. It is one of the most performant aluminium alloys available, making it ideal for applications requiring both high strength and lightweight characteristics.

Density [$\frac{kg}{m^3}$]	E [GPa]	G GPa	$\nu [-]$	$\alpha [\frac{1}{K}]$	σ_u [MPa]	σ_y [MPa]
2810	71.7	26.9	0.33	$2.35 \cdot 10^{-5}$	572	503

Table 62: Al 7075-T6 Characteristics

16.2 Modal Analysis

The Modal Analysis aims to compute the natural frequencies and mode shapes of the S/C in order to ensure the mechanical stability of the structure and avoid resonances caused by vibrations during the launch.

The analysis is conducted in FEMAP using the previously detailed FEM model. The resulting vibration modes are subsequently compared with the lateral and longitudinal frequencies of the launch vehicle to ensure compatibility and mitigate potential resonance issues during launch.

	Vega-C	Ariane 6
Lateral Frequencies [Hz]	≥ 12	≥ 6
Longitudinal Frequencies [Hz]	≥ 20	≥ 20

Table 63: Launchers Lateral & Longitudinal frequencies

The S/C modes were then calculated with a Normal Modes Analysis and eventually compared with the selected launchers frequencies.

Modes	Frequency [Hz]
Mode 1	12.54
Mode 2	13.33
Mode 3	22.14
Mode 4	31.15
Mode 5	31.75
Mode 6	34.47
Mode 7	36.70
Mode 8	42.49
Mode 9	43.17
Mode 10	45.13

Table 64: HORUS structure Modal Frequencies

The first lateral mode, identified as Mode 1, exceeds the strictest condition imposed by the Vega-C lateral frequency requirement. Similarly, the first longitudinal frequency, corresponding to Mode 3, is higher than the longitudinal frequency limits specified for the launchers. Consequently, the vibrational modes of the S/C do not pose any concerns, and no resonance coupling is expected. This ensures structural integrity during the launch event and mitigates the risk of failure for the space drone. The low modal frequencies can be explained by considering the Launcher Ring Adapter selected for the mission. Since the S/C has a cross section of 330×330 mm, while the Launcher Adapter Ring has a diameter of 319 mm, the constraint applied at the base restricts longitudinal motion and limits both the base movement and deformation. As a result, lower frequencies are obtained, yet still within the margins imposed by the launchers User Manuals.

A Modal Analysis of the deployable solar panels was conducted to ensure their proper dimensioning. A constraint on the longer side was applied to the deployable solar array to model the revolute joints. An additional analysis was required since these solar arrays extend beyond the spacecraft and are connected to it solely through the revolute joints. Moreover, as they are modelled as plates, their natural frequencies must be assessed to avoid resonance with the launcher, which could potentially damage the satellite. Initially, with the same thickness as the main body, the lateral and longitudinal requirements of Vega-C were not met. Therefore, to comply with the modal constraints of the launcher, a thickness of 2 mm is required for the deployable solar panels.

16.3 Quasi-Static Analysis

The objective of the Quasi-Static Analysis is to evaluate the structural response to slowly applied loads, effectively simulating dynamic events through static equivalents. The primary goal of the analysis is to ensure that the structure can withstand maximum stress levels without experiencing failure. The analysis is still performed using FEMAP. By applying the maximum QSL values specified in the selected launchers User Manuals, here reported in Table 65, and incorporating a Safety Factor of $K_{QSL} = 1.25$, the stresses are evaluated through a Static Analysis conducted within FEMAP's integrated processing software.

	Vega-C	Ariane 6
Max Lateral QSL [g]	[-5; 3]	[-6; 2.5]
Max Longitudinal QSL [g]	[-1.35; 1.35]	[-2; 2]

Table 65: Launchers Lateral & Longitudinal maximum QSL

Following the completion of the analysis using the aforementioned software, the resulting Von Mises stress values have been carefully evaluated and are presented in table 66. These results provide a detailed assessment of the structural performance under the applied quasi-static loads.

Von Mises Stresses	Vega-C	Ariane 6
σ_{x_C} [MPa]	76.20	91.45
σ_{x_T} [MPa]	45.72	38.10
σ_y [MPa]	82.86	122.77
σ_z [MPa]	81.85	121.26

Table 66: Von Mises Stresses computed with the Max QSL from the launchers User Manuals

The resulting Von Mises stresses were subsequently employed to compute the Quasi-Static Margins of Safety (MoS), following the guidelines provided by the Space Engineering Testing [109]. The calculations were performed using the following formulas:

$$MoS_y = \frac{\sigma_{yield}}{K_m K_p FoS_y \sigma_{FEM}} - 1 \quad MoS_u = \frac{\sigma_{ultimate}}{K_m K_p FoS_u \sigma_{FEM}} - 1$$

where K_m represents the Model Factor and K_p the Project Factor, both set to 1.2. The Yield Design Factor of Safety, FoS_y , is set to 1.25, while FoS_u denotes the Ultimate Design Factor of Safety. All these values are defined in accordance with [109].

The computed MoS values for the selected launchers are reported in Table 67.

Margins of Safety	Vega-C	Ariane 6
MoS_y	2.3722	1.2763
MoS_u	2.8348	1.5885

Table 67: Quasi-Static MoS computed for the Launchers

According to the ECSS Standards for Analysis and Testing, optimal values for the Margins of Safety should range between 0 and 0.5, with values up to 1 being considered acceptable. If the MoS exceeds 1, the structure is deemed highly over-dimensioned. This is the case for the HORUS space drone structure. Attempts were made to reduce the MoS by decreasing the thickness. However, this led to Modal Analysis results that no longer met the launchers requirements for lateral and longitudinal frequencies. Furthermore, since this is a preliminary structural analysis, more conservative results are preferred, as the internal structure has not yet been thoroughly assessed and additional analyses may be incorporated into the overall structural design. Therefore, values slightly above 1 are considered acceptable for the structural analysis.

16.4 Sine Vibration Analysis

The Sine vibration analysis evaluates the response of the structure to harmonic excitations, simulating the vibrational environment during launch or operational conditions. The Sine Vibration Analysis has the objective of verifying the S/C dimensioning, under the flight limit loads multiplied by a Safety Factor $K_{sine} = 1.25$.

The analysis is conducted with FEMAP, using the integrated solver Simcenter Nastran. Firstly, the Boundary Conditions must be analysed. The frequency response, indeed, must be studied considering the set of frequencies given by the Modal Analysis. Starting from the first Mode, the analysis is carried out in the entire frequency spectrum. The Sine Vibration test requires a specific acceleration profile, that can be found in the launchers User Manuals. The Vega-C User Manual [46] and the Ariane 6 User Manual [45] give the lateral and longitudinal loading functions in terms of gravity acceleration.

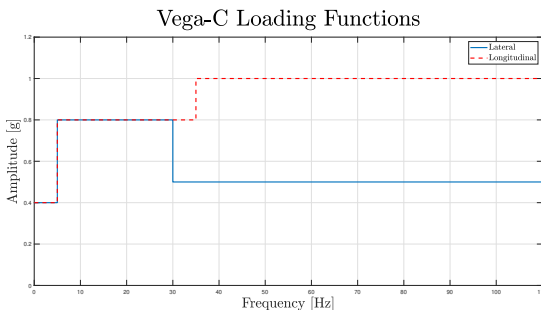


Figure 87: Vega-C Loading Functions

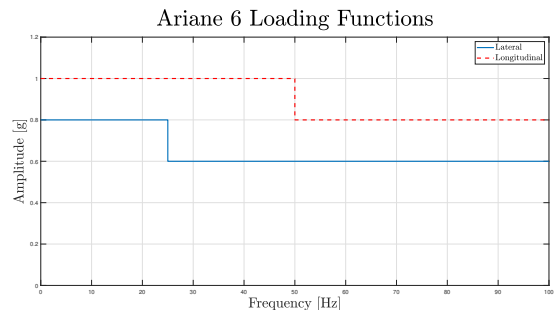


Figure 88: Ariane 6 Loading Functions

For the Sine Vibration Analysis, the constraint is applied as a rigid element at the base, in order to simulate the origin of the loading function, which is the launcher. Moreover, a damping function must be considered in order to perform a correct analysis. Since the structural material is aluminium, a general value for the aluminium is set, which is 2%. Hence, for both the launchers the stresses are computed on the entire spacecraft, and the node where the maximum stress is exhibited is considered. In Table 68 the maximum stresses in the three directions are presented for both the launchers.

Von Mises Stresses	Vega-C	Ariane 6
$\sigma_x [MPa]$	74	92
$\sigma_y [MPa]$	47	47
$\sigma_z [MPa]$	42	41.2

Table 68: Sine Vibration Analysis Von Mises Stresses

The Margins of Safety can be determined based on the stresses obtained from the Sine Vibration Analysis. Their computation follows the guidelines provided by the Space Engineering Testing, now applied to the stresses derived from this analysis. The Margins of Safety for the Sine Vibration Analysis are presented in Table 69.

Margins of Safety	Vega-C	Ariane 6
MoS_y	2.7763	2.0374
MoS_u	3.2943	2.4541

Table 69: Sine Vibration Analysis MoS computed for the Launchers

The Margins of Safety obtained from the Sine Vibration Analysis are slightly higher compared to those from the Quasi-Static Analysis, yet they remain within acceptable limits. This is due to the fact that the maximum Von Mises stresses for both Vega-C and Ariane 6 are lower than those observed in the Quasi-Static Analysis, resulting in higher Margins of Safety.

16.5 Random Vibration Analysis

The Random Vibration Analysis is performed to evaluate the spacecraft dynamic response to external excitations, with a primary focus on the environmental acoustic excitation induced by the launcher. This analysis is crucial to understanding how the structure reacts to the random vibrational loads experienced during launch, which are primarily driven by high-intensity acoustic waves. By assessing these effects, it is possible to verify the spacecraft structural robustness and ensure that it can withstand such dynamic stresses without compromising its integrity or performance. Using the acoustic noise spectrum provided in the launchers User Manual, the Pressure Power Spectral Density Function is determined.

$$PPSD = \frac{p_{ref}^2}{\Delta f_c} 10^{\frac{SPL}{10}} \quad (54)$$

where p_{ref} is the reference pressure, typically set to 10^{-5} , Δf_c is the frequency bandwidth in octave bands for European launchers, and SPL is the Sound Pressure Level obtained from the acoustic noise spectrum of each launcher.

The Pressure Power Spectral Density is then used to generate the pressure load function by imposing a pressure of 1 Pa, which is applied to each node of the structure to create a generic unitary load following the trend of the PPSD across the entire frequency spectrum. From the Pressure Power Spectral Density, considering a Random Vibration Analysis, the Acceleration Power Spectral Density is obtained for each spacecraft axis. Finally, a comparison is made with the SS APSD Qualification Standard Levels from the NASA Goddard Flight Center General Environmental Verification Standard (GEVS).

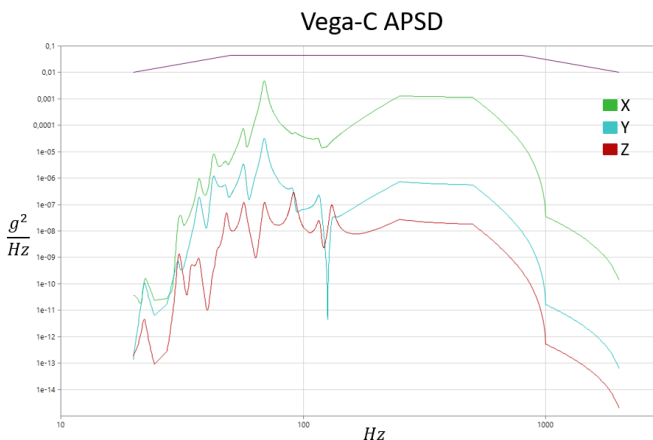


Figure 89: Vega-C APSD

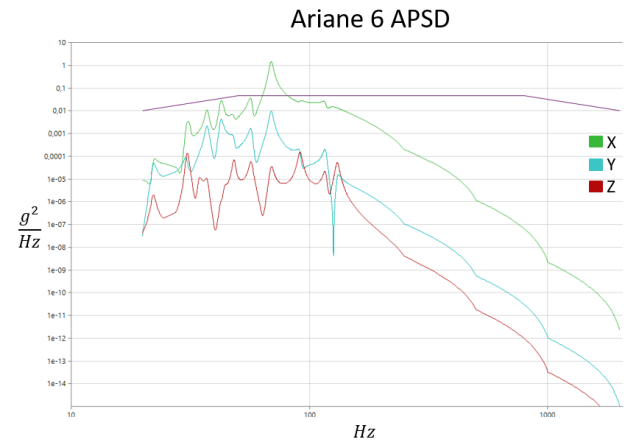


Figure 90: Ariane 6 APSD

Starting with the Vega-C results, it can be observed that the accelerations in all three directions remain below the APSD Qualification Level set by the GEVS. As expected, the highest acceleration occurs in the longitudinal direction, given that the HORUS spacecraft length is greater than its cross-section. A noticeable difference is also present between the two lateral directions, primarily due to the varying positions of internal components within the spacecraft, which lead to different internal forces, accelerations, and resulting stresses. Considering the Ariane 6, the first observation is that the longitudinal acceleration exceeds the qualification level set by the GEVS. This is a concern, as the acceleration in the longitudinal direction surpasses the maximum values that the spacecraft can sustain from random loads, potentially leading to stresses that could compromise the spacecraft structural integrity. However, it is important to note that the Ariane 6 is the newest ESA launcher, with only one launch so far. Additionally, the latest User Manual for Ariane 6, dated 2021, includes values for the Sound Pressure Level that are notably high, as 6 decibels are added to account for uncertainty and minimum qualification levels. This results in a PPSD with elevated values. Moreover, the data provided by the ArianeGroup are tailored for spacecraft with a mass exceeding 4000 kg. Since the HORUS spacecraft is considerably lighter, this factor also influences the results. One potential solution would be to evaluate the mechanical severity to determine whether the acceleration remains within the mechanical severity margins. Alternatively, a more detailed study could be conducted by assessing the APSD of each individual component of the spacecraft. If all components pass the test, the spacecraft can be considered to have successfully passed the Random Vibration Analysis for the Ariane 6 Launcher [110].

16.6 Buckling Analysis

The Buckling Analysis is performed to assess the structural stability under compressive loads, allowing for the estimation of the critical loading factor.

For the HORUS project, a Linear Buckling Analysis is carried out by computing the eigenvalues of the structure under the compressive loads experienced during the mission, particularly during the launch phase. Based on these results, the Buckling Minimal Margin of Safety is then determined.

$$MoS_{buckling} = \lambda_{buckling,min} - 1 \quad (55)$$

For this analysis, the computed eigenvalues represent the critical loading factor that can be applied to the spacecraft before structural instability occurs. Specifically, if the Minimum Buckling Eigenvalue is greater than one, meaning that the $MoS_{buckling}$ is positive, the structure remains stable and can sustain the applied load without collapsing. Conversely, if the eigenvalue is lower than one, resulting in a negative $MoS_{buckling}$, the structure becomes unstable and collapses under the applied load. The Buckling Minimal Margin of Safety provides a straightforward metric for evaluating the stability of the structure at a glance. The Minimum Buckling Eigenvalues $\lambda_{buckling,min}$ are computed for all the points of the Flight Envelope of both the Vega-C and Ariane 6, applying a Safety Factor $K_{SF} = 1.25$. The results are shown in Table 70 for the Vega-C and in Table 71 for the Ariane 6.

Lateral Loads	Longitudinal Loads	$\lambda_{buckling,min}$	$MoS_{buckling}$
1.35	-4.5	9.536752	8.536752
1.3	-4.5	9.750545	8.750545
1.3	-5	9.318286	8.318286
-1.3	-5	8.81766	7.81766
-1.3	-4.5	9.261987	8.261987
-1.35	-4.5	9.071215	8.071215

Table 70: Vega-C Linear Buckling Analysis

Lateral Loads	Longitudinal Loads	$\lambda_{buckling,min}$	$MoS_{buckling}$
-1	-6	9.029892	8.029892
-2	-3.5	7.752577	6.752577
-2	-3.6	7.688178	6.688178
-4	-0.9	11.85108	10.85108
-4.3	-0.5	14.3648	13.3648
-4.5	-0.5	13.92569	12.92569

Table 71: Ariane 6 Linear Buckling Analysis

From the analysis conducted, the Buckling Minimal Margin of Safety obtained with the Vega-C launcher is 7.81766, while for the Ariane 6 the Buckling Minimal Margin of Safety is 6.688178, highlighting the good response of the structure to compressive loads. Indeed, having a $MoS_{buckling}$ in the order of 5 is a good result in terms of critical load factor, enhancing the great capability of the structure itself to withstand compressive loads during the most critical phases and thus ensuring the successful outcome of the mission in terms of structural stability.

17 Configuration

This chapter outlines the configuration of the HORUS space drone, covering both its internal and external architecture. It delves into the key structural and functional components, focusing on the internal arrangement of subsystems and the external design that enables interaction with the space environment. The discussion includes the geometry of the structure, the solutions implemented to optimize performance in VLEO and the general behaviour of the S/C. These aspects form the foundation for the mechanical, thermal, and aerodynamic design of the satellite.

17.1 Internal Configuration

The internal configuration of a S/C is a critical aspect of any space mission success, as it directly influences parameters such as dimensions, cross-section, the position of the Centre of Mass, and the spacecraft's attitude dynamics. A well-optimized internal layout ensures structural stability, minimizes energy consumption, and enhances overall mission performance.

The configuration study for the HORUS spacecraft began by analysing each subsystem in isolation, focusing on the single components, their individual dimensions, masses, and functional roles. Special attention was given to the total mass distribution to optimize the CoM placement. To minimize shifts in the CoM and ensure balanced attitude control, the heaviest subsystems were strategically positioned close to the geometric centre of the spacecraft. This arrangement reduces potential torque imbalances, enhancing stability and manoeuvrability. Moreover, since the only components that change the mass are the tanks, when consuming the propellant, these are positioned in the geometrical centre of the S/C, in order to minimize the most the CoM shift during the entire mission lifetime.

Another critical design consideration was maintaining a low cross-sectional area. A compact cross-section minimizes atmospheric drag, a particularly important factor in VLEO operations, where aerodynamic forces are significant. Consequently, the width and height of the spacecraft were carefully constrained to achieve a streamlined, efficient design without compromising the functionality of onboard systems.

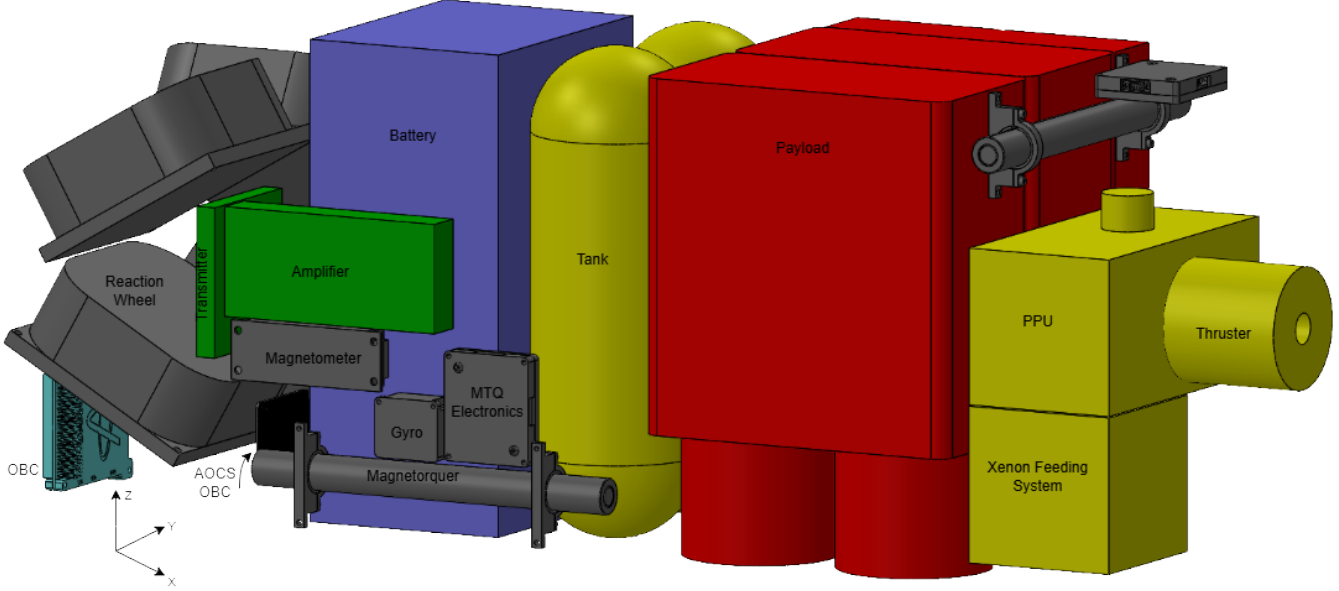


Figure 91: HORUS Internal Configuration

The primary focus was on optimizing the position of the CoM, as the space drones are compact satellites operating in the CoM environment. This orbit requires frequent corrections and exceptional stability to ensure mission success. Maintaining a well-balanced CoM is critical, particularly because the payload consists of a high-performance, high-resolution camera that demands precise pointing capabilities.

In Equation (56) the CoM position with respect to the geometrical centre with full tanks and empty tanks respectively is presented.

$$\begin{cases} x = 20.86 \text{ mm} \\ y = 2.65 \text{ mm} \\ z = 6.69 \text{ mm} \end{cases} \quad \begin{cases} x = 22.50 \text{ mm} \\ y = 1.84 \text{ mm} \\ z = 5.58 \text{ mm} \end{cases} \quad (56)$$

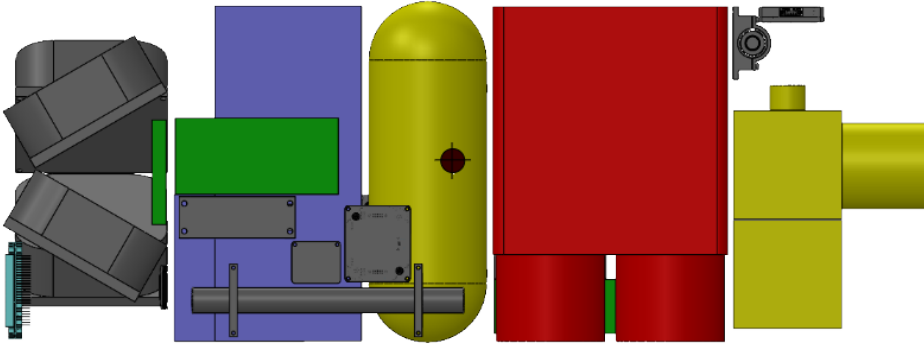


Figure 92: CoM position in the Y axis

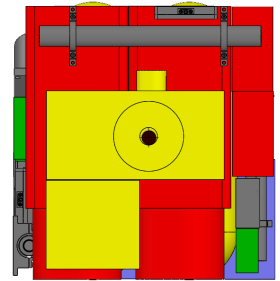


Figure 93: CoM position in the X axis

A carefully positioned CoM minimizes the risk of oscillations or target misalignment caused by external perturbations or the execution of manoeuvres. By reducing the distance between the CoM and the payload's critical pointing axis, the satellite can achieve improved stability, minimizing the adverse effects of dynamic forces. The stability provided by this setup also supports efficient manoeuvre planning, ensuring that the drone can adapt to mission requirements without compromising its performance.

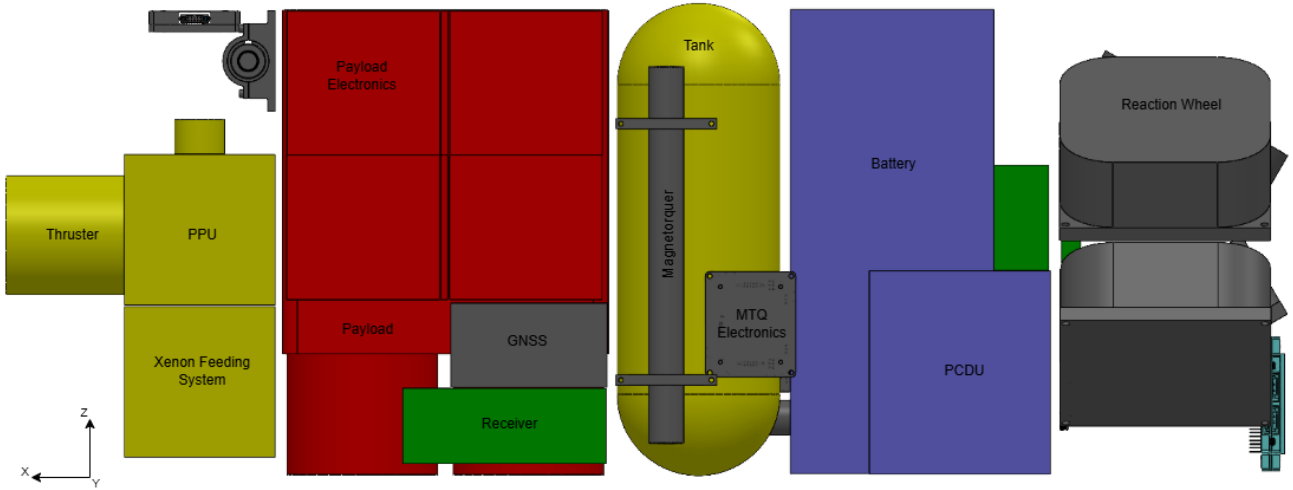


Figure 94: Lateral view

The internal configuration shown here not only considers the precise positioning of each component but also accounts for the spacing between them and their exact distances relative to one another and the main body structure. Ensuring a correct placement of the components is crucial for optimising the inertia of the satellite, which directly contributes to improving the performance of the ADCS. Additionally, a well-planned internal arrangement plays a fundamental role in the thermal analysis, allowing the TCS to operate more efficiently by effectively managing heat distribution and dissipation within the spacecraft.

17.2 External Configuration

The external configuration of the HORUS spacecraft is designed to ensure structural integrity, thermal management, and overall mission performance while meeting all subsystem requirements. A careful balance between aerodynamic efficiency, mechanical robustness, and payload accommodation is maintained to guarantee stability and reliability throughout the mission.

This section provides a detailed analysis of the external layout, focusing on the placement of key structural elements such as solar arrays, antennas, and radiators. The overall geometry and component arrangement are optimised to minimise drag in VLEO, maximise power generation, and enhance thermal control, while ensuring compliance with the requirements of subsystems like TTMTTC and ADCS.

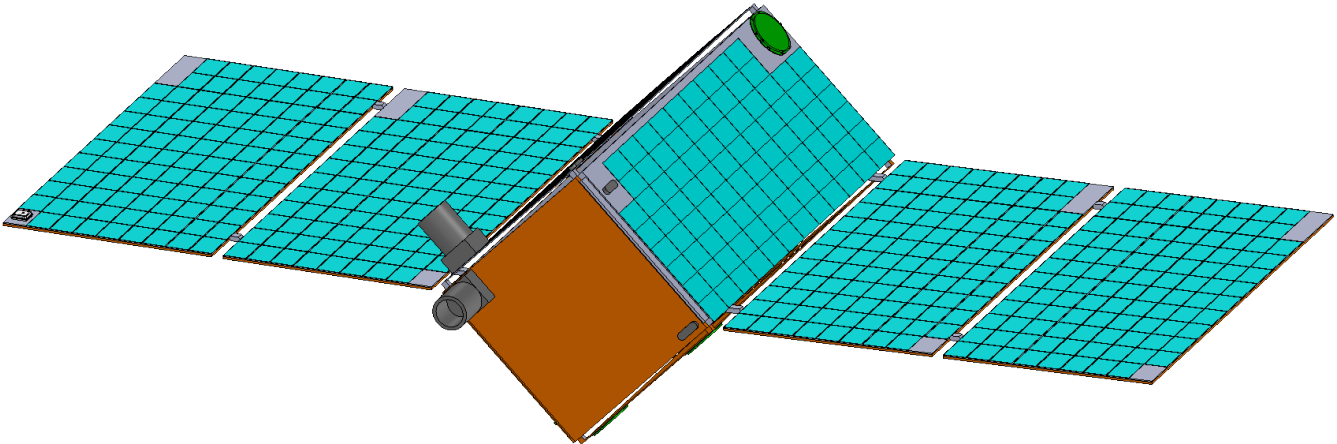


Figure 95: HORUS upper external configuration

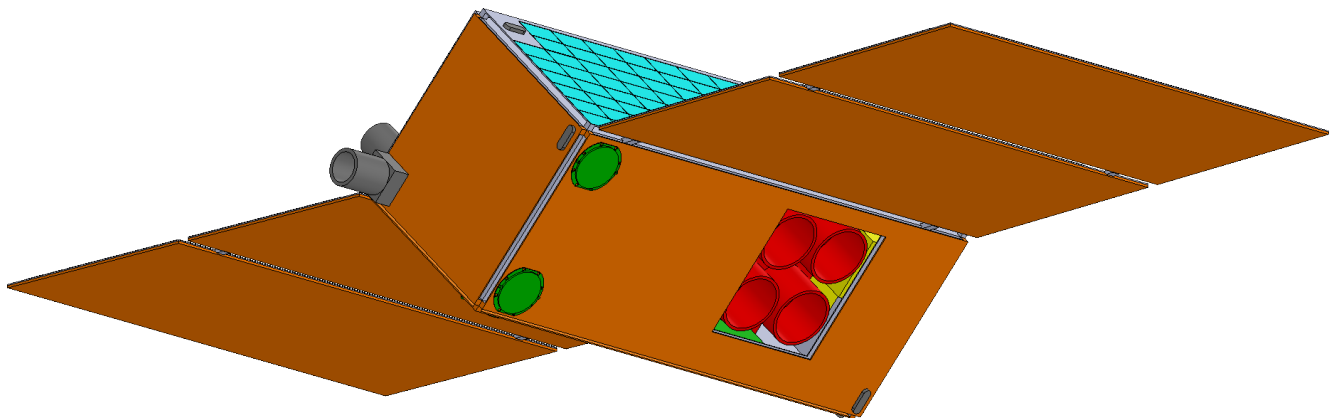


Figure 96: HORUS lower external configuration

As shown in Figure 95 and Figure 96, the external configuration consists of a main body measuring $330 \times 330 \times 830\text{ mm}$, tilted by 45° to ensure that two faces always face the Sun and two always face the opposite direction. The Sun-facing surfaces are primarily covered by solar cells to maximise power generation, along with two Sun sensors, a star sensors, and a patch antenna. The sensors provide the ADCS with the spacecraft precise attitude in space, while the patch antenna supports the TTMTTC for communication with ground stations during the de-tumbling phase. The opposite-facing section is mainly covered by radiators, featuring an opening for the cameras. Additionally, the two non-illuminated surfaces house three patch antennas for continuous ground station communication throughout the mission and two Sun sensors.

The solar arrays, each matching the length of the S/C and with a width of 370 mm, which is 4 cm wider than the lateral edges of the main body, are mounted along the sides of the spacecraft. These arrays are connected to the main body with two damper-spring units, which not only provide stability but also assist in their deployment once in orbit. Each solar array consists of two panels, connected by similar damper-spring units. The Sun-facing surface of the solar arrays is entirely covered by solar cells with a

thin coverglass layer, except for a designated area for the GNSS antenna of the ADCS. The opposite-facing surface is fully equipped with radiators to dissipate heat into deep space, ensuring both the main body and the solar arrays remain within an optimal temperature range. During the launch phase, the solar panels are folded against the S/C surfaces to save space. One array is folded onto the lower surface of the main body, where there is no camera opening, while the other is folded onto the Sun-facing surface with the patch antenna.

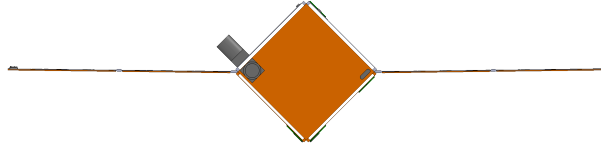


Figure 97: Front view

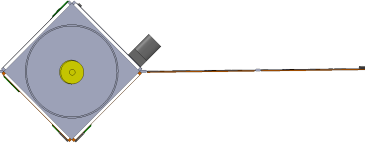


Figure 98: Back view

Considering the front and back views, the front view, shown in Figure 97, is entirely covered by a radiator, with a dedicated space for the second star sensor required by the ADCS to operate in the perpendicular direction to the first one. The back view, shown in Figure 98, features an opening for the thruster, which extends by 2.5 cm , as well as the Launcher Adapter Ring, with a diameter of 319 mm .

As seen in both views, the solar panels on the Sun-facing surfaces and the radiators on the lower part of the spacecraft are raised by 1 cm and 0.8 cm respectively. This design choice enhances internal heat flux between the surfaces and optimises external heat dissipation into deep space, as required by the TCS.

18 Assembly, Integration, Verification, and Testing Development Plan

This section aims to present a mission development plan which emphasizes the required testing for each component and subsystem of the spacecraft. All the tests will be compliant with the ECSS-E-ST-10-03C [109] testing guidelines and the ECSS-E-ST-10-02C verification guidelines.

As our project aims to launch several satellites in multiple missions, with very short time to launch, our main testing campaign will be performed on Qualification Model (QM) and Structural Thermal Model (STM). The flight units of the satellites will only undergo functional, acceptance, and pre-launch testing after the full assembly and integration of the system.

18.1 Model Philosophy and Test Planning

In this section, the model philosophy used for the main components of the spacecraft is explored and the tests performed on each model are better explained. Table 72 highlights the model philosophy used for HORUS. Only the external components were analysed because of their exposure to the external environment.

No breadboard models of any in-house developed component were deemed necessary due to the high design maturity and simplicity of the components. Engineering Model (EM) of each in-house developed component are assembled to initially test performances and ensure functionality. Qualification Model (QM) of the most exposed components are designed to extensively test and to observe their response to the VLEO environment. For non-exposed critical components only a Proto-Flight Model (PFM) is purchased and tested during the first drone launch ³.

Component	TRL	Breadboard	EM	QM	PFM	FM
Solar Cells	7	-	-	×	-	×
PCDU & Battery	9*	-	-	-	×	-
Radiators	4	-	×	×	-	×
Cameras	9	-	-	×	-	×
Patch Antennas	9*	-	-	×	-	×
Sun Sensors	9*	-	-	×	-	×
Star Sensors	9*	-	-	×	-	×
OBC DARA	9*	-	-	-	×	-
OBC A3200	9*	-	-	-	×	-
SPS-25	9*	-	-	×	-	×
Tank	4	-	×	×	-	×

Table 72: Model philosophy for the main system components.

All components which are radiation tolerant in a LEO environment have been deemed tolerant also to VLEO radiation levels. To ensure a complete verification of the system requirements, a **FlatSat testing bench** will be assembled, once the testing cycles of the single subsystems are ended. This model will be used in the development phases to test FM of single components or complete subsystems before integration to newly built satellites.

The tests that will be performed on the QM depend a lot on the functionality of the component and its TRL. The main tests performed have been reported below:

³TRLs followed by * indicate that these levels are reported for LEO environments.

Test	PS	TTMTC	EPS	ADCS	TCS	OBDH	STR	Payload
Physical properties	R	R	R	R	R	R	R	R
Functional performance	R	R	R	R	R	R	-	R
Humidity	O	O	O	O	O	O	O	R
Leak	R	-	R	-	R	-	-	-
Pressure	R	O	R	O	R	-	R	-
Sinusoidal vibration	R	R	R	R	R	R	R	R
Random vibration	R	R	R	R	R	R	R	R
Corona and arcing	R	R	R	R	R	R	R	R
Thermal vacuum	R	-	R	-	R	O	R	R
Thermal cycling	R	R	R	R	R	R	R	R
EMC/ESD	R	R	R	R	R	R	-	R
Software-in-the-Loop	-	R	R	R	R	R	-	O
ATOX degradation	R	R	R	R	R	-	R	R

R = Required O = Optional - = Not required

Table 73: Test schedule for the subsystems

18.2 Assembly and Integration

18.2.1 Assembly

During the assembly phase, individual components of each subsystem are assembled together. For the **ADCS**, reaction wheels, magnetorquers, and sensors (FSS, star trackers, gyroscopes, magnetometers) are carefully mounted ensuring alignment and proper interfacing with the structure. The precise placement of the reaction wheels represent one of the most critical phase for achieving the required pointing accuracy. For the **EPS**, solar panels (body-mounted and deployable) are mounted as designed, and batteries are securely attached with proper thermal insulation. In the **TTMTC** subsystem, antennas are mounted on the external structure, while electronic boxes for the transmitter, receiver, and amplifier are fixed inside the satellite structure. The **OBDH** subsystem involves careful placement of CPUs, microcontrollers, and buses to ensure robust data flow. The **TCS** components, which are distributed across the spacecraft, are attached at the appropriate spots.

During the assembly process, the primary goal is **Minimizing Operations**. Procedures are optimized to reduce the number of operations for individual components and subsystems. Since HORUS is a constellation of drones with identical characteristics, standardizing and streamlining the assembly process is essential for efficiency across all units. Adhering to this guiding principle will reduce the time required for subsequent drones assembly, thereby lowering their cost.

18.2.2 Integration

Hardware integration ensures the mechanical, electrical, and thermal compatibility of all subsystems. This involves testing the deployment mechanisms of solar panels, verifying the positioning accuracy of critical components, and ensuring bus connectivity and electronic compatibility. Additionally, thermal integration is one of the final and most critical procedures, as nearly 50% of the spacecraft external surface is covered by radiators, which must be carefully integrated along with thermal straps and heat switches to ensure efficient heat transfer.

Software integration ensures seamless subsystem functionality, focusing on data flow, communication, subsystem coordination, and payload interfaces, which is critical for maintaining coverage and achieving mission objectives in constellation management.

19 Risk Analysis

In this section, a detailed analysis of the possible risks that can be encountered in the HORUS mission is conducted. This helps to improve mission reliability and safety and reduce uncertainties throughout its life cycle.

19.1 Risk policy and Risk Matrix

Based on the ECSS-M-ST-80C standards, the risk management analysis was conducted to assess the risks related with the development of HORUS and to propose potential mitigation actions. A risk matrix was first created, which uses a color scale to represent different priority levels, as shown in Figure 99. The matrix is composed of two key categories: **severity** and **likelihood**, which are crucial to understand potential risks and guide mitigation efforts. These indices are defined as follows:

- **Severity:** Refers to the potential impact of the risk if it occurs, assessing how serious the consequences would be on the project objectives.
- **Likelihood:** Indicates the probability of the risk event to occur, ranging from very unlikely to almost certain, helping prioritize efforts based on how frequently a risk might happen.

		LIKELIHOOD				
		VERY LOW	LOW	MEDIUM	HIGH	VERY HIGH
SEVERITY	VERY HIGH	MODERATE	SEVERE	SEVERE	Critical	Critical
	HIGH	SUSTAINABLE	MODERATE	SEVERE	Critical	Critical
	MEDIUM	SUSTAINABLE	MODERATE	MODERATE	SEVERE	Critical
	LOW	SUSTAINABLE	SUSTAINABLE	MODERATE	SEVERE	Critical
	VERY LOW	SUSTAINABLE	SUSTAINABLE	SUSTAINABLE	Moderate	Severe

Figure 99: Risk Matrix

Subsequently, a preliminary risk assessment table was produced for each subsystem, enabling a comprehensive risk analysis across the project. The analysis focused on determining the risk indices for each scenario, intending to identify both acceptable and unacceptable risks. The overall objective was to ensure a conservative approach during this first iteration of risk analysis, thereby helping to identify mitigation strategies and prioritize the most critical risks.

The table reporting the risk analysis for each subsystem is reported in figure Figure 101.

ID	RISK DESCRIPTION	CAUSE	SEQUENCES	SEVERITY	LIKELIHOOD	RISK INDEX	MITIGATION ACTION	RESIDUAL SEVERITY	RESIDUAL LIKELIHOOD	RESIDUAL RISK INDEX
GENERAL MISSION RISK										
1	Launch delayed or aborted	The launch could be delayed or aborted due to various factors, such as environmental conditions	The customer would not receive the requested images on time.	HIGH	MEDIUM	SEVERE	Plan for a more flexible launch schedule to mitigate the risk of delays and ensure alignment with the customer's timeline.	HIGH	LOW	MODERATE
2	Launcher Availability	The selected launcher is available for the planned date.	The satellite cannot be launched, resulting in mission failure.	VERY HIGH	HIGH	Critical	Explore options with other launch providers. If no European launcher is available, the possibility of using a non-European launcher needs to be analysed.	VERY HIGH	MEDIUM	SEVERE
3	Injection in the wrong orbit	Issues with the launcher or deployment mechanism.	The mission cannot proceed until the satellite is correctly positioned in its intended orbit.	VERY HIGH	LOW	SEVERE	Design the propulsion system to correct orbit insertion errors for at least a TBD inclination error.	VERY HIGH	VERY LOW	MODERATE
4	Frequent Launches availability	No European launcher offers frequent launch opportunities	Failure to secure frequent launches would prevent the mission from achieving its objectives over the required timeframe.	VERY HIGH	HIGH	Critical	Establish launch schedules to ensure a consistent plan for drone replacements. If non-european launcher is capable to do frequent launches, analyse the possibility of using non-european ones.	VERY HIGH	MEDIUM	SEVERE
5	Multiple Drone collision during deployment	Possible impact of the two drones, due to deployment failure	Loss of deployed drones,	VERY HIGH	VERY LOW	Moderate	Assess deployment risks with the supplier, ensuring collision risk is minimized. If necessary, adjust the launch configuration.	MEDIUM	VERY LOW	SUSTAINABLE
6	Damage of the Optical payload during launch	High vibration levels during the launch process could damage sensitive equipment.	The payload becomes inoperable, the mission objective can't be fulfilled.	VERY HIGH	VERY LOW	Moderate	Verify the payload's resistance to expected launch conditions or conduct a testing campaign to ensure robustness.	MEDIUM	VERY LOW	SUSTAINABLE
Mission Analysis Risk										
8	Collision of the drones on orbit	Risk of collision between drones due to multiple orbital planes being necessary for wide coverage.	Potential loss of drones and degradation in mission performance.	VERY HIGH	MEDIUM	SEVERE	Implement collision avoidance maneuvers, optimize orbital eccentricity for different planes	VERY HIGH	VERY LOW	Moderate
10	Multiple Drone Failure during mission	Environmental factors or hardware malfunctions impacting multiple drones.	Severe mission compromise and degraded performance in achieving objectives.	HIGH	LOW	Moderate	Plan for system redundancy, ensure robust hardware testing and analyse the possibility of phasing manoeuvres to minimize impact.	HIGH	VERY LOW	SUSTAINABLE
9	Faster orbit decay	Need to perform accurate thruster orientation adjustments to achieve proper orbit insertion and plane change.	During the slew, the cross-section increases, resulting in higher drag and a faster orbital decay.	VERY HIGH	MEDIUM	SEVERE	Conduct detailed analyses of slew manoeuvres and of cross-section changes. Develop algorithms to ensure precise control during orbital adjustments.	VERY HIGH	VERY LOW	Moderate
Electrical Power/s Risk										
11	SA string failure	Space environment effects (SEE) or manufacturing defects causing string failures.	Decreased solar panel performance, potentially limiting mission-critical functions.	VERY HIGH	LOW	SEVERE	Incorporate safety margins in solar panel design. Add a string of cell for redundancy	VERY HIGH	VERY LOW	Moderate
12	SA Body mounted Failure	Space environment effects (SEE) or manufacturing defects causing string failures.	Decreased solar panel performance, potentially limiting mission-critical functions.	HIGH	LOW	Moderate	Incorporate safety margins in solar panel design.	HIGH	VERY LOW	SUSTAINABLE
13	Batteries Failure	Battery aging or other degradation mechanisms.	Loss of power, affecting the satellite's operational capabilities.	MEDIUM	LOW	Moderate	Account for redundancy in the design, adding an additional string of cells	MEDIUM	VERY LOW	SUSTAINABLE
14	PCU malfunctioning	Radiation effects causing damage to electronic components. Mechanical stresses or damage during launch	Loss or degradation of power distribution to subsystems, leading to partial or total mission failure.	HIGH	LOW	Moderate	Use radiation-hardened components. Conduct rigorous pre-launch testing for mechanical and thermal stress tolerance.	HIGH	VERY LOW	SUSTAINABLE
15	SA lower power production	Degradation of solar cells over time.	Insufficient power production to meet mission requirements.	MEDIUM	LOW	Moderate	Account for degradation during design and ensure adequate initial power margins.	MEDIUM	VERY LOW	SUSTAINABLE

Figure 100: Risk Matrix

ID	RISK DESCRIPTION	CAUSE	CONSEQUENCES	SEVERITY	LIKELIHOOD	RISK INDEX	MITIGATION ACTION	RESIDUAL SEVERITY	RESIDUAL LIKELIHOOD	RESIDUAL RISK INDEX
Telecommunication and Telecommand s/s Risk										
16	Patch antenna failure	Physical impacts, high launch loads, or electrical faults.	Communication links become unreliable or fail, leading to potential mission-critical data loss.	VERY HIGH	VERY LOW	MODERATE	Introduce redundant antenna units on critical mission facets and perform extensive testing under relevant conditions.	MEDIUM	VERY LOW	SUSTAINABLE
17	Ground station unavailability when needed	Previous contracts with other missions, meteorological events, go closed for maintenance	Failure to downlink mission-critical images, leading to unmet objectives.	VERY HIGH	MEDIUM	SEVERE	Develop an extensive ground station network, including private provider backups.	VERY HIGH	VERY LOW	MODERATE
Propulsion T/s Risk										
18	Thruster Failure	Potential mechanical issues affecting thruster performance.	Failure to maintain or adjust satellite trajectory, compromising the mission.	VERY HIGH	LOW	SEVERE	Conduct exhaustive thruster testing under various conditions	VERY HIGH	VERY LOW	MODERATE
19	Feeding syste Failure	Mechanical stress	Thrusters fail to receive sufficient xenon, reducing propulsion capabilities.	VERY HIGH	LOW	SEVERE	Ensure redundancy in feedline design and conduct intensive testing.	VERY HIGH	VERY LOW	MODERATE
20	Hollow Cathode Failure	Thermal stress, contamination, or erosion of cathode material.	Reduced or complete loss of propulsion capabilities	VERY HIGH	VERY LOW	MODERATE	Investigate failure modes thoroughly and perform extensive reliability testing under mission-specific conditions.	HIGH	VERY LOW	SUSTAINABLE
21	PPU Failure	Electrical faults, component overheating, or inadequate thermal management.	Severe impact on propulsion and power supply, making the satellite inoperable.	VERY HIGH	MEDIUM	SEVERE	Conduct intensive testing of PPU	VERY HIGH	VERY LOW	MODERATE
Attitude Determination and Control s/s Risk										
22	Loss of accurate attitude determination	Optical sensor aging or radiation damages	Loss of accuracy for AAE, or incorrect estimations, leading to mission inaccuracies.	HIGH	MEDIUM	SEVERE	Use radiation-hardened optical sensors, schedule periodic recalibration, and plan for redundancy in critical attitude determination components.	HIGH	VERY LOW	SUSTAINABLE
23	Sun Sensor Failure	Mechanical loads experienced during launch or deployment.	Loss of accuracy for AAE, or incorrect estimations, leading to mission inaccuracies.	HIGH	LOW	MODERATE	Perform extensive shock and vibration testing, and include multiple sun sensors for redundancy.	HIGH	VERY LOW	SUSTAINABLE
24	Star Tracker Failure	Mechanical loads experienced during launch or deployment.	Loss of redundancy, incorrect attitude determination, and inability to perform fine pointing during NOM.	VERY HIGH	MEDIUM	SEVERE	Perform extensive shock and vibration testing, and include multiple star trackers for redundancy.	VERY HIGH	VERY LOW	MODERATE
25	GNSS Receiver Failure	Mechanical loads experienced during launch or deployment; electrical failures	No possibility to perform precise Orbit determination	HIGH	LOW	MODERATE	Implement algorithms to perform orbit determination using IMU and other sensors on board	LOW	LOW	SUSTAINABLE
26	Magnetorquer failure	Mechanical loads experienced during launch or deployment; electrical failures	Detumbling and desaturation performances strongly reduced	VERY HIGH	MEDIUM	SEVERE	Perform extensive test, analyse the possibility of performing detumbling and desaturation only with 2/3 rods	VERY HIGH	VERY LOW	MODERATE
27	Reaction wheel Failure	Mechanical loads during launch or deployment; wear or electrical faults,	Loss of control authority	VERY HIGH	MEDIUM	SEVERE	Incorporate reaction wheel redundancy, perform life-cycle durability tests	VERY HIGH	VERY LOW	MODERATE
Structure s/s Risk										
28	Solar panels deployment failure	Mechanical failure in deployment mechanisms.	Solar panels become non-functional, and the mission cannot meet required power demands.	VERY HIGH	MEDIUM	SEVERE	Ensure actuator redundancy and conduct extensive pre-deployment testing to identify potential failures.	VERY HIGH	VERY LOW	MODERATE
On Board Data Handling s/s Risk										
29	Main OBC permanent failure due to SEU	SEU, SEL or SEB could cause irreversible damage to the OBC electronics	Complete mission loss due to the inability to control the platform.	VERY HIGH	HIGH	Critical	Ensure redundancy with a secondary OBC capable of managing the main functionalities, even with reduced performance.	VERY HIGH	LOW	SEVERE
30	Secondary OBC permanent failure due to SEU	SEU, SEL or SEB could cause irreversible damage to the OBC electronics	Degraded performance in the ADCS, reducing mission effectiveness.	HIGH	HIGH	Critical	Ensure redundancy with the main OBC, ensuring it can fully control the ADCS subsystem if necessary.	HIGH	LOW	MODERATE

Figure 101: Risk Matrix

From the risk matrix above, 30 high-level risks have been identified that could compromise the mission. A more detailed examination of the results highlights the following risks:

- **Critical risks:** The most significant are the availability of the launcher and the potential failure of the main onboard computer. While strategies have been identified to reduce the probabilities of these events, completely preventing them is still difficult. As a result, thorough planning is required to limit their impact on the project.
- **Severe risks:** These mainly involve the proper functioning of the propulsion systems, attitude determination, and power management. Although not classified as critical, these risks could still have significant consequences. Extensive testing and redundancy strategies are essential to minimize potential failures or mission damage.
- **Moderate risks:** Among these are some risks, such as solar panel degradation and partial loss of attitude control. Although they do not pose an immediate risk to mission success, poor management could result in cumulative effects over time, with a possible reduction of mission operational lifespan or performance.

To mitigate these risks, it is important to implement a strategy based on system redundancy, extensive testing, high-reliability components, and well-defined emergency procedures. Moreover, a flexible planning approach will be crucial to ensure project feasibility and maximizing the chances of success.

This is a preliminary risk analysis conducted in the early phases of the HORUS mission lifecycle. As the lifecycle evolves, continuous monitoring and updates will be necessary to refine mitigation strategies, to further reduce the impact of each risk.

20 Mission Timeline

The mission timeline for HORUS is structured with the goal of achieving launch readiness by the beginning of 2029, marking a four-year development period starting from the second semester of 2024. This time frame of development is considered realistic, as no new technologies will need to be designed and tested. Indeed, the majority of the components will be COTS, allowing the design phase to progress quickly.

The phase that will require the most time is Phase D, which involves rigorous testing of all hardware to ensure compliance with the VLEO environmental conditions. Additionally, starting from Phase C, the construction of a parallel production facility will begin, with completion and availability expected by the end of Phase D. This facility will significantly enhance drone production, enabling the manufacture of approximately 20 drones per year.

A significant external constraint on the timeline is the availability of a suitable launcher. While HORUS is expected to be ready for launch by 2029, the timeline may need to be adjusted if no European launch vehicle with the required flexibility is available at that time. To address this potential issue, the mission schedule will be strongly influenced, and the option of using non-European launchers should be considered. The HORUS mission timeline is reported in Figure Figure 102. The mission phases are temporally arranged to align with the distribution of reviews in accordance with ECSS-M-ST-10C guidelines.

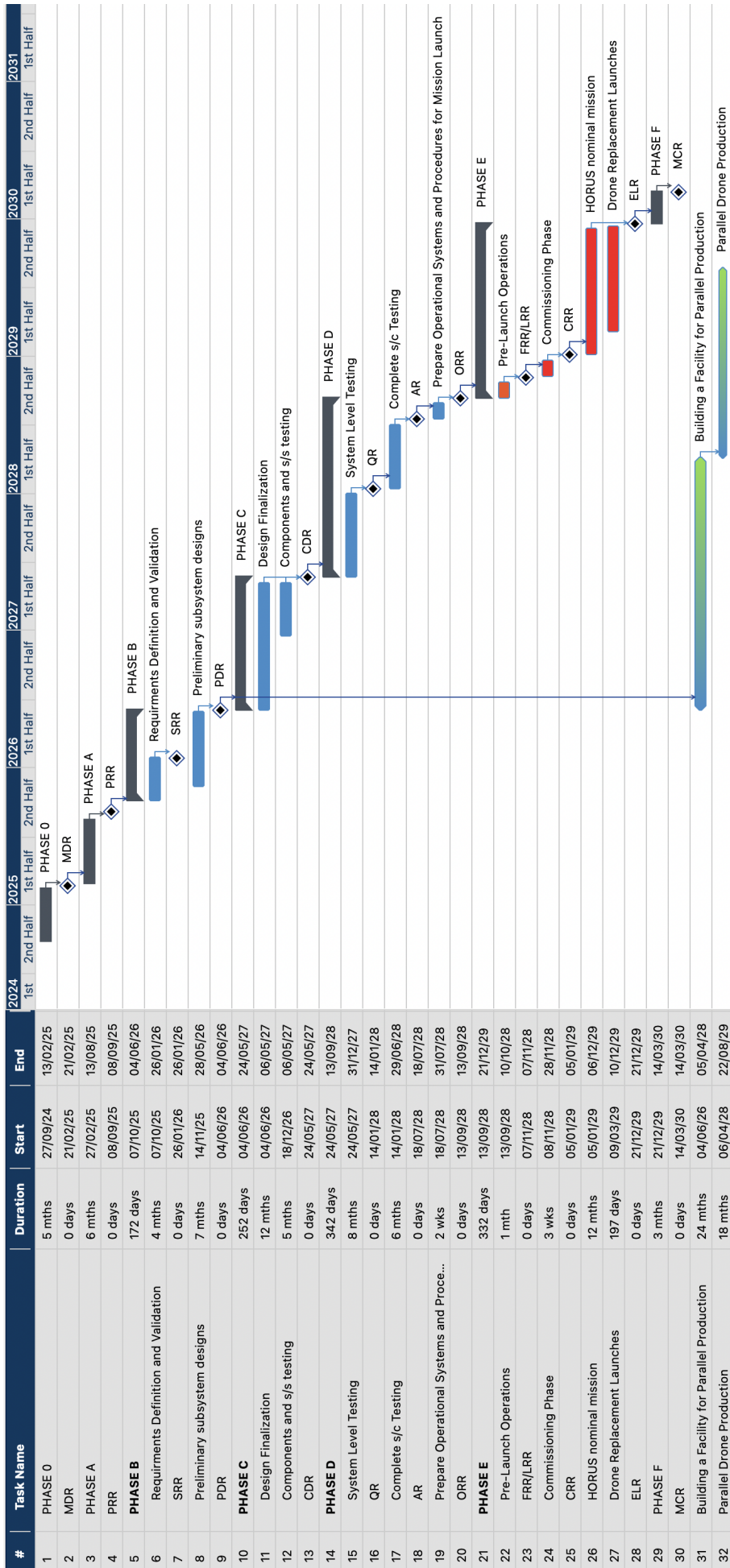


Figure 102: HORUS mission timeline

21 Costs Analysis

This section aims to present a preliminary cost estimation for the HORUS mission. The analysis relies on the **Parametric Estimation Approach**, which has been adopted due to the limited availability of reliable data and cost figures during the early stages of the project. This method is based on Cost Estimating Relationship (CERs), constructed using historical data and past trends. For this analysis, the Small Satellite Costs Model (SSCM) was employed [17]. This model provides a more comprehensive view of the costs of modern, small satellites, highlighting the greater complexities involved.

21.1 Space Segment

Table 74, below, presents the costs related to the space segment, including hardware, software, and program-level costs. The latter accounts for labor-intensive activities, where a defined level of manpower is allocated over a specified performance period. These costs are estimated as a percentage of the hardware costs and cover functions such as management, systems engineering, and product assurance [17]. The analysis also considers costs related to payload, AIVT at the subsystem level, expenses related to ground support equipment, support during launch, and orbital operations. The payload cost has been provided directly by the supplier. Moreover, AIVT activities are yet to be finalized. In some instances, specific components need to be developed in-house to guarantee full consistency with the design requirements and the expected performance. Specifically, the propulsion system tanks, the ADCS software, and the TCS heat switches will be developed internally. All other components have been considered as COTS and are characterized by a high TRL in LEO, that, as already mentioned, need to be tested in VLEO environment. Figure 103 shows the percentages estimated by the CERs regarding the fraction of the space bus for the various subsystems.

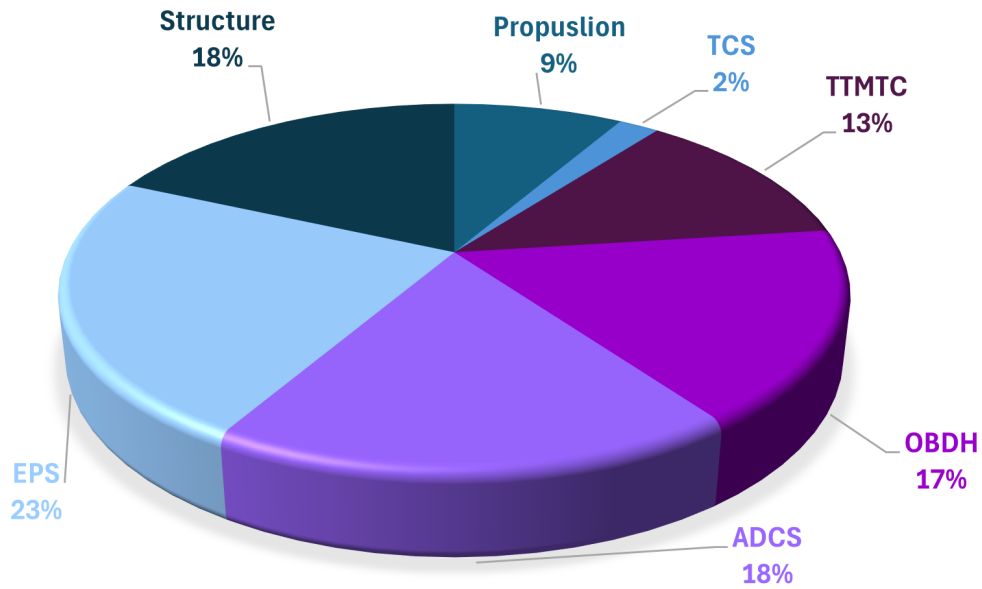


Figure 103: Space Bus Distribution

In general, the costs have been divided into non-recurring costs, as the Research, Development, Test & Evaluation (RDT&E) costs needed for the first unit, and recurring costs, as the one related to hardware supply. Regarding the costs related to the flight software, they have been estimated using the Constructive Cost Model (COCOMO)[111], with an estimated value of 42 Thousand of Lines of Code (KLOC). The cost distribution is shown in the table below.

Cost Item	RDT&E	Recurring Costs	Total Cost
Propulsion	0.382	0.382	0.764
TCS	0.091	0.091	0.182
TTMTC	0.115	1.032	1.147
OBDH	0.156	1.401	1.557
ADCS	0.620	1.055	1.675
EPS	0.212	1.909	2.121
Structure	1.166	0.500	1.666
Payload	-	0.400	0.400
AIV/AIT	-	1.267	1.267
GSE	-	0.601	0.601
Program Management	0.208	0.313	0.521
System Engineering	0.417	0.208	0.625
Product Assurance	0.208	0.313	0.521
System Evaluation	0.208	0.208	0.416
On-Board Software	-	2.689	2.689
Total First Unit	3.787	12.369	16.156

Table 74: Space Segment Cost, M€

As the space segment includes several recurring items, a learning curve was applied to model the reduction in costs for subsequent units, with a slope of 95% up to the fourth unit, 90% from the fifth to the tenth, and 85% from the eleventh to the fifteenth.

Space Segment	Number of Units	Cost of all units
Space Bus	9	44.056
Payload	18	3.6
AIV/AIT	9	8.762
GSE	-	0.601
program Level	9	7.213
On-Board Software	1	2.689
Total		66.921

Table 75: Total cost for 9 units, in M€

21.2 Launch and Operations Costs

The launch segment costs, shown in Table 76, were estimated considering the Vega-C launcher, as it represents the most expensive option according to Table 20. The cost of the Vega-C launcher has been considered 0.0115 M€/kg, this also includes all the costs related to the operations and monitoring activities required during this phase. As presented in Section 7.1.1, nine units per launch are considered.

Launch Segment	Vega-C [M€/kg]	Mass of one unit [kg]	Number of unit	Total Cost
Case 1	0.0115	104.67	1	1.204
Case 2	0.0115	104.67	9	10.83

Table 76: Launch segment cost, M€

The **operations costs** are composed by the costs for communications and personnel. The estimated duration for operations is approximately one year and a half, though it remains to be finalized. Personnel costs have been estimated based on the duration of the various mission phases, on the number of employees, and on role of the personnel involved. The salary values were derived from industry data and relevant sources. The final estimation amounts to 4.644 M €.

Regarding communication costs, the analysis considers the ground stations owned by ESA, SSC and LeafSpace. According to the available data, the communication cost for one satellite pass over the ground station is 35 €/pass. Three scenarios have been evaluated for the communication costs of the HORUS mission with the selected ground stations:

- **Case 1:** one satellite is used, which allows three passages per day over the selected ground stations, providing direct coverage unless the ground stations are already occupied.
- **Case 2:** nine drones are used, considering launcher constraints, allowing 27 passages per day over the chosen ground stations. This estimate is consistent with the cost analysis of a scalable production of nine units.
- **Case 3:** 20 drones are used, allowing 60 passages per day over the chosen ground stations, with direct coverage available within an hour from 19 drones.

Operations Costs	Cost
Personnel	4.644
Ground Station	
Case 1	0.058
Case 2	0.517
Case 3	1.150
Total	
Case 1	4.702
Case 2	5.161
Case 3	5.794

Table 77: Operations Segment Costs, in M€

21.3 Results and Conclusions

The following tables present the overall budget for the HORUS mission in two scenarios: one considering the development, the testing, and the production of the first drone and the other considering the same for successive nine units.

Components	Cost [M€]
Space Segment	16.156
Launch Segment	1.204
Operation Costs	4.702
Total Cost	22.062
Total Cost with 20% of margin	26.474

Table 78: Total cost of HORUS in case of the first drone

The final costs have been calculated by applying a 20% margin, which will help mitigate potential issues such as uncertainties in material supply, supplier availability, and transportation costs. This margin was introduced due to the use of different estimation models: the launch segment costs were based on general data regarding the launcher costs, while the space segment costs were determined using a parametric approach. Furthermore, as the mission progresses into later development phases, a more detailed cost analysis will be conducted.

Components	Cost [M€]
Space Segment	66.921
Launch Segment	10.83
Operation Costs	5.161
Total Cost	82.912
Total Cost with 20% of margin	99.494

Table 79: Total cost of HORUS in case of nine drones

References

- [1] C. Y. Chi, I. U. Wanigaratne, and D. Dubinsky, “How low can you go: Advocating very low Earth orbit as the next frontier for satellite operations,” in *8th European Conference on Space Debris, Darmstadt, Germany*, 2021.
- [2] V. Ray, T. Berger, Z. Waldron, and E. Sutton, “The impact of space weather on very low Earth orbit (VLEO) satellites,” in *Advanced Maui optical surveillance and space technologies conference*, 2022.
- [3] U. G. P. Office, *U.S. Standard Atmosphere, 1976*. Washington, D.C.: U.S. Government Printing Office, 1976.
- [4] M. P. F. Gamgami, M. Sinnhuber and C. V. Savigny, “In-situ exploration of Earth’s atmosphere using novel spacecraft design,” in *IAC-09-B1.2.2*, 2009.
- [5] NOAA. Solar euv irradiance. [Online]. Available: <https://www.swpc.noaa.gov/phenomena/solar-euv-irradiance>
- [6] M. Mahooti, “Jacchia-bowman atmospheric density model,” <https://www.mathworks.com/matlabcentral/fileexchange/56163-jacchia-bowman-atmospheric-density-model>, 2024, MATLAB Central File Exchange.
- [7] G. Chen, X. Li, M. He, S. Liu, H. Man, H. Gao, and Y. Li, “Longitudinal variation of thermospheric density during low solar activity from apod observations,” *Atmosphere*, vol. 14, no. 1, p. 155, 2023.
- [8] J. Xu, A. K. Smith, W. Wang, G. Jiang, W. Yuan, H. Gao, J. Yue, B. Funke, M. Lòpez-Puertas, and J. M. I. Russell, “An observational and theoretical study of the longitudinal variation in neutral temperature induced by aurora heating in the lower thermosphere,” *Journal of Geophysical Research: Space Physics*, vol. 118, no. 11, pp. 7419–7434, 2013.
- [9] H. Above, “ISS Height Above Ground Track,” <https://www.heavens-above.com/IssHeight.aspx>, 2024, accessed: 2024-10-18.
- [10] S. A. Rawashdeh and J. James E. Lumpp, “Aerodynamic stability for CubeSats at ISS orbit,” *Journal Of Small Satellites*, vol. 2, pp. 85–104, 2013.
- [11] J. Walsh and L. Berthoud, “Distribution of Atomic Oxygen within the internal cavities of VLEO Satellites,” 2023.
- [12] B. E. Holmes, V. T. Oiko, and P. C. Roberts, “A review of satellite-based atomic oxygen sensing methods,” 2023. [Online]. Available: <https://doi.org/10.1016/j.paerosci.2023.100886>
- [13] ESA (European Space Agency). (2024) SPENVIS: Space Environment Information System. [Online]. Available: <https://www.spenvis.oma.be/>
- [14] M. Mahooti, “Nrlmsise-00 atmosphere model,” <https://www.mathworks.com/matlabcentral/fileexchange/56253-nrlmsise-00-atmosphere-model>, 2024.
- [15] S. Avcu and B. Celik, “Structural material selection and processing for low earth orbit spacecraft regarding atomic oxygen effects,” in *International Conference on Recent Advances in Space Technologies, 2003. RAST’03. Proceedings of*. IEEE, 2003, pp. 589–594.
- [16] S. Yagnamurthy, Q. Chen, C. Chen, and I. Chasiotis, “Erosion yield of epoxy–silica nanocomposites at the lower earth orbit environment of the international space station,” *Journal of composite materials*, vol. 47, no. 1, pp. 107–117, 2013.
- [17] J. R. Wertz, W. J. Larson, D. Kirkpatrick, and D. Klungle, *Space mission analysis and design*. Springer, 1999.

- [18] A. Henderson-Sellers and M. Wilson, "Surface albedo data for climatic modeling," *Reviews of Geophysics*, vol. 21, no. 8, pp. 1743–1778, 1983.
- [19] S. Dewitte and N. Clerbaux, "Decadal changes of earth's outgoing longwave radiation," p. 1539, 2018.
- [20] E. O. S. Missions, "Earth Science Reference Handbook."
- [21] NASA Earth Observations (NEO), "Nasa earth observations: Data and imagery," 2024. [Online]. Available: <https://neo.gsfc.nasa.gov/>
- [22] J. Virgili Llop, "Spacecraft flight in the atmosphere," 2014.
- [23] B. R. Bowman *et al.*, "A New Empirical Thermospheric Density Model JB2006 Using New Solar Indices," in *AIAA/AAS Astrodynamics Specialists Conference*. Keystone, CO: AIAA, August 2006, (Paper AIAA 2006-6166).
- [24] A. E. Stiegan and R. H. Liang, "Ultraviolet and vacuum-ultraviolet radiation effects on spacecraft thermal control materials," in *The Behavior of Systems in the Space Environment*. Springer, 1993, pp. 259–266.
- [25] D. Gilmore and R. Collins, "Spacecraft thermal control handbook."
- [26] T. Mikaelian, "Spacecraft Charging and Hazards to Electronics in Space," Master's thesis, York University, May 2001. [Online]. Available: <https://arxiv.org/pdf/0906.3884>
- [27] D. Cilden-Guler, Z. Kaymaz, and C. Hajiye, "Geomagnetic disturbance effects on satellite attitude estimation," *Acta Astronautica*, vol. 180, pp. 701–712, 2021. [Online]. Available: <https://www.sciencedirect.com/science/article/pii/S0094576520307888>
- [28] A. Zinecker, B. Spivey, G. Jayne, and M. Hasegawa, "Solar absorptivity degradation of spacecraft materials due to uv and charged particles in the gateway environment," in *IOP Conference Series: Materials Science and Engineering*, vol. 1287, no. 1. IOP Publishing, 2023, p. 012009.
- [29] N. H. Crisp, P. C. Roberts, F. Romano, K. Smith, V. Oiko, V. Sulliotti-Linner, V. Hanessian, G. Herdrich, D. García-Almiñana, D. Kataria *et al.*, "System modelling of very low Earth orbit satellites for Earth observation," *Acta Astronautica*, vol. 187, pp. 475–491, 2021.
- [30] V. C. Muñoz, D. González, J. Becedas, R. Dominguez, P. Roberts, N. Crisp, V. T. A. Oiko, S. Edmondson, S. Worrall, S. Haigh *et al.*, "Attitude control for satellites flying in VLEO using aerodynamic surfaces," *JBIS-Journal of the British Interplanetary Society*, vol. 73, no. 3, pp. 103–112, 2020.
- [31] J. V. Llop, P. C. E. Roberts, Z. Hao, L. R. Tomas, and V. Beauplet, "Very Low Earth Orbit mission concepts for Earth Observation: Benefits and challenges," in *Reinventing Space Conference 2014*, ser. BIS-RS-2014-37, Bedfordshire, UK, 2014. [Online]. Available: <https://www.researchgate.net/publication/271499606>
- [32] EO Portal, "Colony 1 Satellite Mission," accessed: 2024-10-14. [Online]. Available: <https://www.eoportal.org/satellite-missions/colony-1>
- [33] ——, "Planet Satellite Missions-SuperDove," accessed: 2024-10-14. [Online]. Available: <https://www.eoportal.org/satellite-missions/planet>
- [34] Planet Labs PBC, "Planet Imagery Product Specifications-SkySat," 2023, accessed: 2024-10-14. [Online]. Available: <https://www.planet.com>
- [35] I. Sakraker, E. Umit, T. Scholz, P. Testani, G. Baillet, and V. Van der Haegen, "Qarman: An atmospheric entry experiment on cubesat platform," in *Envisat Symposium SP-636*. European Space Agency, 2015. [Online]. Available: https://www.researchgate.net/publication/277891078_QARMAN_AN_ATMOSPHERIC_ENTRY_EXPERIMENT_ON_CUBESAT_PLATFORM

- [36] G. F. C. Team, “GOCE End-of-Mission Operations Report,” European Space Agency (ESA), Cranfield University, Bedfordshire, UK, Tech. Rep. GO-RP-ESC-FS-6268, 2014, issue 1, Revision 0. [Online]. Available: <https://www.esa.int>
- [37] J. Virgili Llop, “Spacecraft flight in the atmosphere, PhD Thesis,” Ph.D. dissertation, Cranfield University, 2014.
- [38] C. Steiger, J. Piñeiro, and P. P. Emanuelli, “Operating GOCE, the European Space Agency’s Low-flying Gravity Mission,” in *Proceedings of the European Space Operations Conference*. Darmstadt, Germany: European Space Agency, 2010, european Space Operations Centre (ESOC), Robert-Bosch Str. 5, 64293 Darmstadt, Germany.
- [39] E. S. D. M. W. Group, *ESA Space Debris Mitigation Requirements*, October 2023, approved by ESB on 30 October 2023.
- [40] ESA. (2012) Margin philosophy for science assessment studies. [Online]. Available: https://sci.esa.int/documents/34375/36249/1567260131067-Margin_philosophy_for_science_assessment_studies_1.3.pdf
- [41] A. T. Kent M. Price, David Pidgeon, “Mass and Power Modeling of Communication Satellites,” NASA, Tech. Rep. SS/L-TR00821, 1991. [Online]. Available: <https://ntrs.nasa.gov/api/citations/19920019663/downloads/19920019663.pdf>
- [42] T. Nemetzade, “Dimensional Analysis for the Design of Satellites in LEO,” 2010. [Online]. Available: http://strategic.mit.edu/docs/Diplomarbeit_Tanja_Nemetzade.pdf
- [43] M. C. Alonso, M. A. Sanz, and J. A. Malpica, “Classification of high resolution satellite images using texture from the panchromatic band,” in *International symposium on visual computing*. Springer, 2007, pp. 499–508.
- [44] Satlantis, *iSIM-90 Micro Camera*, 2024. [Online]. Available: <https://satlantis.com/isim-90/>
- [45] Arianespace, “ARIANE 6 User’S Manual,” February 2021. [Online]. Available: https://ariane.group/app/uploads/sites/4/2024/10/Mua-6_Issue-2_Revision-0_March-2021.pdf
- [46] ——, “VEGA C User’S Manual,” May 2018. [Online]. Available: https://newspaceconomy.ca/wp-content/uploads/2022/06/vega-c-user-manual-issue-0-revision-0_20180705.pdf
- [47] E. Spaceflight. European Rocket Index. [Online]. Available: <https://europeanspaceflight.com/european-rocket-index/>
- [48] Arianespace, “VEGA-C SSMS User’S Manual,” September 2020.
- [49] ——, “Ariane-6 MLS User’S Manual,” July 2021.
- [50] “Analytical Approximations for Low Thrust Maneuvers,” 2015. [Online]. Available: https://ocw.mit.edu/courses/16-522-space-propulsion-spring-2015/7f725e54b9be201164d56ebbd5e08023/MIT16_522S15_Lecture6.pdf
- [51] O. Petrenko, “Electric propulsion system SPS-25 with Hall Thruster,” 2019. [Online]. Available: <https://sets.space/wp-content/uploads/2020/02/IAC-19C444x50659.pdf>
- [52] ESA. (2024) New Space Debris Mitigation Policy and Requirements in effect. [Online]. Available: <https://esoc.esa.int/new-space-debris-mitigation-policy-and-requirements-effect>
- [53] NASA. (2024) Deorbit systems. [Online]. Available: <https://www.nasa.gov/smallsat-institute/sst-soa/deorbit-systems/>
- [54] B. Bowman, W. K. Tobiska, F. Marcos, and C. Huang, “The thermospheric density model jb2008 using new euv solar and geomagnetic indices,” *AIAA/AAS Astrodynamics Specialist Conference*, vol. 37, p. 367, 01 2008.

- [55] K. Khalil and S. Samwel, “Effect of air drag force on low earth orbit satellites during maximum and minimum solar activity,” *Space Research Journal*, vol. 9, pp. 1–9, 03 2016.
- [56] R. Falck *et al.*, “Comparison of Low-Thrust Control Laws for Applications in Planetocentric Space,” in *Conference Paper*, July 2014. [Online]. Available: <https://www.researchgate.net/publication/269207909>
- [57] A. Ruggiero, P. Pergola, S. Marcuccio, and M. Andrenucci, “Low-Thrust Maneuvers for the Efficient Correction of Orbital Elements,” in *IEPC-2011-102*, Alta, Pisa, 56100, Italy, University of Pisa, Pisa, 56100, Italy, September 2011, presented at the 32nd International Electric Propulsion Conference, Wiesbaden, Germany, September 11-15, 2011.
- [58] A. Garulli, A. Giannitrapani, M. Leomanni, and F. Scortecci, “Autonomous low-earth-orbit station-keeping with electric propulsion,” *Journal of Guidance, Control, and Dynamics*, vol. 34, no. 6, pp. 1593–1600, 2011. [Online]. Available: <https://doi.org/10.2514/1.52985>
- [59] B. J. Naasz, “Classical element feedback control for spacecraft orbital maneuvers,” Ph.D. dissertation, Virginia Polytechnic Institute and State University, Blacksburg, Virginia, May 2002, chapter 4. [Online]. Available: <https://vttechworks.lib.vt.edu/handle/10919/29203>
- [60] M. Leomanni, A. Garulli, A. Giannitrapani, and F. Scortecci, “Propulsion Options for Very Low Earth Orbit Microsatellites.” [Online]. Available: <https://www3.diism.unisi.it/~control/Aerospace/papers/AA16.pdf>
- [61] T. Andreussi, E. Ferrato, and V. Giannetti, “A review of air-breathing electric propulsion: from mission studies to technology verification,” 2022. [Online]. Available: <https://www.iris.sssup.it/retrieve/ea75eb42-2e80-462b-be1e-588ed43871e3/Andreussi%20et.al.%202022.pdf>
- [62] T. Misuri, “Low Power Electric Propulsion At Sitael,” 2017. [Online]. Available: https://agenda.infn.it/event/12546/contributions/14697/attachments/10924/12274/Low-Power_Electric_Propulsion_at_SITAEL.pdf.pdf
- [63] “National Institute of Standards and Technology WebBook.” [Online]. Available: <https://webbook.nist.gov/chemistry/>
- [64] Consultative Committee for Space Data Systems (CCSDS), *Lossless Data Compression*, green book, issue 4 ed., CCSDS Secretariat, Washington, D.C., USA, 2020. [Online]. Available: <https://public.ccsds.org/Pubs/120x0g4.pdf>
- [65] C. C. for Space Data Systems (CCSDS). (2024) Sls publications: Space link services. [Online]. Available: <https://public.ccsds.org/Publications/SLS.aspx>
- [66] T. Yamada, “Ccsds telemetry/telecommand standards restructured as communications protocols,” in *Proceedings of the Institute of Space and Astronautical Science*. 3-1-1 Yoshinodai, Sagamihara 229-8510, Japan: Institute of Space and Astronautical Science.
- [67] A. C. SPace, *Datasheet of [PULSAR-SANT]*, 2023. [Online]. Available: <https://www.aac-clyde.space/wp-content/uploads/2021/10/PULSAR-SANT-2.pdf>
- [68] CubeCom, *Datasheet of [STXG2]*. [Online]. Available: <https://cubecom.space/s-band/>
- [69] A. C. Space, *Datasheet of [AAC SpaceQuest RX-2000]*, 2024. [Online]. Available: <https://www.aac-clyde.space/wp-content/uploads/2021/11/RX-2000-1.pdf>
- [70] M. amps, *Datasheet of [AM38A]*. [Online]. Available: https://microwaveamps.co.uk/product/power-amplifiers-am38a/?_gl=1*k88uye*_up*MQ..&gclid=Cj0KCQiAsOq6BhDuARIsAGQ4-zi-nRUKsYLrm2pcrHiygTY3dNcS5hiwayfDSbtei-oW07tmAMqmDFwaAocxEALw_wcB
- [71] A. E. N. Saeed and H. Almorad, “Cubesat communications: Recent advances and future challenges,” pp. 1839–1861, 2020.

- [72] S. S. Tyokighir, *BER performance*, 2018. [Online]. Available: https://www.researchgate.net/figure/BER-Performance-for-OQPSK_fig3_352689424
- [73] ESA. (2025) Redu ground station. [Online]. Available: <https://connectivity.esa.int/about-esat-redu-centre>
- [74] ——, *Estrack ground station network*, 2025. [Online]. Available: https://www.esa.int/Enabling-Support/Operations/ESA_Ground_Stations/Estrack_ESA_s_global_ground_station_network
- [75] NASA. (2024) Nasa to embrace commercial sector. [Online]. Available: <https://www.nasa.gov/centers-and-facilities/goddard/nasa-to-embrace-commercial-sector-fly-out-legacy-relay-fleet/>
- [76] B. E. BV, *SUPERNOVA HIGH POWER PCDU Datasheet*, Bradford Space Deep Space Industries, Luxembourg, 2021, non-contractual document, subject to changes. [Online]. Available: <https://fra1.digitaloceanspaces.com/bradford/documents/Bradford%20SuperNova%20PCDU%20Datasheet%20rev%20B.pdf>
- [77] I. VPT, *VSC100-2800S DC-DC Converters Datasheets*, VPT, Inc, 19909 120th Avenue NE Suite 102 Bothell, WA 98011, -. [Online]. Available: <https://www.vptpower.com/products/datasheet/vsc100-2800s-series-pdf>
- [78] SPECTROLAB, *32.2% XTE-SF (Standard Fluence)*, 2024. [Online]. Available: https://www.spectrolab.com/photovoltaics/XTE-SF%20Data%20Sheet%20_07.27.22.pdf
- [79] P. R. K. Chetty, “Electrical power system for low-earth orbit spacecraft applications,” *Intersociety Energy Conversion Engineering Conference (IECEC), Philadelphia, PA*, 1990. [Online]. Available: <https://arc.aiaa.org/doi/10.2514/3.23224>
- [80] J. J. P. Wertz, David F. Everett, *Space Mission Engineering: The New SMAD*. Microsom Press, 2011.
- [81] A. E. T. C. QIOPTRIC, *Solar Cell Coverglasses*, Excelitas Technologies Corp. [Online]. Available: https://www.excelitas.com/product/space-qualified-cover-glass?utm_source=chatgpt.com
- [82] S. S. . D. Division, *VES16 Battery Data Sheet*, Saft America, Inc. and Saft Space & Defense Division, France, Cockeysville, MD, USA and Poitiers Cedex 9, France, 2020, data subject to change without notice. Becomes contractual only after written confirmation by Saft. [Online]. Available: https://spw.aerospace.org/files/2021/07/2019_04_02_IV-e_Borthomieu.pdf
- [83] F. L. Markley and J. L. Crassidis, *Fundamentals of Spacecraft Attitude Determination and Control*, ser. Space Technology Library. Springer, 2014, vol. 33.
- [84] MDA Corporation, “Sirc - space infra-red camera datasheet,” MDA Corporation, Tech. Rep., February 2025, local file reference.
- [85] D. P. C. Limited, “3.7v 4500mah lithium-polymer battery specification,” Battery Datasheet, 2025. [Online]. Available: <https://www.fpbattery.com/3-7v-4500mah-lithium-polymer-battery/>
- [86] Vectronic Aerospace, “Reaction wheels for aerospace applications,” Vectronic Aerospace, Tech. Rep., February 2025.
- [87] AAC Clyde Space, “Mtq800 magnetorquer datasheet,” AAC Clyde Space, Tech. Rep., February 2025.
- [88] Honeywell Aerospace, “Smart digital magnetometer hmr2300,” Honeywell Aerospace, Tech. Rep., February 2025.
- [89] Senonor, “Stim210 multi-axis gyro module,” Senonor, Tech. Rep., February 2025.
- [90] AAC Clyde Space, “Gnss-701 high-performance spaceborne gps receiver,” AAC Clyde Space, Tech. Rep., February 2025.

- [91] Solar MEMS Technologies, “Nanossoc-d60 sun sensor,” Solar MEMS Technologies, Tech. Rep., February 2025.
- [92] Terma A/S, “Terma t3 star tracker data sheet,” Terma A/S, Tech. Rep., February 2025.
- [93] Space Electric Thruster Systems (SETS), “Power processing unit (ppu),” Space Electric Thruster Systems (SETS), Tech. Rep., February 2025.
- [94] Valiant Space, “Coaxial solenoid valve (csv) datasheet,” Valiant Space, Tech. Rep., February 2025.
- [95] SITAEL, “Low power electric propulsion at sitael,” INFN Workshop, Tech. Rep., 2017.
- [96] Zoppas Industries, “Flexible heaters for space,” Zoppas Industries, Tech. Rep., February 2025.
- [97] Collins Aerospace, “Rosemount model 0118mm temperature sensor,” Collins Aerospace, Tech. Rep., February 2025.
- [98] CubeCom, “S-band transceiver datasheet,” CubeCom, Tech. Rep., February 2025.
- [99] Skylabs, “Sky-nanolink-s interface control document v1.5,” Skylabs, Tech. Rep., February 2025.
- [100] EXA, “Ssa02-34db wide bandwidth amplified s-band patch antenna,” EXA, Tech. Rep., February 2025.
- [101] F. Czerwinski, “Thermal stability of aluminum alloys,” *Materials (Basel)*, vol. 13, no. 15, p. 3441, 2020.
- [102] Vallen Systeme GmbH, “Acoustic emission sensors specification,” Vallen Systeme GmbH, Tech. Rep., 2017.
- [103] GomSpace, “Nanomind hp mk3,” GomSpace, Tech. Rep., February 2025.
- [104] GomSpace, *Datasheet of [NanoMind A3200]*, 2024. [Online]. Available: <https://gomspace.com/shop/subsystems/command-and-data-handling/nanomind-a3200.aspx>
- [105] ANSYS Granta, “Granta EduPack 2021 R2,” ANSYS, Inc., 2021, material intelligence software for education and engineering. [Online]. Available: <https://www.ansys.com/products/materials/granta-edupack>
- [106] A. S. GmbH, “Flexible thermal links,” 2025. [Online]. Available: <https://www.azimutspace.com>
- [107] Sierra Space Corporation, “Thin plate heat switch,” Sierra Space Corporation, Tech. Rep., Jan. 2024. [Online]. Available: <https://www.sierraspace.com/wp-content/uploads/2024/01/THERMAL-CONTROL-SYSTEMS-Thin-Plate-Heat-Switch.pdf>
- [108] A. Space, *Datasheet of [DARA OBC]*, 2024. [Online]. Available: <https://alen.space/products/dara-obc/>
- [109] E. Secretariat, “Space engineering - Testing,” ESA-ESTEC Requirements Standards Division, Tech. Rep., 2022. [Online]. Available: [https://ecss.nl/wp-content/uploads/2022/05/ECSS-E-ST-10-03-Rev.1\(31May2022\).pdf](https://ecss.nl/wp-content/uploads/2022/05/ECSS-E-ST-10-03-Rev.1(31May2022).pdf)
- [110] Pietro Nali, “Analysis and Testing of Space Structures,” Politecnico di Milano, 2024.
- [111] NASA (National Aeronautics and Space Administration). (2021) COCOMO: Constructive Cost Model. [Online]. Available: <https://strs.grc.nasa.gov/repository/forms/cocomo-calculation/>